# SLOSHING IN RESERVOIRS WITH MULTI-DEGREES-OF-FREEDOM BASE MOTIONS

by

Sundaralingam Premasiri

B.Sc.Eng., University of Peradeniya, Sri Lanka, 1992

M.Eng., University of Tokyo, Japan, 1995

M.A.Sc., University of British Columbia, 1997

A THESIS SUBMITTED IN PARTIAL FULFILLMENT OF
THE REQUIREMENTS FOR THE DEGREE OF
DOCTOR OF PHILOSOPHY

in

THE FACULTY OF GRADUATE STUDIES
DEPARTMENT OF CIVIL ENGINEERING

We accept this thesis as conforming
to the required standard

THE UNIVERSITY OF BRITISH COLUMBIA

May 2000

In presenting this thesis in partial fulfillment of the requirements for an advanced degree at the University of British Columbia, I agree that the library shall make it freely available for reference and study. I further agree that permission for extensive copying of this thesis for scholarly purposes may be granted by the head of my department or by his or her representatives. It is understood that copying or publication of this thesis for financial gain shall not be allowed without my written permission.

Department of Civil Engineering
The University of British Columbia
2324 Main Mall
Vancouver, B.C., V6T 1Z4
Canada

Date: June 8, 2000

# Abstract

This thesis describes an investigation of the influence of multiple base motion components and hydrodynamic damping on the hydrodynamic loads and fluid surface elevation in a fluid filled reservoir subjected to base excitation. The investigation is carried out for two configurations: rectangular and circular cylindrical reservoirs. The multiple motions are horizontal and rocking excitations and the hydrodynamic damping is due to boundary layers along the reservoir walls and baffles in the reservoir. Initially, the boundary value problem for the case of an inviscid fluid and a harmonic base motion is solved on the basis of linearized potential flow theory. The case of energy dissipation of a real fluid is then treated by a extension to this, which involves an assumption of dissipation at the free surface and a corresponding modification to the free surface boundary condition. In order to treat earthquake-induced motions, this solution is then extended to a simplified method of estimating maximum forces using a modal analysis and involving earthquake response spectra. The estimation of hydrodynamic damping is also discussed. The combined effect of the two component excitations on the overall fluid elevation and hydrodynamic forces are calculated using superposition.

An experimental investigation for liquid filled rectangular tanks has been carried out. The tanks were subjected to component motions (horizontal and rocking) and combined motions, both for harmonic and earthquake motions. The important parameters are the size of the tank, depth of fluid, frequency of excitation, and amplitude of the base motion. The resulting parameters of interest include the maximum fluid surface elevation, the maximum horizontal force and the maximum overturning moment at the base of the tank.

The experiments were extended to investigate the effects of damping, whereby the experiments were repeated with baffles in the rectangular reservoir. The theoretical results are compared with existing solutions and experimental results. The effects of additional degrees of freedom motions and of hydrodynamic damping on the hydrodynamic loading and fluid elevations are discussed in detail. The effects of

damping on hydrodynamic loading and the fluid surface elevation are also discussed. Finally, conclusions are given including the effect of multi-degree-of-freedom base motion, the effect of hydrodynamic damping and the effectiveness of various baffle configurations.

# Table of Contents

# List of Tables

# List of Figures

# List of Symbols

| | |
|---|---|
| a | radius of the circular tank or half length of rectangular tank |
| A | plate area normal to flow |
| b | half width of the rectangular tank |
| $C_a$ | added mass coefficient |
| $C_d$ | drag coefficient |
| $C_\lambda$ | dimensionless damping coefficient |
| d | fluid depth |
| $d_0$ | effective elevation correspond to high frequency mass |
| $d_n$ | effective elevation correspond to modal masses |
| $d'_0$ | effective elevation correspond to high frequency mass |
| $d'_n$ | effective elevation correspond to modal masses |
| D | energy dissipation rate |
| E | total energy of oscillation |
| $E_0$ | total initial energy of the oscillation |
| $f_w$ | friction coefficient |
| F | horizontal resultant force |
| $F_0$ | force component related to high frequency mass |
| $F_{max}$ | maximum horizontal force |
| $F_n$ | maximum force associated with n-th mode sloshing |
| $F_H$ | horizontal force due to horizontal excitation |
| $F_R$ | horizontal force due to rocking excitation |
| g | gravitational constant |
| h | elevation of horizontal baffle |
| $G_n$ | frequency dependent function |
| i | $=(\sqrt{-1})$ |
| $I_1$ | modified Bessel function of the first kind |
| $I'_1$ | derivative of modified Bessel function of the first kind with respect to their arguments |

$J_1$ Bessel function of the first kind

$J'_1$ derivative of Bessel function of the first kind with respect to their arguments

$k_s$ Nikuradse roughness

$k_n$ wave number

K kinetic energy

$\ell$ length of baffle

m mass of fluid in tank

$m_0$ high frequency effective mass

$m_a$ added mass

$m_e$ effective mass

$m_n$ modal mass

M overturning moment about tank base

M′ overturning moment about tank base including the component due to pressure distribution over the base of the tank

p hydrodynamic pressure

r radial coordinate (see Fig.1(b))

Re Reynolds number based on boundary layer thickness

RE local Reynolds number based on the local amplitude of fluid displacement just out side the boundary layer

$S_a$ spectral acceleration

$S_d$ spectral displacement

$S_v$ spectral velocity

t time

$T_n$ natural period

u horizontal velocity

$u_r$ velocity of the flow relative to the plate

$\dot{u}$ horizontal acceleration

U horizontal velocity amplitude

$U_r$ amplitude of $u_r$

V potential energy

| | |
|---|---|
| $x$ | coordinate in x-direction |
| $y$ | coordinate in y-direction |
| $z$ | coordinate in z-direction |
| $\alpha$ | relative baffle length for horizontal baffle ($\ell$/a) |
| $\beta$ | relative baffle length for vertical baffle ($\ell$/d) |
| $\delta$ | oscillatory boundary layer thickness |
| $\phi$ | velocity potential |
| $\phi_c$ | convective part of the velocity potential (f(x,y,z)) |
| $\phi_I$ | impulsive part of the velocity potential (f(x,y,z)) |
| $\Phi$ | total velocity potential (f(x,y,z,t)) |
| $\eta$ | free surface elevation |
| $\lambda$ | dimensional damping coefficient |
| $\mu$ | viscosity |
| $\nu$ | kinetic viscosity |
| $\theta$ | angle |
| $\rho$ | density of the liquid |
| $\tau$ | shear stress at the boundary |
| $\upsilon$ | logarithmic decrement of damping |
| $\omega$ | excitation frequency |
| $\omega_n$ | natural sloshing frequency |
| $\psi$ | angular velocity |
| $\Psi$ | angular velocity amplitude |
| $\zeta$ | dimensionless damping coefficient |

# Acknowledgments

The author would like to express his sincere appreciation and gratitude to his thesis supervisor, Dr. Michael Isaacson, for his advice, constant support and guidance throughout this research. As well, I am personally indebted to him for securing financial support for my graduate studies at UBC. I am also grateful to Dr. Carlos Ventura for his advice on the experimental part of this study, to Mr. John Baldwin for engaging me in useful discussions related to this thesis and to Drs. Sheldon Green, Ricardo Foschi and Carlos Ventura for reviewing an early draft of the thesis and providing useful feedback.

The experimental section of this thesis would not have been possible without the assistance of technicians of the Department of Civil Engineering, particularly Mr. Howard Nichol for his invaluable advice for the testing and Mr. Kurt Nielsen for the construction of the experimental model.

The author wishes to express his deep gratitude to his wife, Anushiya, for her strong support and encouragement throughout this study. The author would also like to thank his colleagues and friends, particularly T. Thavaraj and S. Sivathayalan, for their help and support.

Finally, financial support in the form of a research assistantship from the Department of Civil Engineering is greatly acknowledged.

# 1 Introduction

## 1.1 Introduction

The description of liquid sloshing in accelerated containers is a difficult problem which is of considerable practical importance in marine, aerospace and civil engineering. In a civil engineering context, the forces due to earthquake-induced sloshing in fluid-filled tanks and reservoirs are important considerations in the design of such structures. Thus, seismic safety of ground-based and elevated liquid-filled containers is of great concern because of the potential adverse economic and environmental impacts associated with failure of the container and liquid spillage on the surrounding area. The hazardous effect of liquid sloshing and the extensive damage sustained by liquid-filled tanks were evident in past seismic events such as the 1964 Alaska, 1979 Imperial Valley and 1983 Coalinga earthquakes, and more recently, the 1989 Loma Prieta, 1994 Northridge and 1996 Kobe earthquakes. As a result, a considerable amount of research effort has been devoted to a better determination of the seismic behaviour of liquid tanks and reservoirs and the improvement of associated design codes. In spite of this, there have been relatively few studies on the influence of simultaneous vertical, horizontal and rocking excitations with respect to the hydrodynamic problem of liquid sloshing.

The traditional approach to estimating earthquake-induced hydrodynamic loads has been outlined, for example, by Housner (1957), the U.S. Atomic Energy Commission (1963) and in the AWWA (1984) and API (1993) standards. The method involves the use of an impulsive, or high frequency, effective fluid mass which accelerates with the container, together with an additional effective fluid mass which undergoes resonant motions at the lowest natural frequency of sloshing. The traditional approach is based on a number of assumptions which may not be applicable to the general case, and a variety of additional factors may require consideration in particular situations. Such factors include fluid compressibility, rigidity of the reservoir walls, reservoirs with sloping sides, reservoirs

with irregular planforms, the direction of base motion, base motions with several degrees of freedom and hydrodynamic damping. Of these, multi-degree-of-freedom motions and hydrodynamic damping are the focus of the present study.

# 1.2 Literature Review

## 1.2.1 Horizontal Excitation

### 1.2.1.1 Rigid Tanks

An early solution for the impulsive pressure on harmonically excited, rigid vertical dams was developed by Westergaard (1933). Hoskins and Jacobsen (1934) subsequently reported on analytical and experimental observations of rigid rectangular and cylindrical tanks under a simulated horizontal earthquake excitation. Jacobsen (1949) and Jacobsen and Ayre (1950) provided the first approximate solution for a rigid cylindrical tank on the basis of a closed-form solution of the Laplace equation that satisfies specified boundary conditions.

Housner (1957, 1959) described an approximate solution for rectangular and circular reservoirs based on the assumption that the forces are made up of an impulsive component, corresponding to high frequency oscillations of the container, and a convective component corresponding to the lowest mode of liquid sloshing. That is, the influence of the higher modes of sloshing was ignored. Furthermore, the analysis is based on the assumption that there is no transverse fluid motion (which may be questionable for the case of a circular reservoir).

Isaacson and Subbiah (1991) outlined the complete solution for rigid circular and rectangular tanks under harmonic and irregular base motion. The boundary value problem for the case of an inviscid fluid and a harmonic base motion is solved on the

basis of linearized potential flow theory. Isaacson and Ryu (1998 a) described the hydrodynamic loads and fluid surface elevations for a rectangular reservoir for base motions in an oblique direction, based on an appropriate superposition of solutions for a uni-directional motion parallel to a pair of sides. They found that earthquake-induced motions in a direction of motion parallel to the shorter pair of sides always give the highest loads and surface elevations.

### 1.2.1.2 Flexible Tanks

The overview given so far is based on the assumption that the tank walls are rigid. However, during strong earthquakes, tank walls may be deformed significantly, and so cause loads which are significantly different from those of geometrically identical rigid tanks. Therefore the flexibility of tank walls may need to be accounted for in earthquake-induced loads on tanks.

Veletsos (1974) and Veletsos and Yang (1976, 1977) presented solutions for the dynamic pressure and the impulsive mass under the assumption of certain deformations patterns of the tank wall. A comprehensive overview of the hydrodynamic forces on tanks under assumed wall deformation patterns, the vibrational behavior of empty tanks, and the application of those results to fluid-tank systems subjected to lateral excitation has been given by Yang (1976).

Clough (1978) and Clough and Niwa (1979) have shown through experimental investigation on a flexible cylindrical tank that imperfections in the tank geometry give rise to significant cross-sectional distortion of a circular tank, even though the primary seismic loads tend to induce only translation of the circular section. Hydrodynamic pressures predicted by linear theory for rigid tanks show good agreement with experimental results only when tank wall displacements are small.

Haroun and Housner (1981, 1982) have also analyzed liquid sloshing in flexible, cylindrical tanks for the case of a horizontal base excitation using the boundary element and finite element methods. Haroun (1983) subsequently confirmed that the coupling between liquid sloshing modes and the shell vibrational modes is weak, and consequently the convective pressure can be evaluated with reasonable accuracy by considering the tank walls to be rigid, while the impulsive pressure can be determined by analyzing the liquid-shell system and neglecting the sloshing motion.

Aslam (1981) used a finite element method to predict the sloshing displacements and hydrodynamic pressures in liquid-filled tanks subjected to earthquake ground motions. Finite element equations were derived using the Galerkin formulation, and the predicted results were checked against test data.

### 1.2.1.3 Nonlinear Sloshing

Traditionally, small-amplitude or linear wave theory has been used as the basis for evaluating the seismic performance of liquid-filled containers. However, the use of linear theory has limited the simulation of the actual behaviour of sloshing, possibly leading to the underestimation of hydrodynamic pressures and fluid surface elevations. Various attempts to account for nonlinear sloshing behaviour have been made using perturbation methods, finite element methods and boundary element methods.

Nakayama and Washizu (1981) analyzed the two-dimensional nonlinear sloshing problem using the boundary element method for forced horizontal, vertical or pitching motions of a rectangular container. The mathematical problem was formulated as a nonlinear initial-value boundary-value problem based on the Laplace equation with suitable boundary conditions, assuming the fluid to be inviscid and incompressible and the flow to be irrotational. The governing equations, except for the dynamic free surface boundary condition, were transformed into an integral equation by applying Green's formula, while

the dynamic free surface condition was reduced to a weighted residual equation by employing the Galerkin method.

Hwang et al. (1992) carried out a three-dimensional numerical nonlinear analysis of liquid sloshing in dynamically excited spherical containers. The panel method was applied based on the boundary integral technique. The effects of sloshing were followed in the time domain using an incremental multi-step scheme that ensures numerical stability.

Chen et al. (1996) developed a numerical method to simulate nonlinear finite-amplitude liquid sloshing in two-dimensional rectangular containers. The method employs a curvilinear mesh system to transform the nonlinear sloshing problem from the physical domain with an irregular free-surface boundary into a computational domain with rectangular grids which can be analyzed by the finite difference method.

Nonlinear sloshing effects are apparent in the fluid surface elevations which are higher than linear theory predictions. It has generally been found that linear theory is often non-conservative with respect to predicting the fluid surface elevation but is reasonably accurate in predicting peak hydrodynamic forces.

## 1.2.2 Vertical Excitation

Earthquake-induced motions are three-dimensional and recent observations of recorded ground motions have shown that the maximum amplitude of the vertical component of ground acceleration can exceed the peak horizontal amplitude, especially near the epicenter. Because of the inherent stiffness of typical structures in the vertical direction, the effect of the vertical component of ground acceleration has often been ignored. However, in a liquid-filled tank, vertical accelerations can be transmitted into horizontal hydrodynamic loads. For a rigid tank, vertical motions do not give rise to a resultant

horizontal force, therefore responses due to vertical excitation for a rigid tank will not be discussed further. However, it is noted that fluid surface elevations and hydrodynamic pressures are affected.

For flexible tanks, Yang (1976) presented an analytical study of the dynamic behaviour of a fluid-tank system under vertical accelerations. Luft (1984) described an approximate normal mode solution for a flexible cylindrical tank filled with an inviscid and incompressible liquid and subjected to vertical accelerations. The solution, in the form of uncoupled single-degree-of-freedom oscillator equations, gives both the periods of vibration and the load participation factors for each mode.

Haroun and Tayel (1985) presented a method for analyzing the earthquake response of flexible, cylindrical liquid storage tanks under vertical excitation. The method is based on the superposition of the free axisymmetrical vibrational modes obtained numerically by the finite element method. Both fixed and partly fixed tanks were considered in order to evaluate the effect of base fixation on tank behaviour. Tank responses under the simultaneous action of both vertical and lateral excitations were calculated in order to evaluate the relative importance of the vertical component of ground acceleration.

Veletsos and Tang (1986) presented a method for evaluating the dynamic response of an upright circular cylindrical liquid storage tank to a vertical component of ground shaking, considering the flexibility of the supporting medium. The tank was presumed to be supported through a rigid circular mat at the surface of a homogeneous elastic half-surface, and it was analyzed approximately by the application of Galerkin's method.

Kim et al (1995) developed an analytical method to evaluate the dynamic response characteristics of partially filled two-dimensional and three-dimensional flexible rectangular fluid containers under horizontal and vertical ground excitation. The rectangular container is assumed to be symmetric, with four side-walls and a rigid base

slab fixed to the ground. The side-walls are modeled as rectangular plates of uniform thickness. The equation of motion of the coupled system is obtained by applying the Raleigh-Ritz method using the assumed vibration modes as an admissible function.

### 1.2.3 Rocking Excitation

Analysis of the sloshing problems of liquid containing tanks to horizontal ground shaking are normally carried out on the assumption that the tank base moves horizontally without any rotation. In reality, because of the flexibility of the supporting soil, the tank base experiences a rocking component of motion even under a purely translational free-field ground motion. Therefore, an understanding of the rocking response of the liquid-tank system is important.

Haroun and Ellaithy (1985) developed an analytical model for flexible cylindrical tanks taking into consideration the effect of rigid base rocking motion. Explicit analytical expressions for the parameters of the model were given, and numerical values of these parameters were displayed in charts. This model can be used to evaluate the maximum dynamic response of rigid and flexible cylindrical tanks subjected to earthquake loading.

Veletsos and Yang (1987) analyzed the dynamic response of circular cylindrical tanks to a rocking base motion with an arbitrary temporal variation. Both rigid and flexible tanks were examined. Critical response quantities for rigid tanks were evaluated. The inter-relationship of the responses of the system to rocking and lateral base motions of the same temporal records was established, and it was shown that some of the effects of base rocking may be determined from available data concerning the response of laterally excited tanks.

## 1.2.4 Effects of Energy Dissipation

The motion of a real fluid gives rise to damping which may be associated with various forms of energy dissipation. These include viscous effects associated with boundary layers on the tank wall; flow separation effects as the fluid oscillates past baffles or other obstacles in the container; and free surface effects associated with breaking waves. The damping coefficient due to boundary layers may be estimated, but typically, a value of 0.5% is assumed in design (e.g. ASCE, 1984).

Case and Parkinson (1958) calculated the damping of small amplitude surface waves in a circular tank. Viscous dissipation in laminar boundary layers was taken to be the primary cause of damping. Experimental results were obtained to describe the logarithmic decrement of damping as a function of the ratio of liquid height to cylinder radius.

Miles (1958) carried out an approximate analysis of the effect of viscous damping in an annular ring on the sloshing oscillations of liquid in a cylindrical tank. For moderate amplitudes, the logarithmic decrement of damping was predicted to be proportional to the square root of the amplitude and the three-halves power of the ring area.

Faltinsen (1978) presented a numerical method for studying nonlinear sloshing in rectangular tanks, and modelled the hydrodynamic damping by assuming this to occur at the free surface as through the free surface boundary conditions. Using Faltinsen's approach, Isaacson (1991) obtained closed form solutions for a rigid circular reservoir both for no energy dissipation as well as some level of energy dissipation corresponding to a specified damping coefficient. The solutions provide a description of the corresponding fluid motion, and thereby provide the resultant pressure and force on the reservoir walls.

## 1.3 Objectives

In spite of the wide range of studies relating to fluid sloshing that have been indicated above, there remains a need for a better understanding of various additional factors that affect the hydrodynamic response of tanks and reservoirs subjected to base excitation. Additional factors that need to be considered include fluid compressibility, rigidity of the reservoir wall, reservoirs with sloping sides, reservoirs with irregular planforms, the direction of base motion, multi-degree-of-freedom base motions, hydrodynamic damping, and differences with full time-domain simulations. In this context, the primary objectives of the present research are to investigate two such effects for which a better understanding is required in order to improve design procedures:

1. the influence of multiple degrees of freedom of base motions on hydrodynamic loads on and fluid surface elevations in reservoirs.
2. the effects of damping on liquid sloshing in reservoirs.

With regard to the first of these (multiple motions), although authors such as Housner, Veletsos and Haroun have examined the sloshing response of reservoirs for various component motions, there remains a need to provide a solution for multiple base motions based on superposition and to compare this with experiments. With respect to the second item (damping), while previous authors have examined damping due to laminar boundary layers, there is a need to develop theoretical predictions of turbulent boundary layer damping and baffle damping, and to compare these with experiments. These represent the original contribution of this thesis. Thus, the original contributions of this thesis are to outline and verify experimentally linear superposition for multiple motions, and to develop and outline theoretical predictions for turbulent boundary layer damping and for baffle damping and to compare these with experiments.

The investigation is carried out for both harmonic excitation and earthquake-induced excitation; and for horizontal and rocking motions considered separately and together; and for a rectangular tank (Fig. 1(a)) and a circular tank (Fig. 1(b)), although experiments have been carried out for a rectangular tank alone.

# 2 Analytical Solution For Harmonic Excitation

## 2.1 Rectangular Reservoir

Initially, the closed-form solution for the hydrodynamic loads, overturning moments and fluid surface elevation for a rigid rectangular tank subjected to a harmonic motion parallel to a pair of sides is outlined. The system considered is shown in Fig. 1(a). The tank has a length 2a in the x direction, a width 2b in the y direction, and is filled with an incompressible fluid to a depth d. Thus the total fluid mass m in the tank is given as $m = 4\rho abd$, where $\rho$ is the fluid density. A fixed Cartesian coordinate system (x, y, z) as indicated in Fig. 1(a) is used. The vertical coordinate z is measured upwards from the bottom of the tank, and the x-axis is parallel to a pair of sides.

The solution is obtained on the basis of assumptions that the reservoir is rigid, the fluid is inviscid, the flow is irrotational, and the oscillation amplitude is small (such that the corresponding boundary value problem is linearized). Thus the flow can be described by a velocity potential $\Phi$ which satisfies the Laplace equation within the fluid region, and is also subject to linearized dynamic and kinematic conditions at the free surface, and to kinematic conditions at the bottom and sides of the tank.

### 2.1.1 Horizontal Motion

The following derivations are based on Isaacson and Subbiah (1990). Initially, the closed-form solution for the hydrodynamic loads and fluid surface elevation in a rectangular tank subjected to a harmonic motion parallel to a pair of sides is summarized. The reservoir undergoes a sinusoidal base motion in a direction parallel to the x-axis and with velocity u(t) given in complex notation as:

$$u(t) = U\exp(-i\omega t) \tag{2.1}$$

in which U is the velocity amplitude, $\omega$ is the angular frequency, t is time and $i=\sqrt{-1}$.
An expression for $\Phi$ may be developed in terms of a set of eigenvalues $k_n$ corresponding to each mode of liquid sloshing in the tank in the form:

$$\Phi = U\left\{x - 2a\sum_{n=1}^{\infty}\left[\frac{(-1)^{n-1}}{(k_n a)^2}\right]\left[\frac{\cosh(k_n z)}{\cosh(k_n d)}\right]\sin(k_n x)G_n^H(i\omega)\right\}\exp(-i\omega t) \tag{2.2}$$

The eigenvalues $k_n$ correspond to $\cos(k_n a)=0$, and thus are given as:

$$k_n a = \frac{\pi}{2},\ \frac{3\pi}{2},\ \frac{5\pi}{2},\ \cdots \qquad \text{for } n = 1, 2, 3, \ldots.. \tag{2.3}$$

$G_n(i\omega)$ is a frequency dependent function given as:

$$G_n^H(i\omega) = \frac{\omega^2}{\omega^2 - \omega_n^2} \tag{2.4}$$

Here $\omega_n$ is the natural frequency corresponding to the n-th sloshing mode, and may be obtained from equation:

$$\omega_n^2 = g\,k_n \tanh(k_n d) \tag{2.5}$$

where g is the gravitational constant.
The maximum free surface elevation $\eta$ at the tank walls is given as:

$$\eta = \frac{i\omega U a}{g}\left\{1-\sum_{n=1}^{\infty} E_n\, G_n^H(i\omega)\right\}\exp(-i\omega t) \tag{2.6}$$

where

$$E_n = \frac{2}{(k_n a)^2} \tag{2.7}$$

It may readily be shown that Eq. 2.6 leads to $\eta \to 0$ in the high frequency limit.

The pressure on the container walls may be obtained in terms of the velocity potential from the unsteady Bernoulli equation, and the force F on the reservoir may then be obtained by a suitable integration of the pressure. In fact, the force F may be expressed in terms of a set of modal masses $m_n$ associated with the various modes of sloshing as:

$$F = i\omega U m\left[1-\sum_{n=1}^{\infty} h_n\, G_n^H(i\omega)\right]\exp(-i\omega t) \tag{2.8}$$

where $h_n$ are the modal masses given in dimensionless form as:

$$h_n = \frac{m_n}{m} = \frac{2}{(k_n a)^2}\left[\frac{\tanh(k_n d)}{k_n d}\right] \tag{2.9}$$

and $m_n$ are the corresponding modal masses.

At high frequencies, the force given by Eq. 2.8 may be expressed as:

$$F = i\omega U m_0 \exp(-i\omega t) \tag{2.10}$$

such that the high frequency effective mass $m_0$ is given in terms of the modal masses as:

$$m_0 = m - \sum_{n=1}^{\infty} m_n \tag{2.11}$$

The corresponding overturning moment M about the base of the tank, excluding the component due to the pressure distribution over the base of the tank, denoted M, is obtained by an appropriately weighted integration of the sectional force over depth, and is thereby given by

$$M = i\omega U m d\left\{\frac{1}{2} - \sum_{n=1}^{\infty} g_n G_n^H(i\omega)\right\}\exp(i\omega t) \tag{2.12}$$

where

$$g_n = \frac{2}{(k_n a)^2}\left[\frac{(k_n d)\sinh(k_n d) - \cosh(k_n d) + 1}{(k_n d)^2 \cosh(k_n d)}\right] \tag{2.13}$$

An additional moment $\Delta M$ due to the pressure distribution over the base of the tank is given by:

$$\Delta M = i\omega U m d\left[\frac{1}{3}\left(\frac{a}{d}\right)^2 - \sum_{n=1}^{\infty}\frac{2}{(k_n a)^2}\frac{1}{(k_n d)^2\cosh(k_n d)} G_n^H(i\omega)\right]\exp(-i\omega t) \tag{2.14}$$

Thus, the overturning moment $M'$ about the base of the tank is given by $M' = M + \Delta M$:

$$M' = i\omega U m d\left[\frac{1}{2} + \frac{1}{3}\left(\frac{a}{d}\right)^2 - \sum_{n=1}^{\infty} g_n' G_n^H(i\omega)\right]\exp(-i\omega t) \tag{2.15}$$

where

$$g_n' = \frac{2}{(k_n a)^2} \frac{(k_n d)\sinh(k_n d) - \cosh(k_n d) + 2}{(k_n d)^2 \cosh(k_n d)} \tag{2.16}$$

## 2.1.2 Rocking Motion

Initially, the closed-form solution for the hydrodynamic loads and fluid surface elevation in a rectangular tank subjected to a harmonic rocking motion is summarized. This solution is derived here following the approach used for circular cylinder by Veletsos and Tang (1987). The tank undergoes a harmonic rocking base motion about the y axis and with angular velocity $\psi(t)$ given in complex notation as:

$$\psi(t) = \Psi \exp(-i\omega t) \tag{2.17}$$

in which $\Psi$ is the angular velocity amplitude. An expression for $\Phi$ may be developed in terms of a set of eigenvalues $k_n$ corresponding to each mode of liquid sloshing in the tank in the form:

$$\Phi = \Psi \left\{ (z-d)x + \sum_{m=1}^{\infty} \frac{2}{\alpha_m^2} \left[ \frac{2}{(\alpha_m d)} - (-1)^{m+1} \right] \frac{\sinh(\alpha_m x)}{\cosh(\alpha_m a)} \cos(\alpha_m z) + ad \sum_{n=1}^{\infty} \frac{2(-1)^{n+1}}{(k_n a)^2} \gamma_n \frac{\cosh(k_n z)}{\cosh(k_n d)} \sin(k_n x)\, G_n^R(i\omega) \right\} \exp(-i\omega t) \tag{2.18}$$

The eigenvalues $k_n$ correspond to $\cos(k_n a) = 0$ as before, and thus are again given as:

$$k_n a = \frac{\pi}{2}, \quad \frac{3\pi}{2}, \quad \frac{5\pi}{2}, \quad \cdots \qquad \text{for } n = 1, 2, 3, \ldots \tag{2.19}$$

$$\text{Also } \alpha_m d=(2m-1)\frac{\pi}{2} \tag{2.20}$$

$G_n^R(i\omega)$ is a frequency dependent function given as before:

$$G_n^R(i\omega)=\frac{\omega_n^2}{\omega^2-\omega_n^2} \tag{2.21}$$

Here $\omega_n$ is the natural frequency corresponding to the n-th sloshing mode, and may be obtained from equation:

$$\omega_n^2 = g\,k_n \tanh(k_n d) \tag{2.22}$$

and

$$\gamma_n = \frac{(k_n d)\sinh(k_n d)-\cosh(k_n d)+2}{(k_n d)\sinh(k_n d)} \tag{2.23}$$

The free surface elevation $\eta$ at the tank walls is given as:

$$\eta=\frac{i\omega\Psi da}{g}\left[\sum_{n=1}^{\infty} E_n\, G_n^R(i\omega)\right]\exp(-i\omega t) \tag{2.24}$$

where

$$E_n=\frac{2}{(k_n a)^2}\gamma_n \tag{2.25}$$

Again, it may readily be shown that Eq. 2.24 leads to $\eta \to 0$ in the high frequency limit.

The pressure on the container walls may be obtained in terms of the velocity potential from the unsteady Bernoulli equation, and the force F on the reservoir may then be obtained by a suitable integration of the pressure. In fact, the force F may be expressed in terms of a set of modal masses $m_n$ associated with the various modes of sloshing as:

$$F = i\omega\Psi dm\left[\frac{1}{2} - \sum_{m=1}^{\infty} h_m^{(r1)} - \sum_{n=1}^{\infty} h_n^{(r2)}\, G_n^R(i\omega)\right]\exp(-i\omega t) \tag{2.26}$$

where

$$h_m^{(r1)} = 2\frac{d}{a}\frac{1}{(\alpha_m d)^3}\left[\frac{2(-1)^{m+1}}{(\alpha_m d)} - 1\right]\tanh(\alpha_m a) \tag{2.27}$$

$$h_n^{(r2)} = \frac{m_n}{m} = \gamma_n\, h_n \tag{2.28}$$

At high frequencies, the force given by Eq. 2.26 may be expressed as:

$$F = i\omega\Psi d\, m_0 \exp(-i\omega t) \tag{2.29}$$

with the high frequency mass $m_0$ given as:

$$\frac{m_0}{m} = \frac{1}{2} - \sum_{m=1}^{\infty} h_m^{(r1)} \tag{2.30}$$

Thus, the force equation can be expressed in terms of the high frequency effective mass and the modal masses as:

$$F = i\omega\Psi d\left[m_0 - \sum_{n=1}^{\infty} m_n\, G_n^R(i\omega)\right]\exp(-i\omega t) \tag{2.31}$$

The corresponding overturning moment M about the base of the tank is obtained by an appropriately weighted integration of sectional force over depth, and is thereby given as:

$$M = i\omega\Psi dmd\left\{\frac{1}{6} - \sum_{m=1}^{\infty} g_m^{(r1)} - \sum_{n=1}^{\infty} g_n^{(r2)}\, G_n^R(i\omega)\right\}\exp(-i\omega t) \tag{2.32}$$

where

$$g_m^{(r1)} = 2\frac{d}{a}\left[\frac{3(-1)^{m+1}(\alpha_m d) - (\alpha_m d)^2 - 2}{(\alpha_m d)^5}\right]\tanh(\alpha_m a) \tag{2.33}$$

$$g_n^{(r2)} = \gamma_n\, g_n \tag{2.34}$$

The additional moment $\Delta M$ due to the pressure distribution over the tank base is expressed by

$$\Delta M = i\omega\Psi dmd\left[\frac{1}{3}\left(\frac{a}{d}\right)^2 - 2\left(\frac{d}{a}\right)\sum_{m=1}^{\infty}\left[\frac{2-(-1)^{m+1}(\alpha_m d)}{(\alpha_m d)^5}\right]\left[\frac{(\alpha_m a)\cosh(\alpha_m a) - \sinh(\alpha_m a)}{\cosh(\alpha_m a)}\right]\right.$$
$$\left. + \sum_{n=1}^{\infty}\frac{2}{(k_n a)^2}\frac{1}{(k_n d)^2\cosh(k_n d)}\gamma_n\, G_n^R(i\omega)\right]\exp(-i\omega t) \tag{2.35}$$

Thus, the total overturning moment $M' = M + \Delta M$ at the base is given by

$$M' = i\omega\Psi dmd\left\{\frac{1}{6} + \frac{1}{3}\left(\frac{a}{d}\right)^2 - \sum_{m=1}^{\infty} gg_m^{(r1)} - \sum_{n=1}^{\infty} gg_n^{(r2)}\, G_n^R(i\omega)\right\}\exp(-i\omega t) \tag{2.36}$$

where

$$gg_m^{(r1)} = 2\left(\frac{d}{a}\right)\left[\frac{4(-1)^{m+1}(\alpha_m d)-(\alpha_m d)^2-4}{(\alpha_m d)^5}\right]\tanh(\alpha_m a)-2\left[\frac{(-1)^{m+1}(\alpha_m d)-2}{(\alpha_m d)^4}\right] \qquad (2.37)$$

$$gg_n^{(r2)} = \gamma_n g'_n \qquad (2.38)$$

# 2.2 Circular Reservoir

The preceding analysis for a rectangular reservoir is now repeated for a circular reservoir. The system considered is shown in Fig. 1(b). The tank is filled to a level d with a fluid of density $\rho$. Fixed Cartesian and cylindrical coordinate systems, (x, y, z) and (r, $\theta$, z) respectively, as indicated in Fig. 1(b), are used. The vertical coordinate z coincides with the axis of the container in the equilibrium position and is measured upwards from the bottom of the container; x is in the direction of the base motion; r is measured radially from the z axis; and $\theta$ is measured from the positive x axis.

The identical assumptions are made as before: thus the fluid is assumed to be invisid, the flow is irrotational, and the amplitude of the base motion and the resulting free surface elevation $\eta$ in the container are assumed to be sufficiently small for a linearization of the free surface conditions to be justified, and for the kinematic condition at the container wall to be applied at the equilibrium position.

## 2.2.1 Horizontal Motion

The following derivations are based on Isaacson and Subbiah (1991). The tank undergoes a sinusoidal base motion with velocity $u(t)$ given in complex notation as

$$u(t)=U\exp(-i\omega t) \tag{2.39}$$

in which U is the velocity amplitude, $\omega$ is the angular frequency, t is time, and $i=\sqrt{-1}$. An expression for $\Phi$ may be developed in term of a set of eigenvalues $k_n$ corresponding to each mode of liquid sloshing in the tank in the form:

$$\Phi=U\left\{r-2a\sum_{n=1}^{\infty}\left[G_n^H(i\omega)\frac{J_1(k_n r)}{\left[(k_n a)^2-1\right]J_1(k_n a)}\frac{\cosh(k_n z)}{\cosh(k_n d)}\right]\right\}\cos\theta\,\exp(-i\omega t) \tag{2.40}$$

where $J_1$ is the Bessel function of the first kind of order 1, and

$$G_n^H(i\omega)=\frac{\omega^2}{\omega^2-\omega_n^2} \tag{2.41}$$

$$\omega_n^2=gk_n\tanh(k_n d) \tag{2.42}$$

The $k_n$ values are obtained from the successive roots of the equation

$$J_1'(k_n a)=0 \tag{2.43}$$

where the prime denotes a derivative with respect to the argument. The first five values of $k_n a$ are indicated in Table 1.

The maximum free surface elevation $\eta$ at the tank wall can be expressed as

$$\eta=\frac{i\omega Ua}{g}\left\{1-\sum_{n=1}^{\infty}E_n\,G_n^H(i\omega)\right\}\exp(-i\omega t) \tag{2.44}$$

where

$$E_n = \frac{2}{(k_n a)^2 - 1} \tag{2.45}$$

The total horizontal force F on the tank is given by

$$F = i\omega U \left\{ m - \sum_{n=1}^{\infty} m_n G_n^H(i\omega) \right\} \exp(-i\omega t) \tag{2.46}$$

or

$$F = i\omega U m \left[ 1 - \sum_{n=1}^{\infty} h_n G_n^H(i\omega) \right] \exp(-i\omega t) \tag{2.47}$$

where $m = \rho \pi a^2 d$ is the mass of fluid in the tank, and

$$h_n = \frac{m_n}{m} = 2 \left[ \frac{1}{(k_n a)^2 - 1} \right] \left[ \frac{\tanh(k_n d)}{k_n d} \right] \tag{2.48}$$

The corresponding overturning moment about the base of the tank, excluding the component due to the pressure distribution over the base of the tank, denoted M, is obtained by an appropriately weighted integration of the sectional force over depth, and is thereby given by:

$$M = i\omega U m d \left\{ \frac{1}{2} - \sum_{n=1}^{\infty} g_n G_n^H(i\omega) \right\} \exp(i\omega t) \tag{2.49}$$

where

$$g_n = \frac{2}{\left[(k_n a)^2 - 1\right]} \frac{(k_n d)\sinh(k_n d) - \cosh(k_n d) + 1}{(k_n d)^2 \cosh(k_n d)} \tag{2.50}$$

An additional moment $\Delta M$ due to the pressure distribution over the base of the tank is given by:

$$\Delta M = i\omega U m d \left[ \frac{1}{4}\left(\frac{a}{d}\right)^2 - \sum_{n=1}^{\infty} \left[ \frac{2}{(k_n a)^2 - 1} \right] \frac{1}{(k_n d)^2 \cosh(k_n d)} G_n^H(i\omega) \right] \exp(-i\omega t) \tag{2.51}$$

Thus the total overturning moment $M'$ about the base is given by $M' = M + \Delta M$:

$$M' = i\omega U m d \left[ \frac{1}{2} + \frac{1}{4}\left(\frac{a}{d}\right)^2 - \sum_{n=1}^{\infty} g_n' \, G_n^H(i\omega) \right] \exp(-i\omega t) \tag{2.52}$$

where

$$g_n' = \left[ \frac{2}{(k_n a)^2 - 1} \right] \left[ \frac{(k_n d)\sinh(k_n d) - \cosh(k_n d) + 2}{(k_n d)^2 \cosh(k_n d)} \right] \tag{2.53}$$

## 2.2.2 Rocking Motion

The following derivations are based on Veletsos and Tang (1987). The tank undergoes a harmonic base motion with angular velocity $\psi(t)$ denoted by

$$\psi(t) = \Psi \exp(-i\omega t) \tag{2.54}$$

in which $\Psi$ is the angular velocity amplitude, $\omega$ is the angular frequency, t is time, and $i=\sqrt{-1}$. An expression for $\Phi$ may be developed in terms of a set of eigenvalues $k_n$ corresponding to each mode of liquid sloshing in the tank in the form:

$$\Phi=\Psi\left\{(z-d)x+\sum_{m=1}^{\infty}\frac{2}{\alpha_m^2}\left[\frac{2}{(\alpha_m d)}-(-1)^{m+1}\right]\frac{I_1(\alpha_m r)}{I_1'(\alpha_m a)}\cos(\alpha_m z)\right.$$
$$\left.+\ ad\sum_{n=1}^{\infty}\frac{2}{\left[(k_n a)^2-1\right]}\gamma_n\frac{\cosh(k_n z)}{\cosh(k_n d)}\frac{J_1(k_n z)}{J_1(k_n a)}G_n^R(i\omega)\right\}\cos\theta\exp(-i\omega t) \tag{2.55}$$

where $I_1$ is the modified Bessel function of the first kind, and

$$\gamma_n=\frac{(k_n d)\sinh(k_n d)-\cosh(k_n d)+2}{(k_n d)\sinh(k_n d)} \tag{2.56}$$

The $k_n$ values are obtained from the successive roots of the equation

$$J_1'(k_n a)=0 \tag{2.57}$$

And $$\alpha_m d=(2m-1)\frac{\pi}{2} \tag{2.58}$$

The maximum fluid surface elevation $\eta$ at the tank wall can be expressed as

$$\eta=\frac{i\omega\Psi ad}{g}\left[\sum_{n=1}^{\infty}E_n\,G_n^R(i\omega)\right]\exp(-i\omega t) \tag{2.59}$$

where

$$E_n = \frac{2}{(k_n a)^2 - 1}\gamma_n \tag{2.60}$$

The pressure on the container walls may be obtained in terms of the velocity potential from the unsteady Bernoulli equation, and the force F on the reservoir may then be obtained by a suitable integration of the pressure. In fact, the force F may be expressed in terms of a set of modal mass $m_n$ associated with the various modes of sloshing as:

$$F = i\omega\Psi dm\left[\frac{1}{2} - \sum_{m=1}^{\infty} h_m^{(r1)} - \sum_{n=1}^{\infty} h_n^{(r2)} G_n^R(i\omega)\right]\exp(-i\omega t) \tag{2.61}$$

where

$$h_m^{(r1)} = 2\frac{d}{a}\frac{1}{(\alpha_m d)^3}\left[\frac{2(-1)^{m+1}}{(\alpha_m d)} - 1\right]\frac{I_1(\alpha_m a)}{I_1'(\alpha_m a)} \tag{2.62}$$

$$h_n^{(r2)} = \frac{m_n}{m} = \gamma_n\, h_n \tag{2.63}$$

At high frequencies, the force given by Eq. 2.61 may be expressed as:

$$F = i\omega\Psi d\, m_0 \exp(-i\omega t) \tag{2.64}$$

Such that the high frequency mass $m_0$ is given as:

$$\frac{m_0}{m} = \frac{1}{2} - \sum_{m=1}^{\infty} h_m^{(r1)} \tag{2.65}$$

Thus, the force equation can be expressed as in terms of high frequency effective mass and the modal masses as:

$$F = i\omega\Psi d\left[m_0 - \sum_{n=1}^{\infty} m_n G_n^R(i\omega)\right]\exp(-i\omega t) \tag{2.66}$$

The corresponding overturning moment M about the base of the tank is obtained by an appropriately weighted integration of sectional force over depth, and is thereby given by:

$$M = i\omega\Psi d\, md\left\{\frac{1}{6} - \sum_{m=1}^{\infty} g_m^{(r1)} - \sum_{n=1}^{\infty} g_n^{(r2)} G_n^R(i\omega)\right\}\exp(-i\omega t) \tag{2.67}$$

where

$$g_m^{(r1)} = 2\frac{d}{a}\left[\frac{3(-1)^{m+1}(\alpha_m d) - (\alpha_m d)^2 - 2}{(\alpha_m d)^5}\right]\frac{I_1(\alpha_m a)}{I_1'(\alpha_m a)} \tag{2.68}$$

$$g_n^{(r2)} = \gamma_n\, g_n \tag{2.69}$$

$$g_n = \frac{2}{\left[(k_n a)^2 - 1\right]}\frac{(k_n d)\sinh(k_n d) - \cosh(k_n d) + 1}{(k_n d)^2\cosh(k_n d)} \tag{2.70}$$

The additional moment ΔM due to the pressure distribution over the tank base is given by:

$$\begin{aligned}\Delta M = i\omega\Psi dmd\Bigg\{&\frac{1}{4}\left(\frac{a}{d}\right)^2 - 2\sum_{m=1}^{\infty}\frac{1}{(\alpha_m d)^3}\left[\frac{2}{(\alpha_m d)} - (-1)^{m+1}\right]\frac{I_2(\alpha_m a)}{I_1'(\alpha_m a)} \\ &- \sum_{n=1}^{\infty}\left[\frac{2}{(k_n a)^2 - 1}\right]\frac{\gamma_n}{(k_n d)^2\cosh(k_n d)} G_n^R(i\omega)\Bigg\}\exp(-i\omega t)\end{aligned} \tag{2.71}$$

Thus, the total overturning moment $M' = M + \Delta M$ at the base is given by:

$$M' = i\omega\Psi dmd\left\{\frac{1}{6}+\frac{1}{4}\left(\frac{a}{d}\right)^2 - \sum_{m=1}^{\infty} gg_m^{(r1)} - \sum_{n=1}^{\infty} gg_n^{(r2)} G_n^R(i\omega)\right\}\exp(-i\omega t) \tag{2.72}$$

where

$$gg_m^{(r1)} = 2\left(\frac{d}{a}\right)\left[\frac{4(-1)^{m+1}(\alpha_m d)-(\alpha_m d)^2-4}{(\alpha_m d)^5}\right]\frac{I_1(\alpha_m a)}{I_1'(\alpha_m a)} - \left[\frac{(-1)^{m+1}(\alpha_m d)-2}{(\alpha_m d)^4}\right]\frac{I_2(\alpha_m a)}{I_1'(\alpha_m a)} \tag{2.73}$$

$$gg_n^{(r2)} = \gamma_n g_n' \tag{2.74}$$

## 2.3 Harmonic Excitation with Energy Dissipation

The motion of a real fluid gives rise to hydrodynamic damping which may be associated with various forms of energy dissipation. These include viscous effects associated with boundary layers on the tank walls; flow separation effects as the fluid oscillates past baffles or other obstacles in the container; and free surface effects associated with breaking waves. Attention is now focussed on an extension to the preceding solution for an inviscid fluid in order to account for such energy dissipation in a real fluid. As an approximation which enables the potential solution to be utilized directly, the dissipation is assumed to occur only at the free surface and is introduced through a modification to the dynamic free surface boundary condition in the manner indicated by Faltinsen (1978) and Isaacson and Subbiah (1991). Although this may be considered somewhat artificial, it does provide a convenient means of developing a solution which readily enables the conventional dynamic theory of damped multi-degree-of-freedom systems to be directly exploited.

As an extension, the linearized dynamic free surface boundary condition is taken as

$$\frac{\partial \Phi}{\partial t} + g\eta + \mu\Phi = 0 \qquad \text{at } z = d \qquad (2.75)$$

where $\mu$ is an effective viscous coefficient; and the Bernoulli constant has been taken as zero, since all other terms are harmonic with time. The term $\mu\Phi$ gives rise to the energy dissipation and may be developed by taking the pressure at the free surface to be proportional to the free surface velocity, corresponding to a linear damping force. This leads to a combined free surface condition in terms of $\Phi$, which is given as:

$$\frac{\partial^2 \Phi}{\partial t^2} + \mu\frac{\partial \Phi}{\partial t} + g\frac{\partial \Phi}{\partial z} = 0 \qquad \text{at } z = d \qquad (2.76)$$

## 2.3.1 Horizontal Excitation

When damping is introduced in the manner described above, $G_n^H(i\omega)$, used in section 2.1.1 and 2.2.1, is now complex and is given as:

$$G_n^H(i\omega) = \frac{\omega^2 + i\omega\mu}{\omega^2 + i\omega\mu - \omega_n^2} \qquad (2.77)$$

where $\mu$ is the damping parameter introduced in Eq. 2.75.

The force F may be expressed in terms of a set of modal mass $m_n$ associated with the various modes of sloshing as before:

$$F = i\omega U\left\{m - \sum_{n=1}^{\infty} m_n G_n^R(i\omega)\right\}\exp(-i\omega t) \qquad (2.78)$$

And the maximum free surface elevation is now given as:

$$\eta = \frac{i\omega Ua}{g}\left(1+\frac{i\mu}{\omega}\right)\left\{1-\sum_{n=1}^{\infty} E_n G_n^R(i\omega)\right\}\exp(-i\omega t) \tag{2.79}$$

## 2.3.2 Rocking Excitation

Once more, the preceding solutions for rocking excitation with zero damping, as given in section 2.1.2 and 2.3.2 may be extended in the same way so that $G_n^R(i\omega)$ is now complex:

$$G_n^R(i\omega) = \frac{\omega_n^2}{\omega^2 + i\omega\mu - \omega_n^2} \tag{2.80}$$

The force F may be expressed in terms of a set of modal mass $m_n$ associated with the various modes of sloshing in the same form as before:

$$F = i\omega\Psi dm\left[\frac{1}{2} - \sum_{m=1}^{\infty} h_m^{(r1)} - \sum_{n=1}^{\infty} h_n^{(r2)} G_n^R(i\omega)\right]\exp(-i\omega t) \tag{2.81}$$

And the maximum fluid surface elevation at the tank walls is now given as:

$$\eta = \frac{i\omega\Psi ad}{g}\left(1+\frac{i\mu}{\omega}\right)\left[\sum_{n=1}^{\infty} E_n\ \gamma_n\ G_n^R(i\omega)\right]\exp(-i\omega t) \tag{2.82}$$

# 2.4 Added Mass

## 2.4.1 Added Mass without Damping

It is convenient to express the total force F in terms of an effective mass of fluid $m_e = m + m_a$, where $m_a$ is an added mass, by taking

$$\begin{aligned} F &= -m_e \ddot{u} = -(m + m_a)\ddot{u} \\ &= i\omega U(m + m_a)\exp(-i\omega t) \end{aligned} \tag{2.83}$$

where a dot denotes a derivative with respect to time. The term involving m corresponds to the component of the fluid force on tank walls which would act if the fluid moves at the container velocity without sloshing; and that involving the added mass $m_a$, which may be positive or negative, accounts for the additional force associated with the sloshing. Since energy dissipation is assumed not to occur for the present, the force is in phase with acceleration, so that there is no corresponding damping coefficient, and Eq. 2.83, with $m_a$ real, adequately represents the force.

Upon comparing Eqs. (2.8) and (2.83), an expression for the added mass is readily obtained. In suitable dimensionless form, a corresponding added mass coefficient $C_a$ can be expressed for the case of horizontal excitation as

$$C_a = \frac{m_a}{m} = -\sum_{n=1}^{\infty} h_n G_n^H(i\omega) \tag{2.84}$$

In similar manner, a corresponding added mass coefficient $C_a$ can be expressed for rocking excitation as

$$C_a = \frac{m_a}{m} = -\left[\frac{1}{2} + \sum_{m=1}^{\infty} h_m^{(r1)} + \sum_{n=1}^{\infty} h_n^{(r2)} G_n^R(i\omega)\right] \tag{2.85}$$

## 2.4.2 Added Mass with Damping

When energy dissipation is assumed to occur, the fluid force is no longer in phase with acceleration and thus Eq. 2.83 may no longer be used to represent F. Instead, the fluid force F is now expressed in terms of components in phase with the velocity and the acceleration of the container, so that Eq. 2.83 is extended to:

$$F = -[(m+m_a)\dot{u} + \lambda u] \tag{2.86}$$

where $\lambda$ is a dimensional damping coefficient, and $m_a$ and $\lambda$ are both taken as real. Equations 2.1 and 2.8 may now be used to substitute for u and F respectively into Eq. 2.86 in order to provide explicit expressions for the added mass coefficient $C_a$ and a dimensionless damping coefficient $C\lambda$. These are given respectively as:

$$C_a = \frac{m_a}{m} = \mathrm{Re}(\Omega) \tag{2.87}$$

$$C_\lambda = \frac{\lambda}{\omega m} = \mathrm{Im}(\Omega) \tag{2.88}$$

where Re[] and Im[] denote the real and imaginary parts respectively, and for horizontal excitation $\Omega$ can be expressed as:

$$\Omega = -\sum_{n=1}^{\infty} h_n G_n^H(i\omega) \tag{2.89}$$

In similar manner, $\Omega$ can be expressed for rocking excitation as:

$$\Omega = -\left[\frac{1}{2} + \sum_{m=1}^{\infty} h_m^{(r1)} + \sum_{n=1}^{\infty} h_n^{(r2)} G_n^R(i\omega)\right] \tag{2.90}$$

Although the dimensional damping coefficient $\lambda$ has been related to the damping parameter $\mu$, it is convenient to introduce a more easily recognizable measure of damping in place of $\mu$. For convenience, this is taken as the fraction of critical damping for first mode free oscillations that would correspond to the same level of damping. This is denoted by $\zeta_1$. An expression relating $\zeta_1$ to $\mu$ may be developed by taking U = 0 or $\Psi$ = 0 in the preceding development, and recognizing that time-dependent terms now occur only in Eq. 2.76. This readily yields

$$\zeta_1 = \frac{\mu}{2\omega_1} = \frac{\mu}{2\sqrt{gk_1 \tanh(k_1 d)}} \tag{2.91}$$

For small values of $\zeta_1$, the logarithmic decrement of damping, $\upsilon = 2\pi\zeta_1$, may also be used.

## 2.5 Combined Motion

Since the preceding closed-form solutions are based on a linearization of the corresponding boundary value problem, the case of combined motion effects may be determined from an appropriate superposition of the closed-form solutions corresponding to the two different base motions.

Therefore the resulting force is given in terms of the force due to a horizontal motion alone, denoted $F_H$ and the force due to rocking motion alone, denoted $F_R$, simply as:

$$F = F_H + F_R \tag{2.92}$$

Substituting Eqns (2.8) or (2.47) and (2.22) or (2.61), one obtains

$$\begin{aligned} F = {} & i\omega_H Um\left[1-\sum_{n=1}^{\infty} h_n G_n^H(i\omega_H)\right]\exp(-i\omega_H t) \\ & +i\omega_R \Psi dm\left[\frac{1}{2}-\sum_{m=1}^{\infty} h_m^{(r1)}-\sum_{n=1}^{\infty} h_n^{(r2)} G_n^R(i\omega_R)\right]\exp(-i\omega_R t) \end{aligned} \tag{2.93}$$

where $\omega_H$ and $\omega_R$ are exciting frequencies for horizontal and rocking motions respectively.

Similarly, the overturning moment at the tank base and fluid surface elevation at the tank wall are given as respectively

$$\begin{aligned} M = {} & i\omega_H Umd\left[\frac{1}{2}-\sum_{n=1}^{\infty} g_n G_n^H(i\omega_H)\right]\exp(-i\omega_H t) \\ & +i\omega_R \Psi dmd\left[\frac{1}{6}-\sum_{m=1}^{\infty} g_m^{(r1)}-\sum_{n=1}^{\infty} g_n^{(r2)} G_n^R(i\omega_R)\right]\exp(-i\omega_R t) \end{aligned} \tag{2.94}$$

$$\begin{aligned} M' = {} & i\omega_H Umd\left[\frac{1}{2}+\kappa\left(\frac{a}{d}\right)^2-\sum_{n=1}^{\infty} g_n' G_n^H(i\omega_H)\right]\exp(-i\omega_H t) \\ & +i\omega_R \Psi dmd\left[\frac{1}{6}+\kappa\left(\frac{a}{d}\right)^2-\sum_{m=1}^{\infty} gg_m^{(r1)}-\sum_{n=1}^{\infty} gg_n^{(r2)} G_n^R(i\omega_R)\right]\exp(-i\omega_R t) \end{aligned} \tag{2.95}$$

$$\begin{aligned} \eta = {} & \frac{i\omega_H Ua}{g}\left(1+\frac{i\mu}{\omega_H}\right)\left[1-\sum_{n=1}^{\infty} E_n G_n^H(i\omega_H)\right]\exp(-i\omega_H t) \\ & +\frac{i\omega_R \Psi da}{g}\left(1+\frac{i\mu}{\omega_R}\right)\left[\sum_{n=1}^{\infty} E_n \gamma_n G_n^R(i\omega_R)\right]\exp(-i\omega_R t) \end{aligned} \tag{2.96}$$

# 3 Earthquake-Induced Motion

Although the preceding solution for harmonic excitation provides insight into the general problem, its extension to a random base excitation is needed so as to account more realistically for earthquake-induced sloshing. The solution indicated in preceding sections is analogous to that of a multi-degree-of-freedom system subjected to harmonic excitation and this analogy may be exploited to extend the solution so as to treat the random motion case. Such extensions to a specified base acceleration record, and to the estimation of maximum hydrodynamic forces, maximum base overturning moments and maximum fluid surface elevations using a modal analysis involving earthquake response spectra are now indicated in the manner described by Isaacson and Subbiah (1991).

## 3.1 Time-Domain Solution

The base acceleration $\dot{u}(t)$ and the hydrodynamic force F(t) may be considered the input and the output respectively of a linear system with known characteristics. For the case of harmonic excitation

$$\dot{u}(t)=A\exp(-i\omega t) \tag{3.1}$$

$$F(t)=\mathscr{F}\exp(-i\omega t) \tag{3.2}$$

with the complex amplitudes $\mathscr{F}$ and A related by

$$\mathscr{F}=H(i\omega)A \tag{3.3}$$

where $H(i\omega)$ is the frequency response function. On the basis of Eq. 2.8, and for the case of the horizontal excitation of a circular reservoir, $H(i\omega)$ is given as:

$$H(i\omega) = -m\left(1 - \sum_{n=1}^{\infty} h_n G_n^H(i\omega)\right) \tag{3.4}$$

The frequency response function may be used to obtain the corresponding impulsive response function, which may subsequently be applied to Duhamel's integral in order to develop a time history of the force. Thus, the time domain solution for the force F(t) may be related to the known acceleration record $\ddot{u}(t)$ as:

$$\begin{aligned} F(t) &= \int_0^t \ddot{u}(\tau) h(t-\tau) d\tau \\ &= \int_0^t \ddot{u}(t-\tau) h(\tau) d\tau \end{aligned} \tag{3.5}$$

where h(t) is the impulsive response function. This is related to the frequency transfer function $H(i\omega)$ as

$$h(t) = \mathcal{L}^{-1}\{H(s)\} \tag{3.6}$$

where $\mathcal{L}^{-1}$ denotes the inverse Laplace transform and s is a subsidiary complex variable which defines the Laplace domain. By applying the known expression for $H(i\omega)$ given by Eq. 3.4, an expression for the impulsive response function h(t) may be developed as:

$$h(t) = -m_0 \delta(t) - \sum_{n=1}^{\infty} \frac{m_n \omega_n^2}{\omega_n^{(d)}} \exp(-\zeta_n \omega_n t) \sin(\omega_n^{(d)} t) \tag{3.7}$$

where $\delta$ is the Dirac delta function, $m_0$ is the high-frequency effective mass and $m_n$ is the $n^{th}$ modal mass given by Eqs. 2.11 and 2.9. Also,

$$\zeta_n = \frac{\mu}{2\omega_n} \tag{3.8}$$

$$\omega_n^{(d)} = \omega_n \sqrt{1-\zeta_n^2} \tag{3.9}$$

The time-domain solution for force F(t) may then be written as

$$F(t) = -m_0 \dot{u}_d(t) + \sum_{n=1}^{\infty} m_n \left[ \frac{\omega_n^2}{\omega_n^{(d)}} \int_0^t \dot{u}_d(\tau) \exp[-\mu(t-\tau)/2] \sin[\omega_n^{(d)}(t-\tau)] d\tau \right] \tag{3.10}$$

In most cases, the damping ratio is small so that $\omega_n^{(d)} \approx \omega_n$ for all n, and a corresponding simplification to Eq. 3.10 may be made:

$$F(t) = -m_0 \dot{u}_d(t) + \sum_{n=1}^{\infty} m_n \left[ \omega_n \int_0^t \dot{u}_d(\tau) \exp[-\mu(t-\tau)/2] \sin[\omega_n(t-\tau)] d\tau \right] \tag{3.11}$$

The first term in the above expression corresponds to the force associated with a constant, frequency-independent mass $m_0$, while successive terms in the series correspond to the force associated with each mode of sloshing.

Similarly, the overturning moment at the base and the fluid surface elevation at the tank walls are given respectively as

$$M(t) = -m_0 d_0 \dot{u}_d(t) + \sum_{n=1}^{\infty} m_n d_n \left[ \omega_n \int_0^t \dot{u}_d(\tau) \exp[-\mu(t-\tau)/2] \sin[\omega_n(t-\tau)] d\tau \right] \tag{3.12}$$

$$M'(t) = -m_0 d_0' \dot{u}_d(t) + \sum_{n=1}^{\infty} m_n d_n' \left[ \omega_n \int_0^t \dot{u}_d(\tau) \exp[-\mu(t-\tau)/2] \sin[\omega_n(t-\tau)] d\tau \right] \tag{3.13}$$

$$\eta(t)=-\left(\frac{a}{g}\right)\sum_{n=1}^{\infty}E_n\left[\omega_n\int_0^t \dot{u}_d(\tau)\exp[-\mu(t-\tau)/2]\sin[\omega_n(t-\tau)]d\tau\right] \tag{3.14}$$

where $\dot{u}_d(t)$ is the acceleration at water level in the reservoir.

## 3.2 Earthquake Spectrum

In the case of a reservoir motion due to an earthquake, the motion is generally described by a specified response spectrum. This enables one to adopt a simplified procedure for estimating maximum loads in design, as commonly carried out in estimating the response of single and multi-degree of freedom structural systems (e.g. National Building Code of Canada, 1995).

For the case of a single-degree of freedom system with small damping ratio $\zeta$ and a natural frequency $\omega_n$, the spectral displacement $S_d$ is defined as (e.g. Clough and Penzien, 1975):

$$S_d(\omega_n,\zeta)=\left\{\frac{1}{\omega_n}\int_0^t \dot{u}(\tau)\exp[-\zeta\omega_n(t-\tau)]\sin[\omega_n^d(t-\tau)]d\tau\right\}_{\substack{\text{maximum with}\\ \text{respect to time}}} \tag{3.15}$$

where t is time. This provides the maximum displacement occuring in such a system as a result of an earthquake record defined by $\dot{u}(t)$. Related to this, the corresponding pseudo spectral velocity $S_v$ and pseudo spectral acceleration $S_a$ are defined as:

$$S_v(\omega_n,\zeta)=\omega_n S_d(\omega_n,\zeta) \tag{3.16}$$

$$S_a(\omega_n,\zeta)=\omega_n^2 S_d(\omega_n,\zeta) \tag{3.17}$$

For a lightly damped system, these correspond to the maximum velocity and acceleration arising in the system. The variations of each of these with natural frequency $\omega_n$, or natural period $T_n = 2\pi/\omega_n$, for specified values of damping ratio $\zeta$ are of particular interest. Because of their inter-relationship, they are commonly shown as a single curve on four-way log paper as given in the National Building Code (1985). In fact, the National Building Code of Canada (1985) gives this curve as a set of straight lines, such that the spectral acceleration for a maximum ground acceleration of 1.0g (where g is the gravitational constant) is expressed in the form:

$$S_a(T_n,\zeta) = \begin{cases} \alpha_1 & \text{for } T_n < \beta_1 \\ \alpha_2/T_n & \text{for } \beta_1 < T_n < \beta_2 \\ \alpha_3/T_n^2 & \text{for } T_n > \beta_2 \end{cases} \qquad (3.18)$$

where $\alpha_1$, $\alpha_2$, and $\alpha_3$, are constants which depend on the damping ratio $\zeta$. For other values of peak ground acceleration, the spectral acceleration is scaled linearly.

## 3.3 Modal Superposition

For the case of a multi-degree of freedom system, the maximum response due to a base motion corresponding to each mode may be evaluated by applying the earthquake response spectrum at the natural frequency corresponding to each mode, so that the maximum displacement corresponding to the n-th mode is simply $S_d(\omega_n,\zeta_n)$. By direct analogy, the maximum force associated with the n-th mode sloshing is taken as $F_n = m_n S_a(\omega_n,\zeta_n)$. However, an additional force component corresponding to the high frequency effective mass $m_0$ and denoted $F_0$ is also present. In a similar manner, a series of overturning moment components $M_n$ will also be present. Thus one can consider a series of force components $F_n$ and moment components $M_n$ acting simultaneously and defined as:

$$F_n = \begin{cases} m_0 \ddot{u}_m & \text{for } n=0 \\ m_n S_a(\omega_n, \zeta_n) & \text{for } n \geq 1 \end{cases} \tag{3.19}$$

$$M_n = \begin{cases} m_0 d_0 \ddot{u}_m & \text{for } n=0 \\ m_n d_n S_a(\omega_n, \zeta_n) & \text{for } n \geq 1 \end{cases} \tag{3.20}$$

$$M'_n = \begin{cases} m_0 d'_0 \ddot{u}_m & \text{for } n=0 \\ m_n d'_n S_a(\omega_n, \zeta_n) & \text{for } n \geq 1 \end{cases} \tag{3.21}$$

where $\ddot{u}_m$ is the maximum ground acceleration for horizontal base motion and the maximum acceleration at fluid level for rocking base motion and $d_n$ and $d'_n$ are the effective elevation above the reservoir base. In the case of the free surface elevation $\eta_0$ = 0 and the corresponding modal elevation amplitudes $\eta_n$ are given simply as

$$\eta_n = \left(\frac{a}{g}\right) E_n S_a(\omega_n, \zeta_n) \qquad \text{for } n \geq 1 \tag{3.22}$$

where

$$E_n = \begin{cases} \dfrac{2}{(k_n a)^2} & \text{for horizontal excitation– rectangular reservoir} \\ \dfrac{2}{(k_n a)^2} \gamma_n & \text{for rocking excitation – rectangular reservoir} \\ \dfrac{2}{(k_n a)^2 - 1} & \text{for horizontal excitation– circular reservoir} \\ \dfrac{2}{(k_n a)^2 - 1} \gamma_n & \text{for rocking excitation – circular reservoir} \end{cases} \tag{3.23}$$

The high frequency effective mass $m_0$ and its effective elevations $d_0$ and $d'_0$ may be obtained from:

$$\frac{m_0}{m}=\begin{cases}1-\sum_{n=1}^{\infty}h_n & \text{for horizontal excitation}\\ \frac{1}{2}-\sum_{m=1}^{\infty}h_m^{(r1)} & \text{for rocking excitation}\end{cases} \tag{3.24}$$

$$\frac{d_0}{d}=\begin{cases}\dfrac{\frac{1}{2}-\sum_{n=1}^{\infty}g_n}{1-\sum_{n=1}^{\infty}h_n} & \text{for horizontal excitation}\\ \dfrac{\frac{1}{6}-\sum_{m=1}^{\infty}g_m^{(r1)}}{\frac{1}{2}-\sum_{m=1}^{\infty}h_m^{(r1)}} & \text{for rocking excitation}\end{cases} \tag{3.25}$$

$$\frac{d'_0}{d}=\begin{cases}\dfrac{\frac{1}{2}+\kappa\left(\frac{a}{d}\right)^2-\sum_{n=1}^{\infty}g'_n}{1-\sum_{n=1}^{\infty}h_n} & \text{for horizontal excitation}\\ \dfrac{\frac{1}{6}+\kappa\left(\frac{a}{d}\right)^2-\sum_{m=1}^{\infty}gg_m^{(r1)}}{\frac{1}{2}-\sum_{m=1}^{\infty}h_m^{(r1)}} & \text{for rocking excitation}\end{cases} \tag{3.26}$$

where $\kappa = 1/3$ for rectangular tank and $\kappa = 1/4$ for circular tank.

The modal masses and corresponding effective elevation above the reservoir base are given respectively as:

$$\frac{m_n}{m}=\begin{cases} h_n & \text{for horizontal excitation} \\ h_n\,\gamma_n & \text{for rocking excitation} \end{cases} \tag{3.27}$$

$$\frac{d_n}{d}=\frac{(k_n d)\sinh(k_n d)-\cosh(k_n d)+1}{(k_n d)\sinh(k_n d)} \qquad \text{for horizontal and rocking excitation} \tag{3.28}$$

$$\frac{d'_n}{d}=\frac{(k_n d)\sinh(k_n d)-\cosh(k_n d)+2}{(k_n d)\sinh(k_n d)} \qquad \text{for horizontal and rocking excitation} \tag{3.29}$$

The overall maximum force or moment or fluid surface elevation cannot be obtained directly from these components because of phase differences between the response at each mode. However, as an upper bound, overall maximum force $F_{max}$ may be taken as the sum of the individual maxima, so that:

$$F_{max}=\sum_{n=0}^{\infty}F_n \tag{3.30}$$

On the other hand, a more common practice to estimating the overall maximum is based on the root of the sum of the squares of the maximum modal responses. That is:

$$F_{max}=\left[\sum_{n=0}^{\infty}F_n^2\right]^{1/2} \tag{3.31}$$

In particular, when only first mode excitation is considered, Eq. 3.31 is simplified to:

$$F_{max}=\left\{[m_0\,\dot{u}_m]^2+[m_1 S_a(\omega_1,\zeta_1)]^2\right\}^{1/2} \tag{3.32}$$

Thus, in Eq. 3.31 the force is estimated by the use of the high frequency fluid mass $m_0$ which accelerates in unison with the reservoir, together with an additional modal mass $m_1$ which undergoes resonant motions at the lowest mode of sloshing frequency. A similar approach may be taken to estimating the maximum overturning moment $M_{max}$. Thus moment components $M_n$, given by Eq. 3.20 and 3.21 , are used in place of the force components $F_n$ in either Eq. 3.30 or Eq.3.31.

## 3.3.1 Combined Motion

The resultant maximum horizontal force due to horizontal and rocking excitation may be written as an extension to Eq. 3.32 using superposition as follows:

$$F_{max}=\left\{\left(m_0^H \dot{u}_m^H\right)^2+\sum_{n=1}^{\infty}\left[m_n^H S_a^H(\omega_n,\zeta_n)\right]^2+\left(m_0^R \dot{u}_m^R\right)^2+\sum_{n=1}^{\infty}\left[m_n^R S_a^R(\omega_n,\zeta_n)\right]^2\right\}^{1/2} \tag{3.33}$$

Similarly, the resultant maximum overturning moment at the base and resultant maximum fluid surface elevation at the tank wall are given respectively as

$$\begin{aligned} M_{max} = \Bigg\{ & \left(m_0^H d_0^H \dot{u}_m^H\right)^2+\left[\sum_{n=1}^{\infty} m_n^H d_n^H S_a^H(\omega_n,\zeta_n)\right]^2 \\ & + \left(m_0^R d_0^R \dot{u}_m^R\right)^2+\left[\sum_{n=1}^{\infty} m_n^R d_n^R S_a^R(\omega_n,\zeta_n)\right]^2 \Bigg\}^{1/2} \end{aligned} \tag{3.34}$$

$$\eta_{max}=\left(\frac{a}{g}\right)\left\{\left[\sum_{n=1}^{\infty} E_n^H S_a^H(\omega_n,\zeta_n)\right]^2+\left[\sum_{n=1}^{\infty} E_n^R S_a^R(\omega_n,\zeta_n)\right]^2\right\}^{1/2} \tag{3.35}$$

# 4 Hydrodynamic Damping

There are three kinds of damping which may influence the behaviour of a fluid filled reservoir: (a) structural damping, (b) material damping, and (c) fluid damping. Structural damping is generated by friction, impacting and rubbing between parts of a structure. Material damping is associated with internal energy dissipation of materials. Fluid damping is the result of energy dissipation within the fluid, as the fluid moves relative to the boundaries of the oscillating structure. Hydrodynamic damping of a system may be associated with various forms of energy dissipation. These include viscous effects associated with boundary layers on the tank walls and flow separation effects as the fluid oscillates past the baffles or perforated bulkheads in the tank.

The preceding formulations are based on the use of a specified level of hydrodynamic damping, and a suitable approach to estimating this is now considered. This involves an assessment of, firstly, the total energy of the oscillation, which is known from the available potential flow solution, and, secondly, the average rate of energy dissipation arising in the fluid, either through the boundary layers along the tank floor and walls or by flow separation around obstacles in the flow.

## 4.1 Methodology

A general methodology to estimating the damping level is now summarized. The decay of energy in a oscillating motion may be conveniently expressed by the logarithmic decrement $\upsilon$ which is defined as follows

$$\upsilon = -\left(\frac{1}{n}\right)\ln\left(\frac{A}{A_0}\right) \tag{4.1}$$

where $A_0$ is an initial fluid surface elevation and A is the fluid surface elevation after n oscillations. For small oscillations, the energy E in the system is proportional to the square of the fluid surface elevation. Therefore:

$$\ln\left(\frac{E}{E_0}\right)=2\ln\left(\frac{A}{A_0}\right) \tag{4.2}$$

where $E_0$ is an initial energy level and E is energy after n oscillations. Substituting Eq. 4.2 into Eq. 4.1:

$$E=E_0\exp(-\upsilon\omega t/\pi) \tag{4.3}$$

The above analysis is based on an assumption that the dissipation is due to a resistive force proportional to the velocity.

The corresponding energy dissipation rate D can be written as

$$D=-\frac{dE}{dt} \tag{4.4}$$

Equations 4.3 and 4.4 can be combined to yield:

$$\upsilon=\left(\frac{\pi}{\omega}\right)\left(\frac{D}{E_0}\right) \tag{4.5}$$

Using $\upsilon=2\pi\zeta$, the damping ratio $\zeta$ can thus be written as:

$$\zeta=\left(\frac{1}{2\omega}\right)\left(\frac{D}{E_0}\right) \tag{4.6}$$

In order to use Eq. 4.6, both the energy dissipation rate D and the energy E need to be estimated. Approaches to estimating D are indicated later in this chapter. The energy E may be estimated by considering separately the kinetic and potential components of E.

The average kinetic energy of the motion per unit horizontal area, denoted K and often termed simply the kinetic energy, may be developed by considering the kinetic energy of a fluid element of height dz, length dx and unit width, and carrying out appropriate integration over the fluid column. In this way K is given as

$$K=\overline{\int_0^{d+\eta}\frac{1}{2}\rho\left[\left(\frac{\partial\phi}{\partial x}\right)^2+\left(\frac{\partial\phi}{\partial z}\right)^2\right]dz} \tag{4.7}$$

where the overbar denotes an average over a oscillation period.

The average potential energy of the system per unit horizontal area, denoted V and termed the potential energy, may be considered in a similar way, except that the potential energy of the undisturbed fluid is non-zero and must be subtracted from the total potential energy in the presence of motion. Thus

$$V=\overline{\int_0^{d+\eta}\rho g z\,dz}-\overline{\int_0^{d}\rho g z\,dz}=\overline{\int_d^{\eta}\rho g z\,dz} \tag{4.8}$$

The average energy density E, that is the average energy (kinetic and potential) per unit horizontal area is simply the sum of the two expressions in Eqs. 4.7 and 4.8. That is

$$E=K+V \tag{4.9}$$

### 4.1.1 Energy Dissipation due to Boundary Layers

Two kinds of approximations are generally made in the development of a hydrodynamic damping theory associated with gravitational waves: one concerns the smallness of the fluid surface elevation such that higher order terms involving a fluid surface elevation perturbation parameter are neglected; the other concerns a boundary layer approximation in which the energy dissipation occurs principally within the bottom and side wall boundary layers. The latter may be considered as the first successive approximations involving powers of $k\delta$ which is a dimensionless boundary layer thickness, where k is the wave number and $\delta$ is the boundary layer thickness defined by:

$$\delta=\sqrt{\frac{2\nu}{\omega}} \tag{4.10}$$

The general theoretical method employed is to calculate the rate of energy dissipation within the fluid, which is given for two-dimensional motion in terms of the Rayleigh dissipation function as

$$2F=\mu\int\left[2\left(\frac{\partial u}{\partial x}\right)^2+2\left(\frac{\partial w}{\partial z}\right)^2+\left(\frac{\partial u}{\partial z}+\frac{\partial w}{\partial x}\right)^2\right]dx\,dz \tag{4.11}$$

where $\mu$ is the dynamic viscosity of the fluid, and the integral is taken over the region occupied by the fluid. The corresponding function for three-dimensional motion is given in Lamb (1945). The average rate of energy dissipation per unit length in the x direction (and per unit width in the two-dimensional case) can be expressed in terms of F and is simply

$$D=\frac{2F}{L} \tag{4.12}$$

A knowledge of the flow field in the boundary layers will enable D to be evaluated. Alternatively D may be expressed in terms of the shear stress acting at the fluid boundaries. For a two-dimensional oscillatory motion over a flat boundary, the average rate of energy dissipation is given as

$$D=\overline{\tau u} \tag{4.13}$$

where $\tau$ is the shear stress at the boundary, u is the fluid velocity at the outer edge of the boundary layer and the overbar denotes a temporal mean. This representation is particularly useful for the case of a turbulent boundary layer.

## 4.1.2 Energy Dissipation due to Baffles

When baffles or perforated bulkheads are present in the container, flow separation effects are expected to dominate, and boundary layer effects are expected to be relatively small. The corresponding damping coefficient may be estimated by considering first the drag force due to an oscillatory flow past a flat plate oriented perpendicular to the flow. This may be expressed as:

$$F=\frac{1}{2}\rho A C_d u_r |u_r| \tag{4.14}$$

where $\rho$ is the mass density of the fluid, A is a suitable area of the plate, $C_d$ is an empirical drag coefficient and $u_r$ is the velocity of the flow relative to the plate. As a suitable approximation, Eq. 4.14 may be linearized as:

$$F=\frac{1}{2}\rho A C_d \frac{8}{3\pi} U_r u_r \tag{4.15}$$

where $U_r$ is the amplitude of $u_r$. The corresponding contribution to the average rate of energy dissipation is then

$$D = \overline{Fu_r} \tag{4.16}$$

The contributions from all the obstacles in the flow may thereby be obtained, with suitable approximations used for effective area A and the velocity amplitude $U_r$. The inertia force on the plate has been omitted since it does not contribute to the energy dissipation. This may be demonstrated by noting that the inertia force and the relative velocity applied to Eq. 4.16 would be out of phase.

## 4.2 Determination of Hydrodynamic Damping for Rectangular Tank

The preceding method is applied to a rectangular tank which has a length 2a in the x direction, width 2b in the y direction, and is filled with an incompressible fluid to a depth d. First, the hydrodynamic damping due to the boundary layers is evaluated and then damping due to baffles in the tank is considered.

The velocity potential of the flow for first mode free oscillations in the tank is given by

$$\Phi = \left(\frac{g\eta_a}{\omega}\right)\frac{\cosh(kz)}{\cosh(kd)}\sin(kx)\exp(-i\omega t) \tag{4.17}$$

where $\omega^2 = gk\tanh(kd)$, $ka = \pi/2$, and $\eta_a$ is the amplitude of sloshing.

The total energy of the motion of undamped oscillations per unit horizontal area can be expressed in terms of the amplitude of fluid surface elevation as:

$$E_0 = \frac{1}{4}\rho g \eta_a^2 \tag{4.18}$$

## 4.2.1 Laminar Boundary Layer

The velocity profile in the oscillating boundary layer on a flat boundary can be expressed in complex form as:

$$u(z,t) = U_w \left[1 - \exp\left(-[1-i]\frac{z}{\sqrt{2\nu/\omega}}\right)\right]\exp(-i\omega t) \tag{4.19}$$

where $U_w$ is the fluid velocity at the outer edge of the boundary layer. The shear stress at the wall is given by

$$\tau_w = \mu\left(\frac{\partial u}{\partial z}\right)_{z=0} \tag{4.20}$$

Substituting Eq. 4.19 into Eq. 4.20, one obtains:

$$\tau_w = \rho\sqrt{\nu\omega}\, U_w \exp[-i(\omega t + \pi/4)] \tag{4.21}$$

The average rate of energy dissipation D is given by Eq. 4.13, and can thus be expressed as

$$D = \frac{1}{2}\rho\sqrt{\frac{\nu\omega}{2}}\int U_w^2\, dA \tag{4.22}$$

The average energy dissipation due to bottom and the individual walls in the tank can be calculated using the appropriate velocities. The bottom wall velocity and average energy dissipation are thus given respectively as:

$$U_{wb} = g\eta_a \frac{k}{\omega} \frac{\cos(kx)}{\cosh(kd)} \tag{4.23}$$

$$D_{wb} = \rho g a b k \sqrt{2\nu\omega}\, \frac{\eta_a^2}{\sinh(2kd)} \tag{4.24}$$

Likewise, the velocity at the two walls $x = \pm a$ and the corresponding average energy dissipation are calculated respectively as:

$$U_{ws,a} = g\eta_a \frac{k}{\omega} \frac{\sinh(kz)}{\cosh(kd)} \tag{4.25}$$

$$D_{ws,a} = \rho g b d k \sqrt{2\nu\omega}\, \frac{1}{\sinh(2kd)} \left[ \frac{\sinh(2kd)}{2kd} - 1 \right] \eta_a^2 \tag{4.26}$$

Similarly, the average energy dissipation due to the side walls at $y = \pm b$ is given as

$$D_{ws,b} = \rho g a \sqrt{\frac{\nu\omega}{2}}\, \eta_a^2 \tag{4.27}$$

The total energy dissipation due to the boundary layers on the bottom and the four walls is given by

$$D = D_{wb} + D_{ws,a} + D_{ws,b} \tag{4.28}$$

Substituting from Eq. 4.6, the damping ratio is eventually given as:

$$\zeta_L = \frac{1}{2} k\delta \left[ \left( 1 - \frac{d}{a} \right) \frac{1}{\sinh(2kd)} + \frac{1}{2(ka)} \left( 1 + \frac{a}{b} \right) \right] \tag{4.29}$$

substitute for $ka = \pi/2$ which corresponds to first mode sloshing

$$\zeta_L = \frac{1}{2} k\delta \left[ \left( 1 - \frac{d}{a} \right) \frac{1}{\sinh(2kd)} + \frac{1}{\pi} \left( 1 + \frac{a}{b} \right) \right] \tag{4.30}$$

where $\delta$ is boundary layer thickness, defined by $\delta = \sqrt{2\nu/\omega}$.

It is noted that the ratio of total damping to the damping due to the bottom is:

$$\frac{\zeta_L}{\zeta_B} = \left( 1 - \frac{d}{a} \right) + \frac{1}{\pi} \left( 1 + \frac{a}{b} \right) \sinh(2kd) \tag{4.31}$$

It should be noted that the preceding analysis is based on steady state sinusoidal oscillations, whereas the onset of motions from rest will lead to transient effects not described by the above formulation. In order to consider such effects, consider an impulsive change of velocity at time t = 0 from zero to a steady value. A boundary layer is created whose thickness is of order $\sqrt{\nu t}$. As time progresses, the boundary layer increases in thickness and gradually distorts the flow until the steady state boundary layer is fully developed. It follows that, because the boundary layer starts as being very thin and increases in thickness, the shear stress at first rises to a large value and then decays to its steady value. In earthquakes, the boundary layer does not reach the steady state condition, so the boundary layer is thinner than predicted by the steady state sinusoidal approximation and the corresponding shear stress and associated damping are consequently higher. Therefore the above method is expected to underpredict damping

with respect to earthquakes. On the other hand, in free vibration tests the steady state boundary layer is developed and damping is predicted well.

## 4.2.2 Turbulent Boundary Layers

The preceding section concerns laminar boundary layers. When the boundary layers are turbulent, the rate of energy dissipation and therefore the hydrodynamic damping will differ appreciably and the following approach may be used.

The shear stress at a wall due to a turbulent boundary layer can be written in terms of a friction coefficient $f_w$ as:

$$\tau_w = \frac{1}{2}\rho f_w \, u|u| \tag{4.32}$$

where u is the instantaneous fluid velocity outside the boundary layer and is given by:

$$u = U_{wb}\cos(\omega t) \tag{4.33}$$

Note that the Eq. 4.32 contains the assumption that the shear stress is in phase with the velocity, although in a more complete treatment any phase difference between these must be accounted for as described, for example, by Kajiura (1968). The friction coefficient $f_w$ is expected to depend on the Reynolds number and the wall roughness, although it should be relatively insensitive to the Reynolds number in turbulent flow conditions. It is assumed that these conditions exist and therefore that $f_w$ is a constant for a particular situation.

For reference, in the case of a laminar boundary layer, $f_w = 2\sqrt{2}$ /Re, where the Reynolds Number $Re = U_w\delta/\nu$.

For a turbulent boundary layer flow, different relations are available to describe the friction coefficient $f_w$ for flow over smooth and rough beds. For smooth beds, the friction coefficient proposed by Jonnson (1967) may be adopted

$$f_{ws} = 0.09\,RE^{-0.02} \tag{4.34}$$

where RE is a local Reynolds number based on the local amplitude A of fluid displacement just outside the boundary layer and defined by:

$$RE = \frac{U_w\, A}{\nu} \tag{4.35}$$

For rough beds, the friction factor $f_{wr}$ depends on the ratio $A/k_s$, where $k_s$ is the Nikuradse roughness of the surface. Swart (1976) proposed the following form for the rough bed turbulent flow region:

$$f_{wr} = \begin{cases} 0.00251 \exp\left[5.21\left(\dfrac{A}{k_s}\right)^{-0.19}\right] & \text{for } \dfrac{A}{k_s} > 1.57 \\ 0.3 & \text{for } \dfrac{A}{k_s} < 1.57 \end{cases} \tag{4.36}$$

The average energy dissipation in the turbulent boundary layer can be written from Eq. 4.13 as

$$D = \frac{2}{3\pi}\rho f_w \int U_w^3 dA \tag{4.37}$$

Substituting Eq. 4.23 into Eq. 4.37, D may be expressed as:

$$D=\left(\frac{8}{9\pi}\right)\rho f_w\left(\frac{g\eta_a}{\omega}\right)^3\frac{k^2}{\cosh^3(kd)} \tag{4.38}$$

Similar to the laminar boundary layer case, the damping coefficient due to turbulent boundary layers can thus be obtained as:

$$\zeta_T=\left(\frac{8}{9\pi}\right)f_w\left(\frac{\eta_a}{a}\right)\left[\frac{1}{\sinh^2(kd)\cosh(kd)}\right] \tag{4.37}$$

The above equation can be organized as follows

$$\zeta_T=\left(\frac{16}{9\pi}\right)f_w\left(\frac{\eta_a}{d}\right)\left(\frac{d}{a}\right)\left[\frac{1}{\sinh\left(\frac{\pi}{2}\frac{d}{a}\right)\sinh\left(\pi\frac{d}{a}\right)}\right] \tag{4.38}$$

The condition of transition to a turbulent boundary layer may be expressed in terms of a Reynolds number $Re = U_w\delta/\nu$, which is based on the oscillatory boundary layer thickness and the velocity amplitude just outside the boundary layer. Values of 566 obtained by Li (1954) and 500 obtained by Sergeer (1966) are probably reasonably reliable indications of a transition Reynolds number, although transition may be expected to take place over a range of Reynolds numbers rather than at one specific value. In particular, Hino, Sawamoto and Takasu (1976) have considered the problem of boundary layer transition in an oscillatory pipe flow, as indicated by experiments employing hot-wire anemometer to observe velocity fluctuations. The flow is found to be intermittently turbulent over a wide range of conditions, and they distinguish between varying degrees of turbulent flow which they describe as weakly turbulent, conditionally turbulent and fully turbulent.

## 4.2.3 Damping due to Baffles

The preceding section considered the estimation of hydrodynamic damping due to the boundary layers on the tank walls. Attention is now given to the hydrodynamic damping due to flow separation effects as the fluid oscillates past baffles. Two types of baffles as shown in Figs. 7(a) and 7(b) are considered here. These correspond, respectively, to two horizontal baffles perpendicular to the side walls and a vertical baffle perpendicular to the bottom of the tank.

### Case I: Horizontal Baffles (Figure 7(a))

The average rate of energy dissipation due to the baffles present in the tank is

$$D=\overline{F_d\, u_r}$$
$$=\frac{2}{3\pi}\rho A C_d U_r^3 \tag{4.39}$$

where:

$$A=2\alpha ab \tag{4.40}$$

and $\alpha = \ell/a$ is defined as relative baffle length corresponds to tank half length a and baffle length $\ell$.

The velocity perpendicular to the horizontal baffle at an elevation h above the base is given as

$$U_r = g\eta_a \frac{k}{\omega}\frac{\sinh(kh)}{\cosh(kd)} \tag{4.41}$$

Substituting Eq 4.41 into Eq 4.40 and applying Eq 4.6, the hydrodynamic damping coefficient due to horizontal baffles is given as:

$$\zeta_H = \frac{4}{3}\alpha C_d \left(\frac{\eta_a}{a}\right)\frac{\sinh^3(kh)}{\sinh(2kd)\sinh(kd)} \tag{4.42}$$

Rearranging the above equation:

$$\zeta_H = \frac{4}{3}\alpha C_d \left(\frac{\eta_a}{d}\right)\left(\frac{d}{a}\right)\frac{\sinh^3\left(\frac{\pi}{2}\frac{h}{a}\right)}{\sinh\left(\pi\frac{d}{a}\right)\sinh\left(\frac{\pi}{2}\frac{d}{a}\right)} \tag{4.43}$$

## Case II: Vertical Baffle (Figure 7(b))

In this case, the average energy dissipation is expressed as

$$D = \frac{4}{3\pi}\rho b C_d \int_0^{\ell} U_r^3 dz \tag{4.44}$$

where

$$U_r = g\eta_a \frac{k}{\omega}\frac{\cosh(kz)}{\cosh(kd)} \tag{4.45}$$

Again, substituting Eq. 4.45 into Eq. 4.44 and applying Eq. 4.6, the hydrodynamic damping due to vertical baffle can be expressed as

$$\zeta_V = \frac{2}{9\pi}C_d \left(\frac{\eta_a}{a}\right)\left[\frac{\sinh(2\beta kd)\cosh(\beta kd)+4\sinh(\beta kd)}{\sinh(2kd)\sinh(kd)}\right] \tag{4.46}$$

Rearranging gives:

$$\zeta_V = \frac{2}{9\pi} C_d \left(\frac{\eta_a}{d}\right)\left(\frac{d}{a}\right)\left[\frac{\sinh\left(\pi\beta\frac{d}{a}\right)\cosh\left(\frac{\pi}{2}\beta\frac{d}{a}\right)+4\sinh\left(\frac{\pi}{2}\beta\frac{d}{a}\right)}{\sinh\left(\pi\frac{d}{a}\right)\sinh\left(\frac{\pi}{2}\frac{d}{a}\right)}\right] \tag{4.47}$$

where $\beta = \ell/d$ is defined as relative baffle length corresponds to water depth d and baffle length $\ell$.

The drag coefficient of a flat plate in an oscillating fluid depends strongly on the Keulegan-Carpenter Number K = UT/$\ell$, where U is the maximum velocity in a cycle, T is the period of oscillation, and $\ell$ is length of the baffle. The case of a wall-bounded plate has been measured experimentally by Sarpkaya and O'Keefe (1996) and Fig. 8 shows the measured values of $C_d$ as a function of Keulegan-Carpenter number. This indicates that the drag coefficient for a wall-bounded plate exhibits a relatively steep variation of $C_d$ with K, and that the effect of the wall is to increase $C_d$ by as much as 50 % in the range 1 < K < 30, relative to the free-plate case. This indicates that drag coefficients obtained from free-plate tests are not particularly applicable to wall-bounded plates, and that wall-bounded plates provide a high degree of damping, particularly at small amplitudes of oscillation.

It is also noted that application of Eqs. 4.38, 4.43 and 4.47 above requires an estimate of the elevation amplitude, $\eta_a$. The $\eta_a$ itself may range up to maximum levels associated with wave breaking (though near the breaking limit the assumptions required for the application of linear wave theory are no longer valid).

# 5 Experimental Study

Small scale physical models of structures provide a convenient means of predicting full-scale performance. Model tests are particularly invaluable when analytical prediction methods are inadequate or unavailable, as in some separated flow and dynamic response problems within the general area of fluid-structure interaction. Such model tests relating to the problem at hand have been carried out using the shake-table of the Earthquake Engineering Laboratory of the Department of Civil Engineering at the University of British Columbia. The following sections describe the equipment and methods used in the experiments. The techniques of signal conditioning and data analysis used to derive pertinent information from measurements are also discussed.

## 5.1 Dimensional Analysis

In planning model tests and the presentation of results, it is useful to carry out a dimensional analysis of the problem in order to identify the governing parameters so that controlled variables in the model can be suitably varied.

A reservoir is subjected to a harmonic uni-directional horizontal base acceleration is considered. Variables defining the system may be taken as:

- $a$ reservoir dimension
- $d$ liquid depth
- $\rho$ density of the liquid
- $\mu$ viscosity of the liquid
- $g$ gravitational acceleration
- $U$ amplitude of base velocity
- $\omega$ exciting frequency

$\xi$ damping coefficient

A number of dependent variables defining the response of the system are of interest:

$\eta$ free surface elevation at a specified location

F hydrodynamic force acting on the reservoir

$\omega_n$ sloshing frequency

On the basis of a dimensional analysis and assuming a linear response, the dimensionless elevation amplitude, dimensionless force amplitude and dimensionless sloshing frequency may be expressed in the form:

$$\frac{g\eta}{\omega Ua} = f_1\left(\frac{d}{a}, \frac{\omega^2 a}{g}, \frac{\rho Ua}{\mu}, \xi\right) \tag{5.1}$$

$$\frac{F}{\rho a^2 d\omega U} = f_2\left(\frac{d}{a}, \frac{\omega^2 a}{g}, \frac{\rho Ua}{\mu}, \xi\right) \tag{5.2}$$

$$\frac{\omega_n^2 a}{g} = f_3\left(\frac{d}{a}, \frac{\omega^2 a}{g}, \frac{\rho Ua}{\mu}, \xi\right) \tag{5.3}$$

d/a is a ratio of characteristic reservoir size to fluid depth; $\omega^2 a/g$ is a frequency parameter indicative of the reservoir size to wave length ratio, and $\rho Ua/\mu$ is a Reynolds number which accounts for viscous effects.

# 5.2 Test Facilities

## 5.2.1 Shake-Table

The shake-table is a 3 m by 3 m (10 ft by 10 ft) cellular structure fabricated from aluminum and weighing 2,100 kg (4,600 lbs). The table motions are produced by five hydraulic actuators, each of which has a maximum displacement $\pm 7.6$ cm ($\pm 3$ inches). The actuator used to produce the horizontal longitudinal motions can generate up to 156 kN (35,000 lbs) of force. The remaining four actuators are used to produce either vertical or rocking motions and can each generate up to 67 kN (15,000 lbs) of force. Figure 2 shows the ground motion direction components. The actuators are mounted in an isolated concrete pit foundation weighing approximately 226,800 kg (500,000 lbs). Test specimens are attached to the table through a system of threaded anchors on a 53.3 cm (21 in) square grid. A block diagram of the shake-table facility is shown in Fig. 3.

## 5.2.2 Signal Generation and Data Acquisition

The facility incorporates a digital computer control system to allow maximum flexibility in designing and performing tests. The shake-table motions are controlled by a specialized state-of-the-art Multi Exciter Vibration Control software package. This software performs a closed-loop control of the shakers and is capable of reproducing recorded earthquake motions with high accuracy.

The laboratory is equipped with several data acquisition systems for data collection and analysis. A 32 channel data acquisition system is generally used for instrumentation of specimens tested on the shake-table. All channels are conditioned by variable cut-off filters to provide optimal control over signal levels and noise reduction.

The control commands for the table are generated by a 10 MHz AST (IBM/AT compatible) computer with 40 MB hard drive and 640 K of RAM. Ground motion records are stored digitally on hard disk which is used to generate table commands during testing. Two Metrabyte DAS boards are installed in the computer to provide 32 A/D channels for data acquisition. The software is capable of acquiring data from all 32 channels at a rate of 500 Hz per channel (16 kHz total), as well as controlling the shake-table simultaneously. The functional block diagram shown in Fig. 3 indicates the relationship between the data acquisition, processing and simulator control systems.

## 5.2.3 Tank Model and Fixtures

A sketch of the tank model and associated fixtures is given in Fig. 4. The rectangular tank model was constructed of plexi-glass. The dimensions of the tank are 0.5 m long, and 0.5 m wide and 0.5 m high. The tank base was fixed with a steel plate to limit flexibility in the vertical direction. The top and bottom of the load cell were attached to circular steel plates, each with 20 threaded bolts. The top plate was fixed to the tank bottom with bolts; and the bottom plate was fixed to a U beam, which in turn is bolted to the shake-table. This fixture prevents uplift motion. Figure 5 shows two side views of the tank model in the shake-table.

## 5.2.4 Instrumentation

### Multi-Component Transducer

A multi-component transducer, manufactured by Advanced Mechanical Technology, Inc. (AMTI), was used to measure the base shear force and overturning moment at the base of the tank. This transducer has six channels of output, i.e., $F_X$, $F_Y$, $F_Z$, and $M_X$, $M_Y$, $M_Z$. The coordinate system axes are shown in Fig. 6. The top and bottom surfaces of this instrument are 5 inches in diameter and are made of high strength anodized aluminum.

Eight 1/4"-20 threaded inserts on a 4 inch bolt circle diameter are provided on each surface. The transducer uses strain gages to perform the force and moment measurements. An elastic member inside the transducer is gaged such that the three forces and three moments applied to the unit may be isolated with minimum crosstalk. The gages are configured in four-arm bridges to provide high thermal stability.

In general the transducer's sensitivities are of the order of 1 μV/lbf for force and 1 μV/in-lbf for moment, so that amplification is necessary to provide sufficiently high levels of output signals for data logging purposes. The following equation is used to determine the required amplifier gain:

$$G = \frac{V_0}{V_e \times S \times FSL}$$

where G is gain, $V_0$ is the desired full-scale output voltage, $V_e$ is the bridge excitation voltage, S is the dynamometer sensitivity, and FSL is the expected full-scale load. It is often desirable to use different gains for different channels depending on the expected full-scale loads for those axes.

## Wave Probe

The wave probe used is based on a design of the Hydraulics Laboratory of the National Research Council, Canada. It is a capacitance-type 'bow-string' sensor consisting of a loop of wire stretched on one side of a metal frame. The wire loop sensor is connected to an amplifier designed to convert the change of capacitance to a measurable change in voltage. This device has a linearity better than 98.5% and a resolution better than 1 mm, the latter being limited by meniscus, and under wave action, by the run-up. A single wave probe was used near the tank wall as shown in Fig. 4.

# 5.3 Test Program

The purpose of the experimental study was to measure the hydrodynamic characteristics of the tank due to the sloshing motion. The hydrodynamic characteristics of interest are the fluid surface elevation, the horizontal force on the tank, the overturning moment at the base of the tank and the hydrodynamic damping. It was expected that the parameters that would have the greatest influence on the performance of the tank would be the fluid depth d, the tank size characterized by the dimension a, the exciting frequency for harmonic motion $\omega$, the dimensions of the baffles in the tank and the location of the baffles. The tank dimensions were kept constant while the fluid depth and exciting frequency were varied. The following series of tests were carried out:

1. Horizontal harmonic motion
2. Rocking harmonic motion
3. Horizontal earthquake-induced motion
4. Simultaneous horizontal and rocking harmonic motions

As well, tests with baffles were carried out for a horizontal harmonic base motion with a constant fluid depth corresponding to d/a = 1.0.

## Harmonic Excitations

The horizontal harmonic excitation tests were carried out for two fluid depths corresponding to d/a = 0.5 and 1.0. The tests for rocking and simultaneous horizontal and rocking harmonic motions were carried out for one depth, d/a = 1.0. The excitation frequency was varied from 0.50 to 2.20 Hz, and the amplitude of excitation was sufficiently small to satisfy the linear condition. Tables 2-5 shows the test cases for horizontal, rocking and combined horizontal and rocking motions.

### Harmonic Excitation with Baffles

Two types of baffles, denoted horizontal and vertical baffles shown in Fig. 7 were used. Horizontal baffles are oriented perpendicular to the side-walls. The length of the baffles was kept constant at $\ell$ = 4 cm and three baffle elevations were used: h/d = 0.6, 0.7 and 0.8, where h is the baffle elevation above the base of the tank. The vertical baffle was oriented perpendicular to the bottom and located at the middle of the base. The lengths of the baffles were varied as $\ell$/d = 0.1, 0.2 and 0.3, where $\ell$ is the baffle length above the base of the tank.

### Earthquake Excitation

For the laboratory tests, the Mexico 1979 earthquake record has been used as the basis for simulating the earthquake excitation. In the present study, the maximum acceleration is scaled to 0.1g without time scale change, so that the velocity and displacement maxima differ from the full-scale condition. The frequency is 0.5 – 12 Hz and overall duration is about 50 s.

## 5.4 Data Analysis

This section describes the techniques used to analyze the base motion record and the corresponding time domain records of the fluid surface elevation, horizontal force and overturning moment, both for harmonic and earthquake excitation.

### System Characteristics and Damping Tests

An initial step in the parameter estimation of the test structure is to measure the natural frequencies of the sloshing motion. The natural frequencies of the sloshing motion are determined experimentally by first exciting the tank-fluid system with a very high frequency harmonic base motion and then suddenly stopping the base excitation. At this

point, the fluid surface elevation decay is recorded for a sufficient duration by the wave probe and a standard Fast Fourier Transform program is used to convert this record into a Fourier Amplitude Spectrum. The natural frequencies of the sloshing motion correspond to the frequencies defining the maximum spectral values of the Fourier Amplitude Spectrum.

Hydrodynamic damping ratios $\zeta$ for a single-degree-of-freedom system may be determined experimentally by one of two methods which are based on linear system theory: the half-power (bandwidth) method, and the logarithmic decrement method.

The second method was utilized in this study. Free vibration tests were carried out to determine the damping ratio of the system. A sample record of the fluid surface elevation near a tank wall from free vibration tests is shown in Fig. 9. If the fluid surface elevation at time $t = t_i$ is denoted by $\eta_i$ and the elevation at time $t = t_i + 2\pi r/\omega_d$ is denoted by $\eta_{i+r}$ where r is the cycle increment and $\omega_d$ is the damped natural frequency equal to $\omega\sqrt{1-\zeta^2}$, then it can be shown that

$$\frac{\eta_{i+r}}{\eta_i} = \exp\left(-\zeta\frac{\omega}{\omega_d}2\pi r\right) \tag{5.4}$$

Expanding $\omega_d$ and eliminating the exponential leads to

$$\ln\left[\frac{\eta_{i+r}}{\eta_i}\right] = -\frac{\zeta}{\sqrt{1-\zeta^2}}2\pi r \tag{5.5}$$

For a lightly damped system (i.e. $\zeta < 0.20$), this may be approximated as:

$$\ln\left[\frac{\eta_{i+r}}{\eta_i}\right] = -2\pi r\zeta \tag{5.6}$$

from which

$$\zeta = \frac{1}{2\pi r}\ln\left[\frac{\eta_i}{\eta_{i+r}}\right] \tag{5.7}$$

## 5.4.1 Noise Filtering Techniques

Most analyses of experimental data provided as time histories usually involve filtering the data to remove unwanted noise which can affect the results. This is a fairly simple procedure which can either be implemented in the form of analog filtering by dedicated circuits during the data collection stage, or by using digital filtering algorithms after the data has been digitized and stored. The treatment of correct noise removal is especially important in this study since the response of tank – liquid system may have frequency information which is in the same range as electric noise. Any filtering technique used for treating such data must ensure that valid signal information is not removed along with the interfering noise.

A variety of sources can produce noise. The power supply lines that run through the laboratory generate electromagnetic noise which shows as a 60 Hz signal mixed with the main signal. Electromagnetic noise is also generated from other devices (e.g. motors) within the laboratory. Thermal noise of a random nature and spread over a range of frequencies is generated within the transducers and circuitry of the amplifiers. Load cell which is relatively sensitive may pick up mechanical noise from the shake-table. In addition, quantization noise is introduced during the analog-to-digital conversion process, but this can be mitigated to a large extent by using the full range of the A/D converter for a given signal.

Digital filtering of time series data can be done in two ways. A non-recursive filtering technique using an FFT-based algorithm provides low-pass, high-pass, band-pass or band-stop filtering capabilities. The other method, known as polynomial filtering is recursive and is based on simple interpolating polynomials which act as low-pass filters.

In the present study, the commercial program *DADisp* is used to filter the data obtained from the experiments. *DADisp* filters allow one to quickly design, analyze and process both FIR (Finite Impulse Response) and IIR (Infinite Impulse Response) digital filters. The FIR module creates lowpass, highpass, bandpass, bandstop, multiband filters, and Hilbert transformers and differentiators using the Parks-McClellan/Remez Exchange optimal design algorithm. The IIR module supports Butterworth, Chebchev I, Chebychev II and Elliptic designs for lowpass, highpass, bandpass and bandstop recursive filters.

The FIR lowpass filter is used in order to remove high frequency noise in the data. The following parameters are needed to design the lowpass filter: the sampling rate, cutoff frequency, passband ripple, stopband attenuation and stopband frequency. The cutoff frequency is obtained from a spectrum analysis of the unfiltered data. The stopband frequency is less than half of the sampling rate.

## 5.4.2 Analysis of Elevation and Force Records

Figure 10 shows a comparison of shake-table acceleration and tank top acceleration conditions. The shake-table and tank top acceleration values agree with each other rather well and confirm the assumption of a rigid tank. The experiments were carried out both with fluid in the tank and without fluid in the tank. When the tank is without fluid, the force is due to the inertia of the tank together with any attached masses, but when the tank is filled with fluid, the force is in part due to the inertia of the fluid and sloshing in the tank. By comparing the load cell records with fluid and without fluid, the forces due to sloshing can be obtained.

The horizontal force and base overturning moment records were filtered using the *DADdisp* software program. Figure 11 shows a sample record from the load cell before and after filtering. The signals generated by the capacitance type wave probe were free from noise and never filtered. The maximum value from each record except for water surface elevation was then recorded with fluid and without fluid. From these values, the relevant dimensionless parameters representing the fluid surface elevation at the tank wall, the horizontal force on the tank, and the overturning moment at the base can be calculated.

# 6 Results and Discussion

This chapter summarizes results obtained from the analytical solutions and the experiments, as described in Chapters 2 - 4, including a comparison with reported results from previous studies. First, analytical results relating to the dimensionless hydrodynamic coefficients are presented. The estimation of the maximum force, maximum overturning moment and maximum fluid surface elevation due to earthquake-induced sloshing are presented using both time-domain solution as well as a modal analysis. Also, analytical results for damping coefficients due to boundary layers and baffles are presented. Finally, experimental results relating to maximum hydrodynamic coefficients and damping coefficients from free vibration tests are presented and compared with analytical results.

## 6.1 Theoretical Results

### 6.1.1 Harmonic Excitation

The solution obtained for harmonic excitation indicates that for the case of a real fluid the dimensionless amplitude of the free surface elevation at a particular location, the dimensionless force amplitude, the dimensionless overturning moment amplitude, the dimensionless added mass $C_a$, and the dimensionless damping coefficient $C_\lambda$ are all functions only of the frequency parameter $\omega^2 a/g$, the relative depth d/a, and the damping ratio $\zeta_1$. Selected results illustrating the above relationships are now presented.

Figures 12 and 13 show the dimensionless amplitude of the free surface elevation at the wall, dimensionless force amplitude and dimensionless overturning moment amplitude as functions of the frequency parameter $\omega^2 a/g$ for d/a = 1.0 for damping values $\zeta_1$ = 0, 0.05, and 0.10, for both horizontal and rocking base motion and for a rectangular reservoir.

Figures 14 and 15 show the corresponding results for a circular reservoir. The expected large amplitudes near the resonant frequencies $\omega_n$ are indicated, with an increase in the degree of damping giving rise to a significant decrease in the amplitudes near these frequencies. On the other hand, as the frequency approaches zero, the dimensionless amplitudes approach constant values independent of the magnitude of damping and given by following expressions:

For horizontal excitation:

$$\frac{g\eta}{\omega U a}=1 \tag{6.1}$$

$$\frac{F}{\omega U m}=1 \tag{6.2}$$

$$\frac{M}{\omega U m d}=\frac{1}{2} \tag{6.3}$$

$$\frac{M'}{\omega U m d}=\frac{1}{2}+\kappa\left(\frac{a}{d}\right)^2 \tag{6.4}$$

For rocking excitation:

$$\frac{g\eta}{\omega \Psi d a}=\sum_{n=1}^{\infty} E_n \tag{6.5}$$

$$\frac{F}{\omega \Psi d m}=\frac{1}{2}-\sum_{m=1}^{\infty} h_m^{(r1)}+\sum_{n=1}^{\infty} h_n^{(r2)} \tag{6.6}$$

$$\frac{M}{\omega \Psi d m d} = \frac{1}{6} - \sum_{m=1}^{\infty} g_m^{(r1)} - \sum_{n=1}^{\infty} g_n^{(r2)} \tag{6.7}$$

$$\frac{M'}{\omega \Psi d m d} = \frac{1}{6} + \kappa \left(\frac{a}{d}\right)^2 - \sum_{m=1}^{\infty} gg_m^{(r1)} + \sum_{n=1}^{\infty} gg_n^{(r2)} \tag{6.8}$$

where $\kappa = 1/3$ for rectangular tank and $\kappa = 1/4$ for circular tank

The above relationships indicate that the dimensionless hydrodynamic coefficients except for dimensionless base moment (considered to include the effects of base pressure) are constant for horizontal excitation for any configuration of tank. On the other hand, for rocking excitation, the dimensionless hydrodynamic coefficients are functions of d/a, but are constant for a particular tank configuration.

Figures 16 and 17 show the added mass, the damping coefficient, and the force amplitude, expressed in suitable dimensionless forms, as functions of the frequency parameter for three different values of damping ratio, $\zeta_l$ = 0, 0.05, and 0.10, for rectangular tank and for horizontal and rocking excitations respectively. Figures 16(a) and 17(a) show that, for the case of zero damping, the effect of the resonant frequencies is marked by large increases in added mass, with a sign reversal in added mass occurring near each resonant frequency. When $C_a < 1$, the added mass becomes negative ($m_e < m$), corresponding to a sloshing-induced force which is out of phase with the reservoir displacement, thus leading to a force reduction from that if sloshing were absent. The added mass is seen to approach zero as $\omega^2 a/g \to 0$, as sloshing effects diminish and the hydrodynamic force becomes associated with true mass m of the fluid. On the other hand, as $\omega^2 a/g \to \infty$ and the damping is non-zero, $C_a$ tends to a constant value corresponding to the high-frequency effective mass $m_0$: $C_a \to (m_0/m) - 1$. As expected, an increase in the degree of damping is seen to reduce significantly the extreme values of added mass in the vicinity of the resonant frequencies, such that the effect of any

resonance is virtually indiscernible at third and higher mode resonances. This is typical of the influence of damping on multi-degree-of-freedom systems where magnification at higher mode resonances becomes small.

Figures 16(b) and 17(b) show the corresponding results for the dimensionless damping coefficient $C_\lambda$. The coefficient exhibits a noticeable peak near $\omega = \omega_1$, with smaller peaks at the higher resonant frequencies. These peaks become higher but narrower as the damping ratio is reduced. Figures 16(c) and 17(c) show the corresponding results for the dimensionless force amplitude. As before, the force amplitude is largest close to the lowest resonant frequency and reduces as the degree of damping is increased. For the case of zero damping, the dimensionless force amplitude corresponds to $|1+C_a|$, whereas when the damping coefficient is nonzero the force amplitude corresponds to an appropriate combination of $C_a$ and $C_\lambda$:

$$\frac{|F|}{\omega U m} = \sqrt{(1+C_a)^2 + C_\lambda^2} \qquad \text{for horizontal excitation} \qquad (6.9)$$

$$\frac{|F|}{\omega \Psi d\, m} = \sqrt{(1+C_a)^2 + C_\lambda^2} \qquad \text{for rocking excitation} \qquad (6.10)$$

Figures 18 and 19 show results similiar to Figs. 16 and 17, but corresponding related to circular tanks. These figures indicate that the results for circular tanks have the same trend as for rectangular tanks.

Figures 20 and 21 show the dimensionless amplitude of the free surface elevation, dimensionless force amplitude and dimensionless moment amplitude as a function of d/a for damping values $\zeta_1$ = 0.01, 0.05 and 0.10 for a rectangular tank for horizontal and rocking excitations respectively. In the case of the surface elevation for horizontal excitation, the maximum elevation is virtually unaffected by changes in d/a for a given

value of $\zeta_1$, and varies only with the degree of damping. This may be revealed by an examination of Eq. 2.6, and 2.44: d/a influences the dimensionless elevation amplitude only through $\omega_n$, and at $\omega = \omega_1$ the dominant term n = 1 corresponds to $\omega_1$ appearing only through the ratio $\mu/\omega_1$ (see Eq. 2.91), which is constant for a given value of $\zeta_1$. This can be observed from Fig. 20(a). As expected, the figure indicates how the maximum amplitude decreases as the damping parameter is increased. On the other hand, the fluid surface elevation due to rocking base motion depends on $\zeta_1$ as well as d/a. This trend is clearly shown in Fig. 21(a). For a given value of $\zeta_1$, the maximum fluid surface elevation amplitude initially decreases with increasing values of d/a, and then becomes a constant at sufficiently high values of d/a. This may be revealed by examination of Eq. 2.24: d/a influences the dimensionless elevation amplitude through $\gamma_n$.

Figures 20(b) and 21(b) show the dimensionless force amplitude as a function of d/a for various values of $\zeta_1$. This is arising on account of the term $\tanh(k_nd)/k_nd$ appearing in $h_n$ given in Eq. 2.8 for horizontal excitation and $h_n^{(r2)}$ given in Eq. 2.28 for rocking excitation. The figure indicates how the dimensionless force amplitude decreases with increasing values of damping ratio $\zeta_1$. For a given value of $\zeta_1$, the force amplitude initially decreases with increasing values of d/a, and then becomes a constant at sufficiently high values of d/a. The dimensionless moment amplitudes exhibits the same trend as the dimensionless force amplitude as shown in Figs. 20(c) and 21(c).

## 6.1.2 Earthquake Excitation

The results presented so far have related to harmonic excitation, and results for irregular base motions are now considered. The solutions are based on the time-domain and modal analysis approaches that have been indicated. In this section, the modal analysis results for horizontal, rocking and combined base motions are discussed. The time-domain solutions for past earthquake records are also discussed.

### 6.1.2.1 Modal masses and elevations

The more usual procedure for estimating the maximum force and the maximum overturning moment is based on a modal analysis involving use of earthquake response spectra, modal masses and effective elevations. This section discusses these.

The full solutions for rectangular and circular reservoirs indicate that the relative masses $m_0/m$, $m_1/m$ and $m_2/m$ and the corresponding relative elevations $d_0/d$, $d_1/d$ and $d_2/d$ each depend, in either case, only on the relative size parameter d/a. Figures 22-30 provide comparisons of alternative predictions of these relationships and are now considered.

The high-frequency effective mass $m_0$ is of particular interest, since this directly provides the force due to high-frequency excitation for which sloshing resonances do not occur. The comparison of high-frequency mass ratio, $m_0/m$ with d/a for circular and rectangular reservoirs for horizontal base motions is shown in Fig. 22(a). The full solutions for the rectangular and circular reservoirs for horizontal base motion are close to each other, both showing an increase with d/a and reaching a constant value at sufficiently high values of d/a. For values of d/a less than about 1, the relationship is nearly linear and for horizontal base motion is given approximately as:

$$\frac{m_0}{m}=0.58\left(\frac{d}{a}\right) \qquad \text{for circular reservoir} \qquad (6.11)$$

$$\frac{m_0}{m}=0.53\left(\frac{d}{a}\right) \qquad \text{for rectangular reservoir} \qquad (6.12)$$

Figure 23(a), which shows $m_0/m$ for rocking base motion indicates that the full solutions for the rectangular and circular reservoirs are again close to each other. The $m_0/m$ values decrease approximately linearly for values of d/a less than about 1.0, and then slowly increase with d/a and reaching constant values at sufficiently high values of d/a.

The effective fluid mass $m_1$, corresponding to the lowest natural frequency of sloshing, is also a important parameter in the analysis of earthquake-induced sloshing. Figure 22(b) shows a comparison of the first mode sloshing mass for rectangular and circular reservoirs with horizontal base motions. These are close to each other and decrease with increasing d/a values, reaching constant values at sufficiently high values of d/a. Figure 23(b) for rocking base motions shows that the results for circular and rectangular reservoirs are again close to each other, and the $m_1/m$ values decrease with d/a. The $m_1/m$ values are very high for smaller values of d/a. This is in contrast to the case of horizontal base motions.

The results for the second mode sloshing mass for circular and rectangular reservoirs are shown by Fig. 22(c) and again are close to each other for horizontal base motion. The $m_2/m$ values decreases with d/a, reaching constant values at sufficiently high values of d/a. Figure 23(c) for rocking base motion exhibits the same trend as for horizontal base motion except that the $m_2/m$ values are very high at smaller values of d/a.

Figure 24 shows a comparison of the high frequency mass ratio $m_0/m$ and the modal masses ratio $m_1/m$ and $m_2/m$ for horizontal and rocking base motions for a rectangular reservoir. The high frequency mass ratio for horizontal and rocking base motions exhibit opposite trends to each other. i.e. $m_0/m$ increases with d/a for a horizontal base motion, and decreases with d/a for a rocking base motion. When d/a = 0.9, the $m_0/m$ value is the same for both horizontal and rocking base motions.

The $m_1/m$ values for horizontal and rocking base motions decrease with d/a, and are close to each other when d/a > 4.0. When d/a = 0.9, the $m_1/m$ value is the same for both horizontal and rocking base motions. The $m_2/m$ values decreases with d/a and are close to each other when d/a > 1.0. The $m_2/m$ value for rocking base motions is much higher than that of horizontal base motions at smaller d/a values.

Figure 25 shows the variation of effective elevations ratio as a function of d/a for circular and rectangular reservoirs for horizontal base motion. The effective elevations ratio for circular and rectangular reservoirs are close to each other and increase with d/a reaching constant values at sufficiently high values of d/a.

Figure 26 shows the variation of effective elevations ratio as a function of d/a for circular and rectangular reservoirs for rocking base motion. The effective elevations ratio for circular and rectangular reservoirs are again close to each other and increases with d/a reaching constant values at sufficiently high values of d/a.

Figure 27 shows the comparison of effective elevations ratio for horizontal and rocking base motions for a rectangular reservoir. The $d_0/d$ values for rocking base motion is less than that of horizontal base motion. The $d_1/d$ and $d_2/d$ values for horizontal and rocking base motions are the same.

Figure 28 shows the comparison of effective elevations ratio for circular and rectangular reservoirs for horizontal base motion when base pressure is considered. Again the effective elevations for circular and rectangular reservoirs are close to each other and decreases with d/a. They reach a constant value when d/a is approximately greater than 1 and have very high values at smaller d/a values. The same trend is observed for rocking base motion as shown in Fig. 29.

Figure 30 shows the comparison of effective elevations for horizontal and rocking base motions for a rectangular tank as function of d/a. The $d'_0/d$ for horizontal and rocking base motions are close to each other and $d'_0/d$ values for horizontal base motion are less than that of rocking base motion. The $d'_1/d$ and $d'_2/d$ values are the same for both rocking and horizontal base motions.

### 6.1.2.2 Comparison with Housner's solution

Housner (1957, 1963) described an approximate method of solution for rectangular and circular reservoirs based on the assumption that the force is made up of an impulsive component, corresponding to $m_0$, and a convective component corresponding to the modal mass of the lowest sloshing mode, $m_1$. That is, the influence of the higher modal masses is ignored. The analysis gives the following expressions for the masses $m_0$ and $m_1$, their corresponding elevations $d_0$ and $d_1$, and the lowest mode frequency $\omega_1$ for rectangular and circular reservoirs:

For a rectangular reservoir:

$$\frac{m_0}{m} = \frac{\tanh\left(\sqrt{3}\,(a/d)\right)}{\sqrt{3}\,(a/d)} \tag{6.13}$$

$$\frac{m_1}{m} = 0.527\,(a/d)\tanh[1.58\,(d/a)] \tag{6.14}$$

$$\frac{d_0}{d} = \frac{3}{8}\left\{1+\alpha\left[\frac{m}{m_1}\left(\frac{a}{d}\right)^2 - 1\right]\right\} \tag{6.15}$$

$$\frac{d_1}{d} = \left[1 - \frac{1}{3}\frac{m}{m_1}\left(\frac{a}{d}\right)^2 + 0.63\beta\frac{a}{d}\sqrt{0.28\left(\frac{m}{m_1}\frac{a}{d}\right)^2 - 1}\right] \tag{6.16}$$

$$\omega_1^2 = 1.58\,(g/a)\tanh[1.58\,(d/a)] \tag{6.17}$$

For a circular reservoir:

$$\frac{m_0}{m} = \frac{\tanh\left(\sqrt{3}\,(a/d)\right)}{\sqrt{3}\,(a/d)} \tag{6.18}$$

$$\frac{m_1}{m} = 0.386\,(a/d)\tanh[1.84\,(d/a)] \tag{6.19}$$

$$\frac{d_0}{d} = \frac{3}{8}\left\{1+\alpha\left[\frac{m}{m_1}\left(\frac{a}{d}\right)^2 - 1\right]\right\} \tag{6.20}$$

$$\frac{d_1}{d} = \left[1 - 0.185\frac{m}{m_1}\left(\frac{a}{d}\right)^2 + 0.56\beta\frac{a}{d}\sqrt{\left(\frac{m}{3m_1}\frac{a}{d}\right)^2 - 1}\right] \tag{6.21}$$

$$\omega_1^2 = 1.84\,(g/a)\tanh[1.84\,(d/a)] \tag{6.22}$$

If the elevations $d_0$ and $d_1$ are determined on the basis of the dynamic fluid pressures exerted on the floor of the tank, the following values should be used for both rectangular and circular reservoirs: $\alpha = 1.33$, $\beta = 2.0$, otherwise $\alpha = 0$, $\beta = 1.0$.

Figures 31(a) and 32(a), which show $m_0/m$ for rectangular and circular reservoirs respectively, indicate that Housner's solution generally agrees closely with the full solutions (but less so for $d/a > 0.5$).

Figures 31(b) and 32(b), which shows $m_1/m$ for rectangular and circular reservoirs respectively, indicate that Housner's solution for a rectangular reservoir also agrees closely with the full solution. However, Housner's result for a circular reservoir is significantly lower than the predictions based on the full solution, and thus appears to be in error.

Figures 33(a) and 34(a), which show $d_0/d$ for rectangular and circular reservoirs respectively, indicate that Housner's solution, which predicts $d_0/d = 0.375$ for $d/a > 0.67$, underpredicts somewhat the full solution over the entire range of d/a. In fact, the higher limit $d/a \rightarrow \infty$ corresponds to $d_0/d = 0.5$, but this is not predicted by the Housner solutions.

Figures 33(b) and 34(b), which shows $d_1/d$ for rectangular and circular reservoirs respectively, indicates that Housner's solution given in Eqs.6.15 and 6.20 agrees resonably well with the full solution except when $d/a < 0.5$.

Figures 35(a) and 36(a), which show $d'_0/d$ for a rectangular and circular reservoirs when base pressure is considered, indicate that Housner's solution underpredicts the full solution when $d/a > 1.5$ and overpredicts the full solution when $d/a < 1.5$ for rectangular reservoir. For circular reservoir, the Housner's solution underpredicts the full solution when $d/a > 3$ and overpredicts $d/a < 3$.

Figures 35(b) and 36(b), which show $d'_1/d$ for rectangular and circular reservoirs when base pressure is considered, indicate that Housner's solutions agree well with the full solution.

### 6.1.2.3 Comparison of force estimates with Housner

#### Modal analysis

In certain situations, the modal masses $m_0$ and $m_1$ and elevations $d_0$ and $d_1$ are incorporated into a full structural analysis, and are not used alone to obtain the maximum hydrodynamic force directly. In such cases, the comparison given above in the previous section should be sufficient to provide guidance on the values of these parameters to be used. However, it is generally also of interest to consider a comparison of the overall force estimates based on the alternative methods of prediction. Differences in force

estimates may arise, in part, because of differences in predictions of $m_0$, $m_1$, $d_0$ and $d_1$, as indicated in the previous section; because other higher modal masses are ignored in Housner formulation; and because alternative versions of an earthquake response spectrum and associated damping levels may be employed.

In order to carry out a comparison of overall force estimates, it is necessary to adopt an assumed representation of an earthquake response spectrum, and to select an associated level of damping. The earthquake response spectrum given by the National Building Code of Canada (1985) with an assumed damping ratio 0.5% is used. Accordingly, the spectral acceleration is assumed to be given by Eq.3.18 with the following parameters: $\alpha_1 = 5$, $\alpha_2 = 2.11$, $\alpha_3 = 9.72$, $\beta_1 = 0.36$ sec, $\beta_2 = 4.69$ sec. Also, the maximum ground acceleration $\dot{u}_m$ has been taken as 0.1g.

First, the influence of the higher sloshing modes contained in the full solution is considered and selections of corresponding results are indicated in Table 6. Such results are shown for a rectangular reservoir with a = 150 m, b = 75 m and d = 10 m. Thus, the fluid mass is taken as m = 450 x $10^6$ Kg. The table shows the modal masses and elevations for a series of sloshing modes, the corresponding force and moment components defined by Eqs.3.19, 3.20 and 3.21, and the overall maximum force and moment obtained by Eq.3.32. The calculation involves the following procedure: the lower resonant periods are obtained from Eqs. 2.3 and 2.5, the spectral acceleration $S_a$ is obtained from the earthquake response spectrum for each value of $T_n$ by Eq. 3.18, scaled by a factor of 0.1; the ratios $m_n/m$, $d_n/d$ and $d'_n/d$ are obtained from Eqs. 3.27, 3.28, and 3.29 respectively; the high frequency mass $m_0$ and corresponding elevations $d_0$ and $d'_0$ are obtained from Eqs. 3.24, 3.25 and 3.26; the modal forces $F_n$ are obtained from Eq. 3.19; and the calculated values of $F_n$ are applied to Eq. 3.31 to obtain the overall maximum force $F_{max}$. A similar procedure is applied to obtain the maximum overturning moment $M_{max}$, except that the elevations $d_n$ are included in the calculation as indicated in Eqs. 3.28 and 3.29.

The table illustrates how second and higher mode resonances contribute to a decreasing extent to the overall force maximum. Thus the table indicates that the force $F_0$, $F_1$ and $F_2$ are estimated to be 36.170, 1.822 and 1.777 MN respectively. The resulting force maximum based on the use of Eq. 3.31 applied in turn to $F_0$ alone, and to $F_0$ and $F_1$ are 36.170 and 36.219 MN respectively, while the complete solution (based on the first 10 sloshing modes) gives $F_{max}$ = 36.376 MN. Likewise, the moment components $M_0$, $M_1$ and $M_2$ are estimated to be 158.733, 9.417 and 8.960 MNm respectively. The resulting moment maximum based on the use of Eq. 3.31 applied in turn to $M_0$ alone, and to $M_0$ and $M_1$ are 158.733 and 159.012 MNm respectively, while the complete solution (based on the first 10 sloshing modes) gives $M_{max}$ = 160.256 MNm. A similar procedure is applied to $M'_{max}$. These results suggest that the masses $m_0$ and $m_1$ should generally be sufficient to estimate the overall force and moment maxima (in this particular case to within about 1% of the full solution). However, more generally such a conclusion would depend on the reservoir size d/a, and on the significant frequency range of the earthquake response spectrum in relation to the lower modal frequencies.

Table 7 shows a more general comparison between the full solution for a rectangular reservoir and the method of Housner for four cases with different values of a corresponding to d/a ratios ranging from 0.1 to 2 for horizontal base motion. The table includes the alternative predictions of the overall maximum force and moment, $F_{max}$, $M_{max}$ and $M'_{max}$. The table also includes results for the full solution based on the use of the first sloshing mode only (denoted $n \leq 1$, and containing terms $m_0$ and $m_1$ terms only), and the full solution with many modes of sloshing. The results generally indicate how the full solution based on the first sloshing mode only is always reasonably close (within 2%) of the more complete solution; and the Housner formulation is also generally in agreement with the full solution, although to a lesser extent. In fact, the Housner formulation overpredicts the maximum force based on the full solution by 6% for case B (d/a = 0.5), and by 10% for case D (d/a = 2). On the other hand, the Housner formulation underpredicts the maximum moment above the base based on the full solution by 12% for

case A (d/a = 0.1) and by 5% for case D (d/a = 2.0). The Housner formulation overpredicts the maximum moment at the base based on the full solution by 559% for case A (d/a =0.1) and by 22% for case D(d/a = 2.0). This large difference may be due to the error in $d'_0/d$ values in Housner's formulation.

Table 8 shows the modal analysis results for a rectangular reservoir with rocking base motion with different values of a corresponding to d/a ratios ranging from 0.1 to 2.0. The table includes the alternative predictions of the overall maximum force and moments. The results generally indicate how the full solution based on the first mode only is always reasonably close (within 1%) of the more complete solution.

It is of interest to compare the results from horizontal and rocking base motion from Table 7 and Table 8 since both experience the same maximum horizontal acceleration of 0.1 g at the fluid level. The maximum forces from horizontal base motion are less than that of rocking base motion for cases A and B. The maximum forces from the horizontal base motion are greater than that of rocking base motion for cases C and D.

## Fluid surface elevation

The traditional approach to estimating maximum forces is based on the assumption that only the first sloshing mode is significant. Using this assumption, the maximum elevation $\eta_1$ is given by:

$$\eta_1 = 0.811 a \left( \frac{\dot{U}_m}{g} \right) S_a(T_1, \zeta) \tag{6.23}$$

However, for a relatively large reservoir, the spectral acceleration may be quite low at the first mode natural period so that the effect of second and higher sloshing modes may not be negligible. This differs from the case of force predictions, since there is now no term

analogous to the impulsive force component. In this case, several modes should be considered simultaneously, and a common practice to estimating the overall maximum elevation $\eta_M$ is based on the root of the squares of the maximum modal responses:

$$\eta_M = \left[\sum_{n=1}^{N} \eta_n^2\right]^{1/2} \tag{6.24}$$

where $\eta_n$ is given by Eq. 3.22, and N is sufficiently large for convergence to occur. Housner (U.S. Atomic Energy Commission, 1963) has described an approximate method of solution for rectangular and circular reservoirs, in which the influence of the second and higher sloshing modes is ignored. His analysis gives the following expression for maximum sloshing height in a rectangular reservoir:

$$\eta_H = \frac{0.527\,a}{\tanh[1.58(d/a)]\left(\frac{g}{\omega_1^2\,\theta\,a} - 1\right)} \tag{6.25}$$

where $\theta$ can be expressed as $\theta = (\dot{U}_M/g)S_a(T_1,\zeta)$. It is noted that, although Housner's solution fails for high values of $\theta$ and does not predict $\eta_H$ to be proportional to base acceleration, for the practical case of low $\theta$ values the expression for $\eta_H$ may be approximated by Eq. 6.23, but with the factor 0.811 replaced by 0.833. Thus, Housner's formulae then gives predictions which are 3% higher than the closed-form solution for first mode sloshing.

For the case of earthquake motions, it is of interest to compare the complete closed-form solution with that for first mode sloshing and with Housner's solution. The comparison between Housner's solution, denoted $\eta_H$, and the closed-form solution for first mode sloshing, $\eta_1$, is conveniently presented as $\eta_H/\eta_1$. This depends on the reservoir size a,

the relative depth d/a, the damping ratio $\zeta$, and the maximum ground acceleration $\ddot{u}_M/g$. In all cases a damping ratio $\zeta = 0.005$ is assumed. Figure 37 shows this ratio for various values of d/a and with $\ddot{u}_M/g = 0.1$ (Fig. 37a), and for various values of $\ddot{u}_M/g$ and with d/a = 1.0 (Fig. 37b). The figure indicates how Housner's solution becomes inaccurate relative to the first order solution for smaller reservoirs and for higher values of base acceleration. Figure 38 provides a comparison of the full closed-form solution and the closed-form solution for first mode sloshing. The ratio $\eta_M/\eta_1$ is shown as a function of reservoir size a for various values of d/a and for $\ddot{u}_M/g = 0.1$. As expected, the figure indicates that the first-mode result underpredicts the results of the complete solution most significantly for larger reservoir sizes. This is most pronounced for relatively shallow large reservoirs. In particular, for the case d/a = 0.2 and for reservoir lengths 2a > 60 m, the maximum elevation based on the complete solution is 50% higher than that based on first mode sloshing.

### 6.1.2.4 Combined motion

This section discusses the overall maximum fluid surface elevation, maximum force and maximum overturning moment due to simultaneous horizontal and rocking motions. The resultant maximum fluid surface elevation, $\eta_T$, due to both horizontal and rocking base motions can be estimated using Eq. 3.35. In a similar way the resultant maximum force and overturning moments, denoted $F_T$, $M_T$ and $M'_T$, can be estimated using Eqs. 3.33 and 3.34. It is of interest to compare the resultant maximum variables for combined motion with those for individual motions. The comparison between combined base motion solution and the horizontal base motion solution is conveniently presented as $\eta_T/\eta_H$, $F_T/F_H$, $M_T/M_H$ and $M'_T/M'_H$. The comparison between the combined base motion solution and the rocking base motion solution is presented as $\eta_T/\eta_R$, $F_T/F_R$, $M_T/M_R$ and $M'_T/M'_R$. These ratios depend on the reservoir size a, the relative depth d/a, the damping ratio $\zeta$ and the maximum relative rocking parameter $(\dot{\Psi}d)_{max}/\dot{U}_{max}$ which is defined by

maximum acceleration at fluid level due to the base motions. In all cases a damping ratio $\zeta = 0.005$ is assumed.

Figure 39 shows the ratio for fluid surface elevation as a function of maximum relative rocking parameter $(\dot{\Psi}d)_{max}/\dot{U}_{max}$ for d/a = 0.5 and a = 100m. The figure indicates that the horizontal base motion influences the overall fluid surface elevation when the relative rocking parameter becomes smaller, and the rocking base motion influences the overall fluid surface elevation when the relative rocking parameter becomes larger. In between, the overall fluid surface elevation is influenced by both horizontal and rocking base motions.

Figure 40 shows the ratio for fluid surface elevation as a function of d/a for a maximum relative rocking parameter $(\dot{\Psi}d)_{max}/\dot{U}_{max} = 0.1$ and a = 100 m. The overall fluid surface elevation is influenced by both horizontal and rocking base motions for smaller d/a values. For larger values of d/a, the overall fluid surface elevation is influenced mainly by horizontal base motions.

Figures 41, 43 and 45 show the variation of ratios for forces and moments as a function of the maximum relative rocking parameter $(\dot{\Psi}d)_{max}/\dot{U}_{max}$ for a relative depth d/a = 0.5 and a = 100 m. These figures indicate the same trend as that of the fluid surface elevation.

Figures 42, 44 and 46 show the variation of ratios for forces and moments as a function of d/a for a maximum relative rocking parameter $(\dot{\Psi}d)_{max}/\dot{U}_{max} = 0.1$ and a = 100 m. Again, these figures indicate the same trend as that of the fluid surface elevation.

### 6.1.2.5 Time-domain solution

It is also possible to develop a numerical time-domain solution in order to predict the force time history corresponding to a specified earthquake record. This approach is not

useful for routine design, but may be used to assess the suitability of Eqs. 3.30 and 3.31. The time-domain solution is based on Eq. 3.11. Three different earthquake records corresponding to Alaska (Adak naval base, 1971), Loma Prieta (Gilroy sewage plant, 1989) and Northridge (Pacoma dam-downstream, 1994) earthquakes are used. The maximum horizontal accelerations are 0.12g, 0.54g and 0.43g, the maximum vertical accelerations are 0.06g, 0.37g and 0.18g for the Alaska, Loma Prieta and Northridge earthquakes respectively. For rocking excitation, the vertical component of the records is also used. The horizontal acceleration records are scaled to 0.1g, and rocking acceleration record was scaled to 0.05g.

Table 9 shows comparisons of results between the time-domain solution and the modal analysis for the Alaska, Loma Prieta, and Northridge earthquake motions for a rectangular reservoir with a = 25 m, b = 10 m and d = 12.5 m. The modal analysis prediction based on the NBC response spectrum for forces is 4 % higher than that based on the complete time-domain solution; and the modal analysis prediction for base moments is about 10 % higher than that based on the complete time-domain solution. The modal analysis predictions based on the actual response spectrum is about 1% higher than that based on the complete time-domain solution for the Alaska and Northridge records and about 2% less than for Loma Prieta records.

Table 10 shows the comparisons between the time-domain solution and the modal analysis solution for the Alaska, Loma Prieta and Northridge earthquake rocking motions for a rectangular reservoir with a = 25 m, b = 10 m and d = 12.5 m. Comparing the different predictions, it is seen that the modal analysis prediction based on NBC response spectrum is about 5 % higher than that based on the complete time-domain solution. The predictions based on the actual response spectrum is about 3% less than that based on the complete time-domain solution for the Alaska and Loma Prieta records and about 1% higher for the Nortridge record.

The frequency range for the lowest 10 sloshing modes for the above mentioned configuration is 0.1 – 0.5 Hz, while the significant frequency range of the earthquake response spectrum is 1.0 – 10.0 Hz. Therefore, the excitation is at a relatively high frequency, and the response corresponds to the use of high frequency parameters. That is, the solutions are particularly influenced by the high frequency mass $m_0$, and hence the difference between time-domain solution and modal analysis is relatively small.

Finally, Table 11 shows a comparison of the time-domain solution with modal analysis solution for combined motion. The modal analysis predictions based on the NBC response spectrum are about 20 % less, 45% less and 20 % more than those based on the complete time-domain solution for the Alaska, Northridge records, Loma Prieta records respectively. The modal analysis prediction based on the actual response spectrum is about 20% less, 20 % more and 30 % more than those based on the complete time-domain solution for the Alaska, Loma Prieta and Northridge records respectively.

## 6.1.3 Hydrodynamic Damping

### 6.1.3.1 Laminar boundary layers

The damping ratio due to energy dissipation in laminar boundary layers is a function of relative water depth d/a, relative size b/a and boundary layer thickness which depends on viscosity and frequency of the motion. Figure 47 shows the variation of damping ratio due to laminar boundary layers as a functions of relative water depth d/a for different values of reservoir length a for an infinity long reservoir (b/a = $\infty$). It is seen that the damping ratio increases as the size of the tank decreases. Figure 48 shows the variation of damping ratio due to laminar boundary layers as a function of relative water depth d/a for different values of relative reservoir size b/a and for a = 100m. The damping ratio decreases with both relative water depth d/a and relative reservoir size b/a. It can be

observed from Figs. 47 and 48 that the damping ratio reaches a constant value when d/a is greater than about 1.5.

Figure 49 shows how the damping ratio decreases with increasing d/a and increasing a as expected. Superimposed on the figure is shown the line corresponding to a Reynolds Number of 500, which might be viewed as a transition between laminar and turbulent boundary layers. The zone to the lower left corresponds to high Reynolds Numbers so that the laminar boundary layer results are not particularly valid in this region.

The ratio of the damping ratio due to all the boundaries to that due to the bottom only is shown in Fig. 50 as a function of d/a for a/b = 1.0 and a = 0.25 m. The damping ratio is seen to increase with d/a as expected. Figure 51 shows the variation of the damping ratio due to the various tank boundaries. The damping ratio due to the bottom decreases with increasing d/a; the damping ratio due to the front and back wall increases with d/a and reaches a constant value when d/a > 1.0; and the damping ratio due to side walls decreases slowly with d/a and reaches a constant value when d/a > 1.0.

### 6.1.3.2 Turbulent boundary layers

For a linear system, the damping ratio remains constant irrespective of the oscillation amplitude. However, the linearized shear stress results in a damping ratio which is generally dependent on the oscillation amplitude. This can be seen from Eq. 4.38. When deriving the equation for the damping due to a turbulent boundary layer, only the bottom wall is considered for simplicity. The solution obtained for damping due to a turbulent boundary layer is a function of relative water depth d/a, relative water surface elevation $\eta_a/d$ and friction coefficient $f_w$. The friction coefficient $f_w$ itself depends on the ratio $A/K_s$ as shown in Eq. 4.36. ($K_s$ is the Nikuradse roughness of the surface and A is the local amplitude of fluid displacement just outside the boundary layer.) Figure 52 shows the variation of the turbulent damping ratio as a function of d/a for different values of $A/K_s$

and for $\eta_a/d = 0.1$. Hydrodynamic damping due to turbulence decreases with increasing d/a and $A/K_s$. This clearly shows that damping ratio increases with the roughness of the surface.

### 6.1.3.3 Baffles

The damping due to horizontal baffles is a function of relative water depth d/a, relative baffle elevation h/d, relative water surface elevation $\eta_a/d$, drag coefficient $C_d$ and relative baffle length $\alpha$; and for a vertical baffle it is a function of relative water depth d/a, relative water surface elevation $\eta_a/d$, drag coefficient $C_d$ and relative baffle length $\beta$. Figure 53 shows the variation of baffle damping due to horizontal baffles as function of relative water depth d/a for various values of relative baffle elevations h/d and for relative baffle length $\alpha = 0.1$ and relative water surface elevation $\eta_a/d = 0.1$. The damping ratio due to horizontal baffles increases with relative water depth d/a to a maximum value and then decreases with the relative water depth d/a. The damping ratio increases with relative baffle elevation h/d. The relative water depth d/a for maximum damping varies with relative baffle elevation h/d. Figure 54 shows the variation of baffle damping due to horizontal baffles as functions of relative water depth d/a for various values of relative baffle length $\alpha$ and relative baffle elevation $h/d = 0.9$ and for relative water surface elevation $\eta_a/d = 0.1$. The damping ratio increases with relative water depth d/a to a maximum value and then decreases with relative water depth d/a. As expected, the damping ratio increases with relative baffle length $\alpha$.

Figure 55 shows variation of damping due to vertical baffle as functions of relative water depth d/a for various values of relative water surface elevation $\eta_a/d$ and for relative baffle length $\beta = 0.05$. The damping ratio increases with relative depth d/a to a maximum value and then decreases with relative water depth d/a. As expected, the damping ratio increases with relative water surface elevation $\eta_a/d$. Figure 56 shows the variations of damping due to a vertical baffle as a function of relative water depth d/a for various

values of relative baffle length $\beta$ and for $\eta_a/d = 0.1$. The damping ratio increases with relative water depth d/a to a maximum value and then decreases. As expected, the damping increases with relative baffle length $\beta$. It is seen that the damping is negligible when relative water depth d/a is greater than 2.5.

A key assumption of the damping predictions for baffles is that the incident velocity is uniform along the length of the baffle. It is appropriate to examine the limitations of this assumption. Figure 57 shows a variation of $\Delta u/u$ with relative baffle length $\alpha$ for horizontal baffles, where $\Delta u$ is velocity variation across the baffle and u is the mean velocity across the plate. The velocity variation across the plate increases with relative baffle length $\alpha$. The figure indicates that the relative baffle length $\alpha$ should be less than 0.28 for the flow variation across the plate to be less than 10% of the mean velocity.

Figure 58 shows a variation of $\Delta u/u$ with relative baffle length $\beta$ for various values of relative water depth d/a for a vertical baffle. The velocity variation across the plate increases with relative baffle length $\beta$ and relative water depth d/a. It is seen that the relative baffle length $\beta$ should be less than 0.29 for the flow variation across the plate to be less than 10% of the mean velocity across the baffle for the case of d/a = 1.0.

## 6.2 Comparison of Theoretical and Experimental Results

### 6.2.1 Free Vibration Tests

Free vibration tests were carried out both with and without baffles in order to determine the hydrodynamic damping associated with the presence of the baffles. Figure 59 shows the variation of fluid surface elevation at the tank wall during the free vibration tests for two relative water depths: d/a = 0.5 and 1.0. Corresponding results for tests with baffles

were obtained but are not shown here. The corresponding damping coefficients were estimated using Eq. 5.7. The damping coefficients without baffles are 0.44 % and 0.28 % for d/a = 0.5 and 1.0 respectively; the damping coefficients with horizontal baffles are 1.4 %, 1.7 % and 2.4 % for h/d = 0.6, 0.7 and 0.8 respectively; and the damping coefficients with vertical baffle are 0.4 %, 1.0 % and 2.0 % for $\ell$/d = 0.1, 0.2 and 0.3 respectively. It can be seen that the high damping coefficient for baffles; the damping coefficient increases with h/d for horizontal baffles and increases with baffle length for vertical baffle.

## 6.2.2 Harmonic Excitation

Figure 60 and 61 show a comparison of experimental and theoretical results for horizontal harmonic excitation for d/a = 0.5 and 1.0 respectively. The dimensionless free surface amplitude, force amplitude, and moment amplitude are shown as functions of the frequency parameter $\omega^2 a/g$. The damping coefficients used in the analytical results are 0.44 % and 0.28 % for d/a = 0.5 and 1.0 respectively and were obtained from the free vibration tests. The experimental results are seen to be in good agreement with the theoretical results. Figures indicate that dimensionless values are large near the first resonant frequency as expected.

Figure 62 shows a comparison of theoretical and experimental results for a rectangular tank under rocking harmonic motion for d/a = 1.0. The dimensionless surface elevation, force amplitude, and moment amplitude are shown as function of frequency parameter $\omega^2 a/g$. The damping coefficient used in the theoretical calculation is 0.44 % which was obtained from the corresponding free vibration test. The experimental results are in reasonable agreement with theoretical results except for a few scattered points.

Figure 63 shows a similar comparison under simultaneous horizontal and rocking harmonic motion, with the relative rocking parameter $\Psi d/U = 0.2$. The theoretical result

was obtained from superposition of component motions using the following equation, which is derived from Eq. 2.96 for component motions with the same phase and frequency:

$$\frac{F^{T}_{max}}{\omega U m} = \frac{F^{H}_{max}}{\omega U m} + \left(\frac{\Psi d}{U}\right)\frac{F^{R}_{max}}{\omega \Psi d m} \tag{6.26}$$

Similar equations apply to the surface elevation amplitude and the overturning moment. Again, the experimental results are seen to be in fairly good agreement with the analytical results.

## 6.2.3 Earthquake Excitation

This section compares the time-domain solution estimated using Eqs. 3.11-3.14 with experimental time series results for the case of a horizontal base excitation corresponding to a specified earthquake record. Figure 64 shows a comparison of analytical results and experimental results for the Mexico '79 earthquake record for d/a = 1.0. The acceleration record is scaled to correspond to a maximum of 0.1g to carry out the tests. In all analytical calculations, a damping coefficient 1 % is used.

Figures 64 (a), (b) and (c) show respectively the fluid surface elevation at the tank wall, horizontal force on the tank and the overturning moment at the tank base. The analytical result slightly underpredicts the maximum fluid surface elevation; slightly overpredicts the maximum horizontal force on the tank. Overall, the analytical results are in good agreement with experimental results. But there is a phase difference in all three estimates between the 30 – 40 s time interval.

Table 12 shows a comparison of the experimental results with various theoretical predictions. A damping ratio of 1% is assumed in the time-domain and actual spectrum

analysis, whereas the NBC response spectrum solution is based on a damping ratio of 0.5 %. The modal analysis results based on the actual response spectrum overpredict the maximum force and moment by 50% and underpredict the maximum water surface elevation by 30%. The results based on the NBC response spectrum overpredict the results by 150% for the maximum force and moment and 50% for maximum water surface elevation. The lowest 10 sloshing frequency range for the experimental condition is 1.2 – 5 Hz. The dominant frequency range of the Mexico earthquake response spectrum is 1.0 – 10 Hz. Therefore the response corresponds to both high frequency and modal parameters.

It is noted that harmonic excitation of a short duration (relative to natural sloshing periods) will not result in steady state conditions. Therefore the duration of earthquake excitation relative to the sloshing period is an important parameter influencing the maximum response. This may be quantified by the strong motion duration to the first mode natural period $T_s/T_1$.

## 6.2.4 Tests with Baffles

This section discusses the results from the tests with baffles in the rectangular tank for the case of horizontal harmonic motion. Two types of baffles, denoted horizontal and vertical baffles, shown in Fig. 6 were used. Horizontal baffles are oriented perpendicular to front and back walls of the rectangular tank and three different baffle elevations were used in the tests. The vertical baffle is oriented perpendicular to the bottom and located at the middle of the base. Three baffle lengths of vertical baffle were used in the tests.

The damping coefficient for each baffle configuration is estimated from the corresponding free vibration tests using Eq. 5.7 as indicated in Section 6.2.1. These damping coefficients are used to estimate the analytical results.

Figures 65 – 67 show a comparison of experimental and theoretical results for horizontal baffles for h/d = 0.6,0.7 and 0.8 respectively and Figs. 68 – 70 show a comparison for vertical baffle with lengths $\ell$/d = 0.1, 0.2 and 0.3 respectively. For both horizontal and vertical baffles, the theoretical results are generally in good agreement with theoretical results.

Table 13 shows the variation of experimental dimensionless hydrodynamic coefficients at various baffle elevations for horizontal baffles for $\omega_1/\omega$ = 1.0 and 1.2. The table illustrates how the dimensionless hydrodynamic coefficients decrease with h/d value near the first natural frequency of the system. The dimensionless fluid surface elevation amplitude, dimensionless force amplitude and dimensionless moment amplitude are reduced by 60 %, 64 % and 65 % respectively for the baffle location h/d = 0.8 near resonance condition. The changes in the dimensionless hydrodynamic coefficients are negligible at $\omega/\omega_1$ = 1.2.

Table 14 shows the variation of experimental dimensionless hydrodynamic coefficients for various baffle lengths for vertical baffle for $\omega/\omega_1$ = 1.0 and 1.2. In this case, the table illustrates how the dimensionless hydrodynamic coefficients decrease with $\ell$/d values near the first natural frequency of the system. The dimensionless fluid surface elevation amplitude, dimensionless force amplitude and dimensionless moment amplitude are reduced by 24 %, 56 % and 44 % respectively for the baffle length $\ell$/d = 0.3 at near resonance condition.

Baffles should be placed in locations which show high velocities in the unbaffled condition. For example, consider the fundamental mode in a rectangular tank undergoing oscillations. The highest vertical velocities of the fluid occur at the ends of tank in the free surface, and the highest horizontal velocities occur at the center of the tank in the free surface. Baffles are most effective in these locations.

### 6.2.5 Damping

Figure 71 shows a comparison of analytical and experimental hydrodynamic damping coefficients with d/a for the laminar regime. The experimental hydrodynamic damping coefficients were obtained from free vibration tests. The experimental hydrodynamic damping coefficients are seen to be greater than the analytical values.

Energy dissipation due to the boundary layers at the free surface and due to surface tension is not considered in the theoretical model. Contamination of the wall surface also increases the damping. These are contributory factors for the discrepancies between predicted and experimental results.

Figures 72 shows a comparison of analytical and experimental hydrodynamic damping with relative baffle elevation h/d for horizontal baffles. Figure 73 shows a comparison of analytical and experimental hydrodynamic damping with relative baffle length $\ell$/d for a vertical baffle. The drag coefficient was estimated from measured values given by Sarpakaya and O'Keefe (1996) as shown in Fig. 8. The Keulegan-Carpenter number varies between 1.3 to 4.0 for the experiments, so that the drag coefficient used varies between 15.6 to 9.8. The experimental hydrodynamic damping seems to be in good agreement with the analytical values. The predicted hydrodynamic damping for horizontal baffles is slightly higher than the experimental values for relative baffle elevations h/d = 0.7 and 0.8. This may be due to effects of the free surface on the drag coefficient.

## 6.3 Example Application

Methods of calculating the water surface elevation, the horizontal force on the tank and the overturning moment at the base of the tank due to harmonic and earthquake excitations for both rectangular and circular tanks have been presented in Chapters 2-3.

The estimation of hydrodynamic damping due to boundary layers and baffles for rectangular tank has been given in Chapter 4. It is now appropriate to summarize limitations in applying these methods to engineering situations, and to illustrate a typical earthquake engineering application of these solutions.

Initially though, a brief assessment is made of various additional factors which may require consideration, including the possible influence of fluid compressibility; the vertical distribution of modal masses; the effects of the rigidity of the reservoir walls; reservoirs with complex planforms; and the influence of the direction of motion.

## 6.3.1 Additional Factors

### Water Compressibility

The possible effects of fluid compressibility may be assessed by considering the corresponding modifications to analytical solutions that are available. In the case of storage tanks, Fisher (1979) has compared solutions for the hydrodynamic pressure for compressible and incompressible liquids. Differences were found to be negligible for actual tanks. In the case of reservoirs, reference is made to Westergaard's solution for the high frequency mass $m_0$ for an infinitely long reservoir. Westergaard's complete solution included the effects of compressibility which may be assessed through a coefficient K given as:

$$K = \sqrt{1 - \frac{16 d^2}{c^2 T^2}} \tag{6.27}$$

where T is the period of motion and c is the speed of sound in water. The approximation of an incompressible fluid is obtained by taking $K \cong 1$. Since the speed of sound in water is approximately $c \cong 1480$ m/sec, the approximation corresponds to the assumption $T >> d/370$, where d is in m and T in sec. Thus for depths up to about 15 m, periods should be

larger than about 0.05 sec. This indicates that compressibility can generally be neglected in the present context. However, in the case of large reservoirs with much larger depths, the effects of compressibility may well become important.

## Effects of wall rigidity

The traditional approaches of Housner (1957, 1963) and the API (1993) and AWWA (1984) design standards are based on the assumption that the reservoir walls can be assumed to be completely rigid and thus experience the same motion as the ground. However, for flexible tanks the accelerations of the container walls are generally different from the maximum ground accelerations, so that the impulsive components of the response can be affected significantly (Veletsos, 1984). Because the characteristic frequencies of the sloshing response are much lower than the characteristic frequencies of the inertial response, the coupling between convective and impulsive components of the hydrodynamic forces is weak (e.g. Fisher, 1979). It is also known that the natural frequencies of the sloshing are not affected by the flexibility of the walls in practice (Parkus, 1982). Thus the assumption of rigid tank walls remains valid for predicting the convective components of the force associated with sloshing, and in practice the effects of the flexibility of the walls need to be considered only for the impulsive components of the response (e.g. Haroun and Housner, 1981; and Balendra *et al.*, 1982). In general, the hydrodynamic effects induced by earthquake ground motions may be appreciably greater than those in rigid tanks (Rammerstorfer *et al.*, 1990). A design procedure for cylindrical tanks with flexible walls was described by Veletsos (1984). More recent results for rectangular tanks have been given by Kim *et al.* (1996).

## Vertical distribution of mass

The masses $m_0$ and $m_1$ are commonly considered to be concentrated at the elevations $d_0$ and $d_1$ above the base of the reservoir, whereas in fact they each correspond to a mass

distribution over depth. In certain circumstances, a description of these distributions may be required. In fact, they can be obtained from the full solutions that are available for both the circular and rectangular reservoirs that have been referred to earlier. For a rectangular reservoir, the distributions of these masses, expressed in dimensionless form, are thereby found to be given by the following expressions:

For all cases (For both rectangular and circular reservoirs for both horizontal and rocking base motions)

$$\xi_n(z)=\frac{m_n'(z)}{m_n/d}=\frac{(k_n d)\cosh(k_n z)}{\sinh(k_n d)} \tag{6.28}$$

For a rectangular tank under horizontal excitation

$$\xi_0(z)=\frac{m_0'(z)}{m_0/d}=\frac{1-2\sum_{n=1}^{\infty}\frac{1}{(k_n a)^2}\left[\frac{\cosh(k_n z)}{\cosh(k_n d)}\right]}{1-2\sum_{n=1}^{\infty}\frac{1}{(k_n a)^2}\left[\frac{\tanh(k_n d)}{(k_n d)}\right]} \tag{6.29}$$

For a rectangular tank under rocking excitation

$$\xi_0(z)=\frac{m_0'(z)}{m_0/d}=\frac{\frac{d-z}{d}-2\left(\frac{d}{a}\right)\sum_{m=1}^{\infty}\frac{1}{(\alpha_m d)^2}\left[\frac{2}{(\alpha_m d)}-(-1)^{m+1}\right]\tanh(\alpha_m a)\cos(\alpha_m z)}{\frac{1}{2}-2\left(\frac{d}{a}\right)\sum_{m=1}^{\infty}\frac{1}{(\alpha_m d)^3}\left[\frac{2(-1)^{m+1}}{(\alpha_m d)}-1\right]\tanh(\alpha_m a)} \tag{6.30}$$

For a circular tank under horizontal excitation

$$\xi_0(z)=\frac{m_0'(z)}{m_0/d}=\frac{1-2\sum_{n=1}^{\infty}\frac{1}{(k_n a)^2-1}\left[\frac{\cosh(k_n z)}{\cosh(k_n d)}\right]}{1-2\sum_{n=1}^{\infty}\frac{1}{(k_n a)^2-1}\left[\frac{\tanh(k_n d)}{(k_n d)}\right]} \tag{6.31}$$

For a circular tank under rocking excitation

$$\xi_0(z)=\frac{m_0'(z)}{m_0/d}=\frac{\frac{d-z}{d}-2\left(\frac{d}{a}\right)\sum_{m=1}^{\infty}\frac{1}{(\alpha_m d)^2}\left[\frac{2}{(\alpha_m d)}-(-1)^{m+1}\right]\left[\frac{I_1(\alpha_m a)}{I_1'(\alpha_m a)}\right]\cos(\alpha_m z)}{\frac{1}{2}-2\left(\frac{d}{a}\right)\sum_{m=1}^{\infty}\frac{1}{(\alpha_m d)^3}\left[\frac{2(-1)^{m+1}}{(\alpha_m d)}-1\right]\left[\frac{I_1(\alpha_m a)}{I_1'(\alpha_m a)}\right]} \tag{6.32}$$

where $m_n'(z)$ and $m_0'(z)$ denote the n-th modal mass and the high frequency mass respectively, both per unit height, at an elevation z above the reservoir base. Plots of these distributions for the case of rectangular and circular reservoirs with a = 100 m and d = 30 m are shown in Figs. 74 and 75 for horizontal and rocking excitations. The figure indicates that the modal mass $m_1$ has virtually a uniform distribution with elevation, whereas the high frequency mass $m_0$ varies strongly with elevation, ranging from zero at the water surface to a maximum at the reservoir base. The variation of high frequency mass $m_0$ varies linearly with elevation for rocking excitation.

## Sloping sides

In many practical applications a reservoir may have sloping sides and the assumptions of a vertical wall must be modified. The solution of Westergaard (1939) for an infinitely long reservoir bounded by a vertical wall which undergoes a horizontal motion has been extended by Chwang and Housner (1978) and Chwang (1978) to a dam with sloping sides. The horizontal component of the force on the dam decreases as the slope of the

face of the dam decreases, while the normal force on the dam remains practically constant for all angles of inclination.

In the case of rectangular or circular reservoirs, Isaacson and Ryu (1999) have used numerical results from the boundary element method applied to a reservoir with sloping sides to develop an approximate method based on the traditional approaches described above. In fact, various configurations of sloping sides may be possible and some degree of judgement needs to be applied when treating specific situations.

## Irregular planform

When a reservoir has an irregular planform that cannot readily be approximated as circular or rectangular, the numerical method described by Isaacson and Ryu (1998 b) may be adopted. This has been developed to predict hydrodynamic loads for an irregular shaped reservoir. The approach used is based on an eigenfunction expansion of the velocity potential with respect to the vertical direction combined with two-dimensional boundary element method with respect to the horizontal plane in which the planform of the reservoir is descretized into a number of short segments. However, such an approach need only be considered when the reservoir planform differs significantly from a rectangular or circular profile.

## Effects of direction

In certain cases, it may be necessary to consider a reservoir motion which is uni-directional but not parallel to a pair of sides. In the case of a circular reservoir, the hydrodynamic loads act in the direction of motion, and because of symmetry the force magnitude does not vary with direction of motion. In the case of a rectangular reservoir, a direction of motion which is oblique can be analyzed by an appropriate superposition of two component motions parallel to the two pairs of sides. This enables the known closed-form solution to be extended to the case of an oblique direction, or even to the

case of a horizontal motion which is not uni-directional. Results for the case of an oblique direction given by Isaacson and Ryu (1998) indicate that for earthquake motion, a direction of motion parallel to the shorter pair of sides always gives the highest loads and surface elevations. Therefore, in engineering design the common assumption that the earthquake motion may act in a direction parallel to either pair of sides is appropriate.

## 6.3.2 Example

In order to illustrate the present approach in the context of a typical earthquake engineering application, consideration is given to a case of a rectangular storage tank. A liquid container with a length of 20 m and a height of 10 m is filled with water to a depth 5 m. The tank is considered to be excited at its base by two earthquakes ground motions: the 1940 El Centro and 1995 Mexico City records. The maximum accelerations are 0.21g and 0.17g for the El Centro and Mexico earthquake records respectively. For each of the ground motions, two cases are considered. In the first case, the corresponding hydrodynamic forces and water surface elevation are calculated using the high frequency component and first mode sloshing in the complete solution; and the second case involves the high frequency component and the first ten sloshing modes in the complete solution. The damping ratio is assumed to be a value of 0.5 %.

The corresponding results are shown in Table 15 for the maximum water surface elevation, the maximum horizontal force on the tank and the maximum overturning moment. The table also shows the deviation of results from the first 10-mode solution. It can be inferred that the results for Mexico City earthquake are influenced significantly by the higher modes. This is due to severe sloshing corresponding to base excitation with predominant long period components in the Mexico City earthquake record.

Table 16 shows a comparison of results for the longitudinal and the transverse directions for the Mexico City earthquake records. The results indicate that for this case the loads

for the transverse direction are significantly higher than for the longitudinal direction. This differences arise largely because the high frequency mass $m_0$ is much larger than the sloshing masses $m_n$ for this case, and because the higher reservoir size ratio d/a for the transverse direction causes a significant increase in $m_0$ and only a slight reduction in $m_n$. In physical terms, this can be explained as follows: in the limit of very high d/a ratio (a short, deep reservoir, representing the transverse case limit), most of the fluid moves with the container so that $m_o/m$ is close to unity, and free surface effects (which cause a reduction in $m_0/m$) do not penetrate the fluid to the same relative extent. On the other hand, for a very low d/a ratio (a long, shallow reservoir, representing the longitudinal case limit), the reduction in effective mass is more pronounced as the free surface effects now extend more fully to the bottom. A second reason for the difference is that the first mode natural period $T_1$ is lower for the shorter transverse length than for the longer longitudinal length, and this implies that the spectral acceleration is then higher.

Now consideration is given to the presence of baffles in the tank. The water surface elevation and drag coefficient are needed in order to calculate the damping ratio from Eqs. 4.43 and 4.47 for horizontal and vertical baffles respectively. The above equations are based on harmonic oscillatory motion. The following steps explain how the water elevation and corresponding drag coefficient can be estimated for a particular earthquake.

The water surface elevation can be estimated using the root of the sum of the squares of the maximum modal responses. The drag coefficient is strongly dependent on Keulegan-Carpenter number. The Keulegan-Carpenter number can be expressed in terms of fluid acceleration as:

$$K=\frac{aT^2}{2\pi\ell} \tag{6.33}$$

where a is the fluid acceleration amplitude, T is the oscillation period, and $\ell$ is the length of baffle.

For an earthquake excitation, acceleration a and oscillation period T are taken as:

$$a = a_{max} \tag{6.34}$$

$$T = T_p \tag{6.35}$$

where $a_{max}$ is the maximum fluid acceleration and $T_p$ is the peak period of the record.

The fluid acceleration perpendicular to vertical baffles at the bottom of the tank can be expressed as

$$a^V(t) = \left[1 - \sum_{n=1}^{\infty} c_n\right] \dot{u}(t) - \sum_{n=1}^{\infty} c_n \left[\omega_n \int_0^t \dot{u}(\tau) \exp[-\zeta_n \omega_n (t-\tau)] \sin[\omega_n (t-\tau)] d\tau\right] \tag{6.36}$$

where

$$c_n^V = 2 \frac{(-1)^{n-1}}{(k_n a)} \frac{1}{\cosh(k_n d)} \tag{6.37}$$

The maximum fluid acceleration can be obtained from the following:

$$a_{max}^V = \left\{\left[\left(1 - \sum_{n=1}^{\infty} c_n^H\right) \dot{u}_{max}\right]^2 + \left[\sum_{n=1}^{\infty} c_n^V S_a(\omega_n, \zeta_n)\right]^2\right\}^{1/2} \tag{6.38}$$

Similarly, the maximum acceleration perpendicular to horizontal baffles at the tank wall can be expressed as:

$$a_{max}^{H} = \left\{ \left[ \left( \sum_{n=1}^{\infty} c_n^H \right) \dot{u}_{max} \right]^2 + \left[ \sum_{n=1}^{\infty} c_n^H S_a(\omega_n, \zeta_n) \right]^2 \right\}^{1/2} \tag{6.39}$$

where

$$c_n^H = \frac{1}{(k_n a)} \frac{\sinh(k_n \ell)}{\cosh(k_n d)} \tag{6.40}$$

Now consideration is given to a pair horizontal baffles located 4 m above the tank base. The relative elevation of the baffles h/d is 0.8. The length of the horizontal baffle is 1.5 m so that relative baffle length $\alpha = 0.15$. The relative free surface elevation is estimated as $\eta_a/d = 0.156$ from the previous example without baffles in the tank. Also, for the Mexico earthquake the maximum fluid acceleration normal to the baffle at the tank wall is 1.95 m/s$^2$. The peak period $T_p$ is 2 s. The Keleugan-Carpenter number from Eq. 7.9 is found to be 0.8, so that corresponding drag coefficient is 16 (see Fig. 8). The hydrodynamic damping is then found from the Eq. 4.43 to be 4 %.

Table 17 shows a comparison of the maximum water elevation, the maximum horizontal force and the maximum overturning moment with and without horizontal baffles. The above comparisons are based on the solution using the first 10 sloshing modes. The maximum water surface elevation, the maximum horizontal forces and the maximum overturning moment at the base of the tank are reduced by 29 %, 7 % and 12 % respectively.

For the case of transverse motions, the corresponding damping is approximately 10 % if the baffle is located perpendicular to the transverse wall.

# 7 Conclusions And Recommendations

## 7.1 Summary

This thesis describes an investigation of the influence of multiple motion components and hydrodynamic damping on the hydrodynamic loads and fluid surface elevation in a fluid filled reservoir subjected to base excitation. The investigation is carried out for two configurations: rectangular and circular cylindrical reservoirs; the multiple motions are horizontal and rocking excitations; and the hydrodynamic damping is due to boundary layers along the reservoir walls and baffles along the reservoir bottom or sides. Initially, the boundary value problem for the case of an inviscid fluid and a harmonic base motion on the basis of linearized potential flow theory is summarized. The case of energy dissipation of a real fluid is then treated by a extension to this, which involves an assumption of dissipation at the free surface and a corresponding modification to the free surface boundary condition. In order to treat earthquake-induced motions, this solution is then extended to a simplified method of estimating maximum forces using a modal analysis and involving earthquake response spectra. The combined effect of the two component excitations on the overall fluid elevation and hydrodynamic forces are calculated using superposition. Theoretical models for prediction of hydrodynamic damping are also outlined. This involves an assessment of, firstly, the total energy of the oscillation, which is known from the available potential flow solution, and, secondly, the average rate of energy dissipation arising in the fluid, either through the boundary layers along the tank floor and walls or by flow separation around obstacles in the flow.

An experimental investigation for liquid-filled rectangular tanks was carried out. The tanks were subjected to component horizontal and rocking motions for both harmonic and earthquake motions as well as combined motions for both harmonic and earthquake motions. The experiments were extended to investigate the effects of damping, whereby the experiments were repeated with baffles in the rectangular reservoir.

The original contributions of this study include:

(a) the derivation of a theoretical solution for sloshing in a rectangular reservoir undergoing rocking base motion;
(b) the experimental verification of linear superposition as a simplified method to calculate effects of combined base motion from component motions;
(c) the development of a hydrodynamic model for predicting the damping due to turbulent boundary layers and due to baffles, for a rectangular reservoir; and
(d) the detailed experimental investigation of sloshing in a rectangular reservoir with and without baffles, and a comparison of these results with theoretical predictions.

## 7.2 Conclusions

The high frequency mass, modal masses and corresponding effective elevations, required to estimate the earthquake-induced hydrodynamic loads, overturning moments and fluid surface elevations are obtained from the analytical results. The full solutions for rectangular and circular reservoirs indicate that the relative masses and the corresponding relative elevations each depend on the relative depth. The relative elevations corresponding to modal masses are the same for both horizontal and rocking base motions, whereas the relative high frequency mass and corresponding relative elevation are different for horizontal and rocking base motions. The relative masses and corresponding relative elevations are similar for both rectangular and circular reservoirs.

### Comparisons with Housner's solution

For the lower values of relative depth, the relative high frequency masses based on Housner's solution generally agrees closely with those based on the full solution for both rectangular and circular reservoirs. The relative modal mass corresponding to the first mode sloshing based on Housner's solution agrees closely with the full solution for a

rectangular reservoir, but is lower than predictions based on the full solution for a circular reservoir. The relative elevation corresponding to high frequency mass based on Housner's solution underpredicts the full solution over the entire range of the relative depth, while the relative elevation corresponding to the first modal masses based on Housner's solution agrees reasonably well with the full solution, except for lower values of relative depth.

## Modal analysis

The modal analysis results suggest that the high frequency mass and modal mass corresponding to first mode sloshing should generally be sufficient to estimate the overall force and moment maxima. However, more generally such a conclusion depends on the relative depth and on the significant frequency range of the earthquake response spectrum in relation to the lower modal frequencies. It is shown that the reliable estimation of the maximum surface elevation in a large reservoir requires the influence of higher sloshing modes to be taken into account. And, as expected, Housner's predictions of fluid surface elevation correspond closely to those based on the closed-form solution for first mode excitation, but give predictions which are slightly higher than the full solution. The estimation based on the modal analysis is higher than that based on the complete time-domain solution. Results from earthquake excitation indicate that the maximum fluid surface elevation, the maximum horizontal force on the tank and the maximum overturning moment depend on the frequency range of the earthquake spectrum in relation to the lower modal frequencies. The modal analysis results for combined horizontal and rocking base motion suggest that the overall maximum force is influenced by rocking motion alone when the rocking parameter is relatively high. It is also noted that the overall maximum force is influenced by horizontal base motion for higher values of relative depth.

## Damping due to boundary layers

The damping coefficient due to energy dissipation in laminar boundary layers depends on the relative depth, the relative reservoir size and the boundary layer thickness. The damping coefficient increases with decreasing size of reservoir. On the other hand, the hydrodynamic damping due to turbulent boundary layers is a function of relative depth, relative fluid surface elevation and relative roughness of the reservoir walls. The hydrodynamic damping increases with the relative roughness of the wall.

## Damping due to baffles

Hydrodynamic damping due to horizontal baffles on the tank sides is a function of relative depth, relative baffle elevation, relative fluid surface elevation, and relative length of the baffle. The damping coefficient increases with relative baffle elevation and relative baffle length, and its variation with relative depth exhibits a maximum. Hydrodynamic damping due to a vertical baffle on the tank base is a function of relative depth, relative baffle length, and relative fluid surface elevation. The damping coefficient increases with relative baffle length and its variation with relative depth exhibits a maximum. It has been found that the horizontal baffles are effective in damping the liquid motions for taller tanks whereas vertical baffles are effective for shallower tanks. It is recognized that the hydrodynamic damping model assumes that the relative baffle length is small as discussed elsewhere in this thesis and therefore the relative baffle length is a limiting parameter of the model.

## Experiments without baffles

Experimental results for the component horizontal and rocking base motions are in good agreement with the respective theoretical results, and such results for combined motions suggest that superposition can be used to evaluate the response of multiple-degree-of-

freedom base motions from the component responses. The measured time-domain results agree reasonably well with predicted time-domain solutions.

### Experiments with baffles

Free vibration tests for two relative depths confirm that the hydrodynamic damping due to boundary layers increase with decreasing size of reservoir. Experimental results for baffles suggest that baffles can be used efficiently to damp liquid motions near resonance conditions, whereas the baffles are not effective in damping the liquid motions at non-resonance conditions. The baffle closer to the free surface gives higher damping than other positions. The measured damping for baffles is in good agreement with the predicted results. The measured damping without baffles exhibits the predicted trends in a somewhat general manner only because of broad assumptions made in the analysis of hydrodynamic damping model.

## 7.3 Recommendations for further study

In this thesis, the problem of determining hydrodynamic loads and water surface elevations for rectangular and circular tanks for component motions (horizontal and rocking) and combined motions, both for harmonic and earthquake motions has been addressed. The estimation of hydrodynamic damping is also discussed.

The experiments have been carried out for horizontal harmonic motion, rocking harmonic motion, horizontal earthquake motion and simultaneous horizontal and rocking harmonic motions. These studies confirmed that superposition could be used to evaluate the response of multiple-degree-of-freedom harmonic base motions from the component responses. Additional experimental studies are needed to investigate the simultaneous horizontal and rocking earthquake excitations.

# *Chapter 7 Conclusions and Recommendations*

The present experimental and theoretical studies have provided some information regarding the effective baffle elevations for side baffles and baffle heights for vertical baffle. Further experimental studies are necessary in order to establish the effect of baffle size and shape and applicability of the hydrodynamic model. Experimental studies are needed to validate the hydrodynamic damping model due to turbulent boundary layer with rough reservoir walls.

In the present study the case of two different types of baffles are considered, whereas it is of interest to consider the different configurations of baffles such as a permeable thin vertical barrier or more barriers spaced in the tank. Effects of draft depth, barrier spacing and porosity on the hydrodynamic forces and water surface elevation would also be of interest. Finally, it would be desirable to conduct a prototype study in which damping coefficients are measured for with and without baffles of various configurations.

# References

American Society of Civil Engineers (ASCE), (1984) "Fluid structure interaction during seismic excitation." Report, ASCE Committee on Seismic Analysis.

American Petroleum Institute (API), (1993) "Welded steel tanks for oil storage." API standard 650, 9th edition.

Aslam, M., (1981) "Finite element analysis of earthquake - induced sloshing in axisymmetric tanks." *International Journal for Numerical Methods in Engineering*, **17**, pp. 159-170.

American Water Works Association (AWWA), (1984) "AWWA standard for welded steel tanks for water storage." No. ANSI/AWWA D100-84.

Balendra, T., Ang, G. H., Paramasivan, P., and Lee, S. L., (1982) "Seismic design of flexible cylindrical storage containers." *Earthquake Engineering and Structural Dynamics*, **10**(3), pp. 477-496.

Case, K. M., and Parkinson, W. C., (1957) "Damping of surface waves in an incompressible liquid." *Journal of Fluid Mechanics,* **2**(2), pp. 172-184.

Chen, W. et al, (1996) "Large amplitude liquid sloshing in seismically excited tanks." *Earthquake Engineering and Structural Dynamics*, **25**, pp. 653-669.

Chwang, T. and Housner, G. W., (1978) "Hydrodynamic pressures on sloping dams during earthquakes. Part 1. Momentum method." *Journal of Fluid Mechanics*, **87**(2), pp. 335-341.

Chwang, T., (1978) "Hydrodynamic pressures on sloping dams during earthquakes. Part 2. Exact theory." *Journal of Fluid Mechanics*, **87**(2), pp. 343-348.

Clough, D. P., (1977) "Experimental evaluation of seismic design methods for broad cylindrical tanks." Report No. EERC 77-10, Earthquake Research Engineering Center, University of California, Berkeley, CA.

Clough, D. P., and Clough, R. W., (1978) "Earthquake simulator studies of cylindrical tanks." *Nuclear Engineering and Design*, **46**, pp. 367-380.

Clough, R. W., Niwa, A., and Clough, D. P., (1979) "Experimental seismic study of cylindrical tanks." *Journal of the Structural Division*, ASCE, **105**, pp. 2565-2590.

Cooper, R. M., (1960) "Dynamics of liquids in moving containers." *ARS journal*, **30**(8), pp. 725-729.

Faltinsen, O., (1978) "A numerical nonlinear method of sloshing in tanks with two-dimensional flow." *Journal of Ship Research*, **22**(3), pp. 193-202.

Fisher, D., (1979) "Dynamic fluid effects in liquid-filled flexible cylindrical tanks." *Earthquake Engineering and Structural Dynamics*, **7**, pp. 587-601.

Haroun, M. A., (1983) "Vibration studies and tests of liquid storage tanks." *Earthquake Engineering and Structural Dynamics*, **11**, pp. 179-206.

Haroun, M. A., and Housner, G. W., (1981) "Seismic design of liquid storage tanks." *Journal of Technical Councils* of ASCE, **107**, pp. 191-207.

Haroun, M. A., and Housner, G. W., (1981) "Earthquake response of deformable liquid storage tanks." *Journal of Applied Mechanics*, **48**, pp. 411-418.

Haroun, M. A., and Housner, G. W., (1982) "Dynamic characteristics of liquid storage tanks." *Journal of Engineering Mechanics*, ASCE, **108**(EM5), pp. 783-800.

Haroun, M. A., and Tayel, M. A., (1985) "Axisymmetrical vibrations of tanks-Numerical." *Journal of Engineering Mechanics*, ASCE, **111**(3), pp. 329-345.

Haroun, M. A., and Tayel, M. A., (1985) "Response of tanks to vertical seismic excitations." *Earthquake Engineering and Structural Dynamics*, **13**, pp. 583-595.

Hoskins, L. M., and Jacobsen, L. S., (1933) "Water pressure in a tank caused by a simulated earthquake." *Bulletin of the Seismological Society of America*, **24**(1), pp. 1-32.

Housner, G. W., (1957) "Dynamic pressures on accelerated fluid containers." *Bulletin of the Seismological Society of America*, **47**, pp. 15-35.

Housner, G. W., (1963) "The dynamic behavior of water tanks." *Bulletin of the Seismological Society of America*, **53**, pp. 381-387.

Hwang, J. H et al, (1992) "Numerical simulation of liquid sloshing in three - dimensional tanks." *Computers & Structures*, **44**, pp. 339-342.

Isaacson, M., (1998) "Earthquake-induced hydrodynamic loads on reservoirs." *Proceedings of the Structural Engineers World Congress*, San Francisco, USA, paper T214-4.

Isaacson, M., and Subbiah, K., (1991) "Earthquake-induced sloshing in circular tanks." *Canadian Journal of Civil Engineering*, **18**(6), pp. 904-915.

Isaacson, M., and Ryu, S., (1998 a) "Earthquake-induced sloshing in a vertical tank of arbitrary section." *Journal of Engineering Mechanics*, ASCE, **124**(2), pp. 158-166.

Isaacson, M., and Ryu, S., (1998 b) "Directional effects on earthquake-induced sloshing in a rectangular tank." *Canadian Journal of Civil Engineering*, **25**(2), pp. 376-382.

Isaacson, M., and Ryu, S., (1999) "Earthquake-induced hydrodynamic loads in reservoirs with sloping sides and floors." *Proceedings of the 8$^{th}$ Canadian Conference on Earthquake Engineering*, CSCE, Vancouver, Canada, pp. 721-726.

Isaacson, M., and Premasiri, S., (1999) "Water surface elevation due to earthquake-induced sloshing." *Proceedings of the 8$^{th}$ Canadian Conference on Earthquake Engineering*, CSCE, Vancouver, Canada, pp. 727-742.

Jacobsen, L. S., (1949) "Impulsive hydrodynamics of fluid inside a cylindrical tank and of fluid surrounding a cylindrical pier." *Bulletin of the Seismological Society of America*, **39**, pp. 189-203.

Jacobson, L. S., and Ayre, R. S., (1951) "Hydrodynamic experiments with rigid cylindrical tanks subjected to transient motions." *Bulletin of the Seismological Society of America*, **41**, pp. 313-346.

Jonnson, I. G., (1967) "Wave boundary layers and friction factors." *Proceedings of the 10$^{th}$ conference on Coastal Engineering*, ASCE, Tokyo, pp. 127-148.

Kajiura, K., (1968) "A model of the bottom boundary layer in water waves." Bulletin of the Earthquake Research Institute, **46**, pp. 75-123.

Kim, J. K. et al, (1995) "Dynamics response of rectangular flexible fluid containers." *Journal of Engineering Mechanics*, ASCE, **122**(9), pp. 807-817.

Liu, Z., and Huang, Y., (1994) "A new method for large amplitude sloshing problems." *Journal of Sound and Vibration*, **175**(2), pp. 185-195.

Luft, R. W., (1983) "Vertical accelerations in pre-stressed concrete tanks." *Journal of Structural Engineering*, ASCE, **110**(4), pp. 706-714.

Miles, J., (1958) "Ring damping of free surface oscillations in a circular tank." *Journal of Applied Mechanics*, **25**, pp. 274-276.

Nakayama, T., and Washizu, K., (1981) "The boundary element method applied to the analysis of two-dimensional nonlinear sloshing problems." *International Journal for Numerical Methods in Engineering*, **17**, pp. 1631-1646.

National Building Code of Canada (1985) "Commentaries on part 4 of the National Building Code of Canada." National Research Council of Canada, Ottawa.

Rammerstorfer, F. G. et al (1990) "Storage tanks under earthquake loading." *Applied Mechanics Reviews*, **43**(11), pp. 261-282.

Sarpkaya, T., and Isaacson, M., *Mechanics of Wave Forces on Offshore Structures*. Van Nostrand Reinhold, New York, 1981.

Sarpkaya, T., and O'Keefe, J. L., (1996) "Oscillating flow about two and three-dimensional bilge keels." *Journal of Offshore Mechanics and Arctic Engineering*, 118, pp. 1-6.

Swart, D. H., (1976) "Coastal Sediment Transport." Delft Hydraulics Lab., Report R968, Part 1.

Yang, J. Y., (1976) "Dynamic behavior of fluid-tank systems." Ph.D. Thesis submitted to Rice University, Houston, Texas.

U.S. Atomic Energy Commission (1963) "Nuclear reactors and earthquakes, Chapter 6: Dynamic pressure on fluid containers." Prepared by Lockheed Aircraft Coporation, Technical Information Document 7024.

Veletsos, A. S., (1984) "Seismic response and design of liquid storage tanks." *Guidelines for Seismic Design of Oil and Gas Pipeline Systems*, Chapter 7, ASCE Technical Council on Lifeline Earthquake Engineering, ASCE, pp. 255-370.

Veletsos, A. S., and Yang, J. Y., (1976) "Dynamics of fixed-base liquid-storage tanks." *Proceedings of U.S - Japan Seminar for Earthquake Engineering Research with Emphasis on Lifeline Systems*, Tokyo.

Veletsos, A. S., and Yang, J. Y., (1977) "Earthquake response of liquid storage tanks." *Advances in Civil Engineering through Engineering Mechanics*, ASCE, pp. 1-24.

Veletsos, A. S., (1974) "Seismic effects in flexible liquid storage tanks." *Proceedings of the International Association for Earthquake Engineering Fifth World Conference*, Rome, Italy, **1**, pp. 630-639.

Veletsos, A. S., and Tang, Y., (1987) "Rocking response of liquid storage tanks", *Journal of Engineering Mechanics*, **113**(11), pp. 1774-1792.

Veletsos, A. S., and Tang, Y., (1986) "Dynamics of vertically excited liquid storage tanks." *Journal of Structural Engineering*, **112**(6), pp. 1228-1246.

Westergaard, H.M., (1933) "Water pressure on dams during earthquakes." *Transactions of the American Society of Civil Engineers*, **98**, pp. 418-433.

# Appendix

## Solution for rocking motion in a rectangular tank

The following outlines the solution for fluid motions in a rectangular tank undergoing rocking, motions, without hydrodynamic damping. The tank-liquid system investigated is shown in Fig. 1(a). It is a rectangular tank of length 2a and width 2b, which is filled to a height d and is excited by an angular or rocking base motion about horizontal axis. The sinusoidal base motion with angular velocity $\psi(t)$ is given as

$$\psi(t)=\Psi\exp(-i\omega t) \tag{A.1}$$

In which $\Psi$ is the angular velocity amplitude. Fixed Cartesian coordinate system (x, y, z), as indicated in Fig. 1(a), is used. The fluid within the container is assumed to be invisid and the flow is irrotational, so that the flow can be described by a velocity potential $\Phi$. Laplace equation which satisfies the potential $\Phi$ within the fluid region can be expressed as

$$\nabla^2\Phi=0 \tag{A.2}$$

The solution of Eq. A.2 must satisfy the following boundary conditions:

The vertical velocity of the liquid along the tank base must equal the corresponding velocity of the ground.

$$\frac{\partial\Phi}{\partial z}=\psi(t)x \qquad \text{at } z=0 \tag{A.3}$$

The velocity along the tank wall and the velocity of the tank wall must be the same.

$$\frac{\partial \Phi}{\partial x} = -\psi(t) z \qquad \text{at } x = \pm a \qquad \text{(A.4)}$$

$\Phi$ must satisfy the linearized free surface boundary condition since the amplitude of the base motion and the resulting free surface elevation in the container are assumed to be sufficiently small for linearization of the free surface boundary conditions.

$$\frac{\partial^2 \Phi}{\partial t^2} + g \frac{\partial \Phi}{\partial z} = 0 \qquad \text{at } z = d \qquad \text{(A.5)}$$

The solution for $\Phi$ can be expressed in the form

$$\Phi(x, z, t) = [\phi_i(x, z) + \phi_c(x, z)] \exp(-i\omega t) \qquad \text{(A.6)}$$

The impulsive component of the solution $\phi_i$ satisfies the actual boundary conditions along the wall and bottom and the condition of zero hydrodynamic pressure at the free surface, whereas the convective component $\phi_c$ corrects for the difference between actual boundary condition at the free surface and the one considered in the development of impulsive solution.

**Impulsive Solution**

The solution for $\phi_i$ may be expressed in the form

$$\phi_i = \Psi(z - d) x + \phi_0 \qquad \text{(A.7)}$$

in which $\phi_0$ must satisfy

$$\nabla^2 \phi_0 = 0 \qquad \text{(A.8)}$$

and the boundary conditions

$$\frac{\partial \phi_0}{\partial z} = 0 \qquad \text{at } z = 0 \qquad \text{(A.9)}$$

$$\frac{\partial \phi_0}{\partial x} = \Psi(d - 2z) \qquad \text{at } x = \pm a \qquad \text{(A.10)}$$

$$\phi_0 = 0 \qquad \text{at } z = d \qquad \text{(A.11)}$$

The velocity potential $\phi_0$ can be obtained by solving Eq. A.8 using the method of separation variables and satisfying Eqs. A.9 and A.11

$$\phi_0 = \sum_{m=1}^{\infty} A_m \cos(\alpha_m Z)\sinh(\alpha_m x) \qquad \text{(A.12)}$$

in which $\alpha_m = {(2n-1)\pi}/{2d}$ and $A_m$ may determined from Eq. A.10. The Eq. A.10 is first multiplied by $\cos(\alpha_i z)$, then integrated with respect to z over the appropriate domain of z (i.e. from z = 0 to d). This gives the equation for $A_m$ as:

$$A_m = 2\Psi \frac{1}{\alpha_m^2}\left[\frac{2}{\alpha_m} - (-1)^{m+1}\right]\frac{1}{\cosh(\alpha_m a)} \qquad \text{(A.13)}$$

**Convective Solution**

The velocity potential $\phi_c$ must satisfy

$$\nabla^2 \phi_c = 0 \qquad \text{(A.14)}$$

along with boundary conditions

$$\frac{\partial \phi_c}{\partial z} = 0 \qquad \text{at } z = 0 \qquad \text{(A.15)}$$

$$\frac{\partial \phi_c}{\partial x} = 0 \qquad \text{at } x = \pm a \qquad \text{(A.16)}$$

$$-\omega^2 \phi_c + g \frac{\partial \phi_c}{\partial z} = -g \frac{\partial \phi_i}{\partial z} \qquad \text{at } z = d \qquad \text{(A.17)}$$

The solution for $\phi_c$ can be obtained in a manner similar to the impulsive solution.

$$\phi_c = \sum_{n=1}^{\infty} B_n \cosh(k_n z) \sin(k_n x) \qquad \text{(A.18)}$$

in which $k_n = {(2n-1)\pi}/{2a}$ and $B_n$ must be determined from Eq. A.17. The Eq. A.17 can be expressed as after substitution of $\phi_i$ and $\phi_c$

$$\sum_{n=1}^{\infty} -B_n \cosh(k_n d) \sin(k_n x) \left[\omega^2 - \omega_n^2\right] = \Psi x - g \sum_{m=1}^{\infty} A_m \alpha_m \sin(\alpha_m d) \sinh(\alpha_m x) \qquad \text{(A.19)}$$

where

$$\omega_n^2 = g k_n \tanh(k_n d) \qquad \text{(A.20)}$$

The Eq. A.19 is first multiplied by $\sin(k_1 x)$, then integrated with respect to x over an appropriate domain of x ( x = -a to a ). This gives an equation for $B_n$:

$$B_n = 2 g \Psi \frac{1}{a} \frac{1}{\cosh(k_n d)} \frac{1}{(\omega^2 - \omega_n^2)} \left\{ \frac{(-1)^{n+1}}{k_n^2} - \sum_{m=1}^{\infty} \frac{(-1)^{n+1}}{\alpha_m^2 + k_n^2} \left[ \frac{2(-1)^{m+1}}{\alpha_m} - 1 \right] \right\} \qquad \text{(A.21)}$$

The above equation can be rearranged as follows

$$B_n = \frac{2(-1)^{n+1}\Psi a^2}{(k_n a)^3} G_n^R(i\omega)\left[\frac{(k_n d)\sinh(k_n d)-\cosh(k_n d)+2}{\sinh(k_n d)\cosh(k_n d)}\right] \tag{A.22}$$

The following identity was used in deriving the above equation

$$\sum_{m=1}^{\infty} 2\left[\frac{2(-1)^{m+1}}{(\alpha_m d)}-1\right]\frac{k_n^2}{\alpha_m^2+k_n^2} = 2[1-\sec h(k_n d)]-(k_n d)\tanh(k_n d) \tag{A.23}$$

Substituting $B_n$ into Eq. A.18

$$\phi_c = 2\Psi a d\sum_{n=1}^{\infty}\frac{(-1)^{n+1}}{(k_n a)^2}\gamma_n G_n(i\omega)\frac{\cosh(k_n z)}{\cosh(k_n d)}\sin(k_n x) \tag{A.24}$$

where

$$\gamma_n = \frac{(k_n d)\sinh(k_n d)-\cosh(k_n d)+2}{(k_n d)\sinh(k_n d)} \tag{A.25}$$

Finally, the velocity potential $\Phi$ can be expressed as

$$\begin{aligned}\Phi = \Psi\{(z-d)x &+ \sum_{m=1}^{\infty}\frac{2}{\alpha_m^2}\left[\frac{2}{(\alpha_m d)}-(-1)^{m+1}\right]\frac{\sinh(\alpha_m x)}{\cosh(\alpha_m a)}\cos(\alpha_m z)\\ &+ a d\sum_{n=1}^{\infty}\frac{2(-1)^{n+1}}{(k_n a)^2}\gamma_n\frac{\cosh(k_n z)}{\cosh(k_n d)}\sin(k_n x)G_n^R(i\omega)\}\exp(-i\omega t)\end{aligned} \tag{A.26}$$

The free surface elevation can now be obtained by substituting the expressions for $\Phi$ given by Eq. A.6 into the following equation

$$\eta = -\frac{1}{g}\left[\frac{\partial \Phi}{\partial t}\right]_{z=d} \tag{A.27}$$

This gives

$$\eta = \frac{2i\omega\Psi ad}{g}\left[\sum_{n=1}^{\infty}\frac{(-1)^{n+1}}{(k_n a)^2}\gamma_n G_n^R(i\omega)\sin(k_n x)\right]\exp(-i\omega t) \tag{A.28}$$

The free surface elevation at tank wall is given as:

$$\eta = \frac{i\omega\Psi da}{g}\left[\sum_{n=1}^{\infty}\frac{2}{(k_n a)^2}\gamma_n G_n^R(i\omega)\right]\exp(-i\omega t) \tag{A.29}$$

The hydrodynamic pressure p within the fluid is given by the linearized Bernoulli equation as

$$P = -\rho\left[\frac{\partial \Phi}{\partial t}\right] \tag{A.30}$$

Substituting for $\Phi$, one will get

$$\begin{aligned} P = i\omega\Psi\rho\{&(z-d)x + 2\sum_{m=1}^{\infty}\frac{1}{\alpha_m^2}\left[\frac{2}{(\alpha_m d)} - (-1)^{m+1}\right]\frac{\sinh(\alpha_m x)}{\cosh(\alpha_m a)}\cos(\alpha_n z) \\ &+ 2ad\sum_{n=1}^{\infty}\frac{(-1)^{n+1}}{(k_n a)^2}\gamma(k_n d)G_n^R(i\omega)\frac{\cosh(k_n z)}{\cosh(k_n d)}\sin(k_n x)\ \}\exp(-i\omega t) \end{aligned} \tag{A.31}$$

The total horizontal force F on the tank is obtained by integrating above equation at $x = \pm a$ over a depth d.

$$F = 2b\int_0^d [P_{x=a} - P_{x=-a}]dz \tag{A.32}$$

The total force is given by

$$F = i\omega\Psi dm\left[\frac{1}{2} - \sum_{m=1}^{\infty} h_m^{(r1)} - \sum_{n=1}^{\infty} h_n^{(r2)} G_n^R(i\omega)\right]\exp(-i\omega t) \tag{A.33}$$

where

$$h_m^{(r1)} = 2\frac{d}{a}\frac{1}{(\alpha_m d)^3}\left[\frac{2(-1)^{n+1}}{(\alpha_m d)} - 1\right]\tanh(\alpha_m a) \tag{A.34}$$

$$h_n^{(r2)} = \frac{m_n}{m} = \gamma_n h_n \tag{A.35}$$

The overturning moment about the base of the tank, excluding the component due to the pressure distribution over the base of the tank, M is obtained by

$$M = 2b\int_0^d [P_{x=a} - P_{x=-a}]z\,dz \tag{A.36}$$

Substituting for pressure variations

$$M = i\omega\Psi dmd\left\{\frac{1}{6} - \sum_{m=1}^{\infty} g_m^{(r1)} - \sum_{n=1}^{\infty} g_n^{(r2)} G_n^R(i\omega)\right\}\exp(-i\omega t) \tag{A.37}$$

where

$$g_m^{(r1)} = 2\frac{d}{a}\left[\frac{3(-1)^{m+1}(\alpha_m d)-(\alpha_m d)^2-2}{(\alpha_m d)^5}\right]\tanh(\alpha_m a) \tag{A.38}$$

$$g_n^{(r2)} = \gamma_n\, g_n \tag{A.39}$$

An additional moment $\Delta M$ due to the pressure distribution over the base of the tank is given by

$$\Delta M = 2b\int_{-a}^{+a} P_{z=0}\, x\, dx \tag{A.40}$$

Substituting for pressure variation into Eq. A.80, the additional moment can be expressed as

$$\Delta M = i\omega\Psi dmd\left[\frac{1}{3}\left(\frac{a}{d}\right)^2 - 2\left(\frac{d}{a}\right)\sum_{m=1}^{\infty}\left[\frac{2-(-1)^{m+1}(\alpha_m d)}{(\alpha_m d)^5}\right]\left[\frac{(\alpha_m a)\cosh(\alpha_m a)-\sinh(\alpha_m a)}{\cosh(\alpha_m a)}\right] + \sum_{n=1}^{\infty}\frac{2}{(k_n a)^2}\frac{1}{(k_n d)^2\cosh(k_n d)}\gamma_n\, G_n^R(i\omega)\right]\exp(-i\omega t) \tag{A.41}$$

Thus, the total overturning moment $M' = M + \Delta M$ at the base is given by

$$M' = i\omega\Psi dmd\left\{\frac{1}{6}+\frac{1}{3}\left(\frac{a}{d}\right)^2 - \sum_{m=1}^{\infty} gg_m^{(r1)} - \sum_{n=1}^{\infty} gg_n^{(r2)}\, G_n^R(i\omega)\right\}\exp(-i\omega t) \tag{A.42}$$

where

$$gg_m^{(r1)} = 2\left(\frac{d}{a}\right)\left[\frac{4(-1)^{m+1}(\alpha_m d)-(\alpha_m d)^2-4}{(\alpha_m d)^5}\right]\tanh(\alpha_m a) - 2\left[\frac{(-1)^{m+1}(\alpha_m d)-2}{(\alpha_m d)^4}\right] \tag{A.43}$$

$$gg_n^{(r2)} = \gamma_n \, g'_n \qquad \text{(A.44)}$$

# Tables

| Mode | $k_n a$ | |
|---|---|---|
| | Rectangular Reservoir | Circular Reservoir |
| 1 | 1.571 | 1.841 |
| 2 | 4.712 | 5.331 |
| 3 | 7.854 | 8.536 |
| 4 | 10.996 | 11.706 |
| 5 | 14.814 | 14.864 |

Table 1. Values of $k_n a$ for the five lowest sloshing modes for rectangular and circular reservoirs.

| Excitation Frequency (Hz) | Excitation Amplitude (mm) |
|---|---|
| 0.50 | 63 |
| 0.64 | 31 |
| 0.80 | 14 |
| 0.95 | 6 |
| 1.00 | 6 |
| 1.11 | 3 |
| 1.19 | 2 |
| 1.27 | 2 |
| 1.35 | 3 |
| 1.43 | 4 |
| 1.59 | 7 |
| 2.08 | 3 |
| 2.13 | 2 |
| 2.20 | 1 |

Table 2 . Test program for horizontal harmonic excitation for d/a = 1.0.

| Excitation Frequency (Hz) | Excitation Amplitude (mm) |
|---|---|
| 0.50 | 40 |
| 0.64 | 20 |
| 0.80 | 10 |
| 0.95 | 3 |
| 1.00 | 2 |
| 1.02 | 2 |
| 1.05 | 1 |
| 1.11 | 2 |
| 1.19 | 2 |
| 1.35 | 6 |
| 1.43 | 12 |
| 2.08 | 3 |
| 2.12 | 2 |
| 2.22 | 1 |

Table 3. Test program for horizontal harmonic excitation for d/a = 0.5.

| Excitation Frequency (Hz) | Excitation Amplitude (rad/sec) |
|---|---|
| 0.95 | 0.10 |
| 1.00 | 0.10 |
| 1.11 | 0.03 |
| 1.19 | 0.01 |
| 1.27 | 0.01 |
| 1.35 | 0.02 |
| 2.15 | 0.02 |

Table 4. Test program for rocking harmonic motion for d/a = 1.0.

| Excitation Frequency (Hz) | Horizontal Excitation Amplitude (mm) | Rocking Excitation Amplitude (rad/s) |
|---|---|---|
| 0.95 | 8 | 0.05 |
| 1.00 | 6 | 0.04 |
| 1.11 | 3 | 0.02 |
| 1.19 | 1 | 0.005 |
| 1.27 | 1 | 0.01 |
| 1.35 | 1 | 0.01 |
| 2.15 | 1 | 0.01 |

Table 5. Test program for combined horizontal and rocking motion for d/a = 1.0.

| Mode | $T_n$(s) | $m_n/m$ | $d_n/d$ | $d'_n/d$ | $S_a$(g) | $F_n$(MN) | $F_{max}$ (MN) | $M_n$ (MNm) | $M_{max}$ (MNm) | $M'_n$ (GNm) | $M'_{max}$ (GNm) |
|---|---|---|---|---|---|---|---|---|---|---|---|
| 0 | - | 0.041 | 0.439 | 12.120 | 1.000 | 36.170 | 36.170 | 158.733 | 158.733 | 4.383 | 4.383 |
| 1 | 60.69 | 0.808 | 0.500 | 91.523 | 0.003 | 1.822 | 36.219 | 9.417 | 159.012 | 1.722 | 4.710 |
| 2 | 20.52 | 0.087 | 0.504 | 10.471 | 0.023 | 1.777 | 36.263 | 8.960 | 159.291 | 0.186 | 4.714 |
| 3 | 12.65 | 0.030 | 0.511 | 3.997 | 0.061 | 1.596 | 36.298 | 8.158 | 159.543 | 0.006 | 4.714 |
| a | 9.37 | 0.014 | 0.521 | 2.225 | 0.111 | 1.378 | 36.324 | 7.181 | 159.751 | 0.003 | 4.714 |
| 5 | 7.62 | 0.008 | 0.534 | 1.509 | 0.168 | 1.157 | 36.342 | 6.179 | 159.912 | 0.002 | 4.714 |
| 6 | 6.53 | 0.005 | 0.549 | 1.158 | 0.228 | 0.957 | 36.355 | 5.251 | 160.032 | 0.001 | 4.714 |
| 7 | 5.81 | 0.003 | 0.565 | 0.968 | 0.288 | 0.786 | 36.364 | 4.443 | 160.118 | 0.000 | 4.714 |
| 8 | 5.28 | 0.002 | 0.583 | 0.859 | 0.348 | 0.646 | 36.369 | 3.764 | 160.180 | 0.000 | 4.714 |
| 9 | 4.89 | 0.001 | 0.600 | 0.795 | 0.406 | 0.534 | 36.373 | 3.205 | 160.224 | 0.000 | 4.714 |
| 10 | 4.58 | 0.001 | 0.618 | 0.758 | 0.460 | 0.442 | 36.376 | 2.733 | 160.256 | 0.000 | 4.714 |

Table 6. Influence of sloshing modes on the maximum loads for a rectangular reservoir with a = 150 m, b = 75 m and d = 10 m, and $\dot{u}_{max}/g = 0.1$.

| Case | a(m) | d/a | | $F_{max}$(MN) | $M_{max}$(MNm) | $M'_{max}$(MNm) |
|---|---|---|---|---|---|---|
| A | 100 | 0.1 | Full (n=1) | 3.40 | 14.40 | 311.27 |
| | | | Full (n=2) | 3.40 | 14.47 | 311.50 |
| | | | Full | 3.42 | 14.61 | 311.53 |
| | | | Housner | 3.41 | 12.83 | 2051.57 |
| B | 20 | 0.5 | Full (n=1) | 3.34 | 13.87 | 56.24 |
| | | | Full (n=2) | 3.35 | 14.81 | 56.26 |
| | | | Full | 3.35 | 14.89 | 56.26 |
| | | | Housner | 3.54 | 13.81 | 95.45 |
| C | 10 | 1.0 | Full (n=1) | 3.10 | 13.20 | 25.25 |
| | | | Full (n=2) | 3.10 | 14.35 | 25.26 |
| | | | Full | 3.10 | 14.37 | 25.26 |
| | | | Housner | 3.34 | 13.32 | 30.19 |
| D | 5 | 2.0 | Full (n=1) | 2.19 | 9.54 | 11.72 |
| | | | Full (n=2) | 2.19 | 10.05 | 11.72 |
| | | | Full | 2.19 | 10.05 | 11.72 |
| | | | Housner | 2.42 | 9.50 | 9.03 |

Table 7. Comparison of alternative predictions of maximum loads for rectangular reservoirs for d = 10 m, b = 15 m and $\dot{U}_m/g=0.1$ for horizontal excitation.

| Case | a(m) | d/a | | $F_{max}$(MN) | $M_{max}$(MNm) | $M'_{max}$(MNm) |
|---|---|---|---|---|---|---|
| A | 100 | 0.1 | Full (n=1) | 30.98 | 112.98 | 20,173.06 |
| | | | Full (n=2) | 31.01 | 113.15 | 20,173.15 |
| | | | Full | 31.01 | 113.17 | 20,173.15 |
| B | 20 | 0.5 | Full (n=1) | 5.62 | 21.56 | 166.54 |
| | | | Full (n=2) | 5.62 | 21.59 | 166.54 |
| | | | Full | 5.62 | 21.59 | 166.54 |
| C | 10 | 1.0 | Full (n=1) | 2.52 | 10.53 | 25.36 |
| | | | Full (n=2) | 2.52 | 10.55 | 25.37 |
| | | | Full | 2.52 | 10.55 | 25.37 |
| D | 5 | 2.0 | Full (n=1) | 1.17 | 5.69 | 6.96 |
| | | | Full (n=2) | 1.17 | 5.70 | 6.96 |
| | | | Full | 1.17 | 5.70 | 6.96 |

Table 8. Comparison of alternative predictions of maximum loads for rectangular reservoirs for d = 10 m, b = 15 m and $\dot{\Psi}_m d/g=0.1$ for rocking excitation.

| Alaska Earthquake | | | |
|---|---|---|---|
| Solution Methods | $F_{max}$ (MN) | $M_{max}$ (MNm) | $M'_{max}$ (MNm) |
| Time Domain Solution | 3.31 | 16.64 | 67.98 |
| NBC Spectrum | 3.43 | 18.49 | 76.61 |
| Actual Response Spectrum | 3.33 | 16.75 | 68.60 |
| Loma Prieta Earthquake | | | |
| Solution Methods | $F_{max}$ (MN) | $M_{max}$ (MNm) | $M'_{max}$ (MNm) |
| Time Domain Solution | 3.38 | 17.12 | 69.67 |
| NBC Spectrum | 3.43 | 18.49 | 76.61 |
| Actual Response Spectrum | 3.32 | 16.74 | 68.58 |
| Northridge Earthquake | | | |
| Solution Methods | $F_{max}$ (MN) | $M_{max}$ (MNm) | $M'_{max}$ (MNm) |
| Time Domain Solution | 3.32 | 16.64 | 68.64 |
| NBC Spectrum | 3.43 | 18.49 | 76.61 |
| Actual Response Spectrum | 3.32 | 16.74 | 68.58 |

Table 9. Comparison of time domain analysis and modal analysis results for horizontal excitation for the Alaska, Loma Prieta and Northridge earthquakes.

| Alaska Earthquake | | | |
|---|---|---|---|
| Solution Methods | $F_{max}$ (MN) | $M_{max}$ (MNm) | $M'_{max}$ (MNm) |
| Time Domain Solution | 2.80 | 12.75 | 106.83 |
| NBC Spectrum | 2.86 | 13.46 | 107.34 |
| Actual Response Spectrum | 2.74 | 12.35 | 105.43 |
| Loma Prieta Earthquake | | | |
| Solution Methods | $F_{max}$ (MN) | $M_{max}$ (MNm) | $M'_{max}$ (MNm) |
| Time Domain Solution | 2.79 | 12.67 | 106.75 |
| NBC Spectrum | 2.86 | 13.46 | 107.34 |
| Actual Response Spectrum | 2.74 | 12.32 | 105.37 |
| Northridge Earthquake | | | |
| Solution Methods | $F_{max}$ (MN) | $M_{max}$ (MNm) | $M'_{max}$ (MNm) |
| Time Domain Solution | 2.72 | 12.41 | 105.57 |
| NBC Spectrum | 2.86 | 13.46 | 107.34 |
| Actual Response Spectrum | 2.74 | 12.32 | 105.38 |

Table 10. Comparison of time domain analysis and modal analysis results for rocking excitation for the Alaska, Loma Prieta and Northridge earthquakes.

| Alaska Earthquake | | | |
|---|---|---|---|
| Solution Methods | $F_{max}$ (MN) | $M_{max}$ (MNm) | $M'_{max}$ (MNm) |
| Time Domain Solution | 5.35 | 25.75 | 152.84 |
| NBC Spectrum | 4.47 | 22.87 | 129.03 |
| Actual Response Spectrum | 4.31 | 20.82 | 125.78 |
| Loma Prieta Earthquake | | | |
| Solution Methods | $F_{max}$ (MN) | $M_{max}$ (MNm) | $M'_{max}$ (MNm) |
| Time Domain Solution | 3.97 | 19.51 | 104.54 |
| NBC Spectrum | 4.47 | 22.87 | 129.03 |
| Actual Response Spectrum | 4.31 | 20.79 | 125.72 |
| Northridge Earthquake | | | |
| Solution Methods | $F_{max}$ (MN) | $M_{max}$ (MNm) | $M'_{max}$ (MNm) |
| Time Domain Solution | 3.32 | 15.76 | 106.65 |
| NBC Spectrum | 4.47 | 22.87 | 129.03 |
| Actual Response Spectrum | 4.31 | 20.79 | 125.73 |

Table 11. Comparison of time domain analysis and modal analysis results for combined horizontal and rocking excitations for the Alaska, Loma Prieta and Northridge earthquakes.

| | $\eta_{max}$ (mm) | $F_{max}$ (N) | $M'_{max}$ (Nm) |
|---|---|---|---|
| Experiment | 43.0 | 41.6 | 8.0 |
| Time Domain Solution | 29.0 | 57.0 | 7.6 |
| NBC Spectrum | 66.6 | 101.1 | 21.5 |
| Actual Response Spectrum | 31.0 | 58.5 | 12.2 |

Table 12. Comparison of experimental results with theoretical results for Mexico 79 Earthquake for horizontal excitation.

| h/d | gη/ωUa | | F/ωUm | | M/ωUmd | |
|---|---|---|---|---|---|---|
| | $\omega/\omega_1 = 1.0$ | $\omega/\omega_1 = 1.2$ | $\omega/\omega_1 = 1.0$ | $\omega/\omega_1 = 1.2$ | $\omega/\omega_1 = 1.0$ | $\omega/\omega_1 = 1.2$ |
| 0 | 25.0 | 1.4 | 22.0 | 2.8 | 9.2 | 1.4 |
| 0.6 | 16.7 | 1.3 | 9.4 | 2.8 | 5.8 | 1.3 |
| 0.7 | 10.8 | 1.6 | 9.5 | 2.8 | 4.6 | 1.6 |
| 0.8 | 9.7 | 1.5 | 8.0 | 2.8 | 3.2 | 1.5 |

Table 13. Variation of experimental dimensionless hydrodynamic coefficients with horizontal baffles.

| $\ell$/d | gη/ωUa | | F/ωUm | | M/ωUmd | |
|---|---|---|---|---|---|---|
| | $\omega/\omega_1 = 1.0$ | $\omega/\omega_1 = 1.2$ | $\omega/\omega_1 = 1.0$ | $\omega/\omega_1 = 1.2$ | $\omega/\omega_1 = 1.0$ | $\omega/\omega_1 = 1.2$ |
| 0 | 25.0 | 2.6 | 22.0 | 2.8 | 9.2 | 1.4 |
| 0.1 | 24.7 | 2.4 | 17.6 | 2.6 | 7.6 | 1.2 |
| 0.2 | 23.6 | 2.4 | 13.5 | 2.4 | 6.5 | 1.4 |
| 0.3 | 19.3 | 2.5 | 9.7 | 2.3 | 5.4 | 1.4 |

Table 14. Variation of experimental dimensionless hydrodynamic coefficients with vertical baffle.

| Maximum Water Surface Elevation | | | |
|---|---|---|---|
| Earthquake | 1 mode | 10 mode | Δ % |
| El Centro | 0.697 | 0.732 | 5 |
| Mexico | 0.332 | 0.781 | 57 |
| Maximum Horizontal Force | | | |
| Earthquake | 1 mode | 10 mode | Δ % |
| El Centro | 798.7 | 802.7 | 0.5 |
| Mexico | 527.7 | 573.6 | 8 |
| Maximum Overturning Moment | | | |
| Earthquake | 1 mode | 10 mode | Δ % |
| El Centro | 1.872 | 2.412 | 22 |
| Mexico | 1.157 | 1.562 | 26 |

Table 15. Comparison between 1 sloshing mode solution and 10 sloshing mode solution for the maximum water surface elevation, maximum force on the tank and maximum overturning moment at the tank base.

| | Longitudinal Direction | Transverse Direction |
|---|---|---|
| $\eta_{max}$ (m) | 0.781 | 1.483 |
| $F_{max}$ (MN) | 0.573 | 1.326 |
| $M_{max}$ (MNm) | 1.562 | 4.530 |

Table 16. Comparison of alternative predictions of maximum water surface elevation and loads.

| | No Baffles | Horizontal Baffles | $\Delta$ (%) |
|---|---|---|---|
| $\eta_{max}$ (m) | 0.781 | 0.554 | 29 |
| $F_{max}$ (KN) | 573.6 | 533.9 | 7 |
| $M_{max}$ (KNm) | 1.562 | 1.369 | 12 |

Table 17. Comparison of the maximum water surface elevation and the maximum hydrodynamic forces with and without horizontal baffles for Mexico earthquake.

# Figures

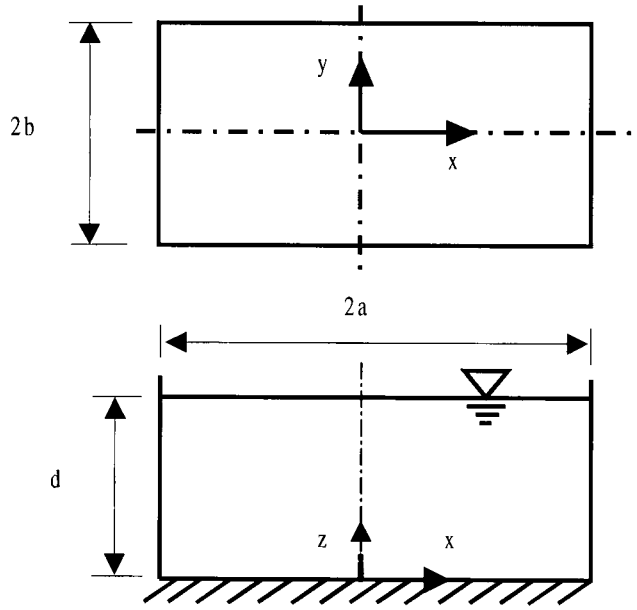


(a) Rectangular tank

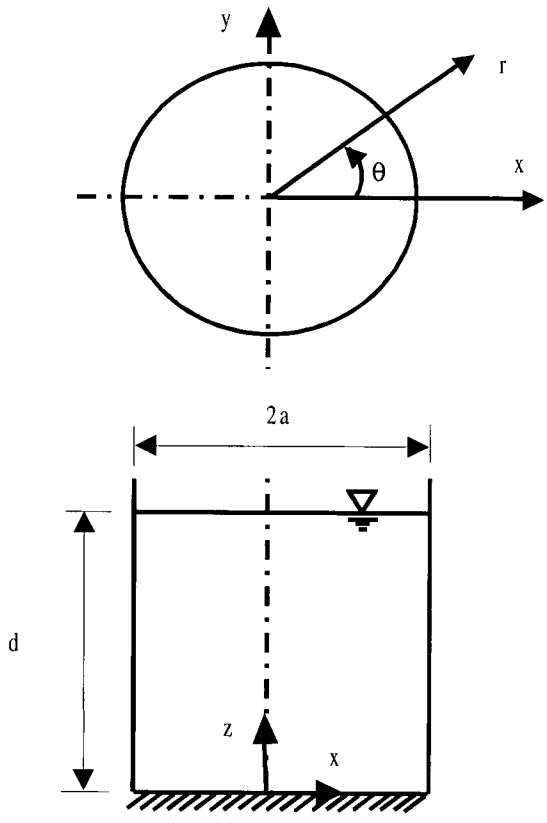


(b) Circular tank

Figure 1. Definition sketch of tank.

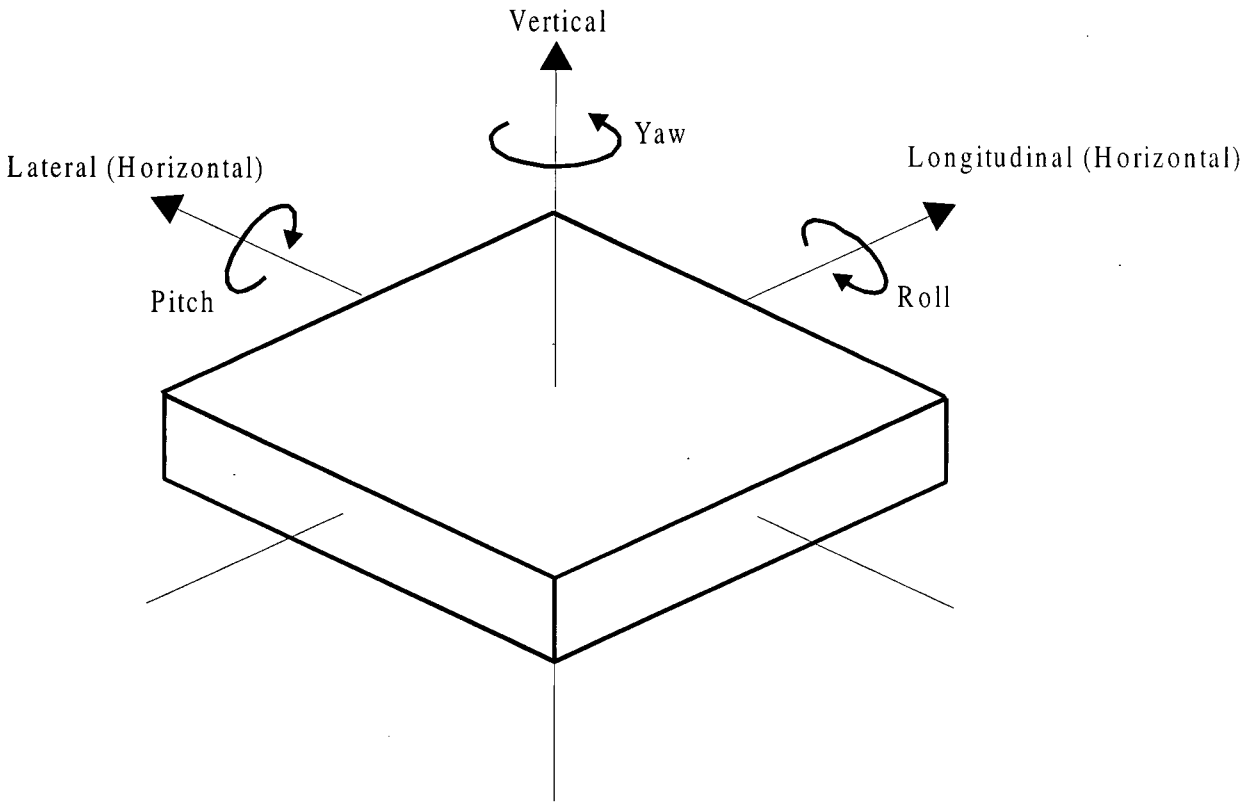


Figure 2. Definition of ground motion direction components.

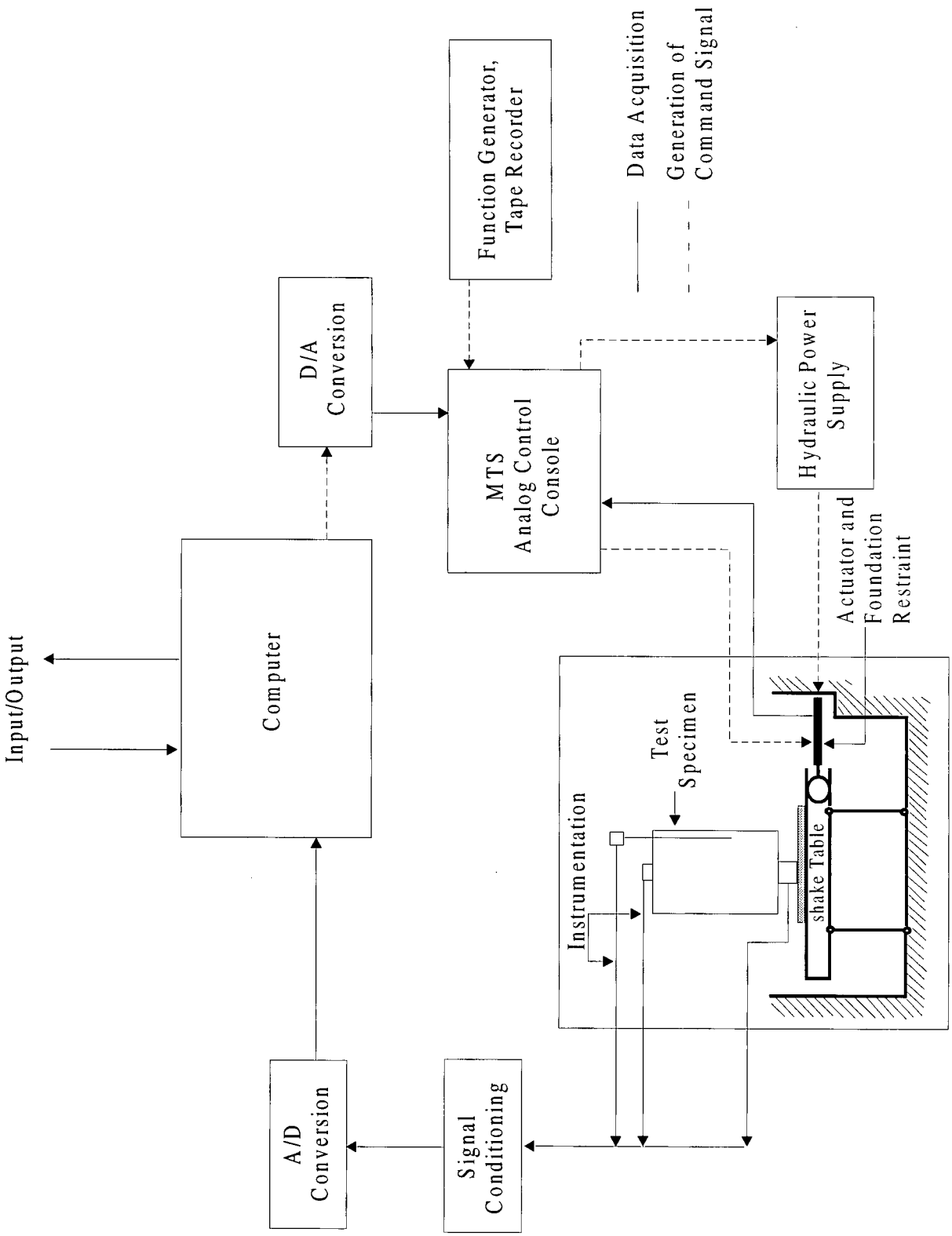


Figure 3. Block diagram of UBC shake-table control and data acquisition system.

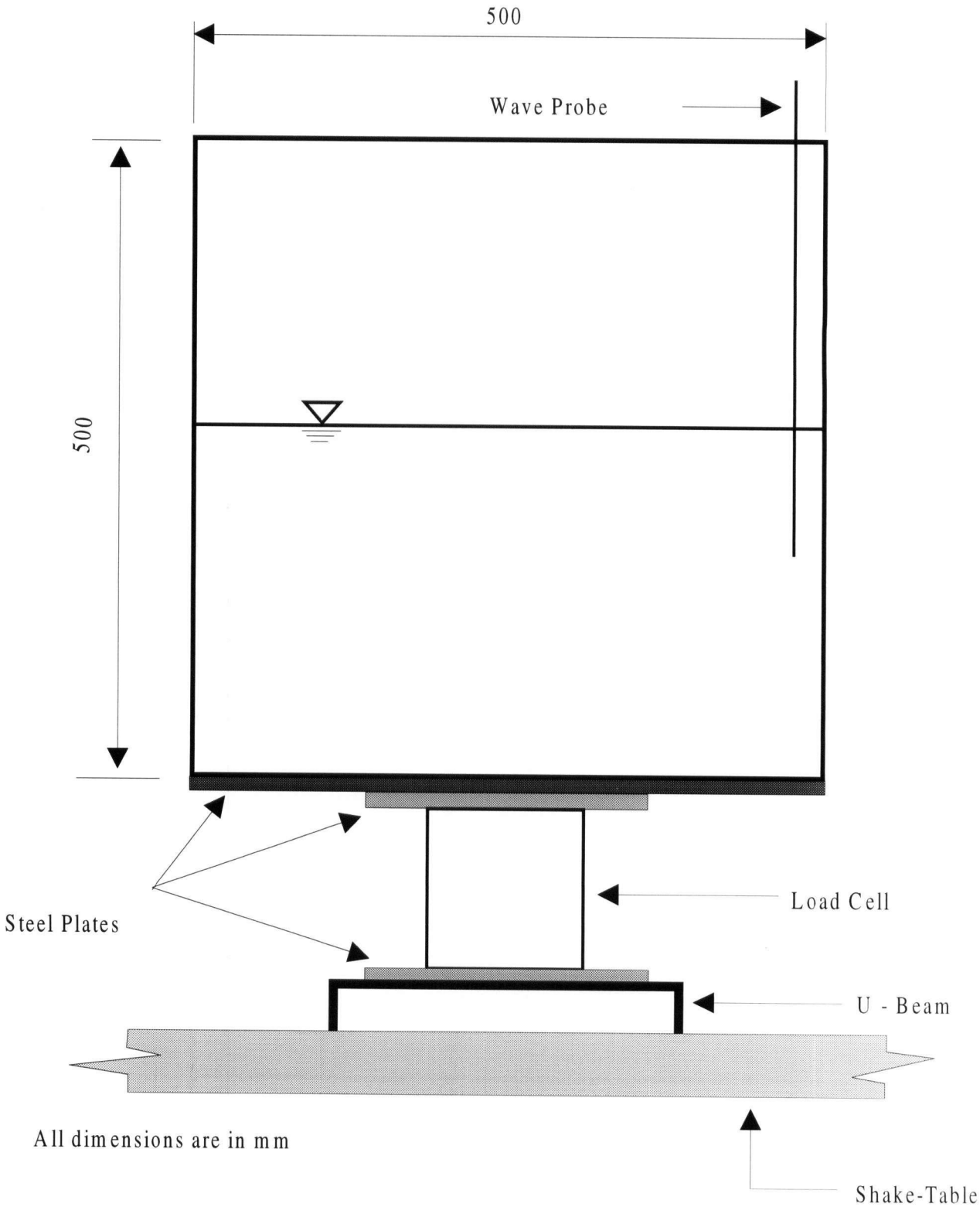


Figure 4. Experimental set-up.

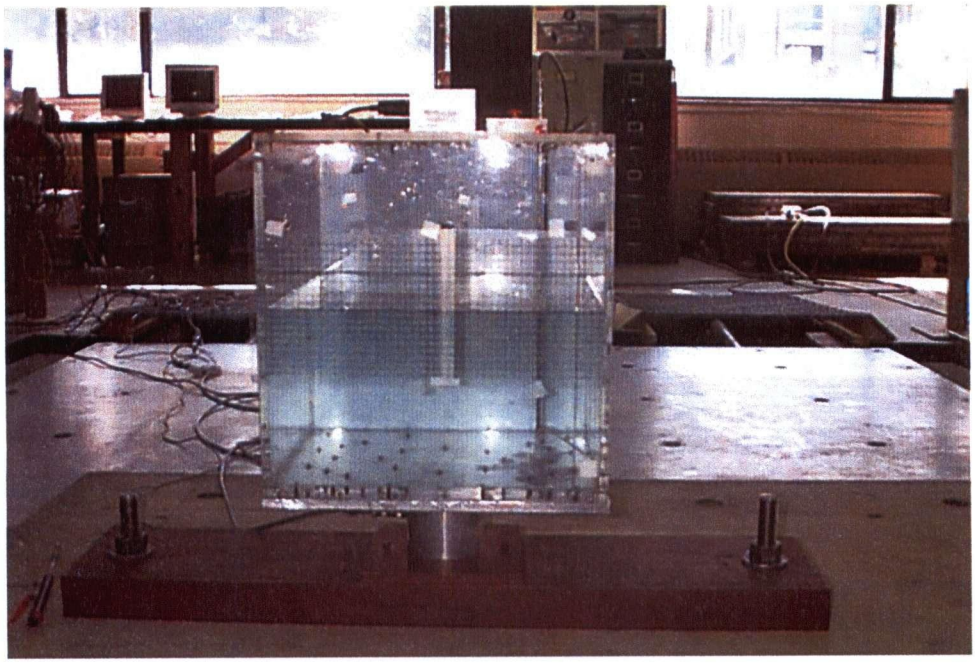

(a) Viewed normal to direction of motion.

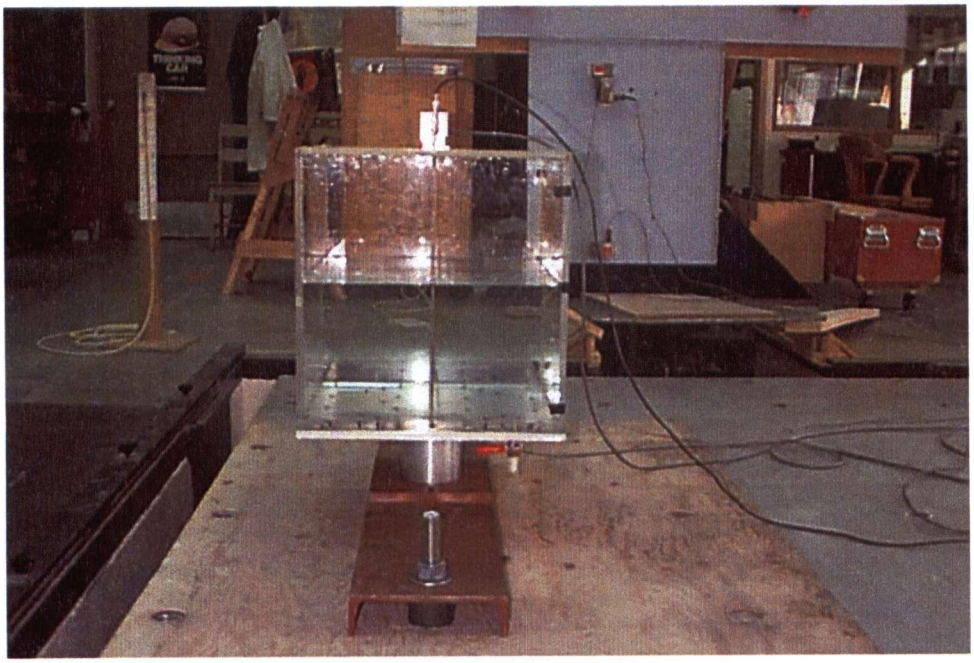

(b) Viewed along the direction of motion.

Figure 5. Views of the tank model mounted on the shake-table.

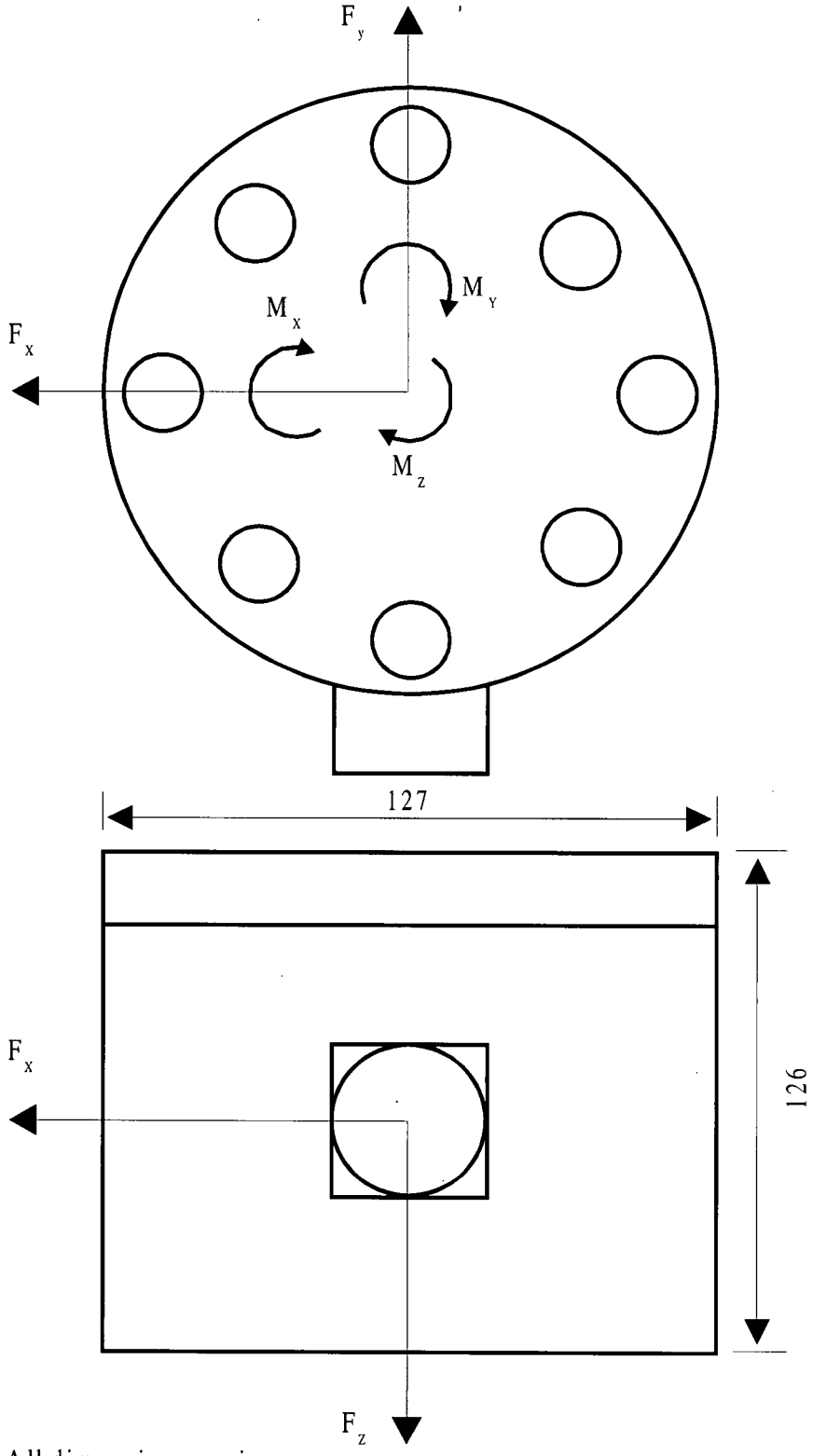


All dimensions are in mm

Figure 6. Load cell.

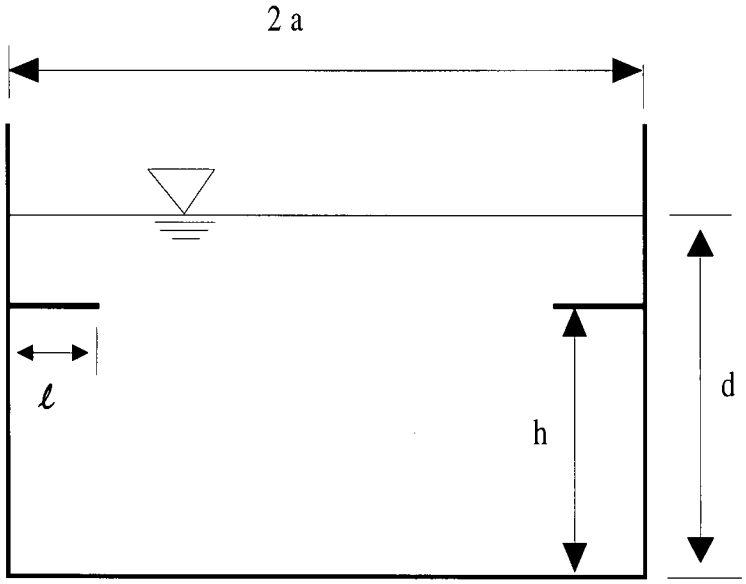


(a) Horizontal baffles

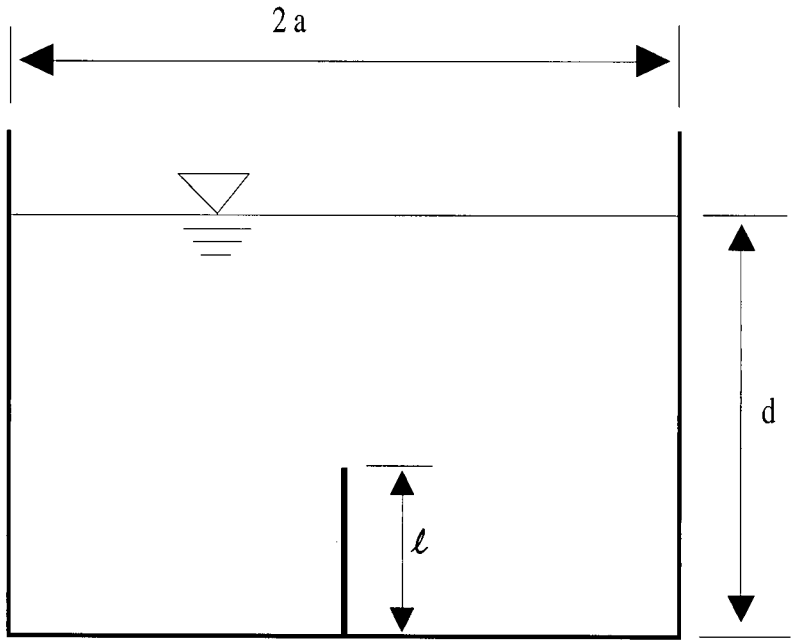


(b) Vertical baffle

Figure 7. Definition sketch showing baffle configurations.

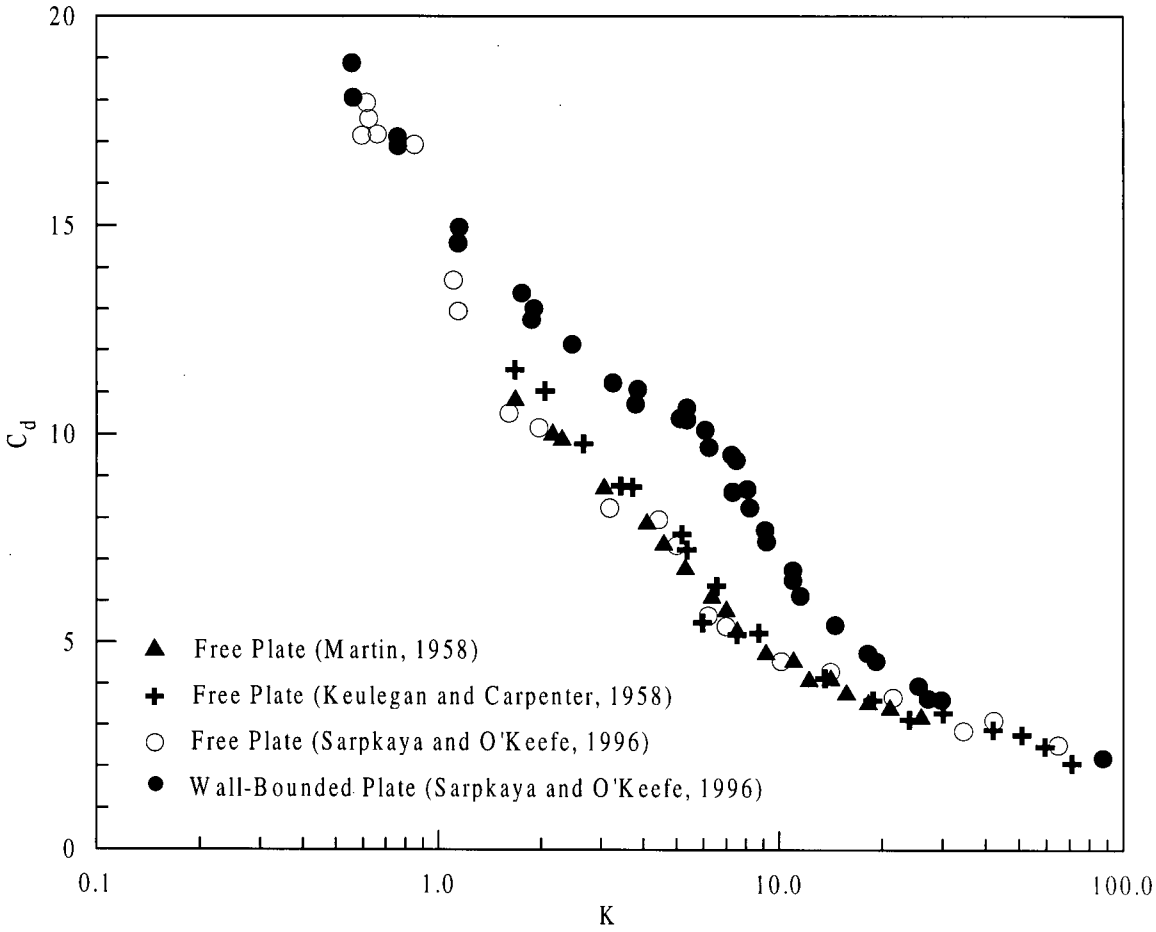


Figure 8. Drag coefficient versus Keulegan-Carpenter number for wall bounded and free plates.

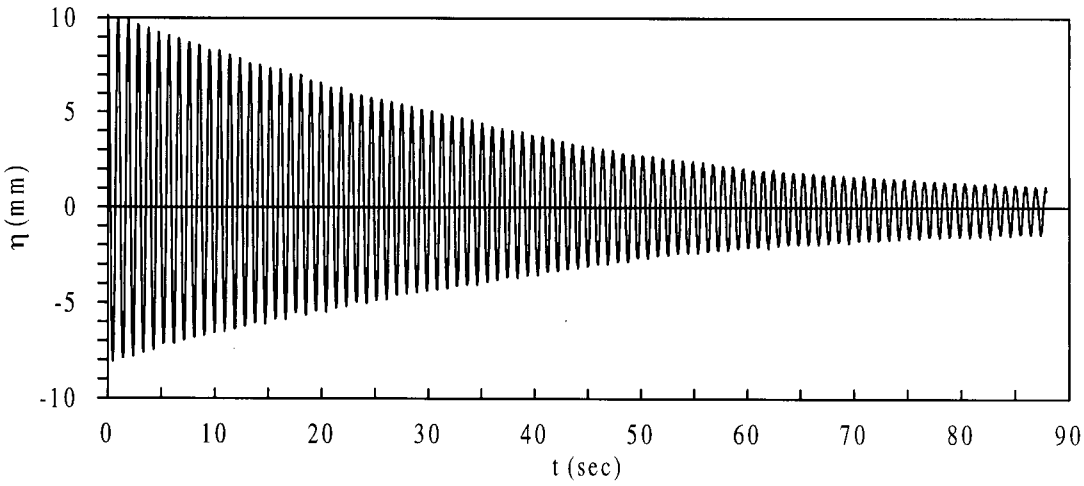


Figure 9. A sample record from free vibration test.

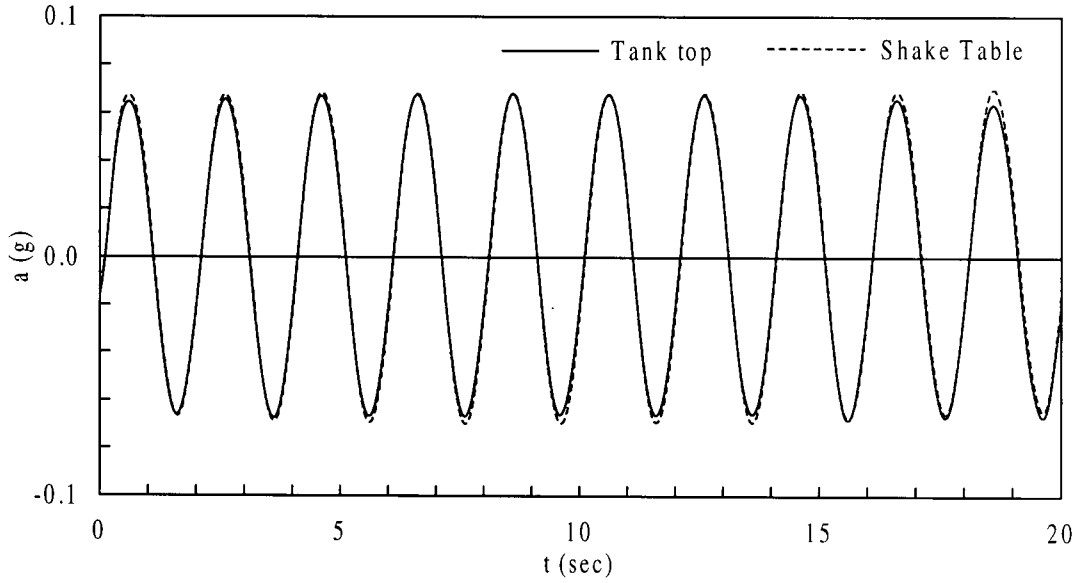


Figure 10. Comparison of shake table and tank top acceleration conditions.

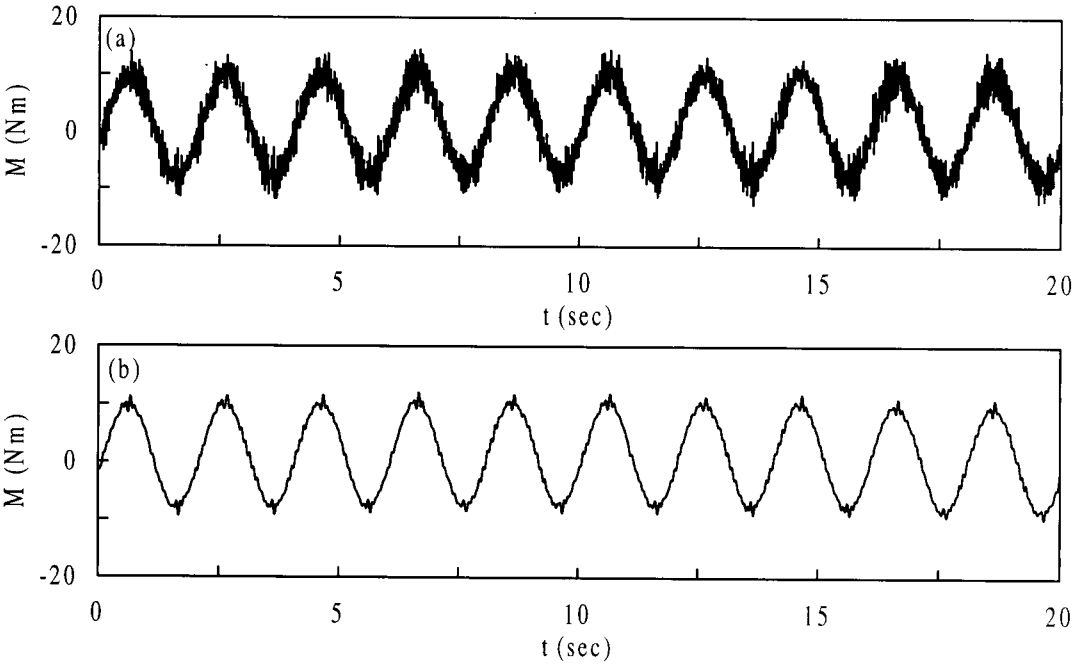


Figure 11. Sample record of overturning moment from load cell. (a) unfiltered, (b) filtered.

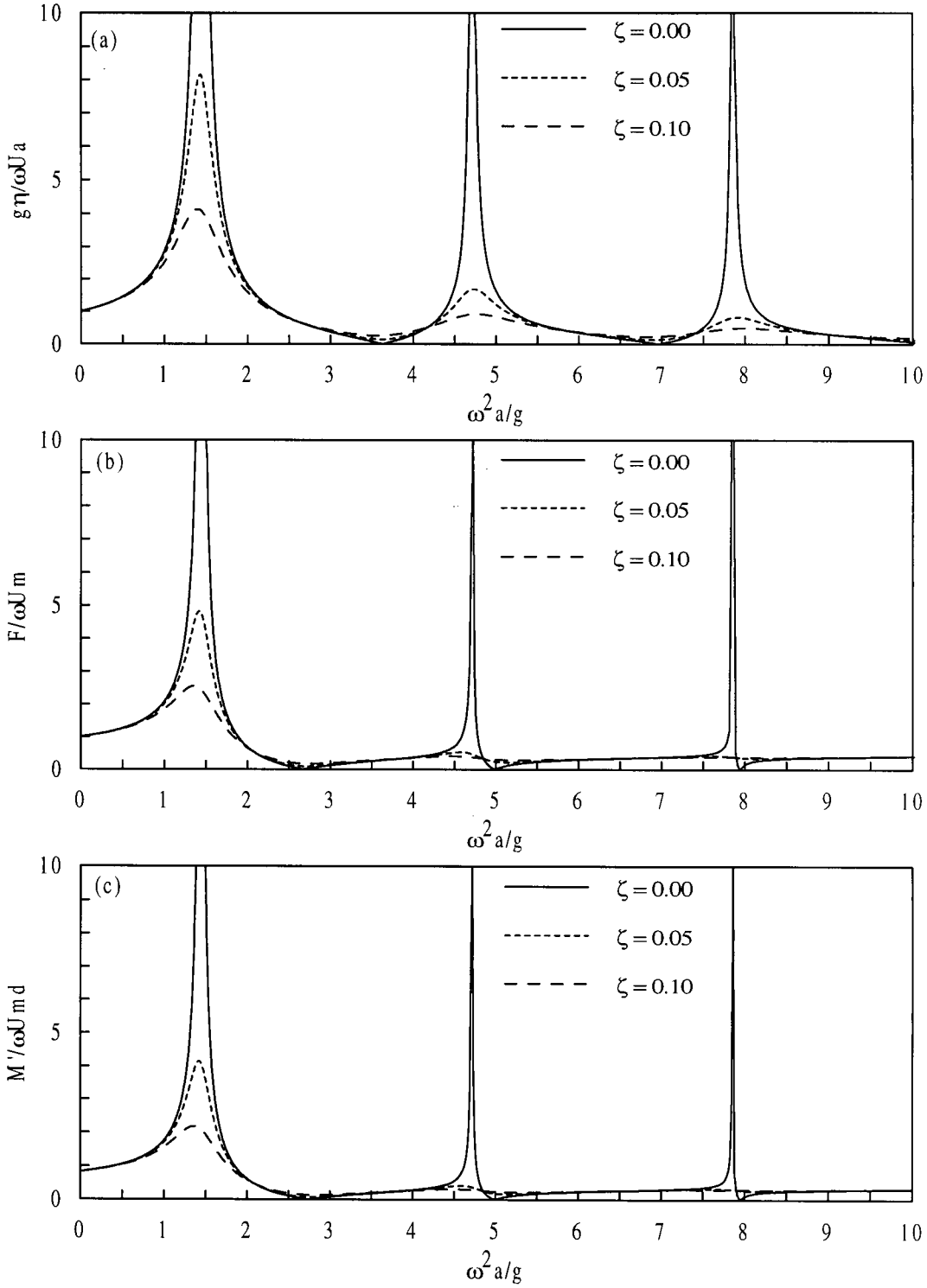


Figure 12. Dimensionless hydrodynamic coefficients as functions of $\omega^2 a/g$ for d/a = 1.0 and for various values of damping ratio - rectangular tank with a horizontal excitation. (a) free surface elevation, (b) horizontal force, (c) overturning moment.

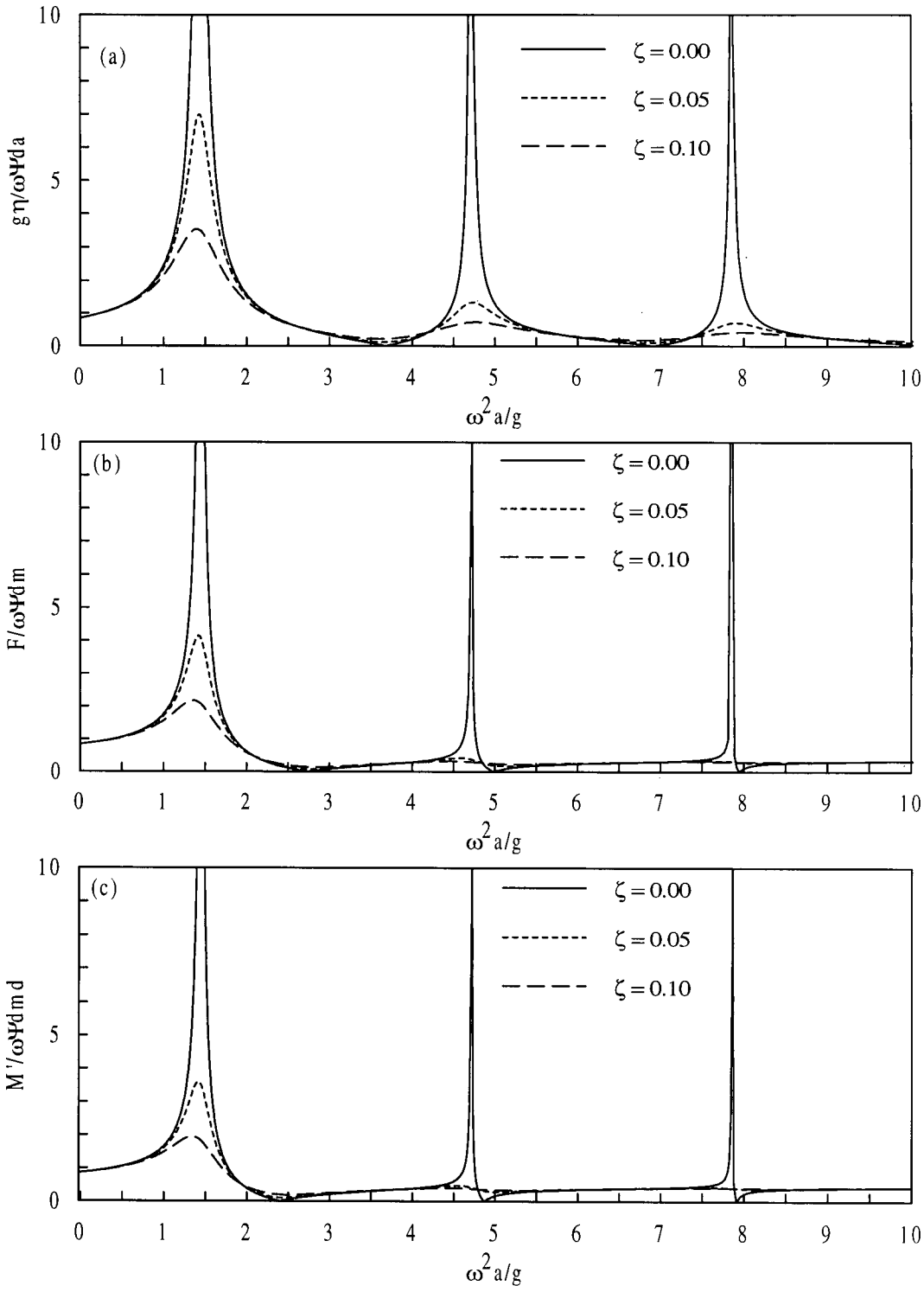


Figure 13. Dimensionless hydrodynamic coefficients as functions of $\omega^2 a/g$ for d/a = 1.0 and for various values of damping ratio - rectangular tank with a rocking excitation. (a) free surface elevation, (b) horizontal force, (c) overturning moment.

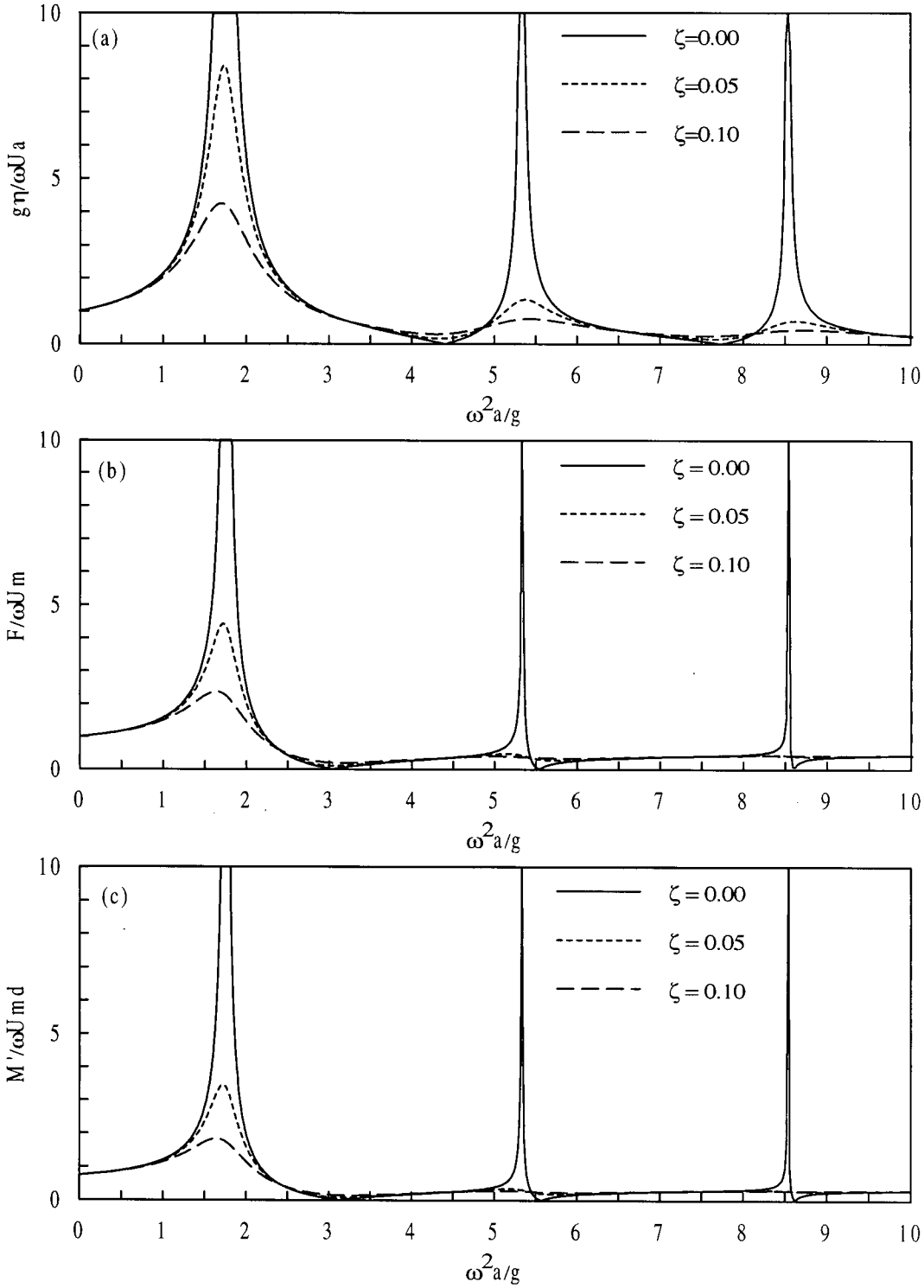


Figure 14. Dimensionless hydrodynamic coefficients as functions of $\omega^2 a/g$ for d/a = 1.0 and for various values of damping ratio - circular tank with a horizontal excitation. (a) free surface elevation, (b) horizontal force, (c) overturning moment.

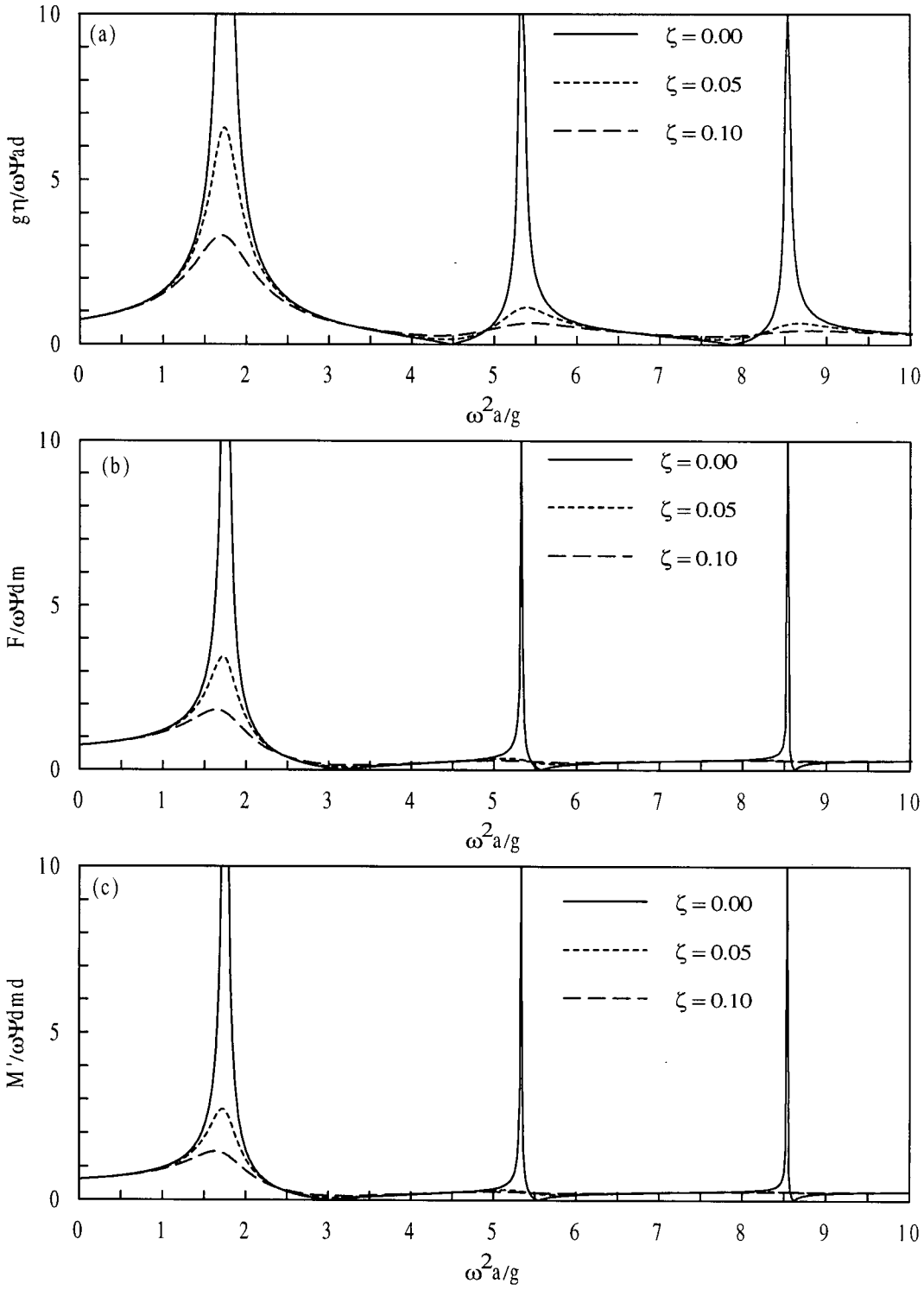


Figure 15. Dimensionless hydrodynamic coefficients as functions of $\omega^2 a/g$ for d/a = 1.0 and for various values of damping ratio - circular tank with a rocking excitation. (a) free surface elevation, (b) horizontal force, (c) overturning moment.

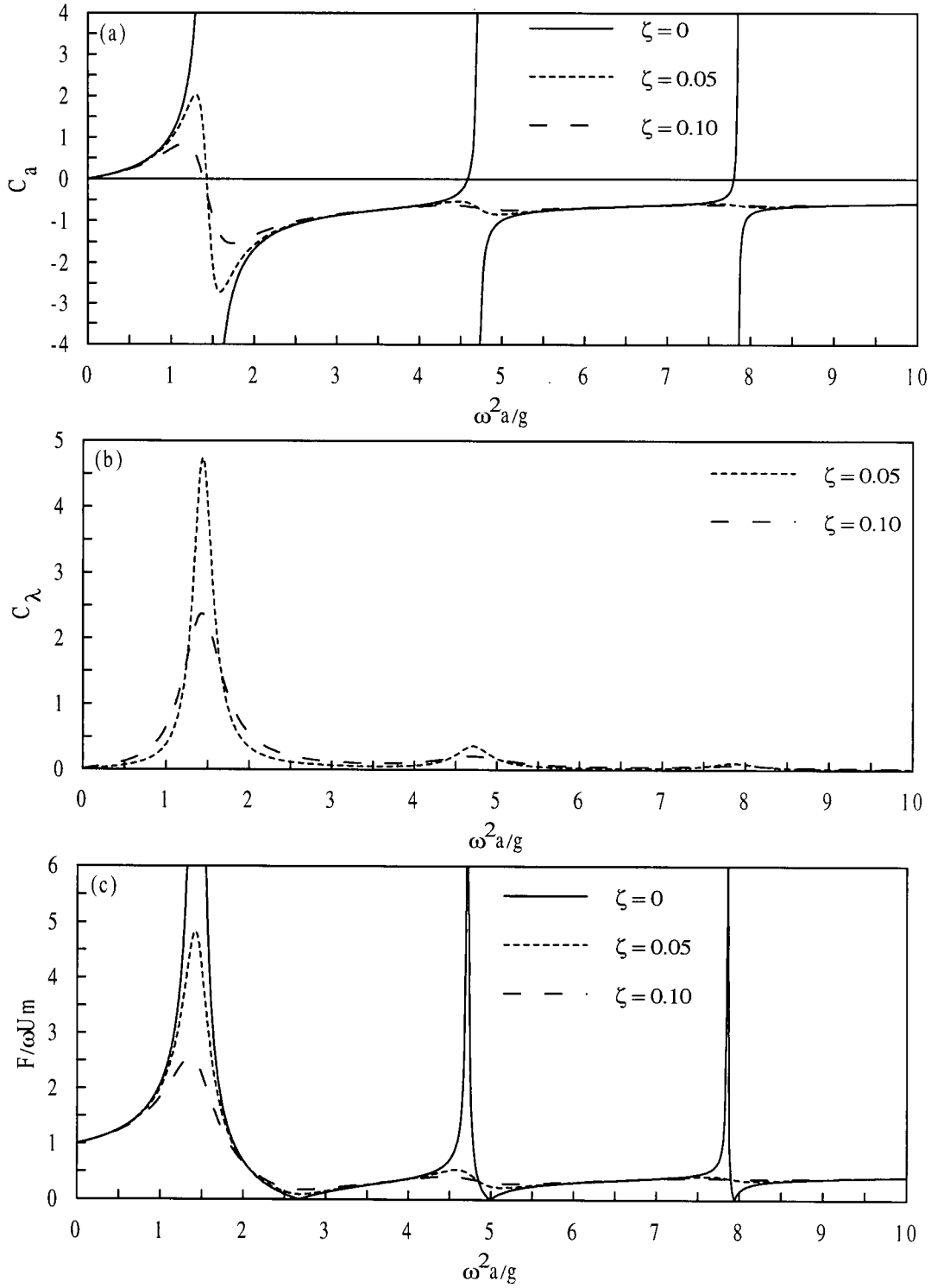


Figure 16. Dimensionless hydrodynamic coefficients as functions of $\omega^2 a/g$ for d/a = 1.0 for rectangular tank for horizontal excitation. (a) added mass, (b) damping coefficient (c) force.

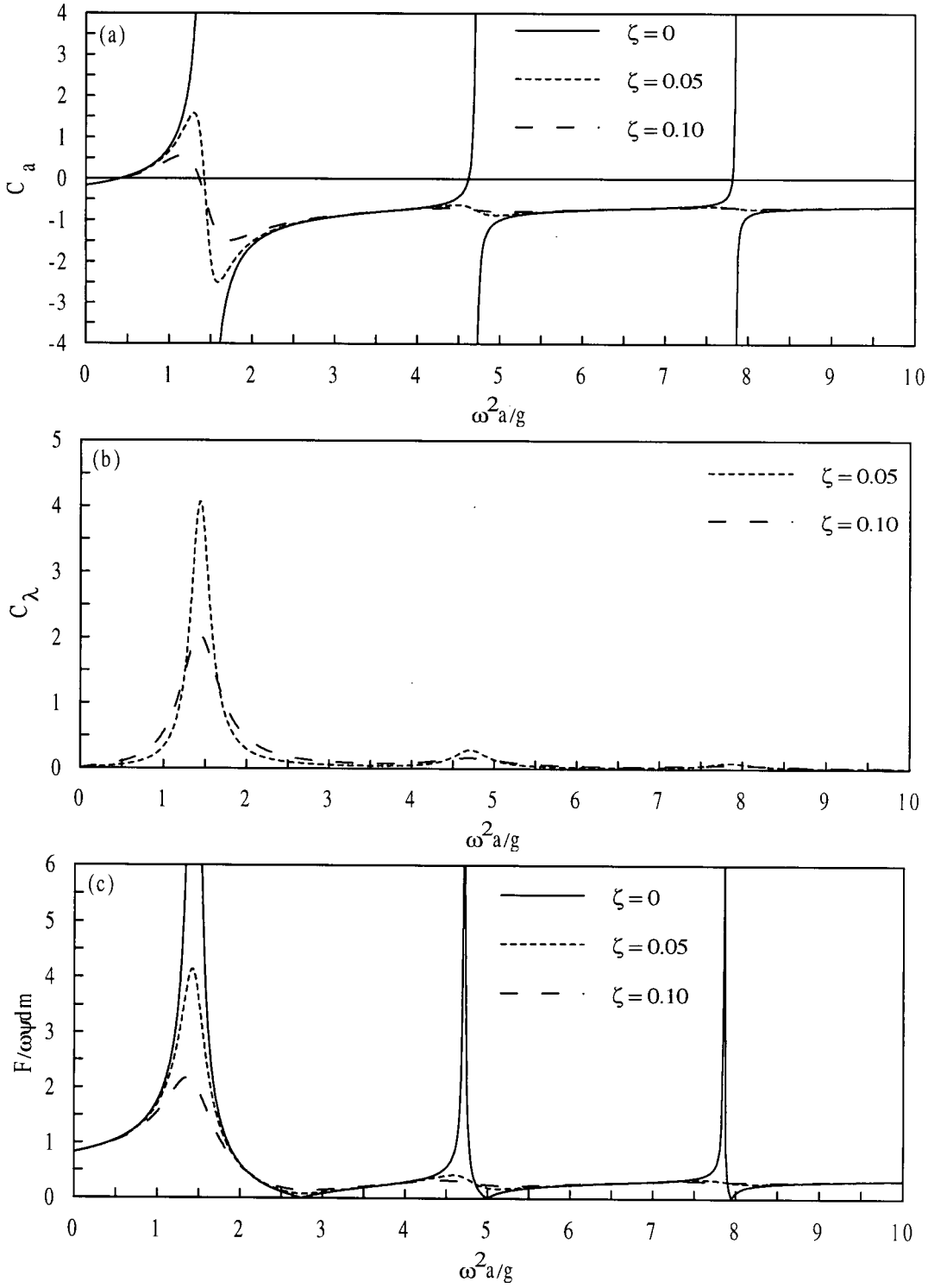


Figure 17. Dimensionless hydrodynamic coefficients as functions of $\omega^2 a/g$ for d/a = 1.0 for rectangular tank for rocking excitation. (a) added mass, (b) damping coefficient (c) force.

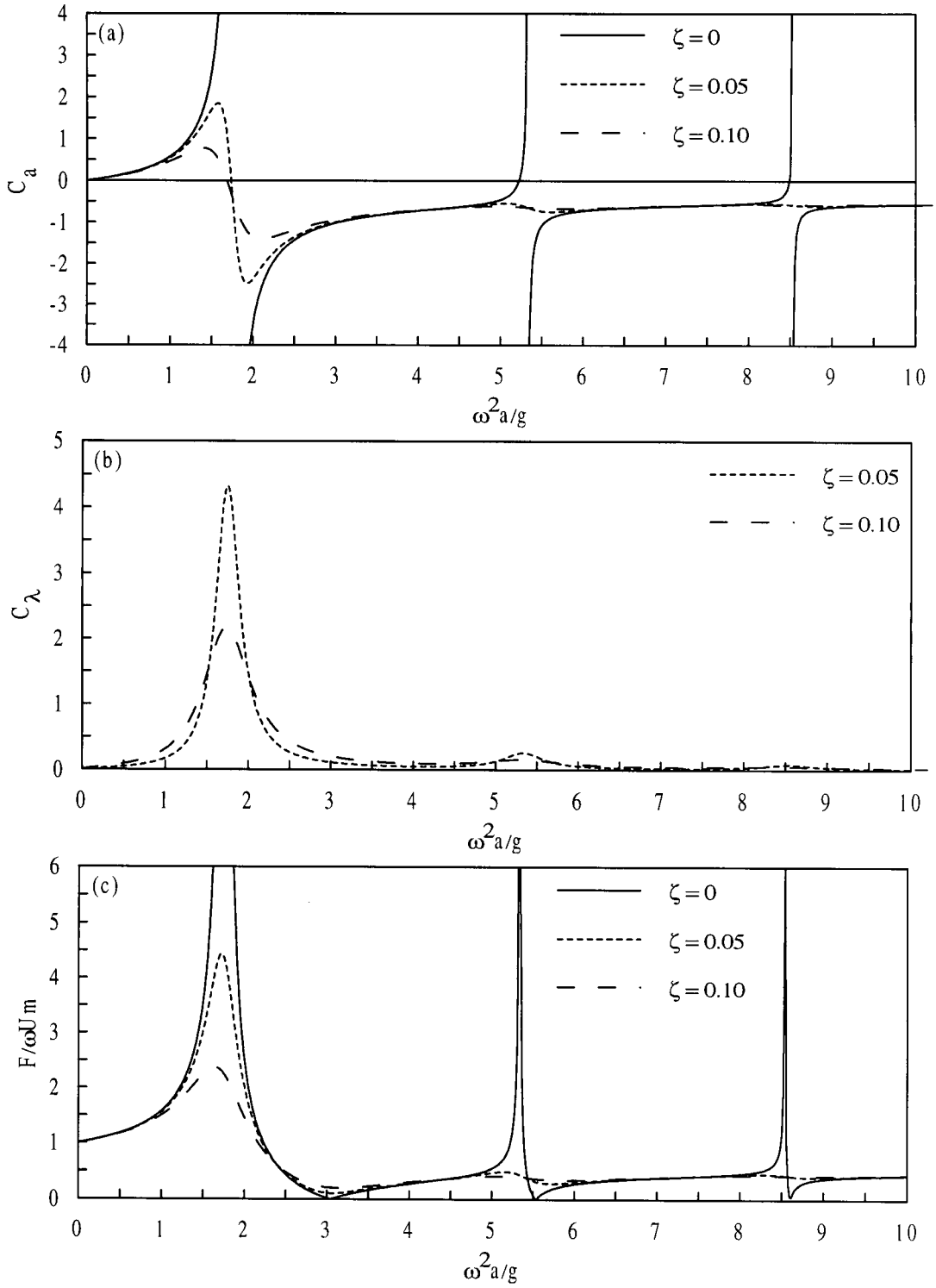


Figure 18. Dimensionless hydrodynamic coefficients as functions of $\omega^2 a/g$ for d/a = 1.0 for circular tank for horizontal excitation. (a) added mass, (b) damping coefficient (c) force.

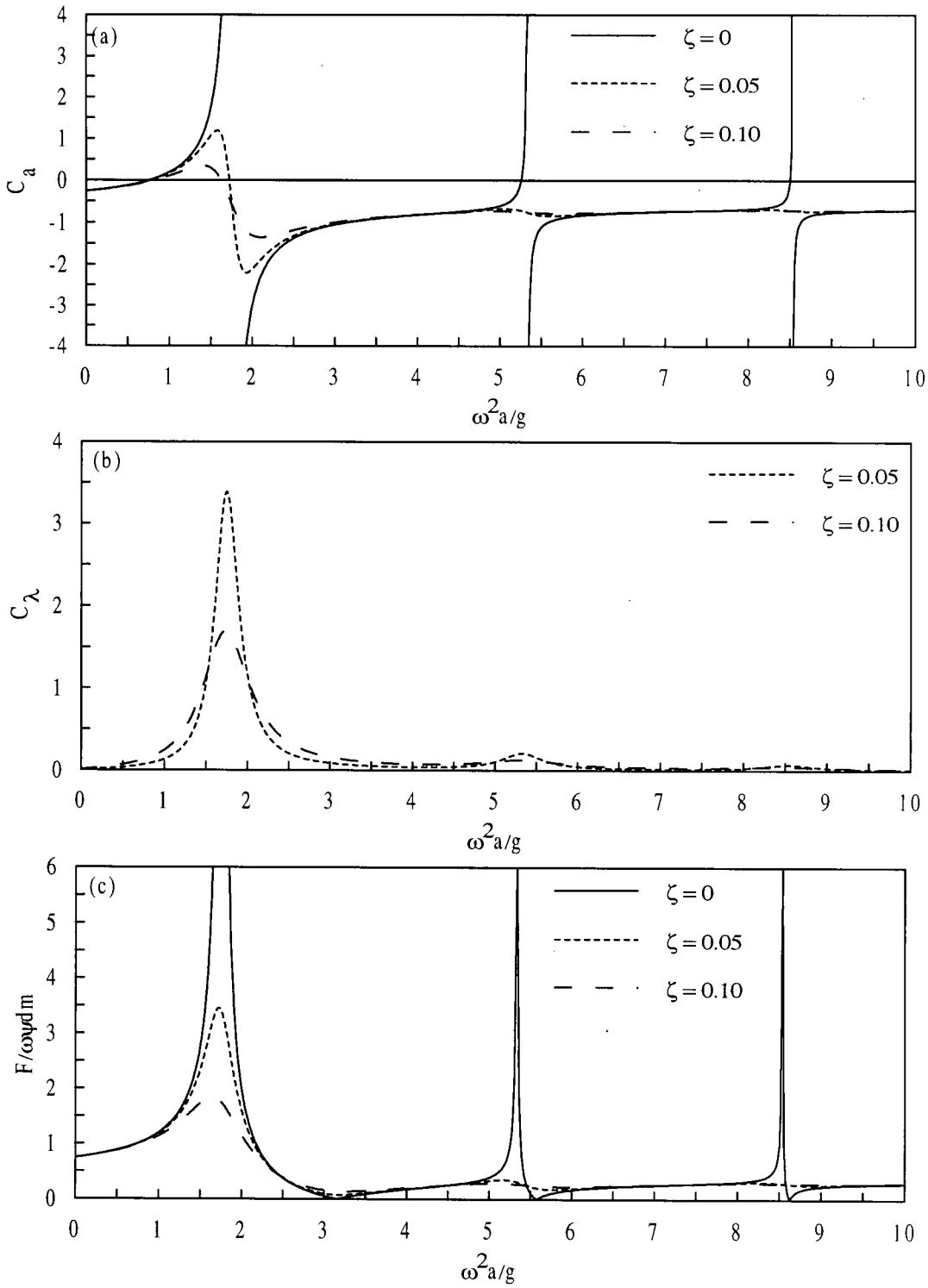


Figure 19. Dimensionless hydrodynamic coefficients as functions of $\omega^2 a/g$ for d/a = 1.0 for circular tank for rocking excitation. (a) added mass, (b) damping coefficient (c) force.

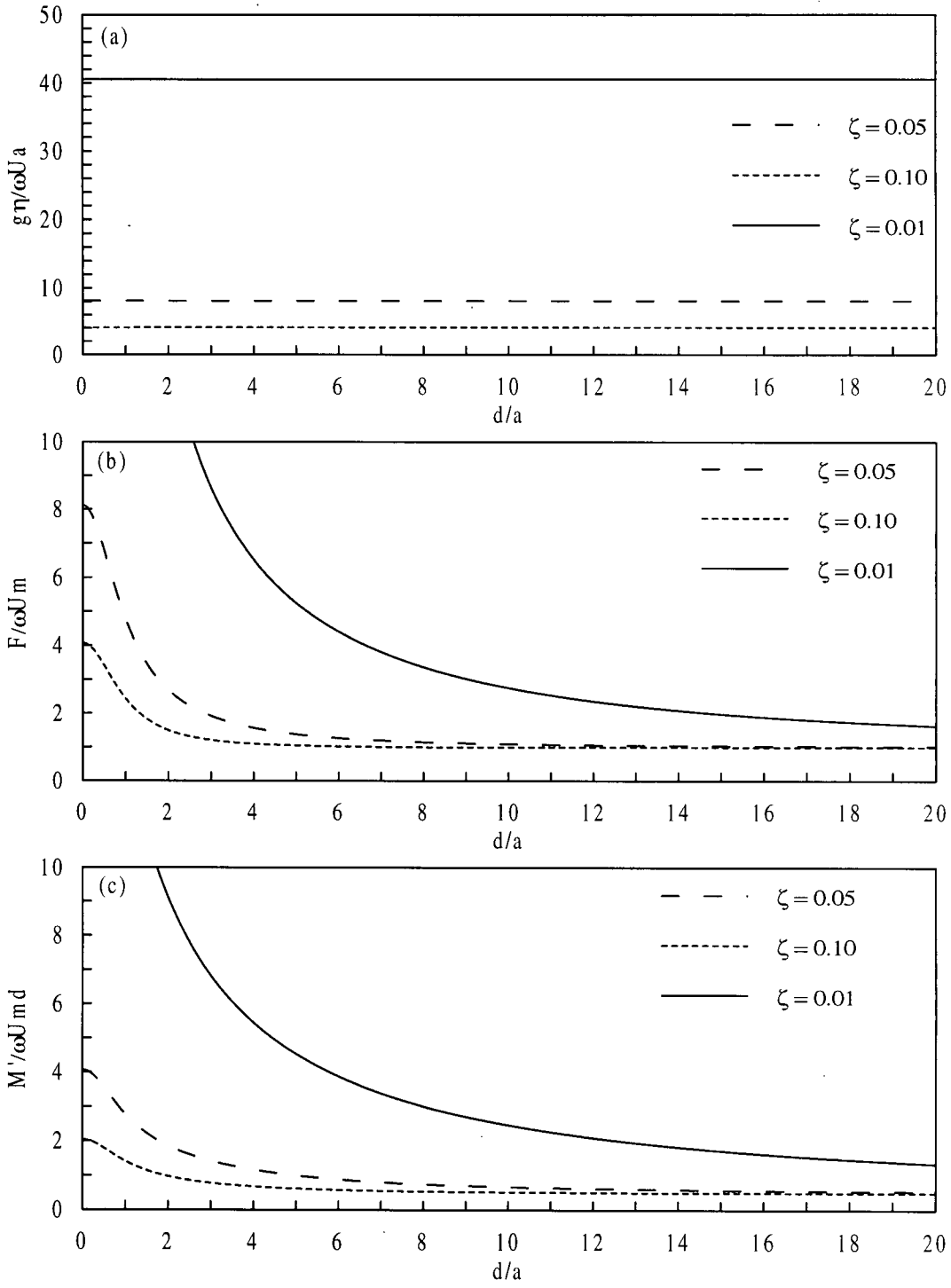


Figure 20. Variation of dimensionless hydrodynamic coefficients as functions of d/a for various values of damping ratio, for a rectangular tank with horizontal excitation. (a) free surface elevation, (b) horizontal force, (c) overturning moment.

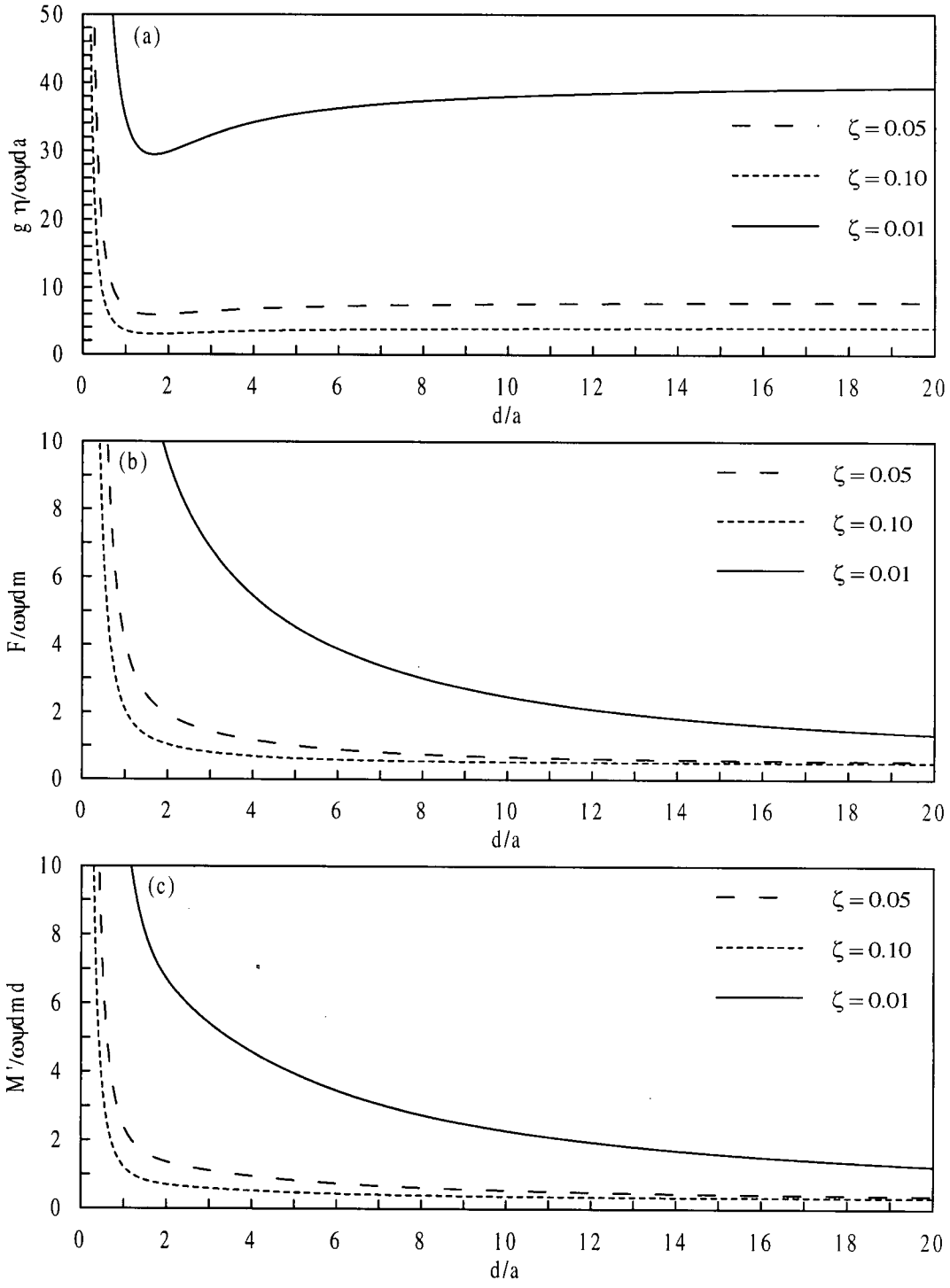


Figure 21. Variation of dimensionless hydrodynamic coefficients as functions of d/a for various values of damping ratio, for a rectangular tank with rocking excitation. (a) free surface elevation, (b) horizontal force, (c) overturning moment.

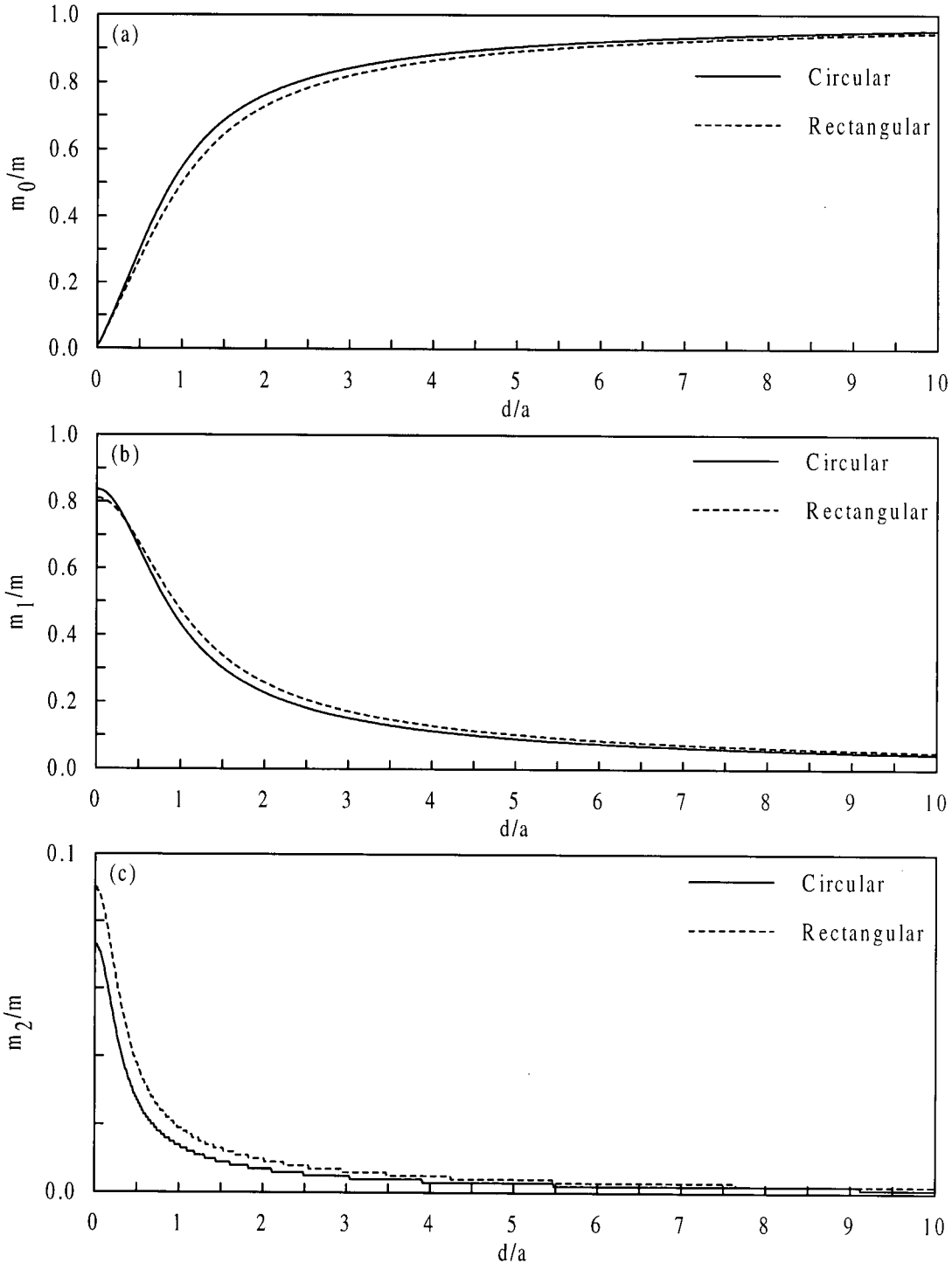


Figure 22. Comparison of hydrodynamic masses as functions of d/a for rectangular and a circular tanks for horizontal excitation. (a) high frequency mass, (b) first mode sloshing mass, (c) second mode sloshing mass.

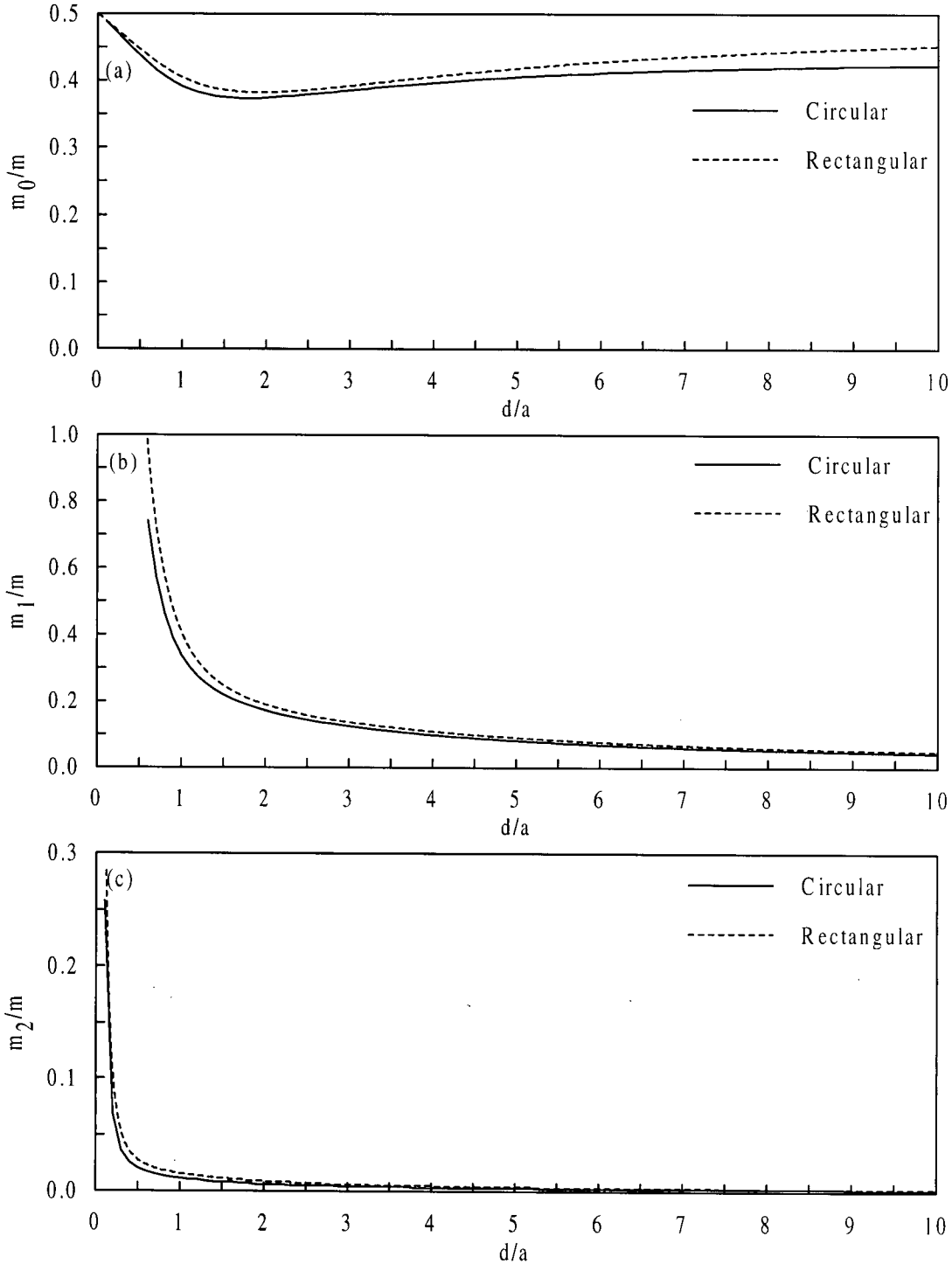


Figure 23. Comparison of hydrodynamic masses as function of d/a for rectangular and circular tanks for rocking excitation. (a) high frequency mass, (b) first mode sloshing mass, (c) second mode sloshing mass.

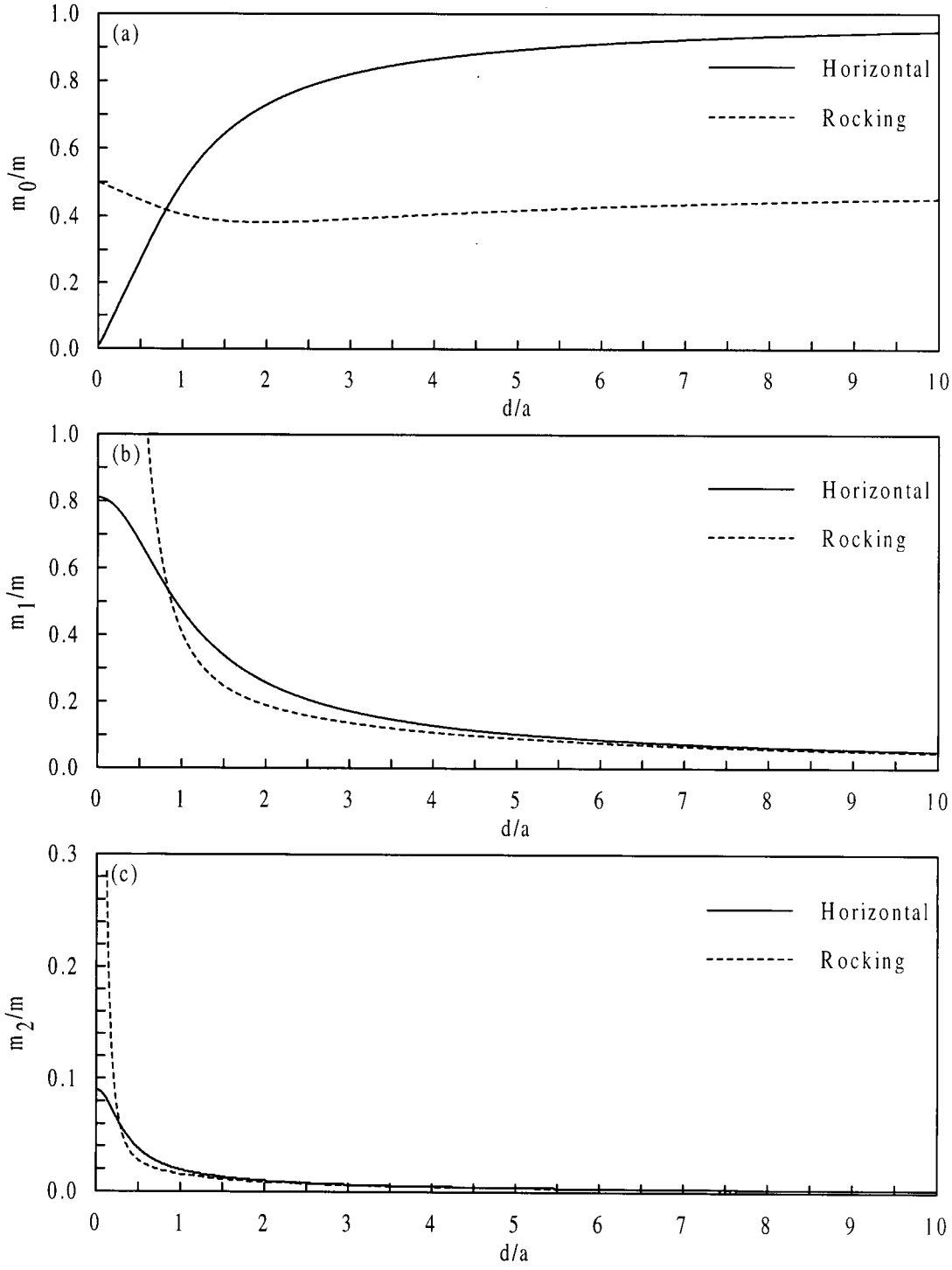


Figure 24. Comparison of hydrodynamic masses as functions of d/a for horizontal and rocking excitations for a rectangular tank. (a) high frequency mass, (b) first mode sloshing mass, (c) second mode sloshing mass.

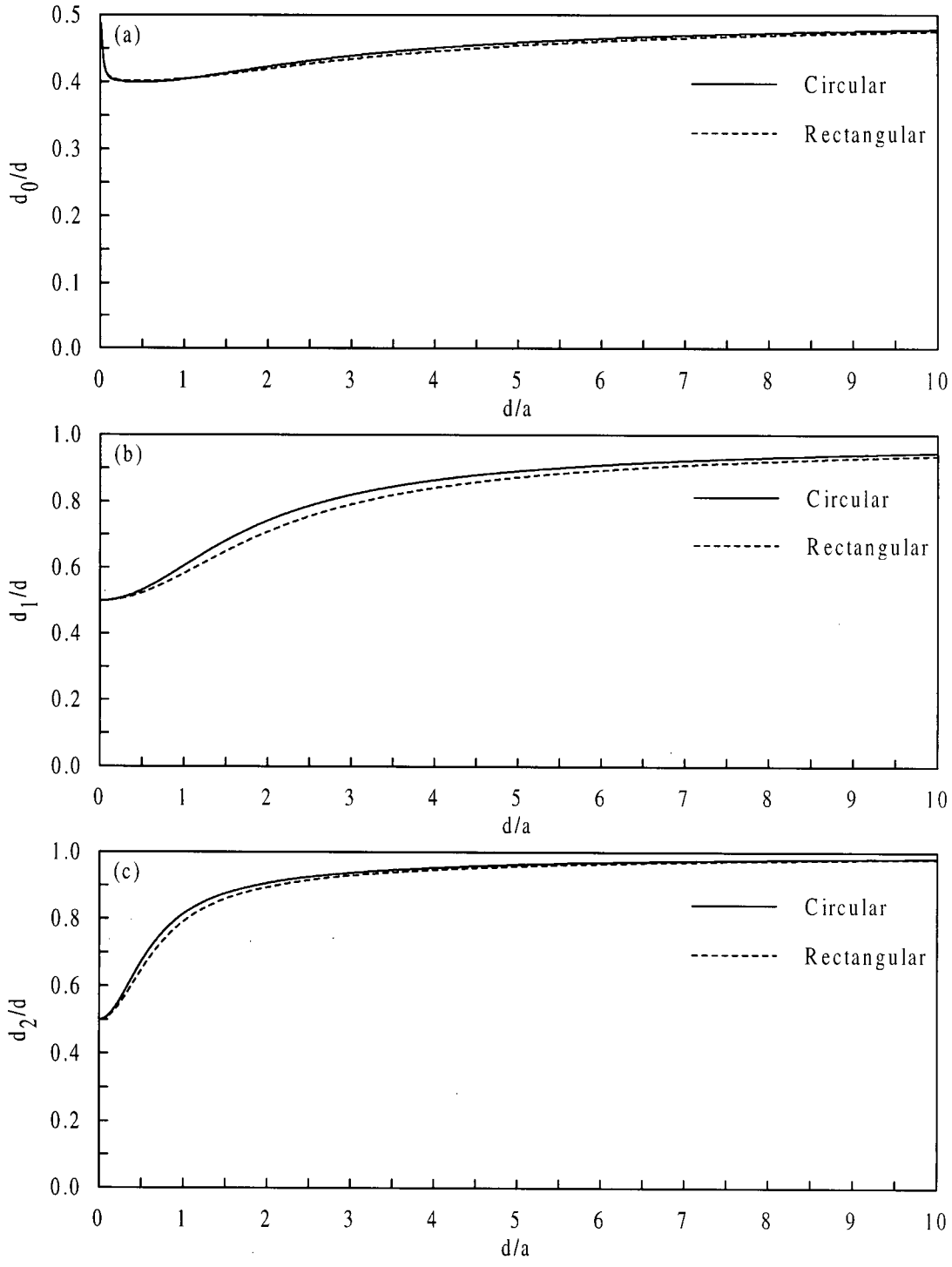


Figure 25. Comparison of effective elevations as functions of d/a for rectangular and circular tanks for horizontal excitation.

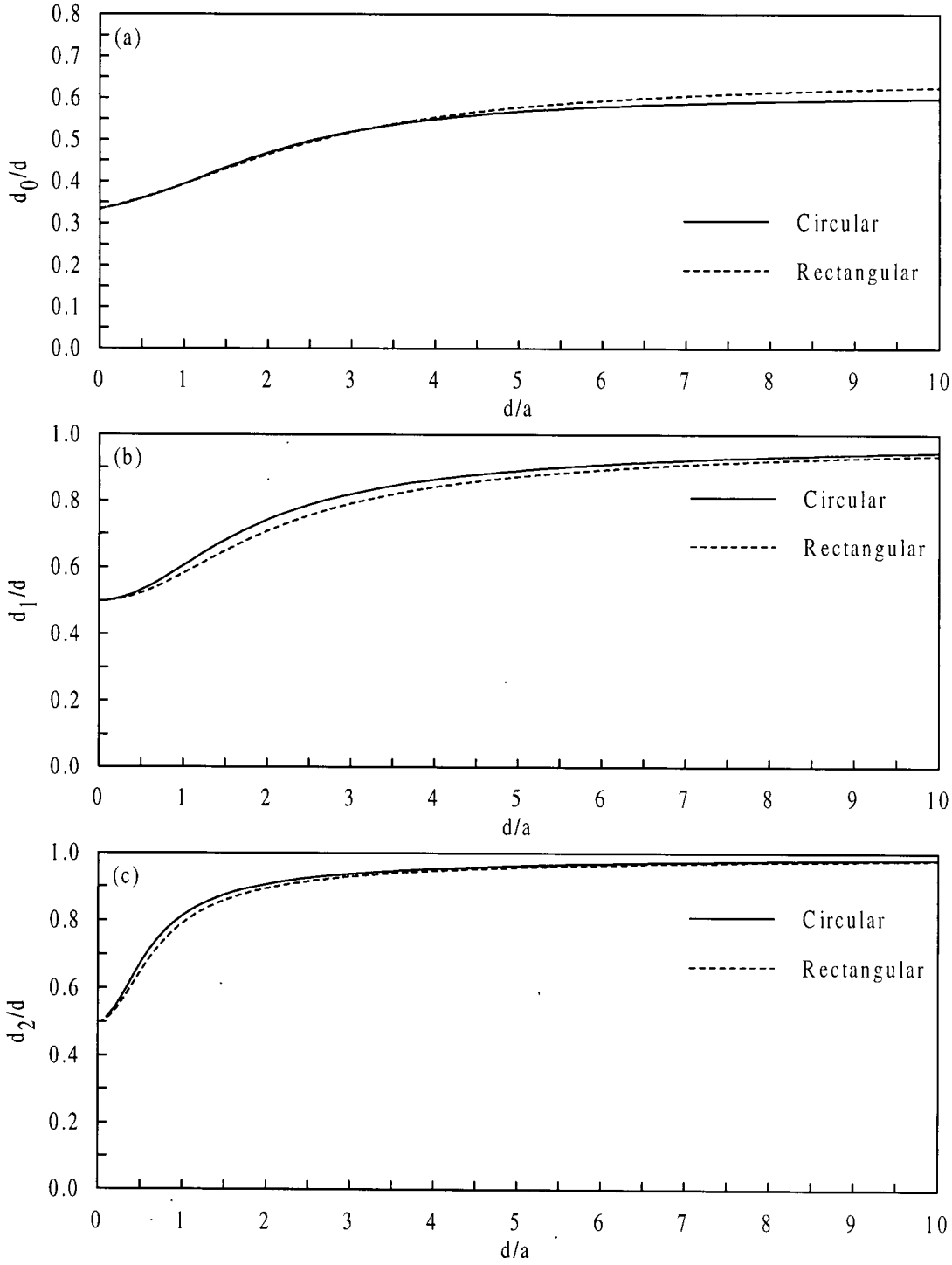


Figure 26. Comparison of effective elevations as function of d/a for rectangular and circular tanks for rocking excitation.

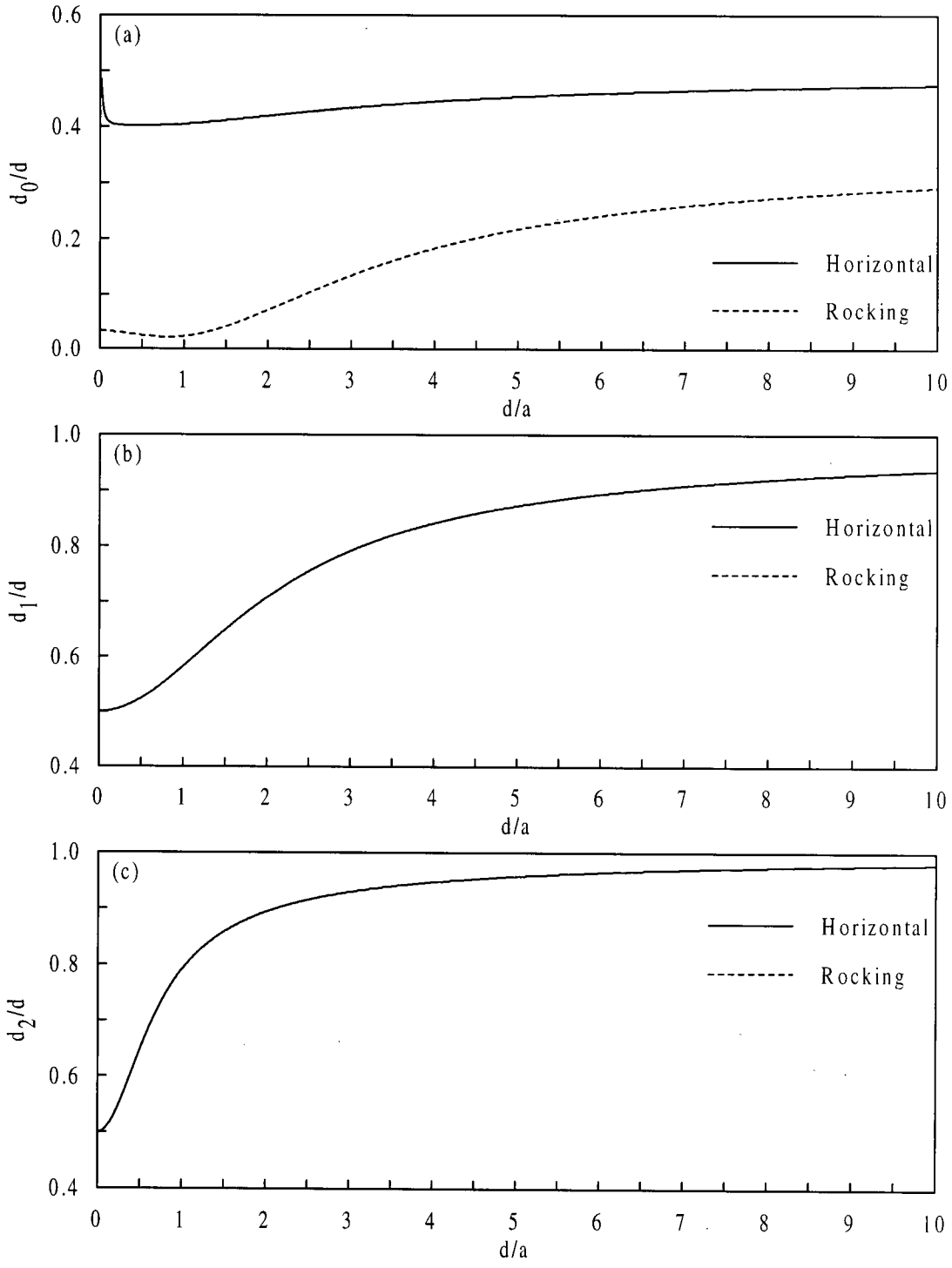


Figure 27. Comparison of effective elevations as functions of d/a for horizontal and rocking excitations for a rectangular tanks.

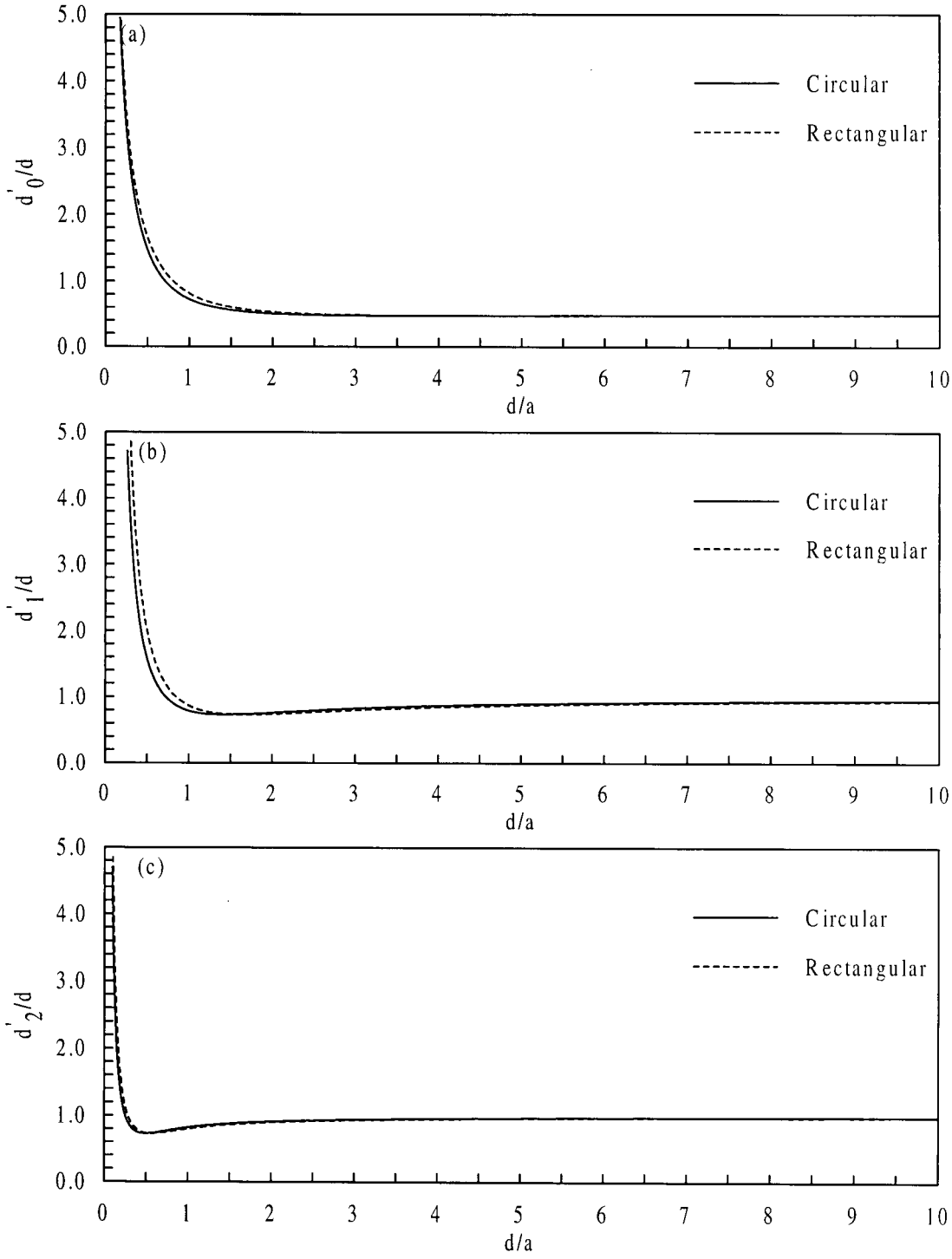


Figure 28. Comparison of effective elevations as functions of d/a for rectangular and circular tanks for horizontal excitation.

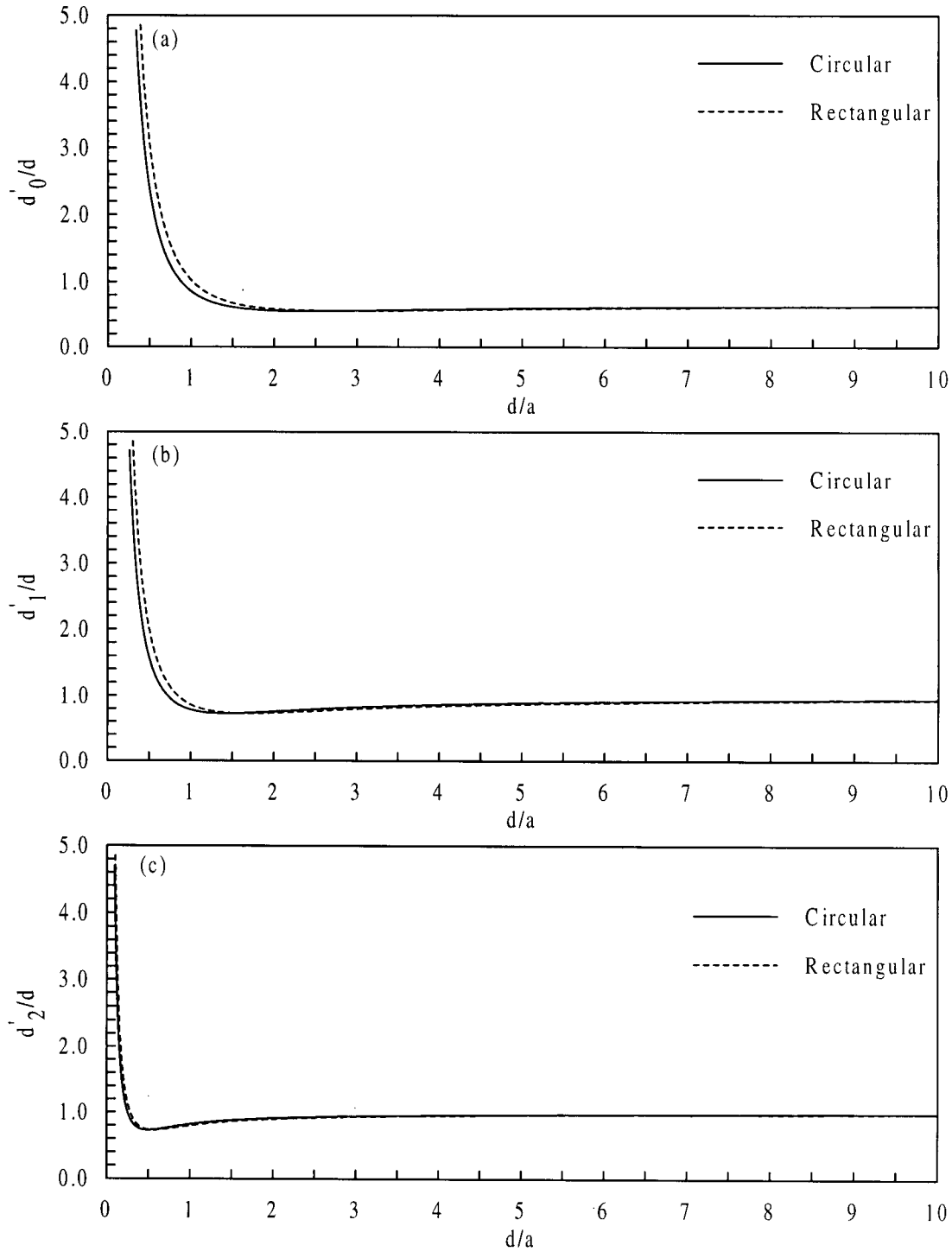


Figure 29. Comparison of effective elevations as functions of d/a for rectangular and circular tanks for rocking excitation.

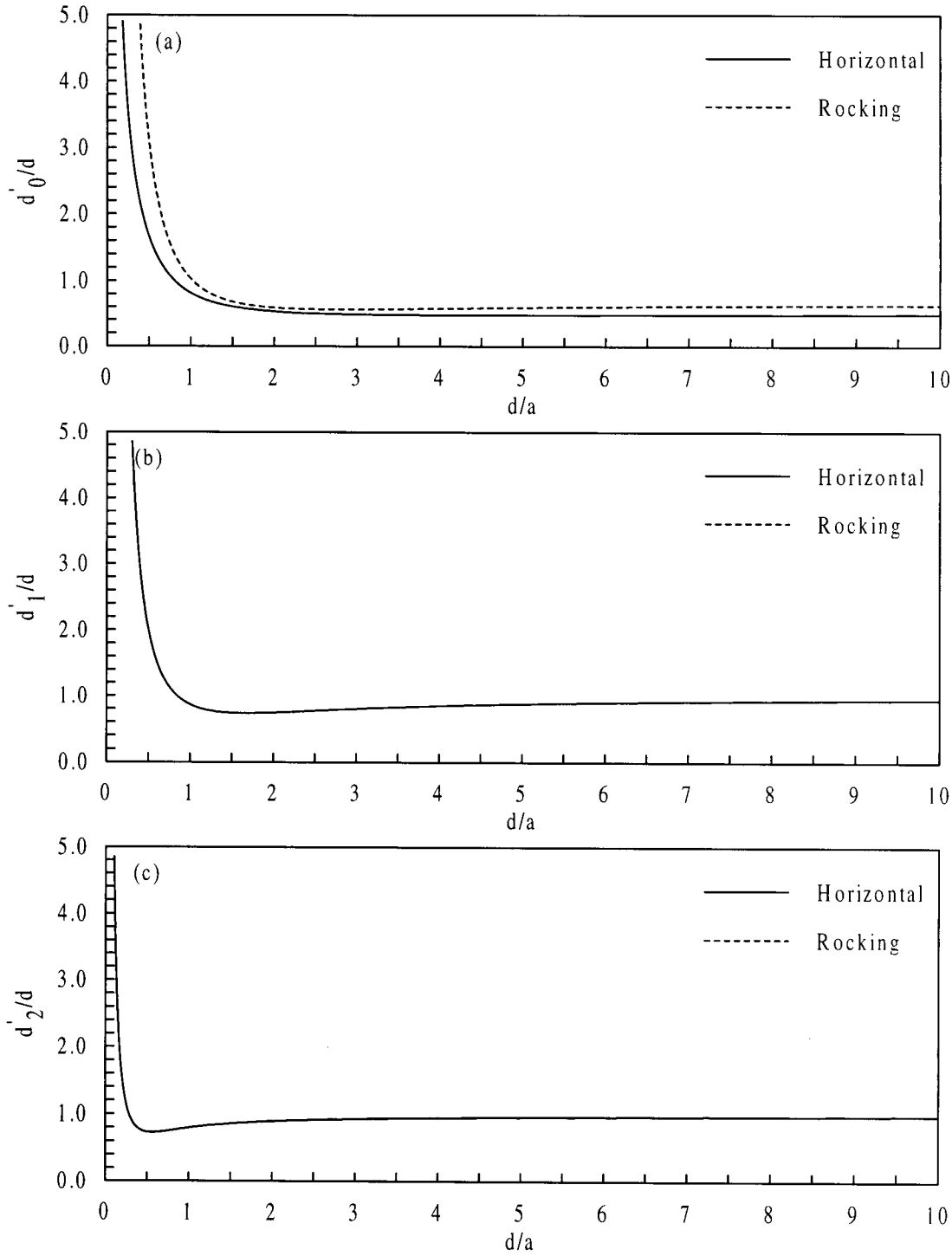


Figure 30. Comparison of effective elevations as functions of d/a for horizontal and rocking excitations for rectangular tank.

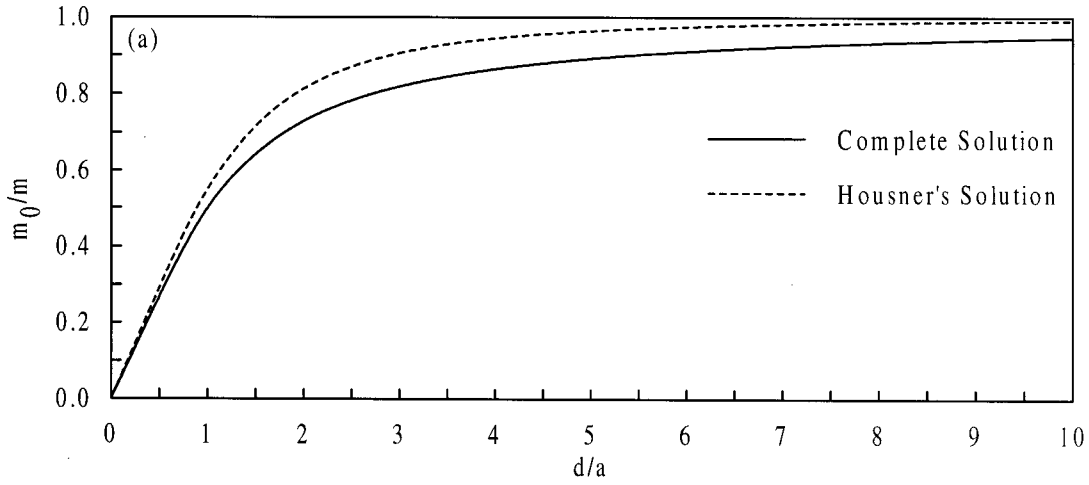


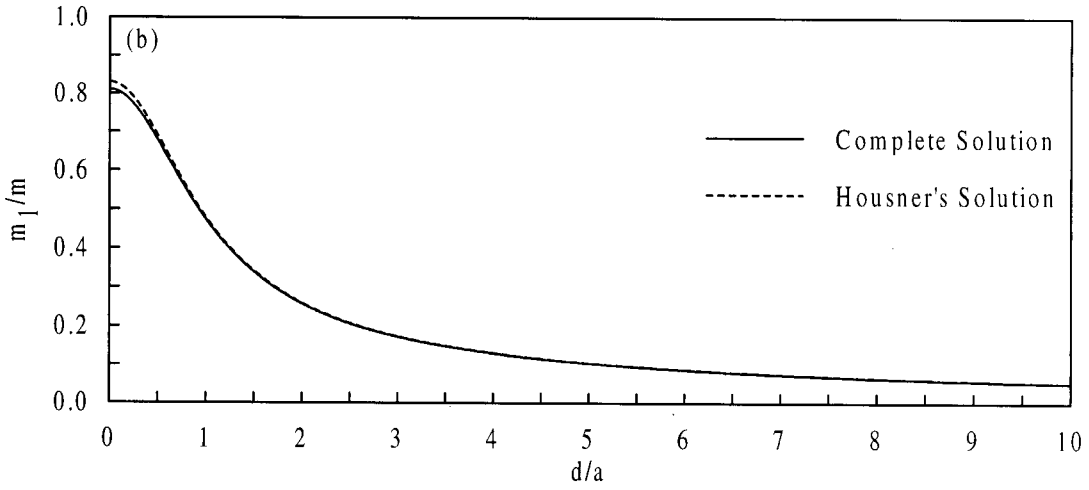


Figure 31. Comparison of Housner's solution and complete solution for hydrodynamic masses as function of d/a for horizontal excitation for a rectangular tank. (a) high frequency mass, (b) first mode sloshing mass.

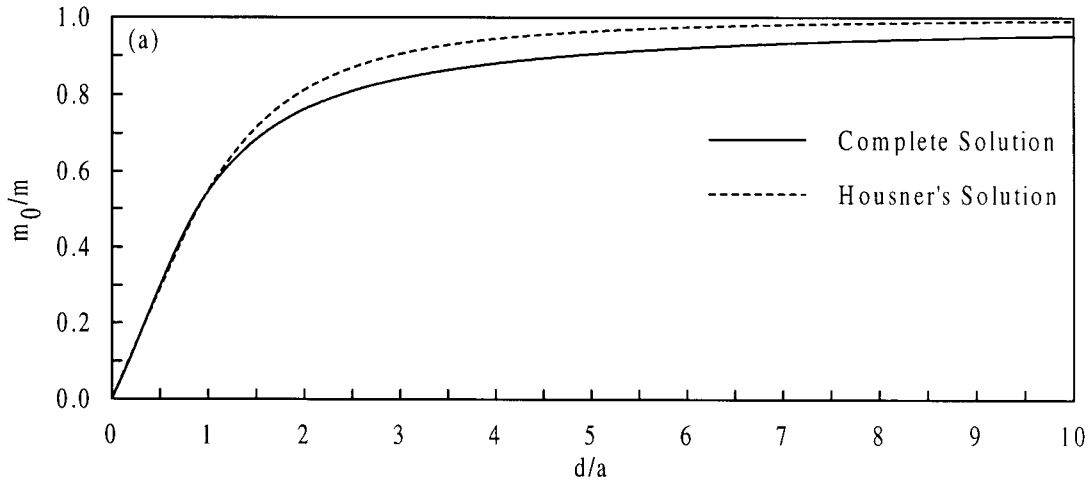


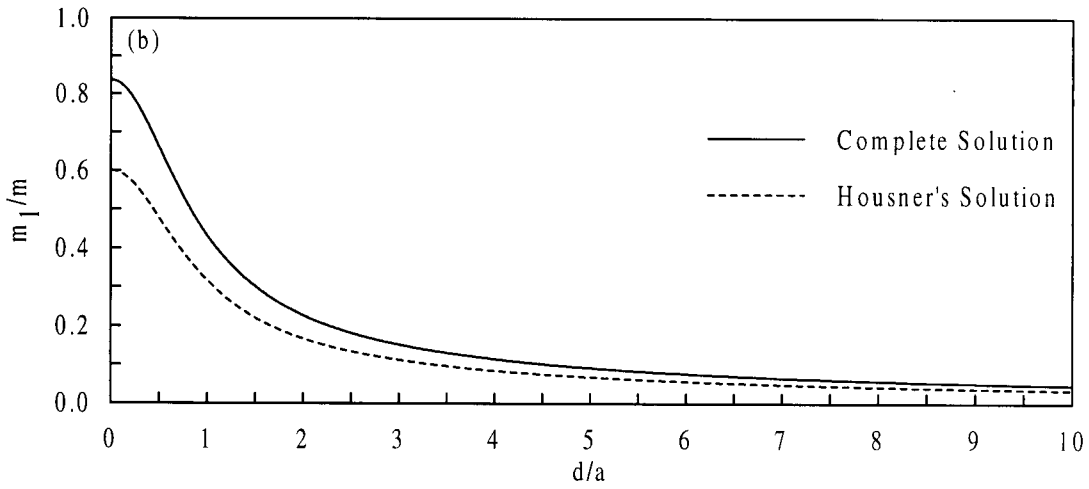


Figure 32. Comparison of Housner's solution and complete solution for hydrodynamic masses as functions of d/a for horizontal excitation for a circular tank. (a) high frequency mass, (b) first mode sloshing mass.

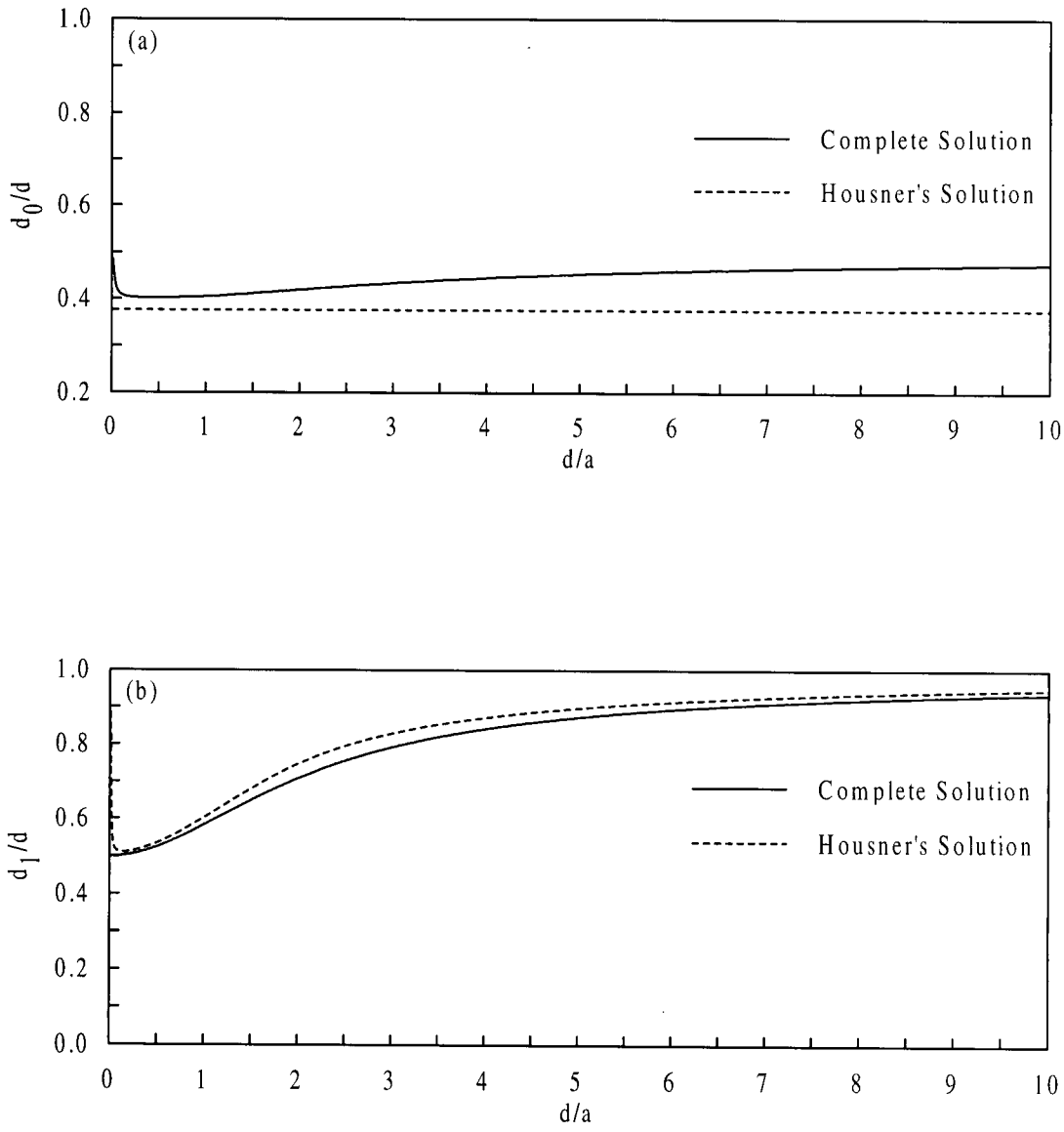


Figure 33. Comparison of Housner's solution and complete solution for effective elevation as functions of d/a for horizontal excitation for a rectangular tank.

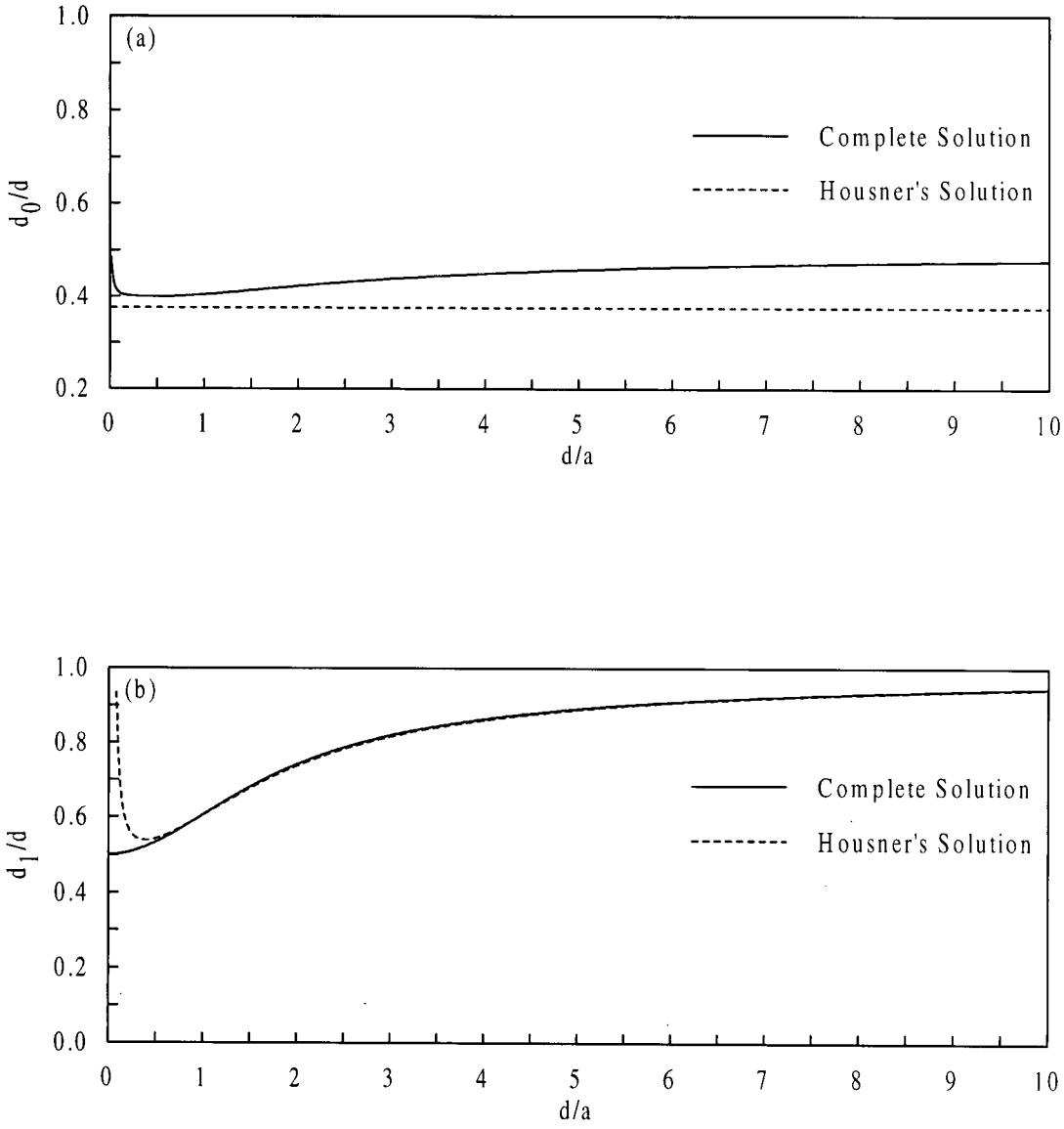


Figure 34. Comparison of Housner's solution and complete solution for effective elevation as functions of d/a for horizontal excitation for a circular tank.

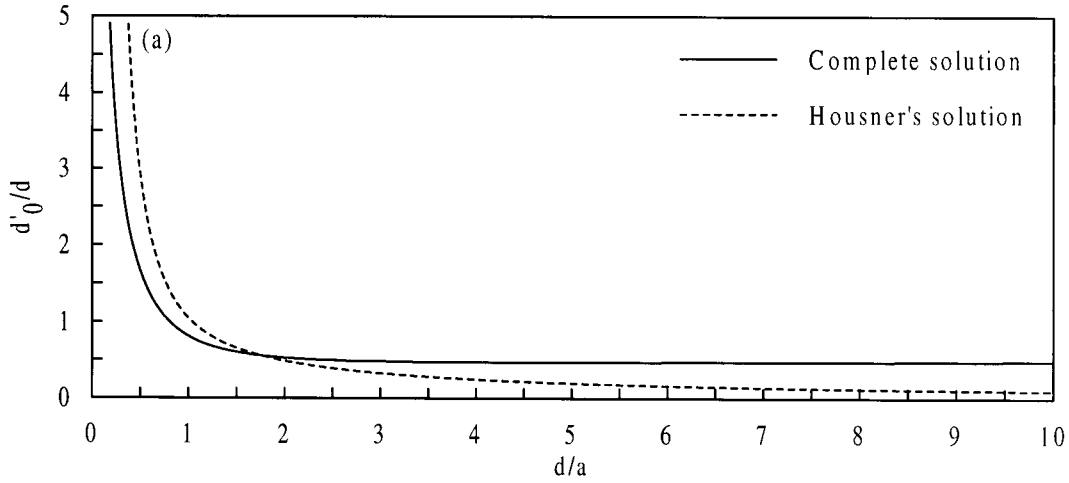


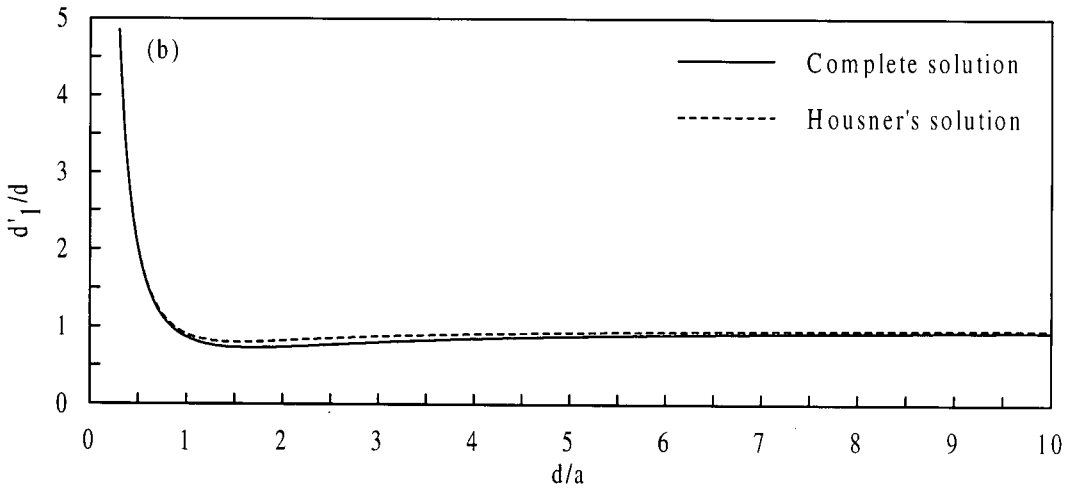


Figure 35. Comparison of Housner's solution and complete solution for effective elevation as functions of d/a for horizontal excitation for a rectangular tank.

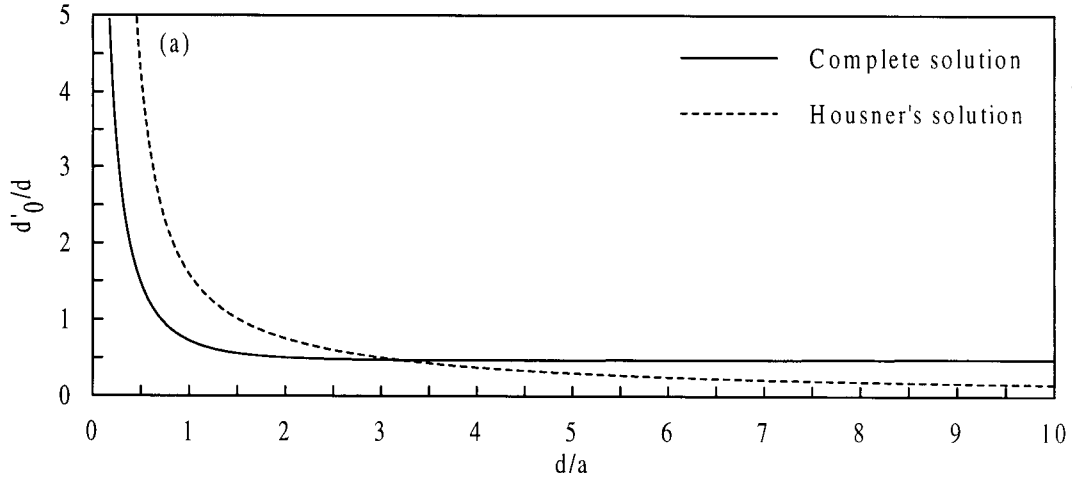


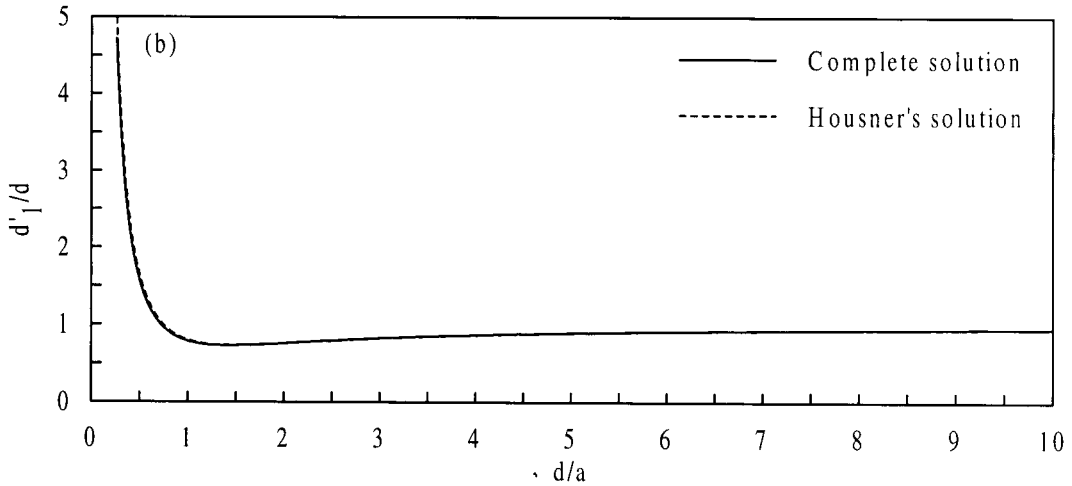


Figure 36. Comparison of Housner's solution and complete solution for effective elevation as functions of d/a for horizontal excitation for a circular tank.

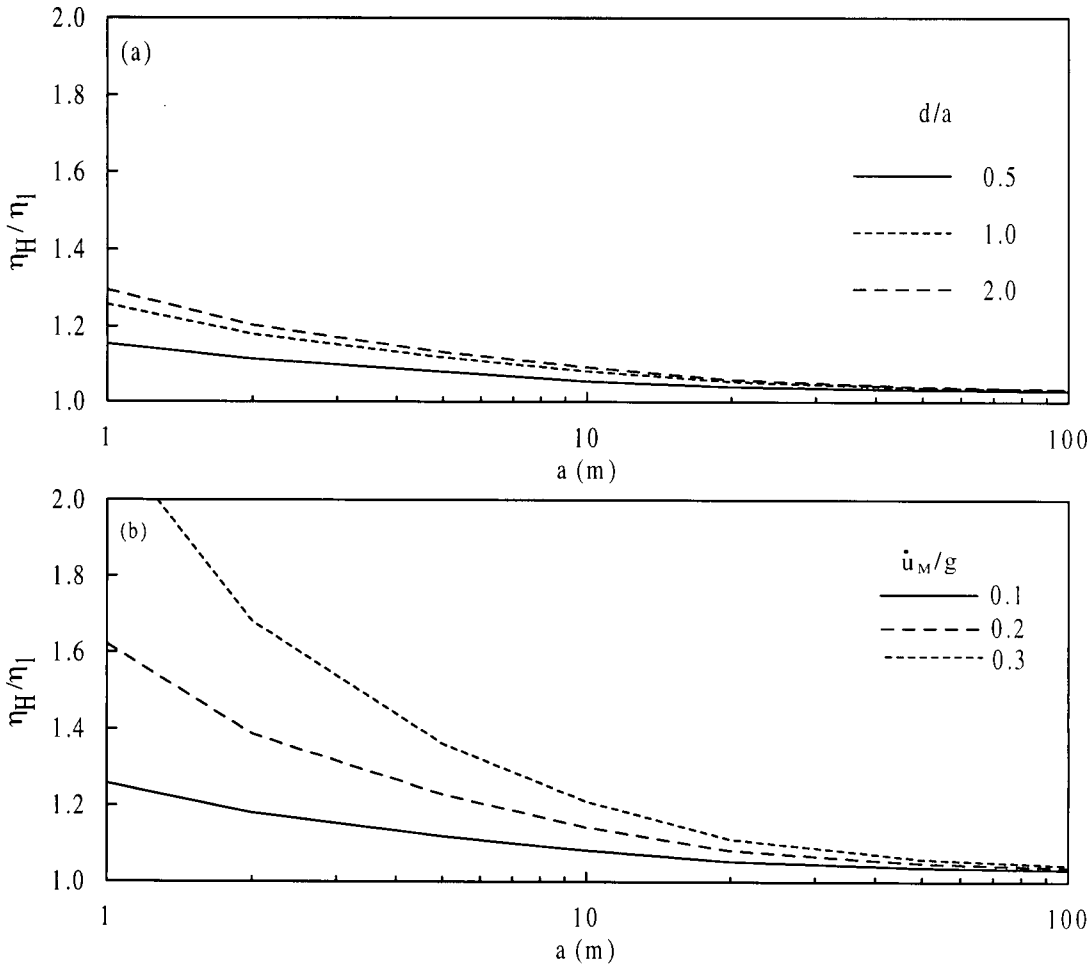


Figure 37. Comparison of elevations based on Housner's solution and the closed-form solution for first mode sloshing. (a) $\dot{u}_M/g=0.1$ and various d/a values; (b) d/a = 1.0 and various $\dot{u}_M/g$ values.

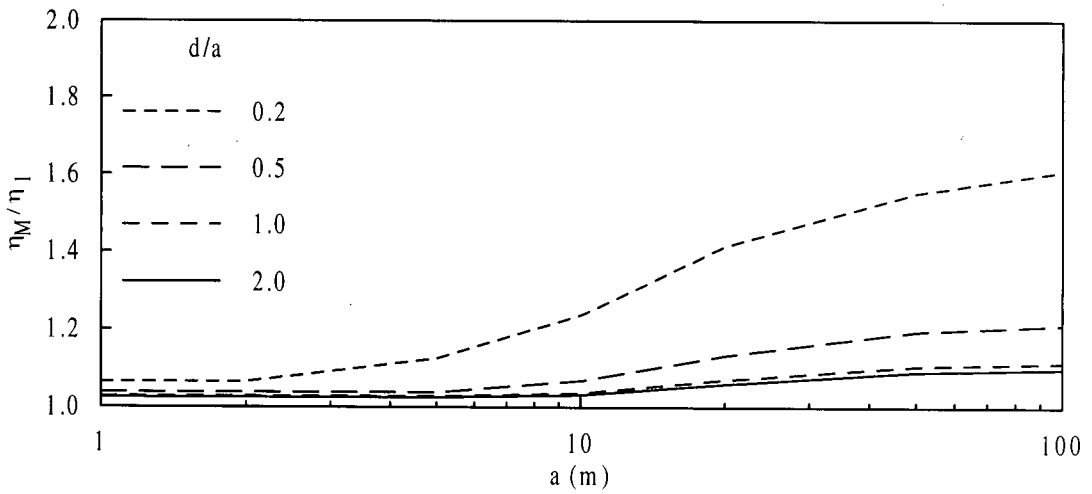


Figure 38. Comparison of elevations based on the complete closed-form solution and the first mode solution for $\dot{u}_M/g=0.1$ and various d/a values.

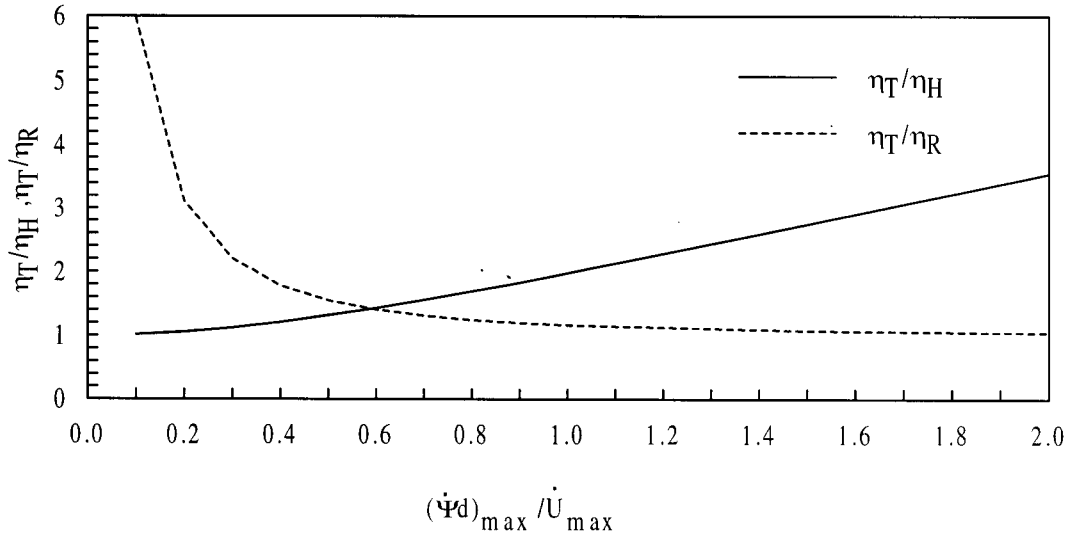


Figure 39. Variation of $\eta_T/\eta_H$ and $\eta_T/\eta_R$ with relative rocking parameter $(\dot{\Psi}d)_{max}/\dot{U}_{max}$ for d/a = 0.5 and a = 100 m.

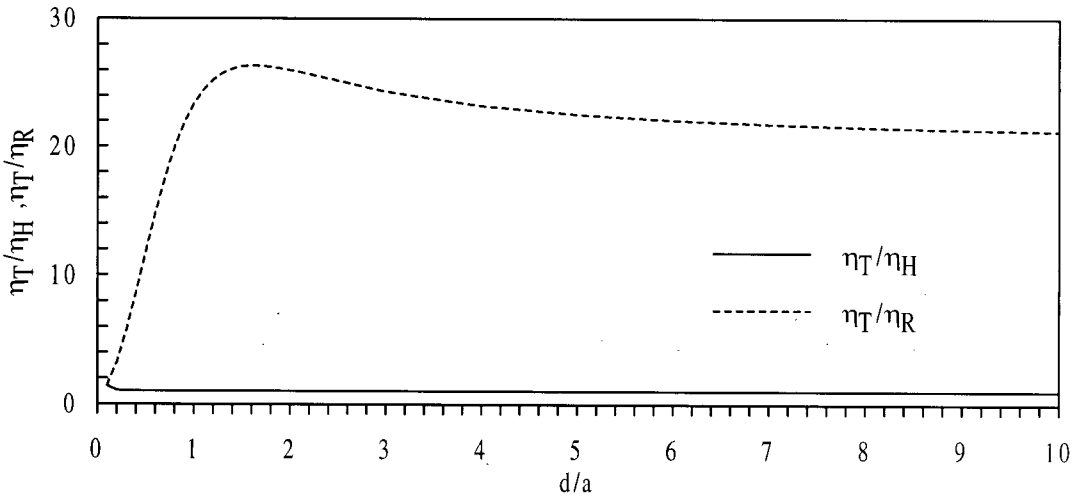


Figure 40. Variation of $\eta_T/\eta_H$ and $\eta_T/\eta_R$ with d/a for a relative rocking parameter $(\dot{\Psi}d)_{max}/\dot{U}_{max}$ =0.1 and a = 100 m.

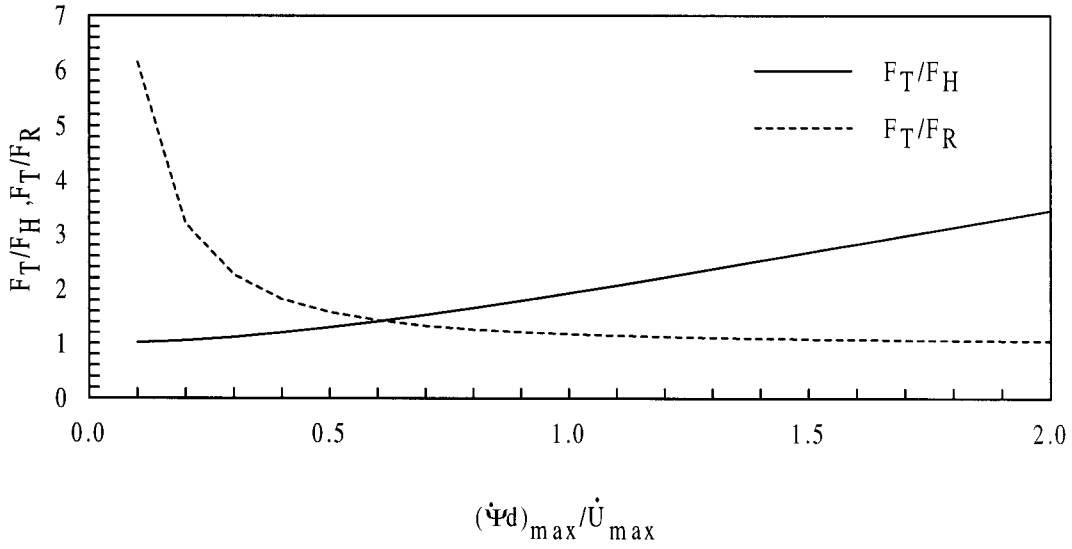


Figure 41. Variation of $F_T/F_H$ and $F_T/F_R$ with relative rocking parameter $(\dot{\Psi}d)_{max}/\dot{U}_{max}$ for d/a = 0.5 and a = 100 m.

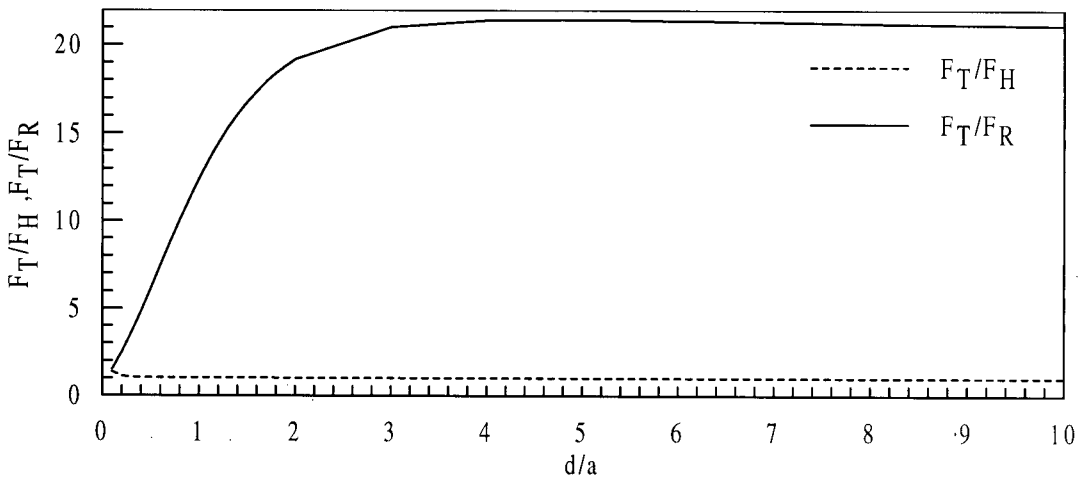


Figure 42. Variation of $F_T/F_H$ and $F_T/F_R$ with d/a for a relative rocking parameter $(\dot{\Psi}d)_{max}/\dot{U}_{max}$ =0.1 and a = 100 m.

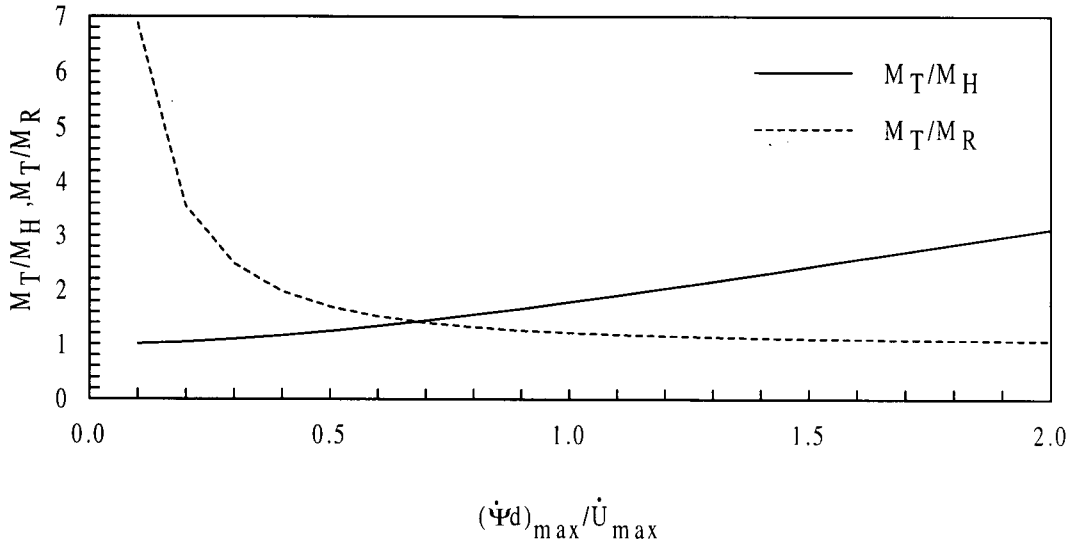


Figure 43. Variation of $M_T/M_H$ and $M_T/M_R$ with relative rocking parameter $(\dot{\Psi}d)_{max}/\dot{U}_{max}$ for d/a = 0.5 and a = 100 m.

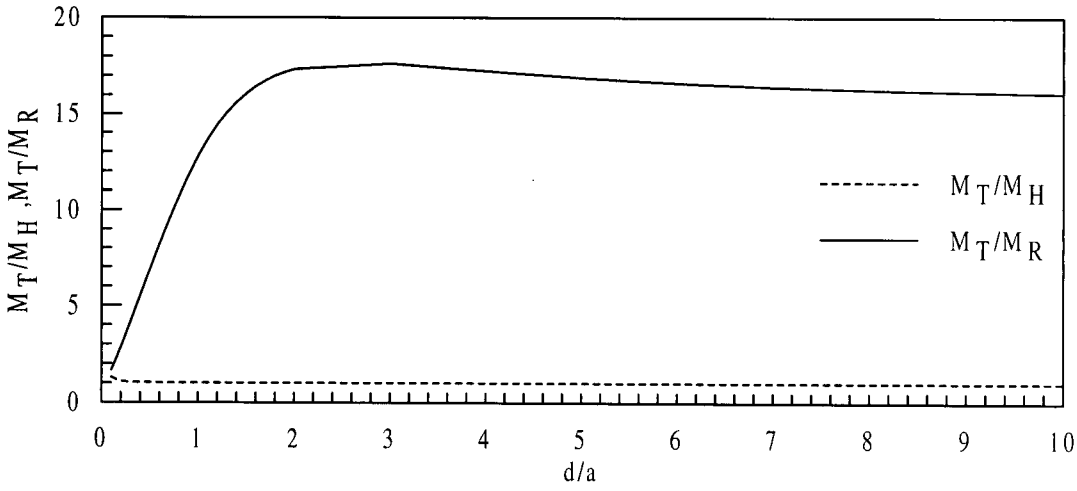


Figure 44. Variation of $M_T/M_H$ and $M_T/M_R$ with d/a for a relative rocking parameter $(\dot{\Psi}d)_{max}/\dot{U}_{max}$ =0.1 and a = 100 m.

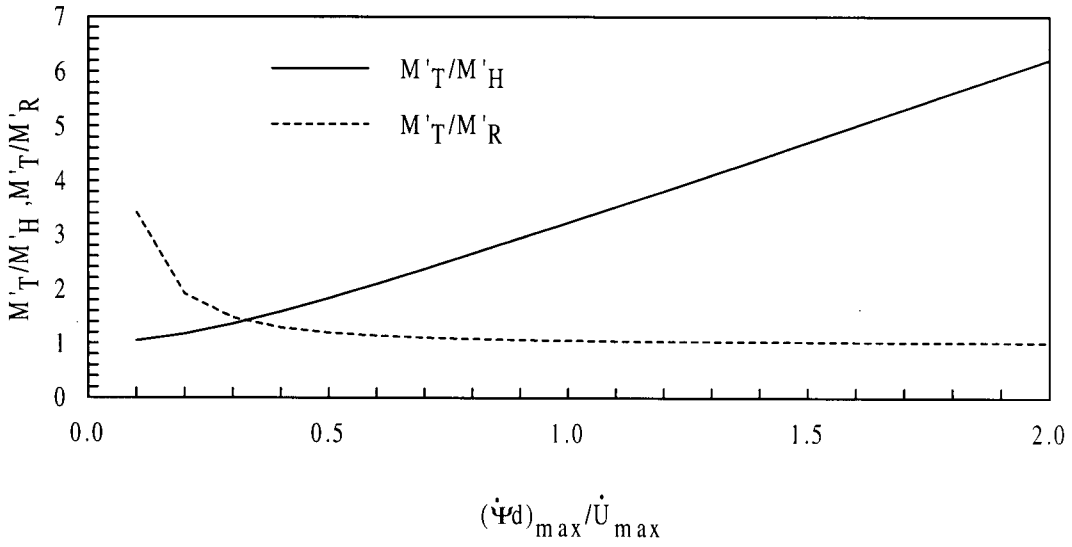


Figure 45. Variation of $M'_T/M'_H$ and $M'_T/M'_R$ with relative rocking parameter $(\dot{\Psi}d)_{max}/\dot{U}_{max}$ for d/a = 0.5 and a = 100 m.

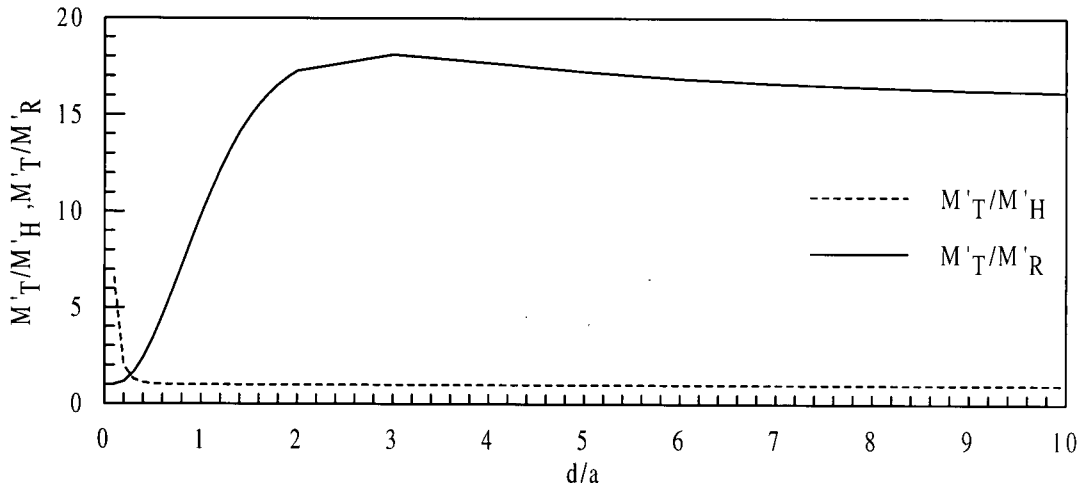


Figure 46. Variation of $M'_T/M'_H$ and $M'_T/M'_R$ with d/a for a relative rocking parameter $(\dot{\Psi}d)_{max}/\dot{U}_{max}$ =0.1 and a = 100 m.

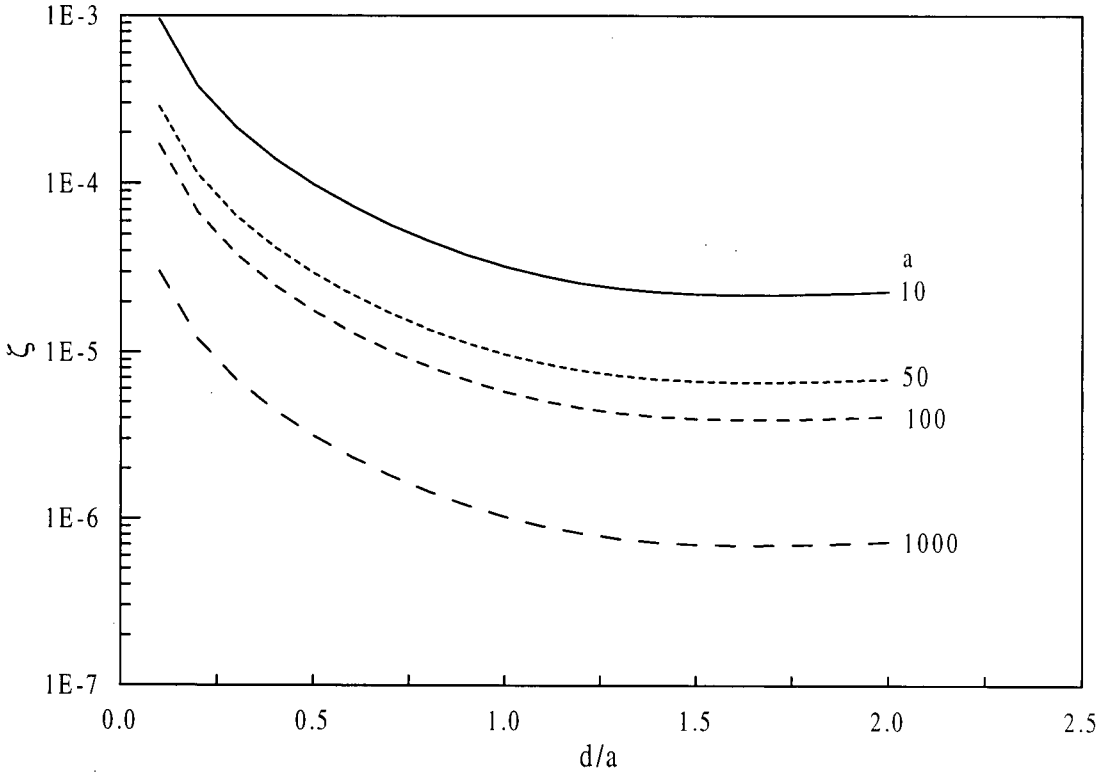


Figure 47. Variation of laminar damping for different values of a and for b/a = ∞

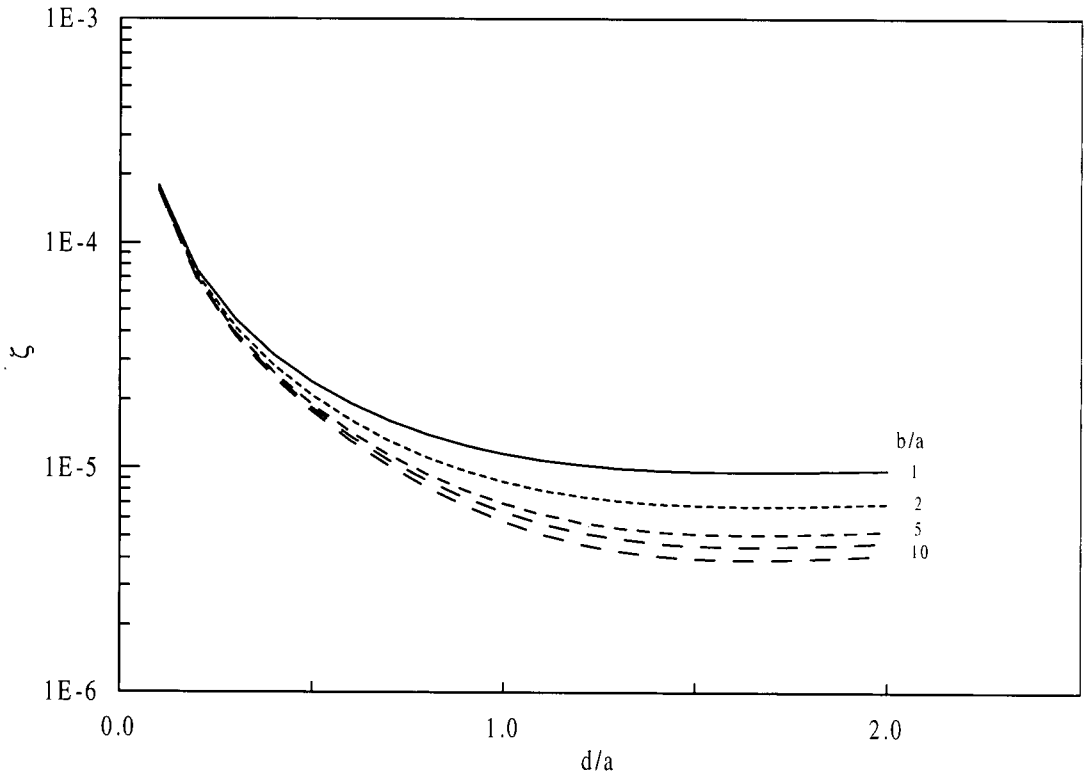


Figure 48. Variation of laminar damping for different values of b/a and for a = 100 m.

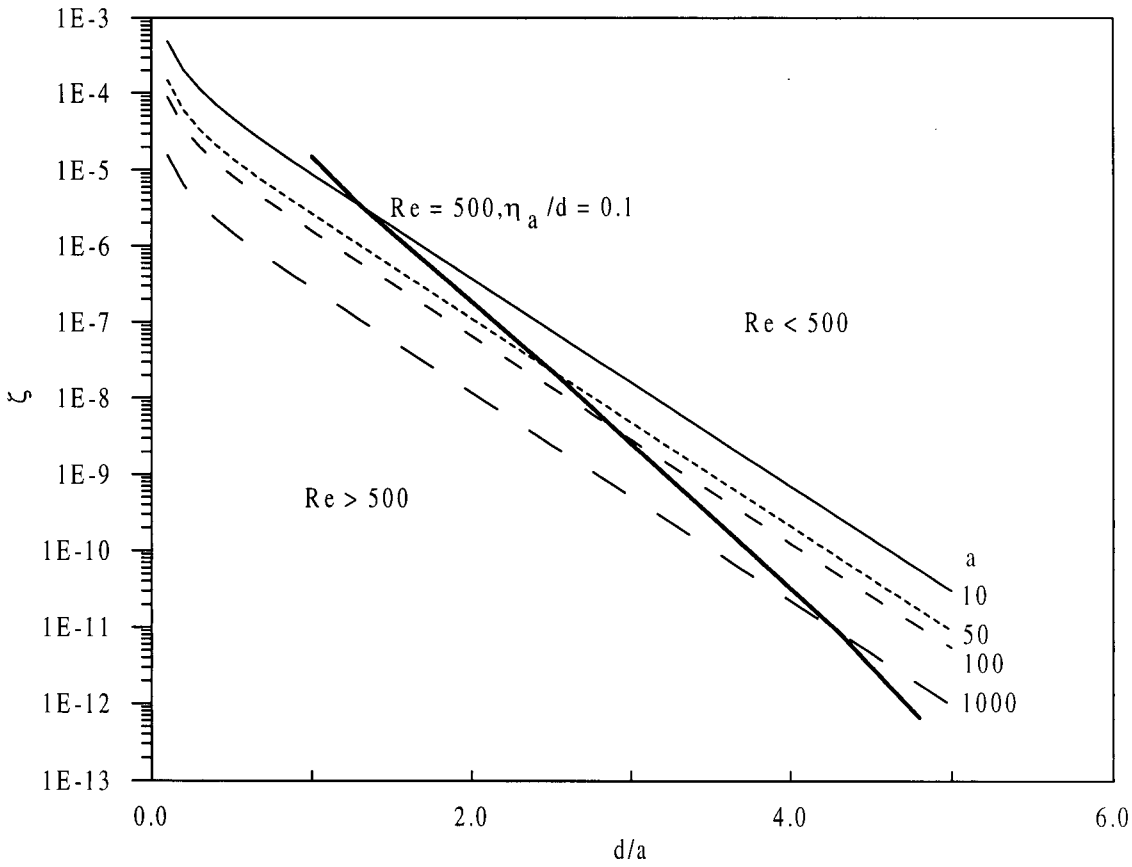


Figure 49. Variation of laminar damping with d/a showing laminar region and turbulent region.

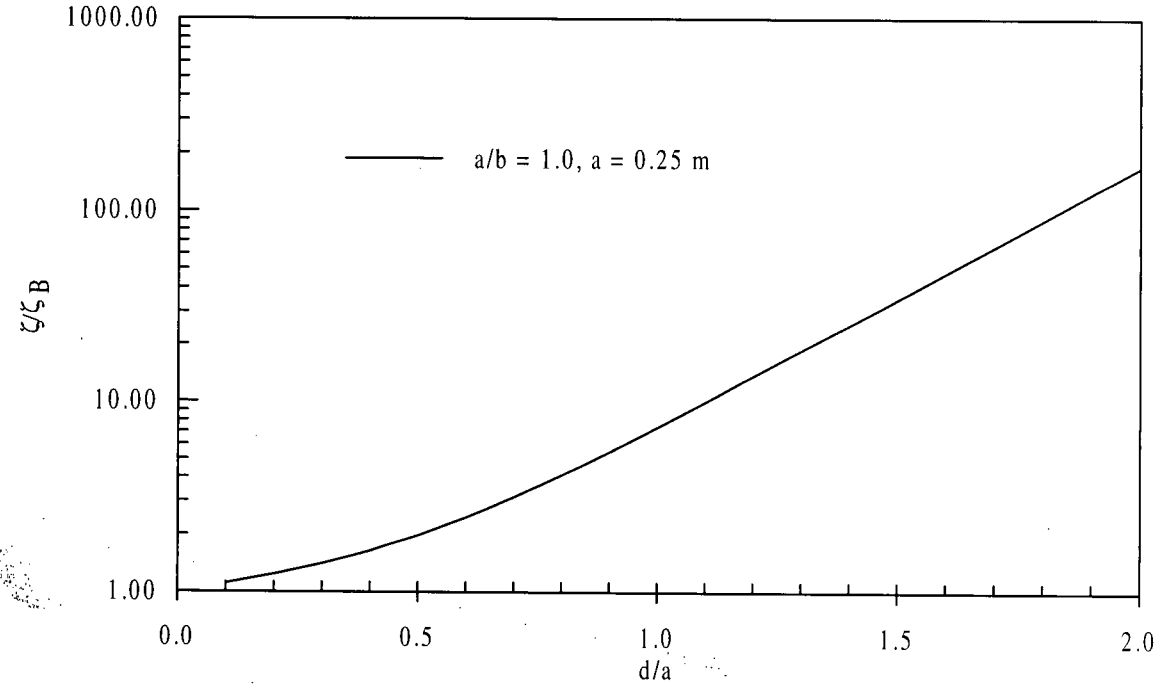


Figure 50. Variation of total damping to bottom boundary damping in laminar regime.

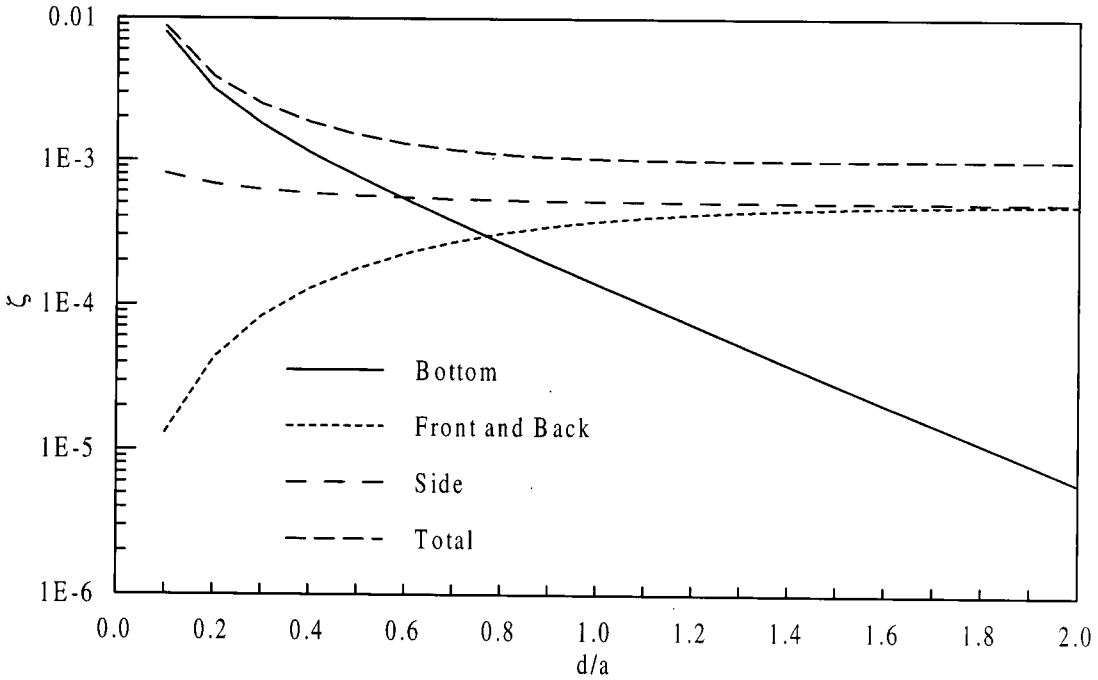


Figure 51. Variation of damping due to different components of the tank due to laminar boundary layer.

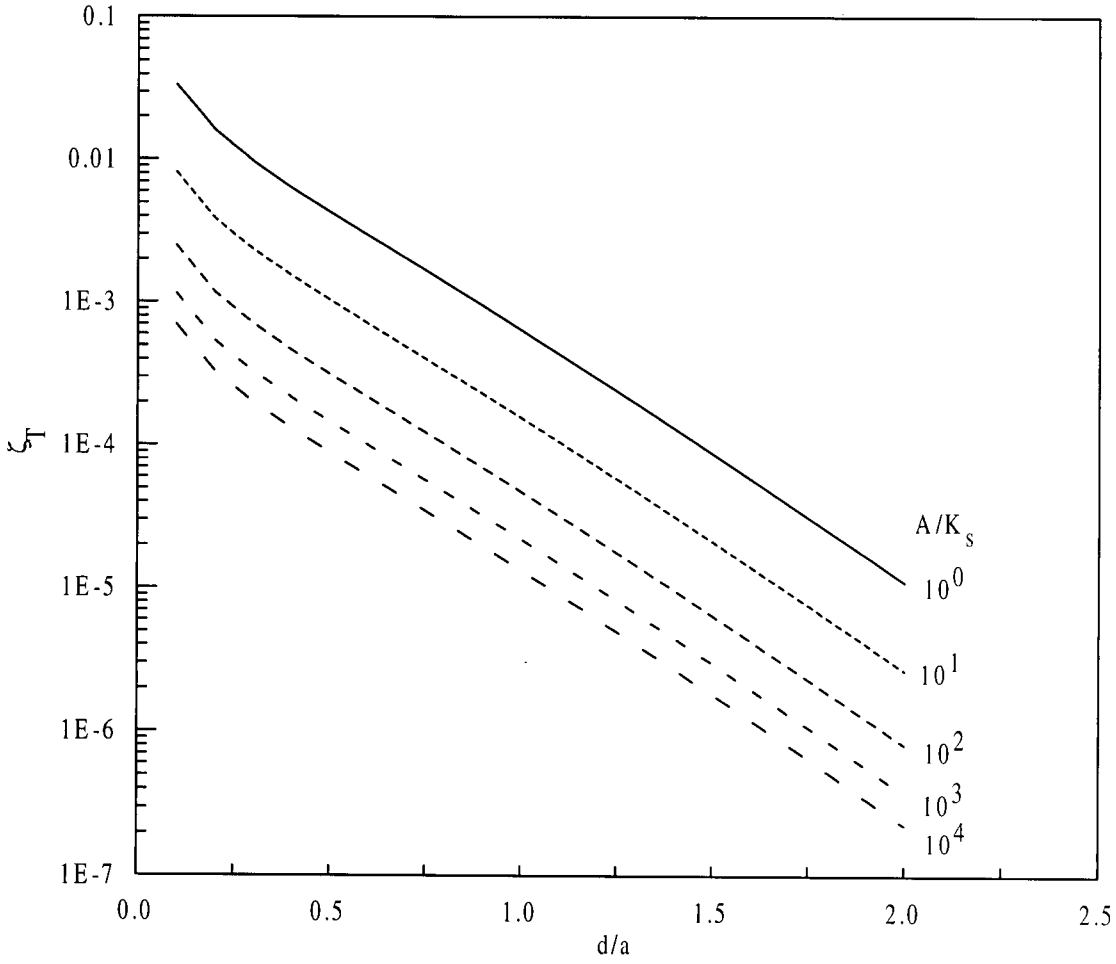


Figure 52. Turbulent damping as functions of d/a and $A/K_s$ for $\eta_a/d = 0.1$.

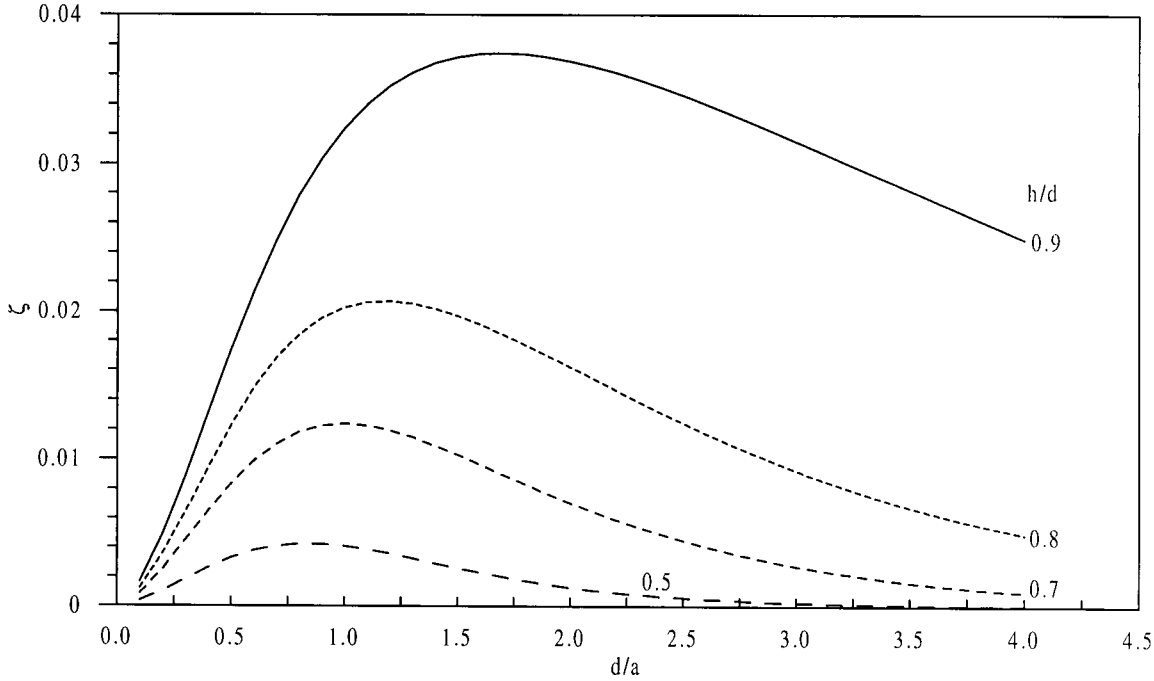


Figure 53. Damping due to horizontal baffles for different values of h/d and for $\alpha = 0.1$ and $\eta_a/d = 0.1$.

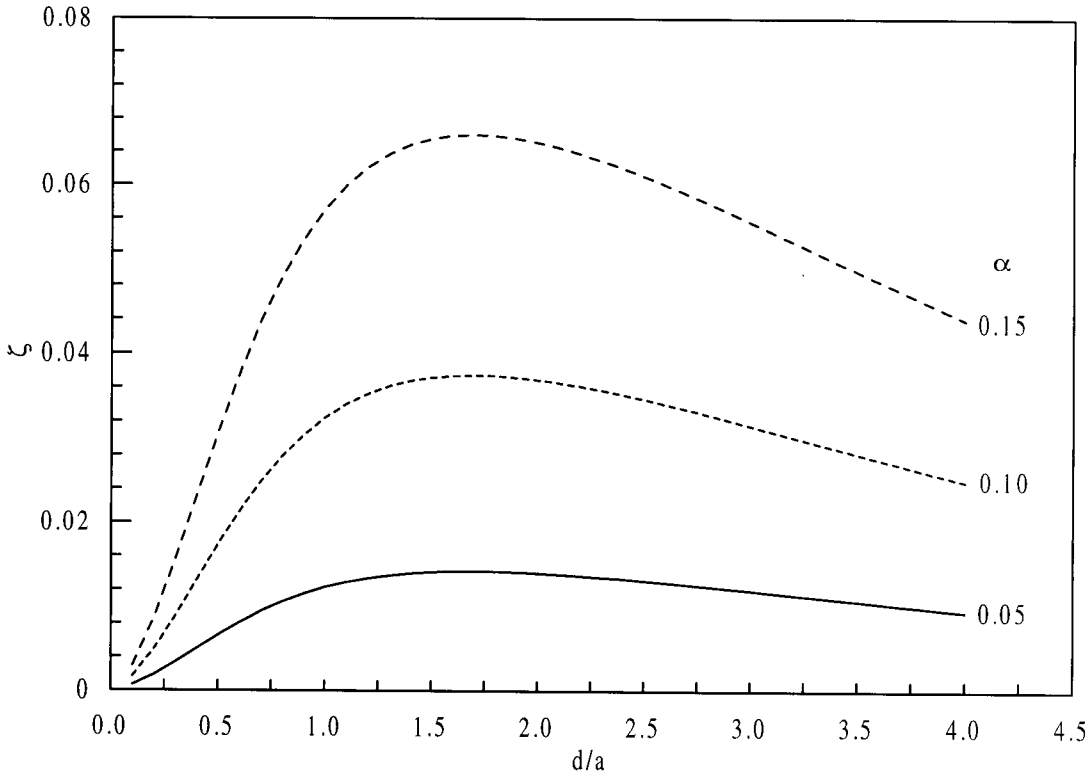


Figure 54. Damping due to horizontal baffles for different values of $\alpha$ and for h/d = 0.9 and $\eta_a/d = 0.1$.

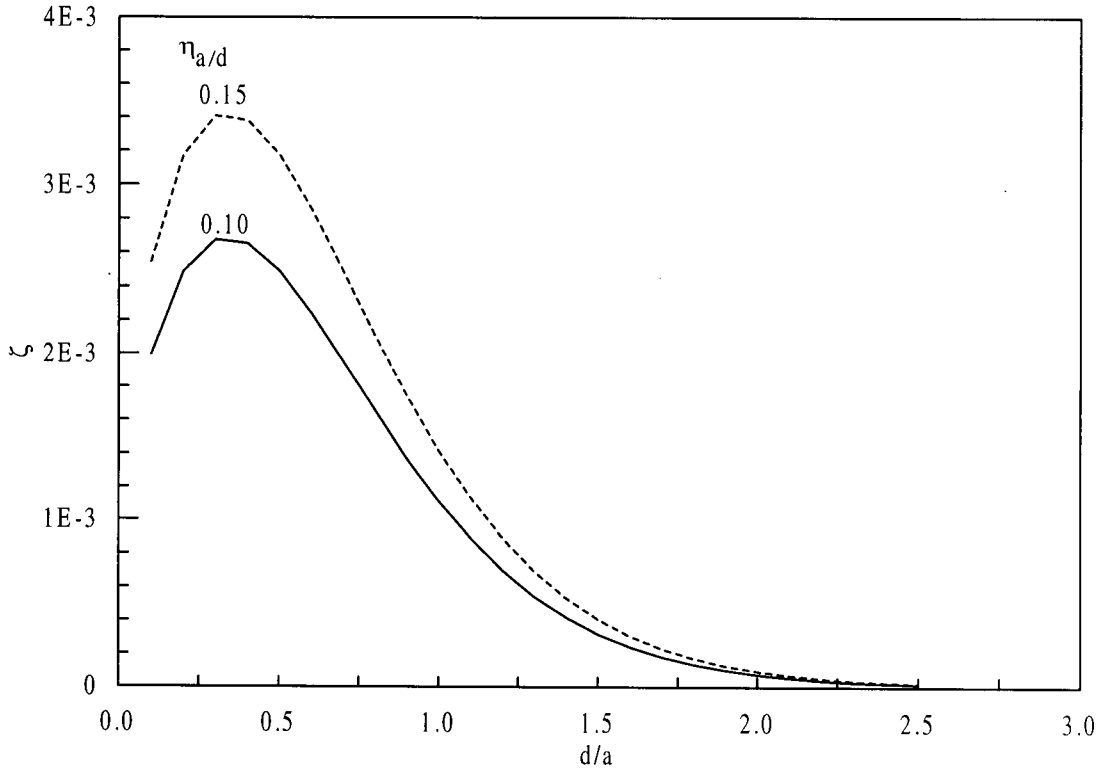


Figure 55. Damping due to a vertical baffle for different value of $\eta_a/d$ values and $\beta = 0.05$.

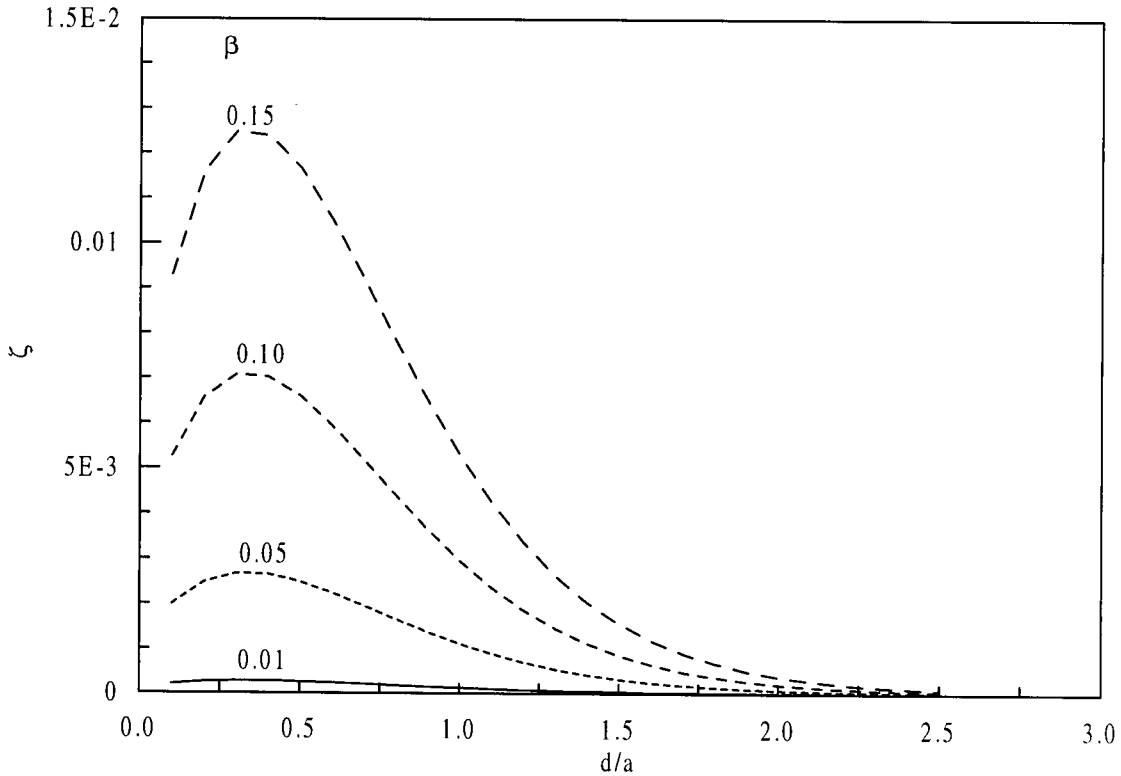


Figure 56. Damping due to vertical baffle for different values of $\beta$ and $\eta_a/d = 0.1$.

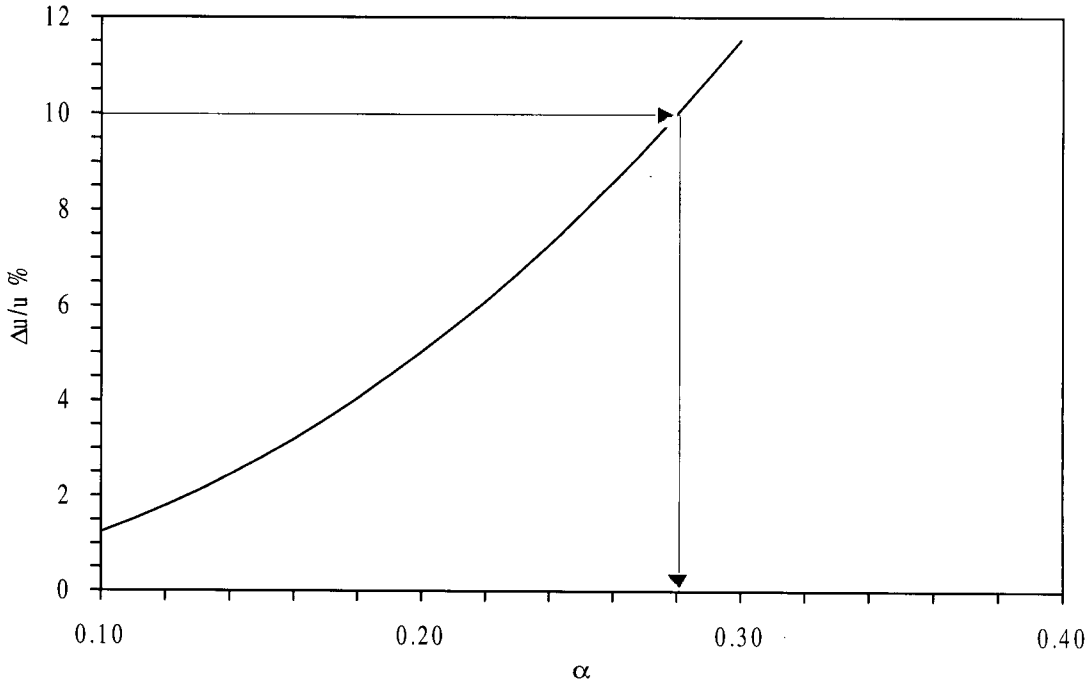


Figure 57. Variation of $\Delta u/u$ with relative baffle length $\alpha$ for horizontal baffles.

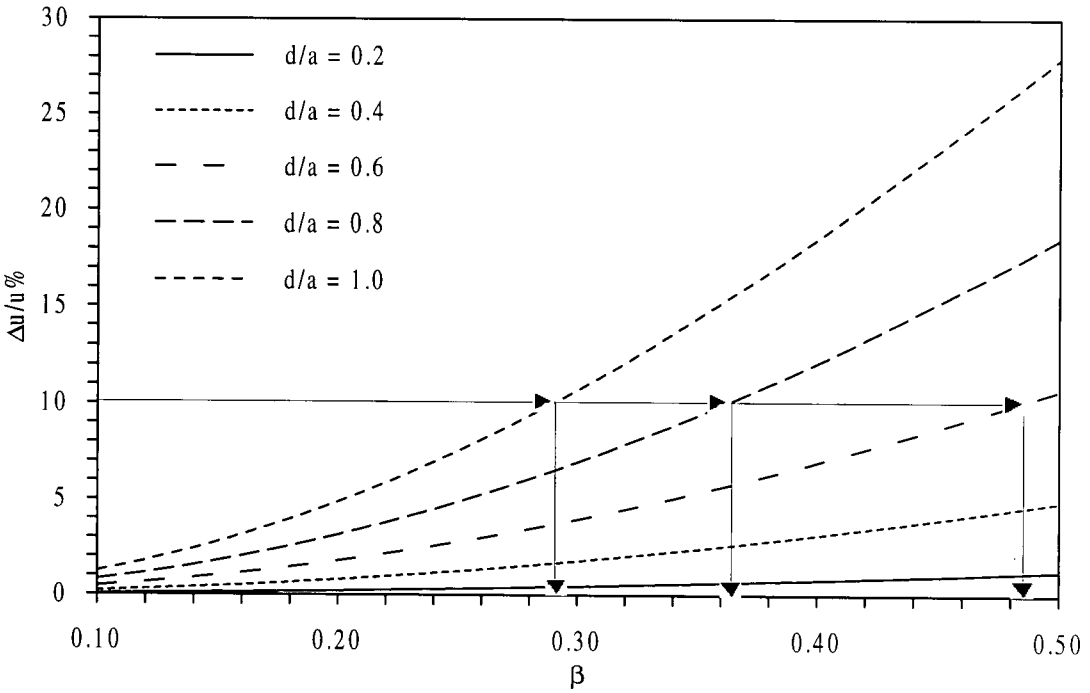


Figure 58. Variation of $\Delta u/u$ with relative baffle length $\beta$ for vertical baffle.

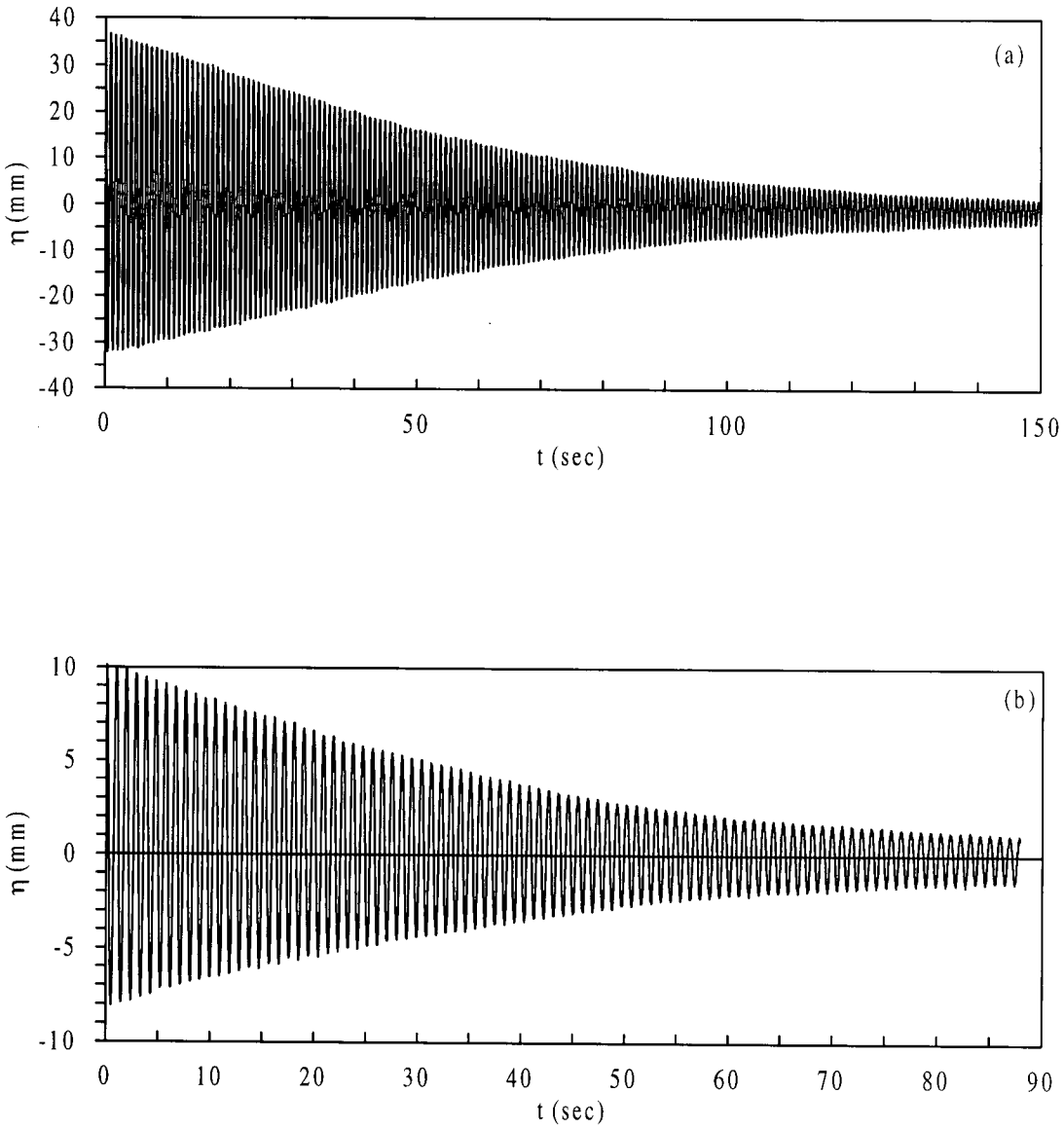


Figure 59. Free vibration test for (a) d/a = 1.0, and (b) d/a = 0.5

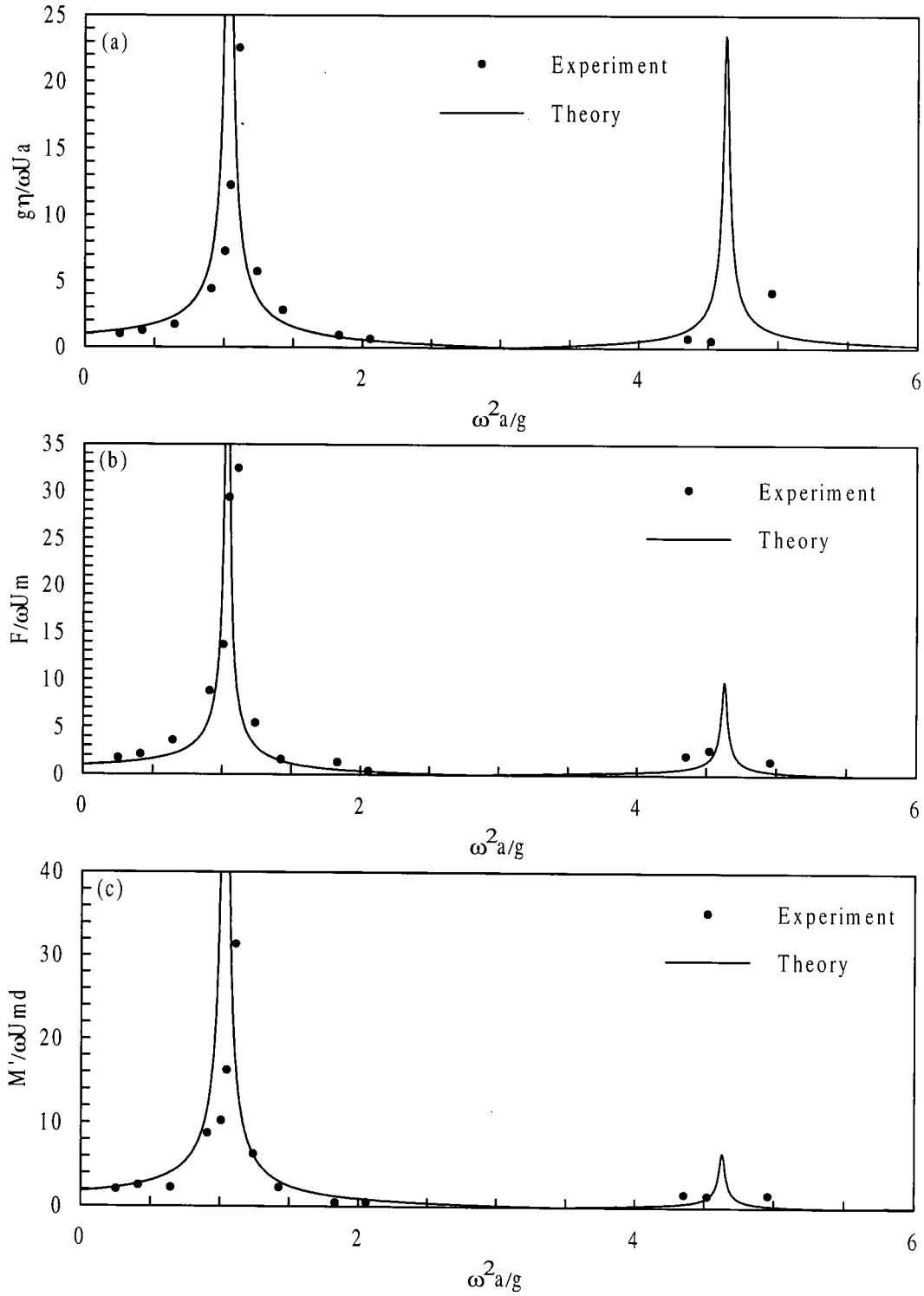


Figure 60. Comparison of theoretical and experimental values for rectangular tank under horizontal harmonic base motion for d/a = 0.5. (a) Free surface elevation, (b) Horizontal force on the tank, (c) Overturning moment at the base.

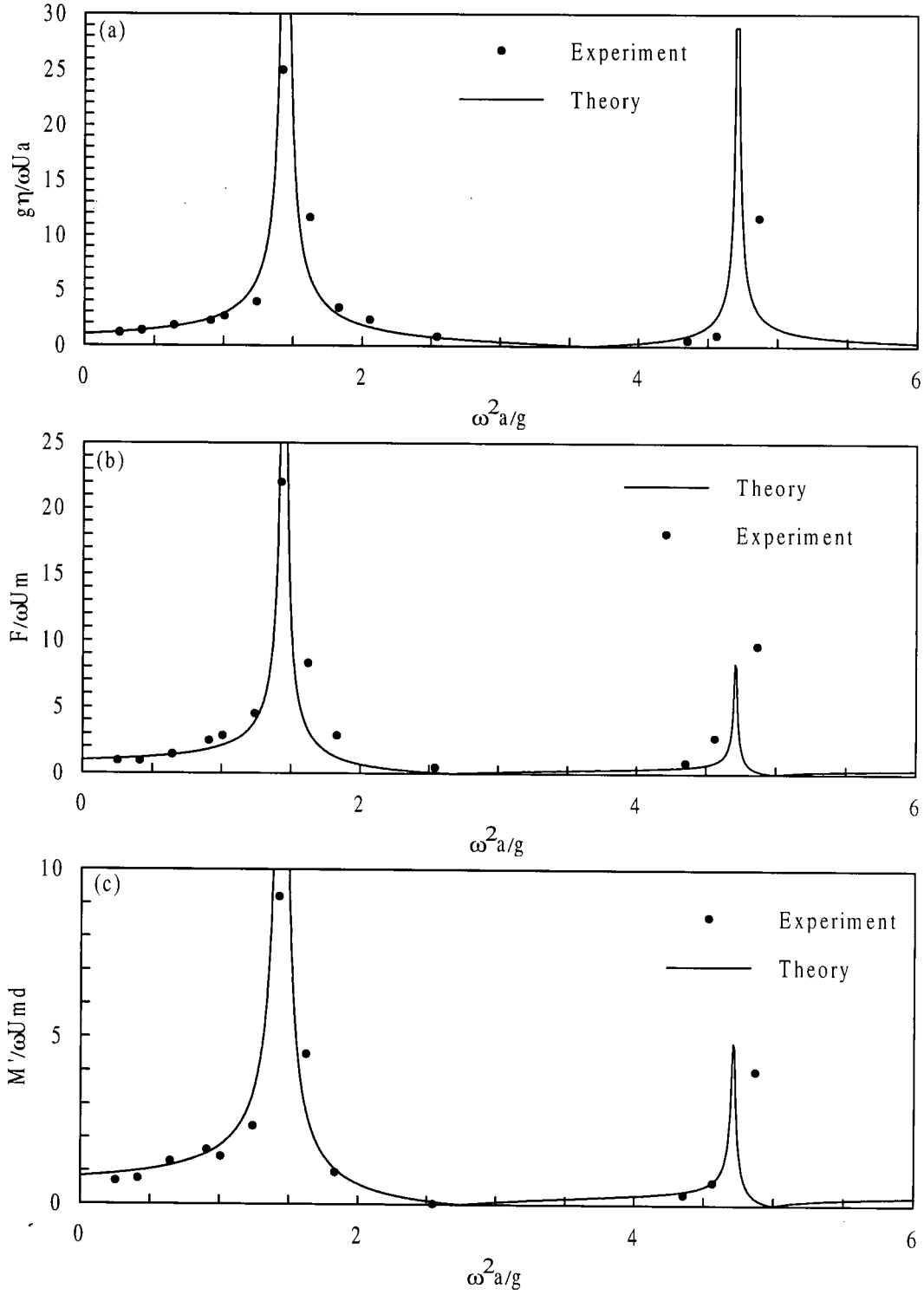


Figure 61. Comparison of the theoretical and experimental values for rectangular tank under horizontal harmonic base motion for d/a = 1.0. (a) Free surface elevation, (b) Horizontal force on the tank, (c) Overturning moment at the base.

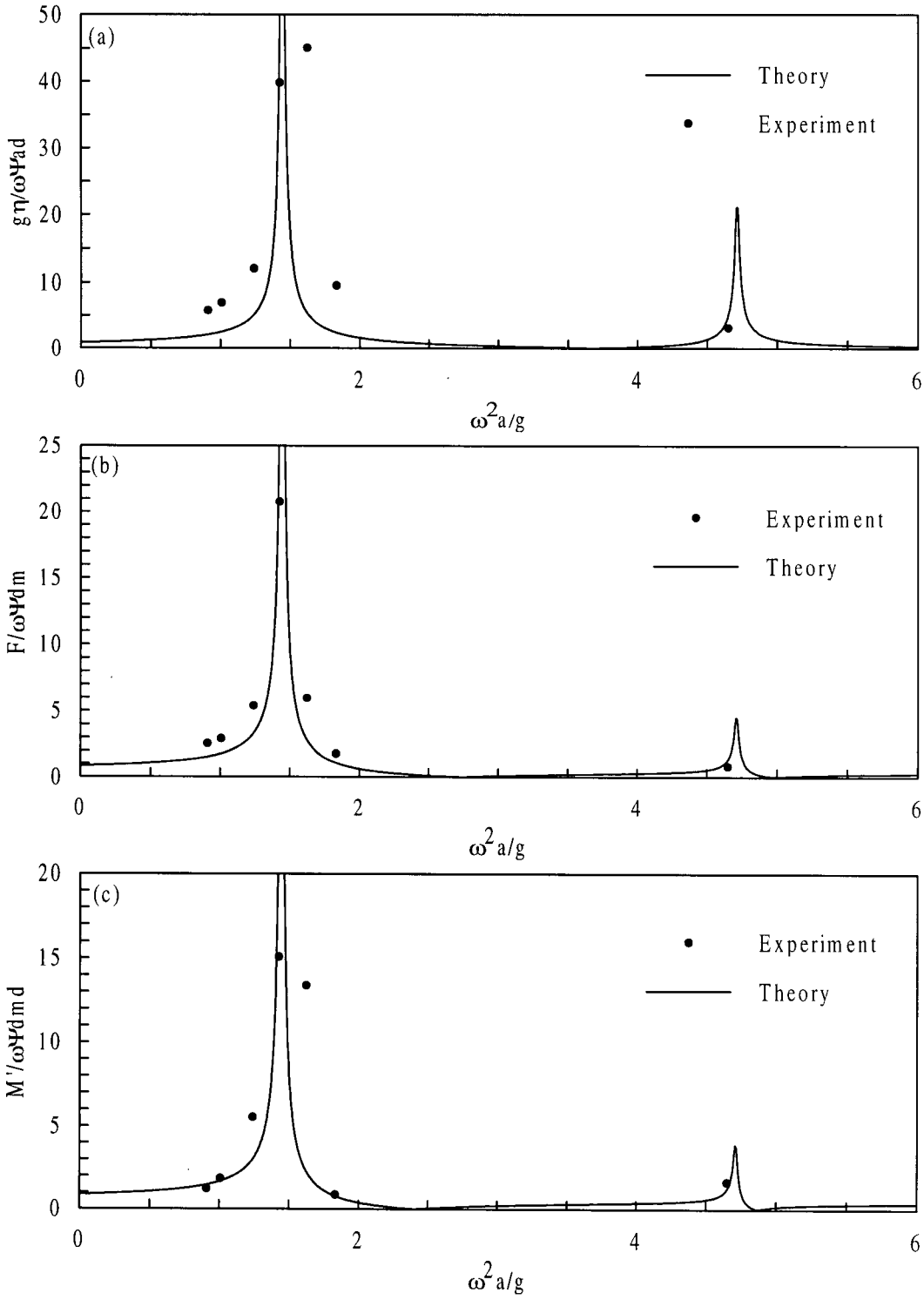


Figure 62. Comparison of theoretical and experimental values of rectangular tank under rocking motion for d/a = 1.0. (a) free surface elevation, (b) horizontal force on the tank, (c) overturning moment at the base.

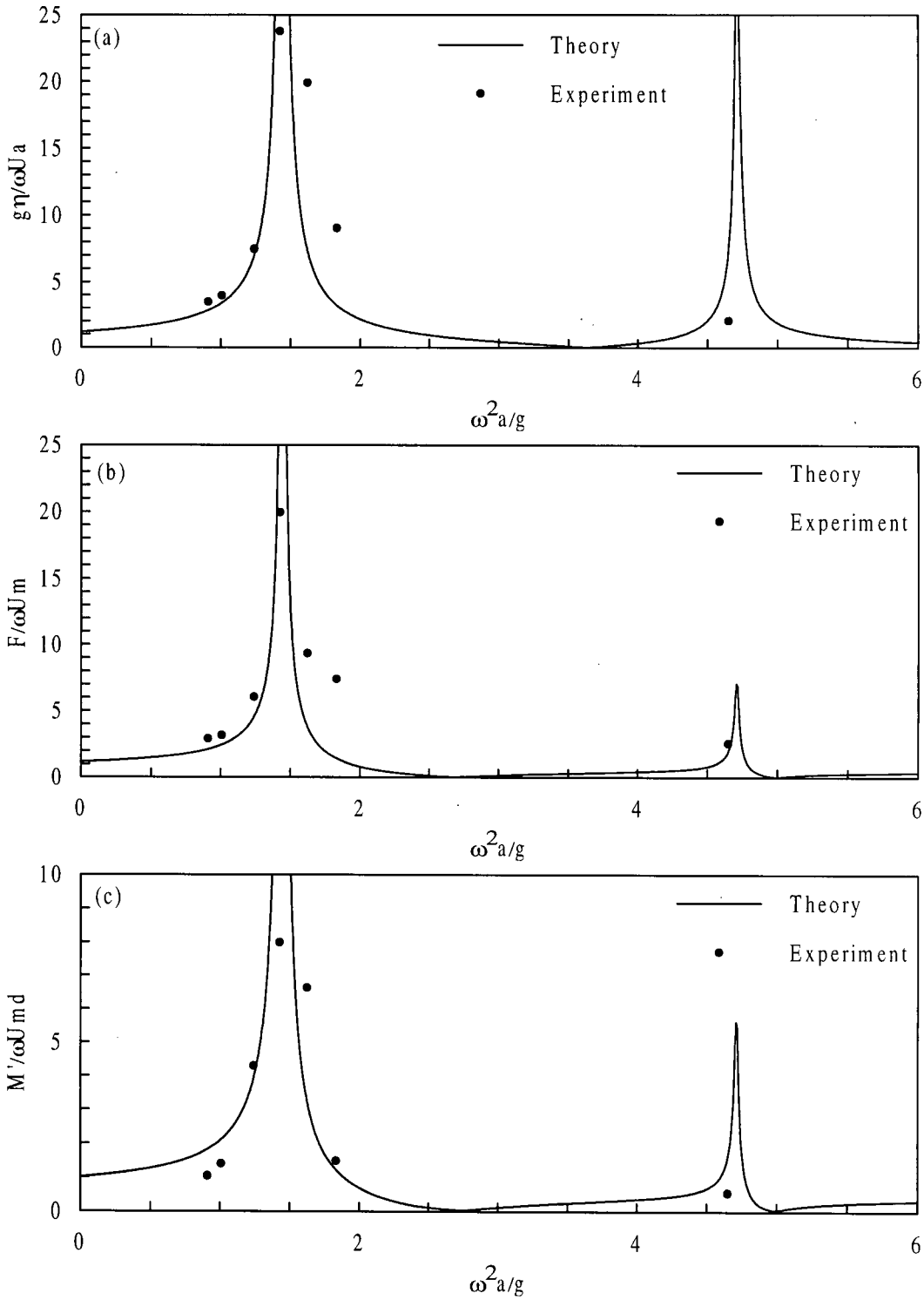


Figure 63. Comparison of theoretical and experimental values for rectangular tank with simultaneous horizontal and rocking motion with relative rocking parameter, $\psi d/U = 0.2$, for $d/a = 1.0$. (a) free surface elevation, (b) horizontal force on the tank, (c) overturning moment at the base.

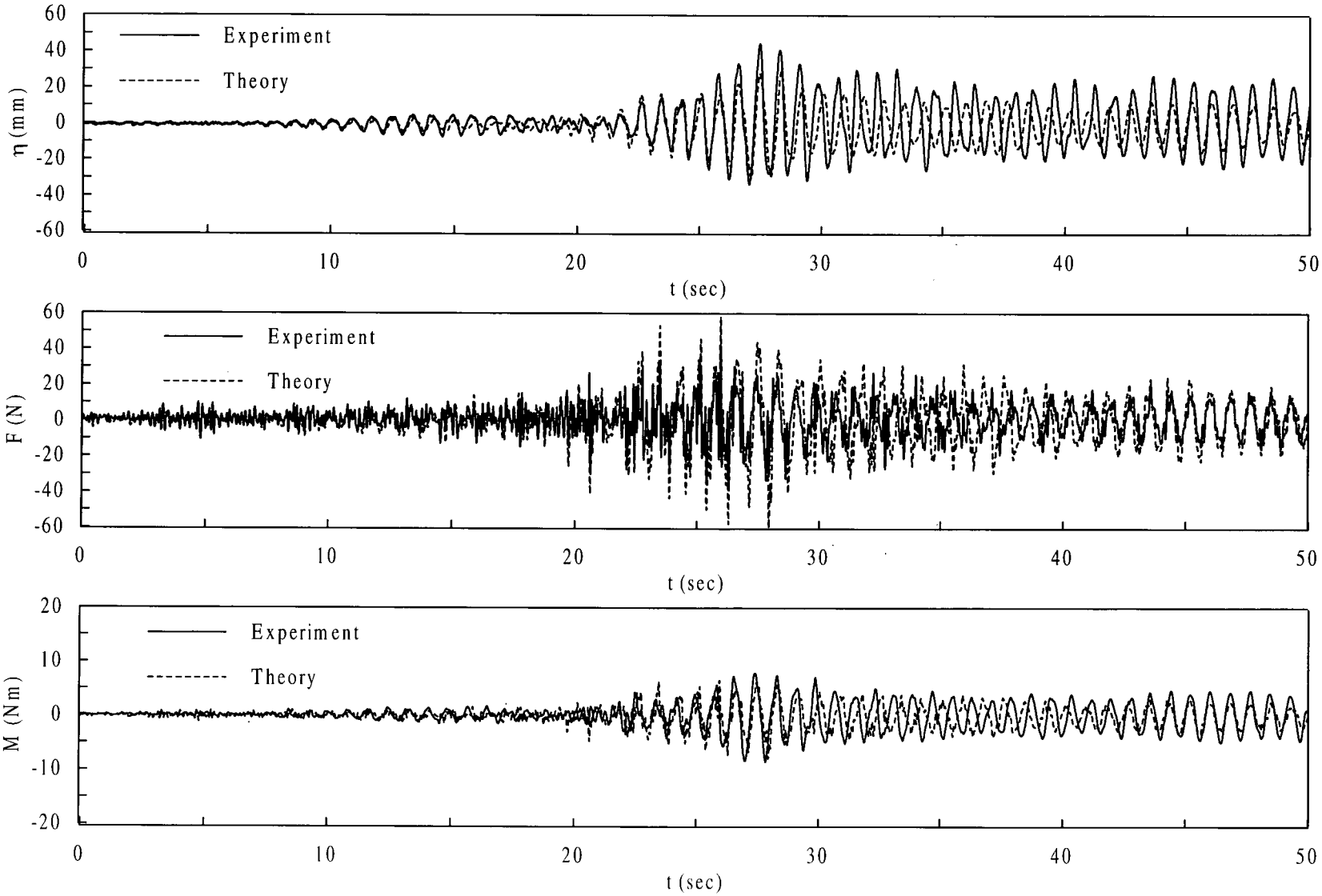


Figure 64. Comparison of theoretical and experimental results for Mexico earthquake.

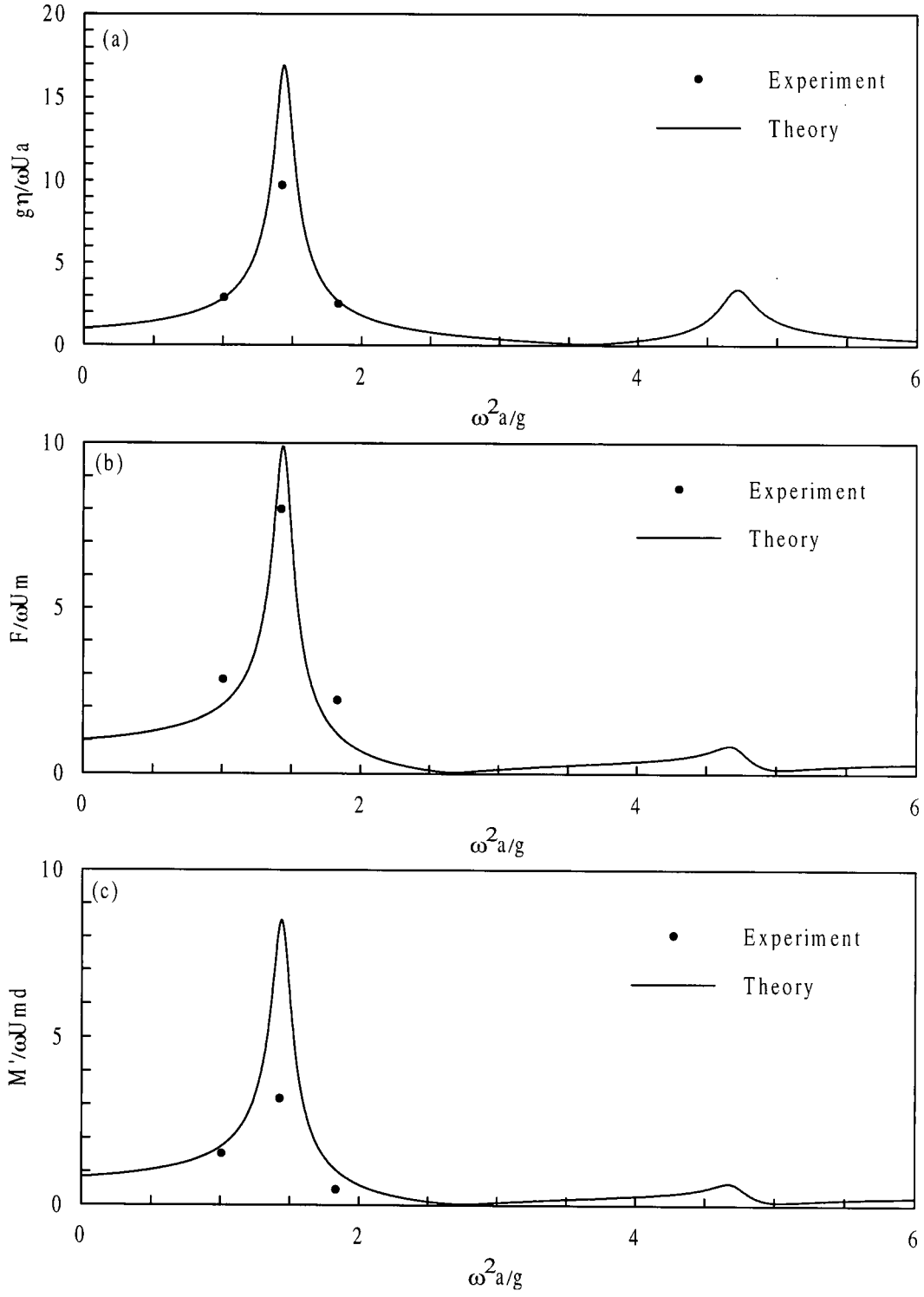


Figure 65. Comparison of theoretical and experimental values for rectangular tank with horizontal baffles under horizontal harmonic base motion for d/a = 1.0 and h/d = 0.8. (a) free surface elevation, (b) horizontal force on the tank, (c) overturning moment at the base.

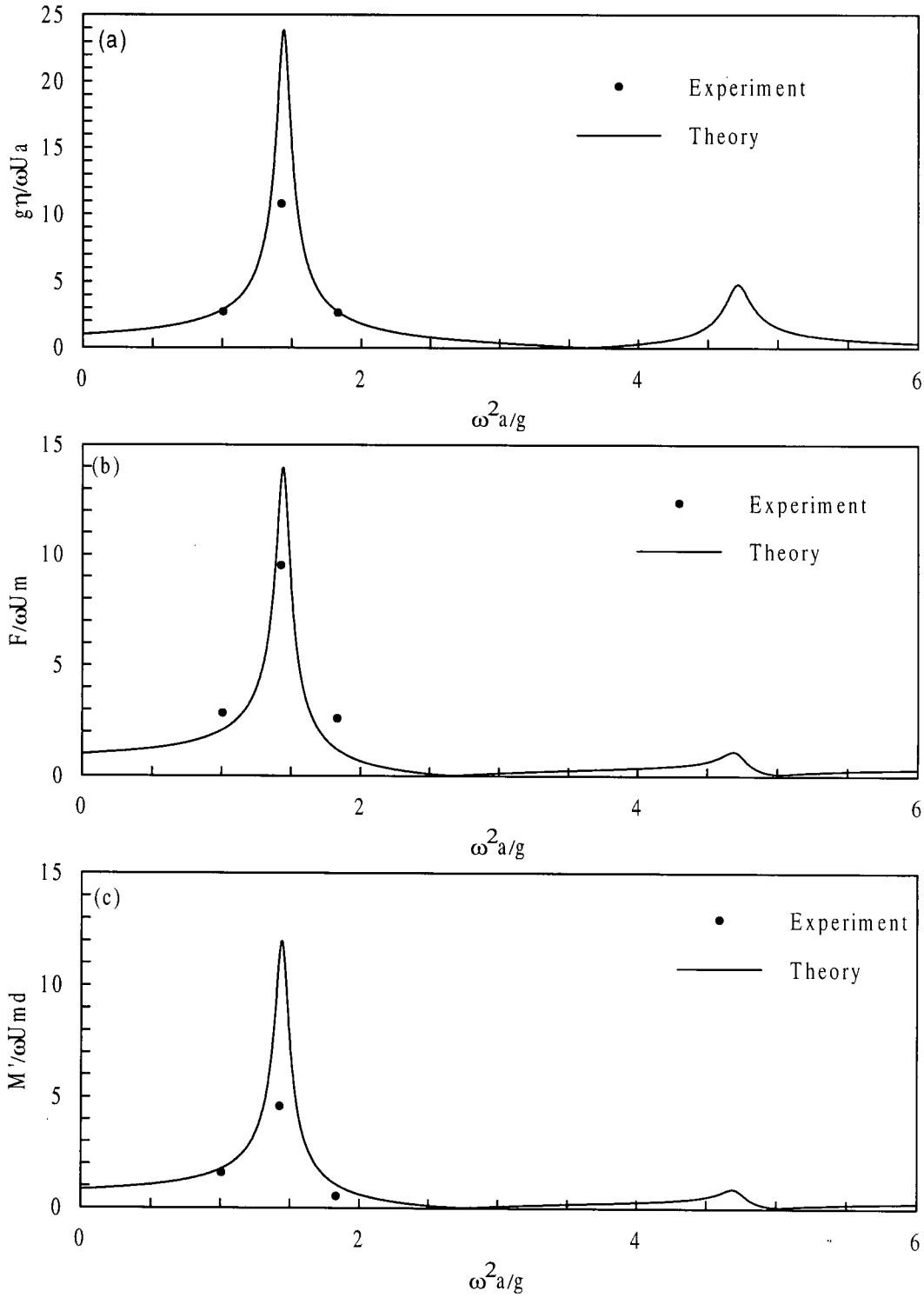


Figure 66. Comparison of theoretical and experimental values for rectangular tank with horizontal baffles under horizontal harmonic base motion for d/a = 1.0 and h/d = 0.7. (a) free surface elevation, (b) horizontal force on the tank, (c) overturning moment at the base.

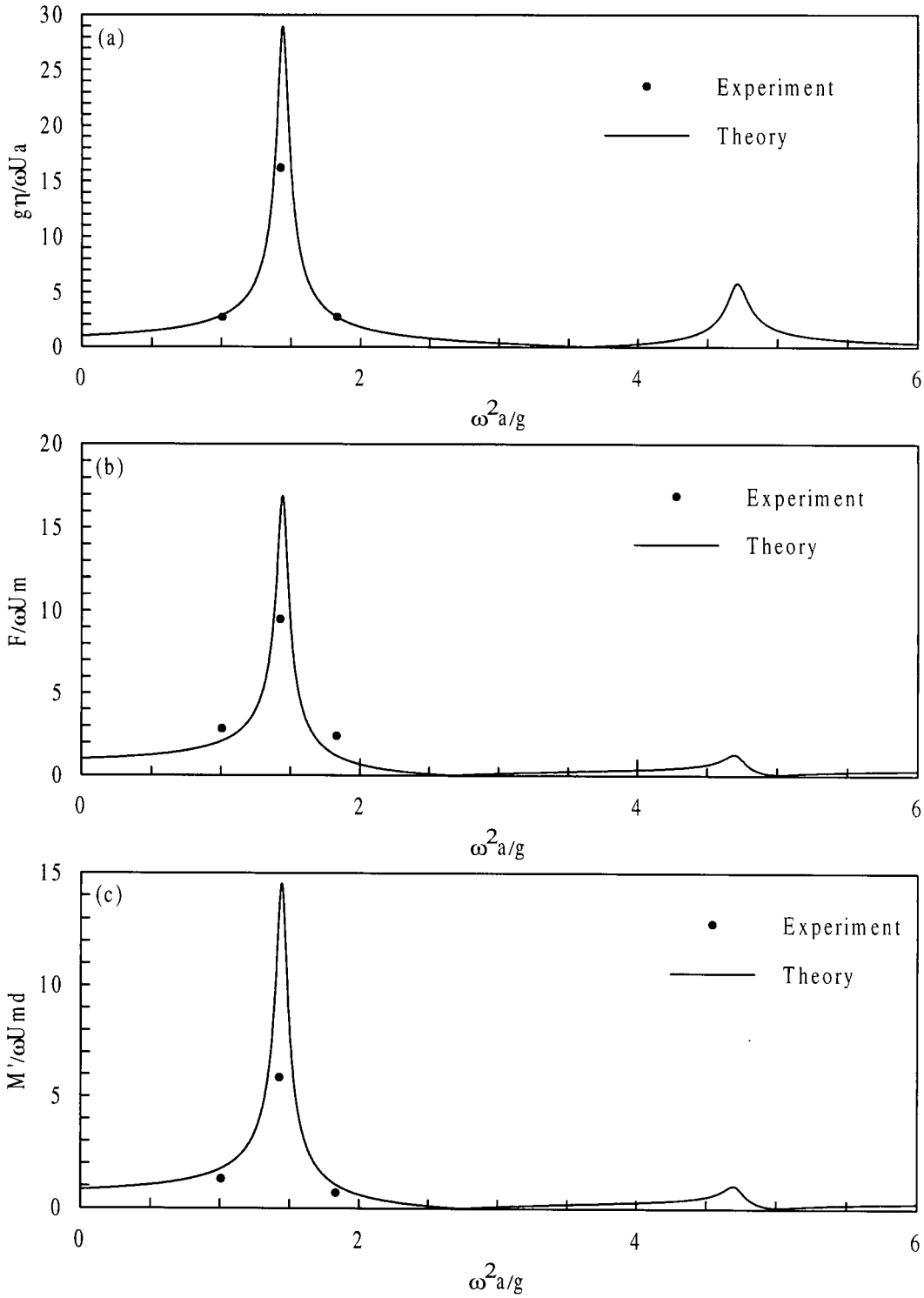


Figure 67. Comparison of theoretical and experimental values of rectangular tank with horizontal baffles under horizontal harmonic base motion for d/a = 1.0 and h/d = 0.6. (a) free surface elevation, (b) horizontal force on the tank, (c) overturning moment at the base.

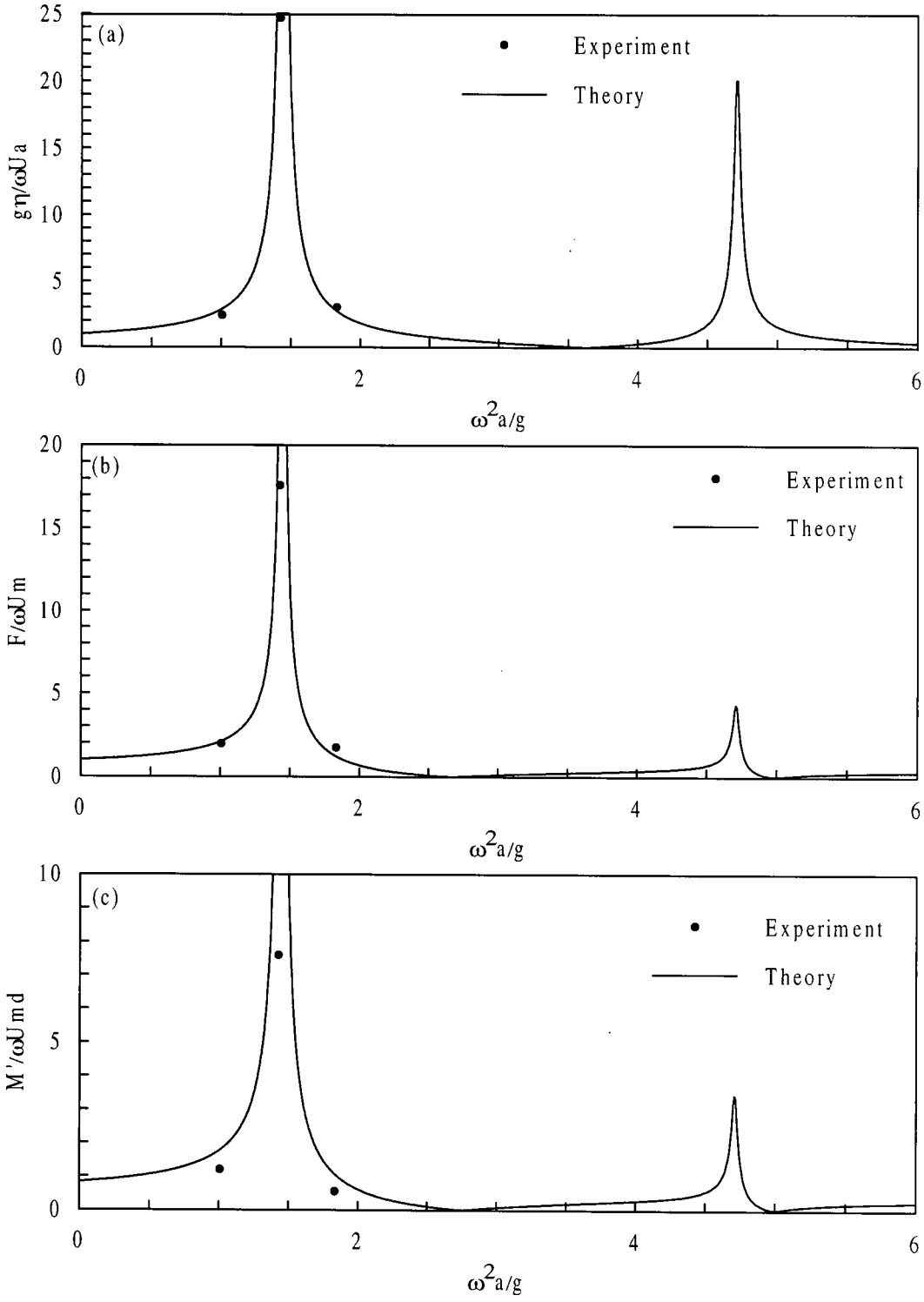


Figure 68. Comparison of theoretical and experimental values for rectangular tank with vertical baffle under horizontal harmonic base motion for d/a = 1.0 and $\ell$/d = 0.1. (a) free surface elevation, (b) horizontal force on the tank, (c) overturning moment at the base.

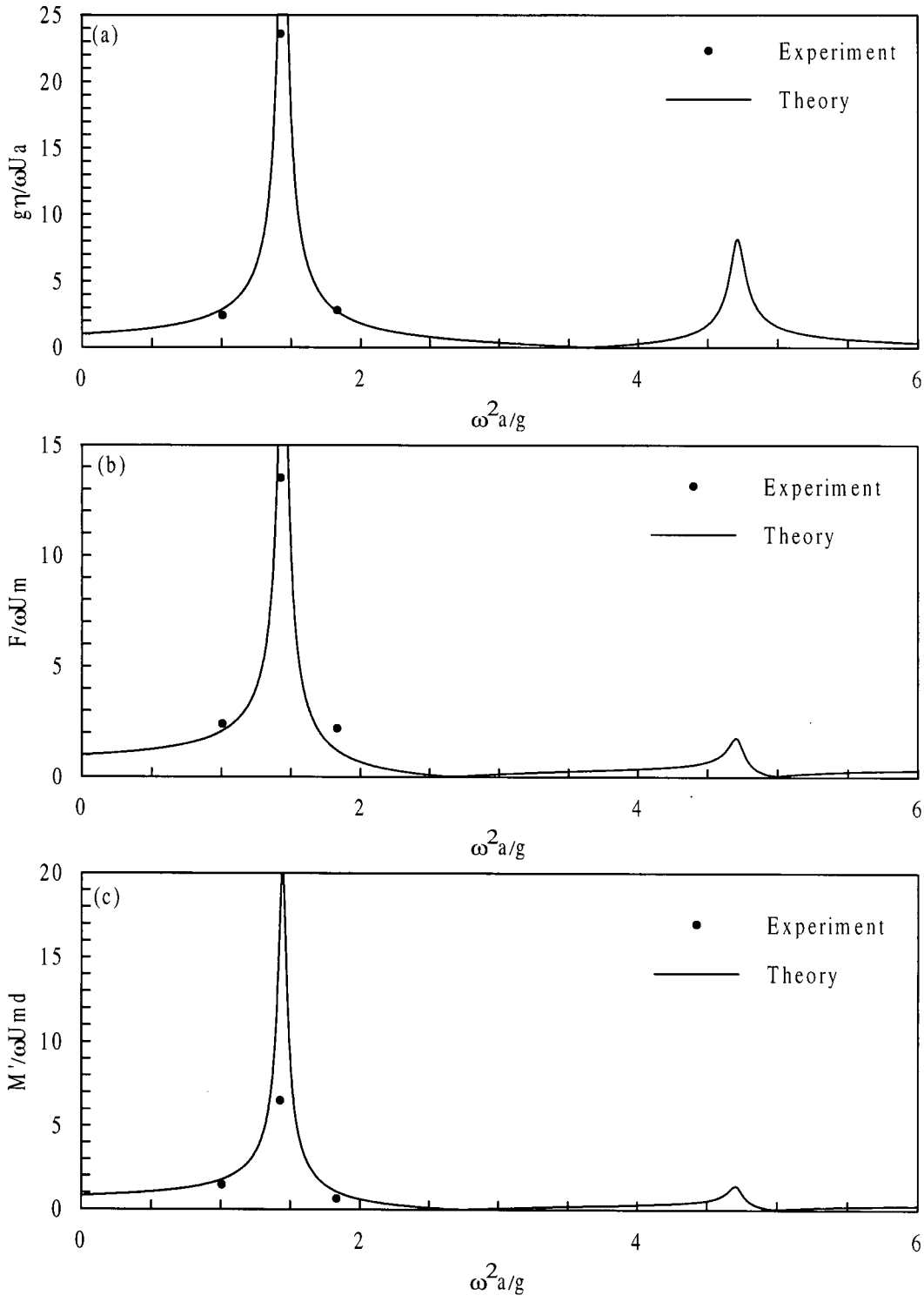


Figure 69. Comparison of theoretical and experimental values for rectangular tank with vertical baffle under horizontal harmonic base motion for d/a = 1.0 and $\ell$/d = 0.2. (a) free surface elevation, (b) horizontal force on the tank, (c) overturning moment at the base.

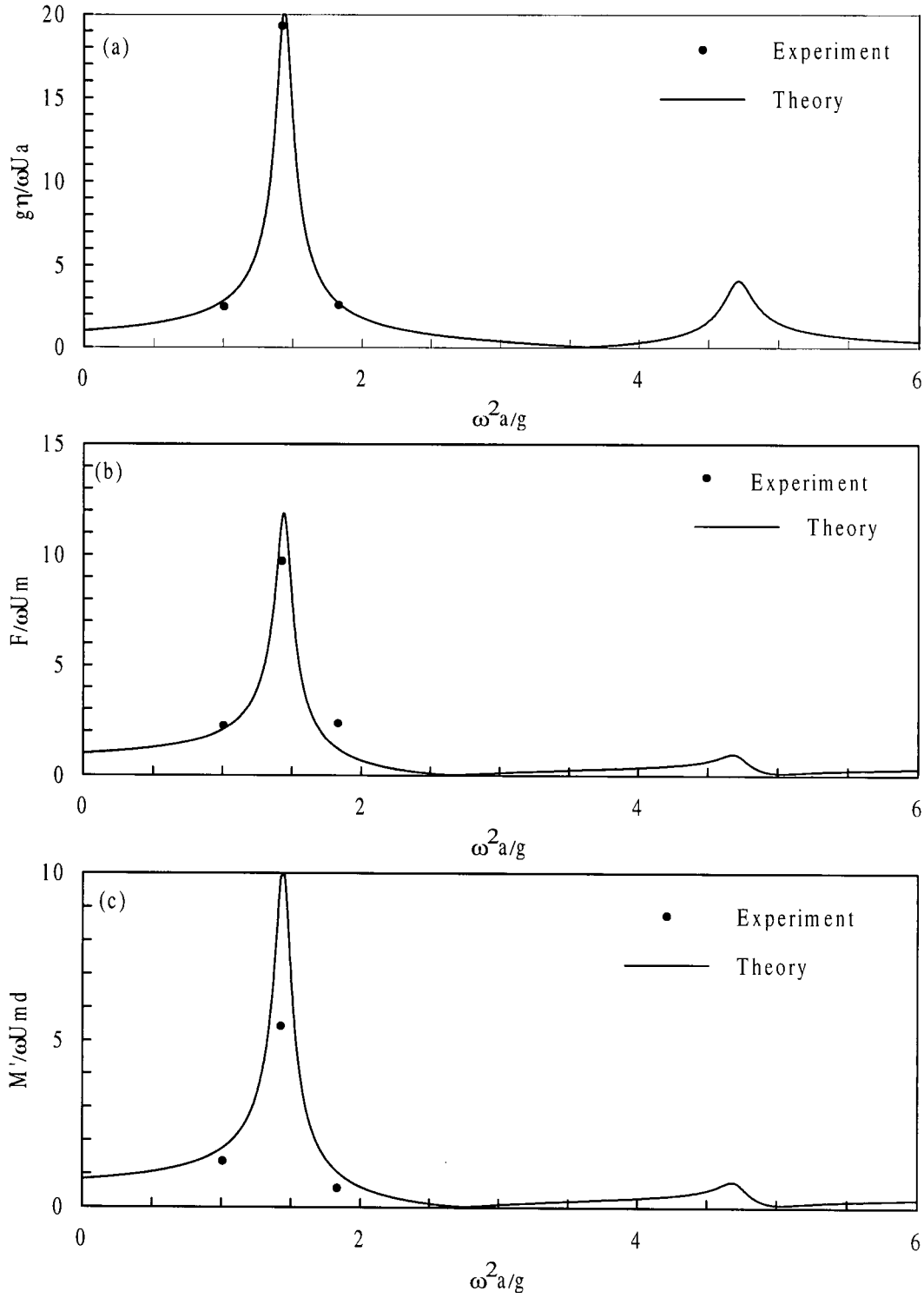


Figure 70. Comparison of theoretical and experimental values for rectangular tank with vertical baffle under horizontal harmonic base motion for d/a = 1.0 and $\ell$/d = 0.3. (a) free surface elevation, (b) horizontal force on the tank, (c) overturning moment at the base.

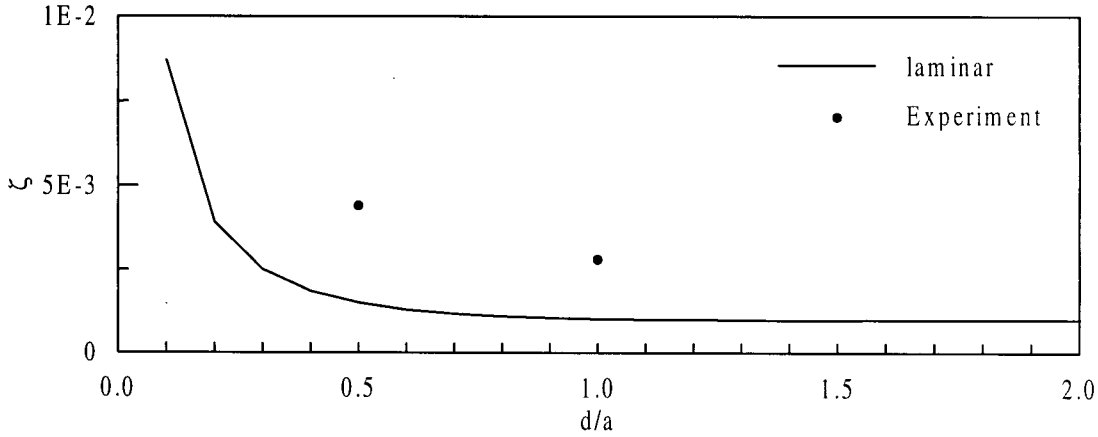


Figure 71. Comparison of theoretical and experimental damping coefficient.

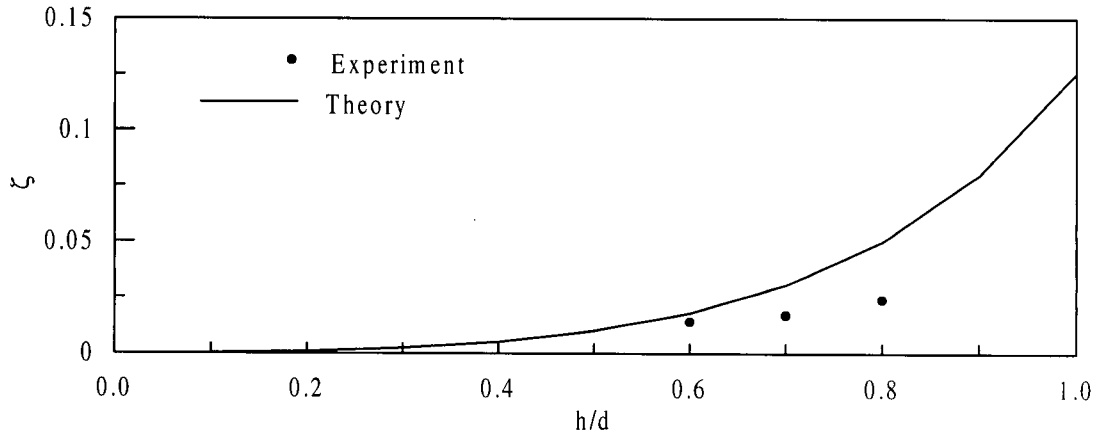


Figure 72. Comparison of theoretical and experimental damping coefficient in the presence of horizontal baffles.

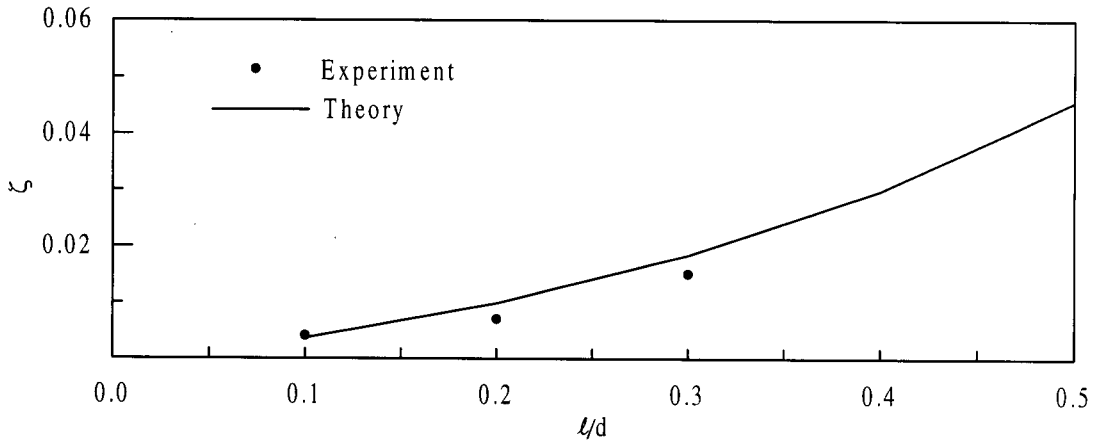


Figure 73. Comparison of theoretical and experimental damping coefficient in the presence of a vertical baffle.

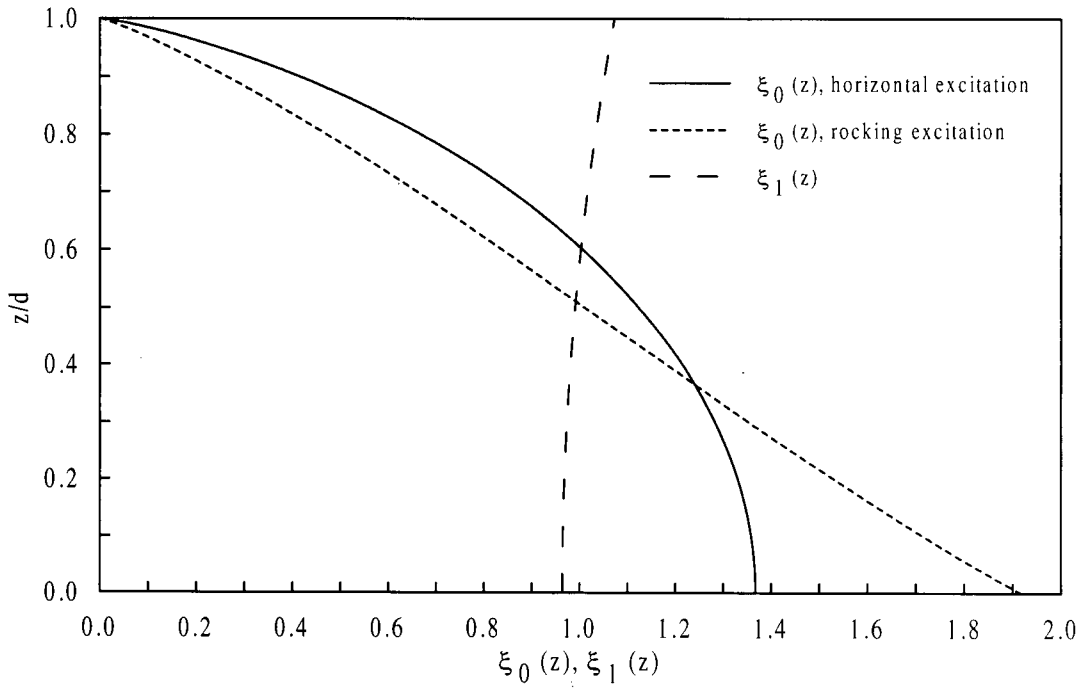


Figure 74. Distribution of dimensionless masses $m_0/m$ and $m_1/m$ with elevation for a rectangular tank with a = 100m and d = 30m.

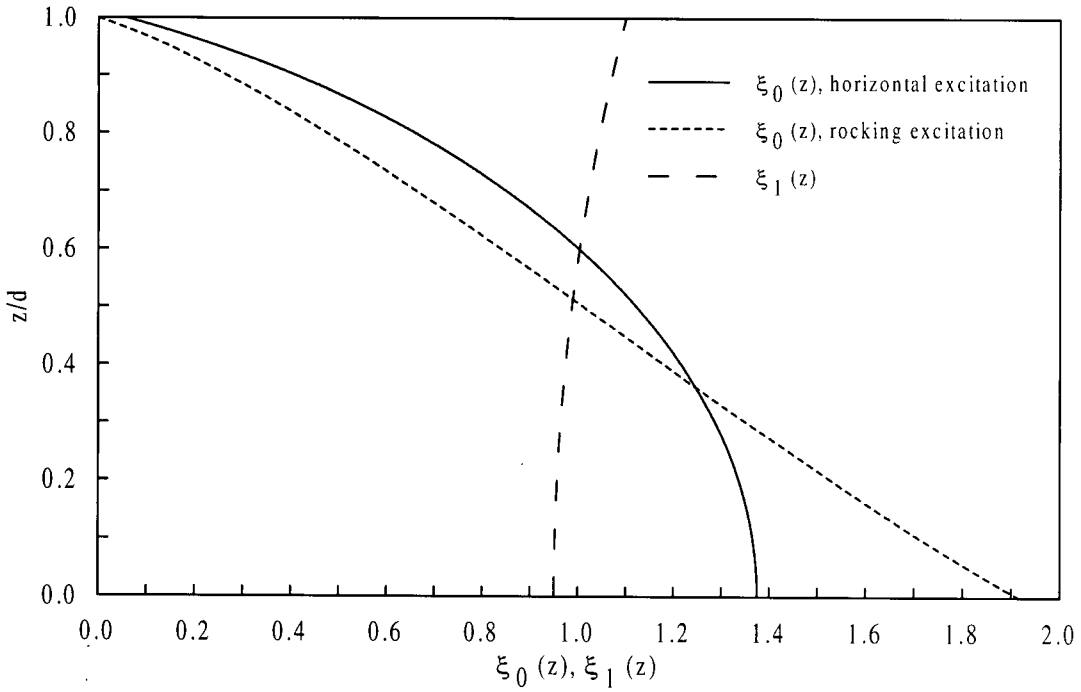


Figure 75. Distribution of dimensionless masses $m_0/m$ and $m_1/m$ with elevation for a circular tank with a = 100m and d = 30m.